UNIVERSITÀ
DEGLI STUDI
DI PADOVA

FACSIMILE FRONTESPIZIO TESI

Sede Amministrativa: Università degli Studi di Padova

Dipartimento di
Ingegneria Industriale

CORSO DI DOTTORATO DI RICERCA IN: Ingegneria Industriale
CURRICOLO: Energia
CICLO: XXIX

Numerical simulations of fires in road and rail tunnels with structural and fluid dynamic analysis

Coordinatore: Ch.mo Prof. Colombo Paolo

Dottorando : Matteo Pachera

UNIVERSITY OF PADUA

DOCTORAL THESIS

Numerical simulations of fires in road and rail tunnels with structural and fluid dynamic analysis

Author:
Matteo Pachera

Supervisor:
Prof. Pierfrancesco Brunello

A thesis submitted in fulfillment of the requirements for the degree of Doctor of Philosophy

at the

Post-Graduate Course in Industrial Engineering

XXIX CYCLE

Declaration of Authorship

I, Matteo Pachera, declare that this thesis titled, "Numerical simulations of fires in road and rail tunnels with structural and fluid dynamic analysis" and the work presented in it are my own. I confirm that:

- This work was done wholly or mainly while in candidature for a research degree at this University.
- Where any part of this thesis has previously been submitted for a degree or any other qualification at this University or any other institution, this has been clearly stated.
- Where I have consulted the published work of others, this is always clearly attributed.
- Where I have quoted from the work of others, the source is always given. With the exception of such quotations, this thesis is entirely my own work.
- I have acknowledged all main sources of help.
- Where the thesis is based on work done by myself jointly with others, I have made clear exactly what was done by others and what I have contributed myself.

Signed: _____

Date: _____

"Knowing is not enough, we must apply.
Willing is not enough, we must do. "

Johann Wolfgang von Goethe

UNIVERSITY OF PADUA

Summary

School of Engineering
Department of Industrial Engineering

Doctor of Philosophy

Numerical simulations of fires in road and rail tunnels with structural and fluid dynamic analysis

by Matteo Pachera

The present works investigates with numerical methods the performance of longitudinal ventilation system and the structural response of a tunnel in case of fire. Computational fluid dynamics allows to simulate the flow field in a generic domain solving the equations of Navier Stokes. Several codes have been developed for the purpose and due to its specific development the code Fire Dynamic Simulator has been chosen, FDS. FDS is used to simulate the flow field induced by a fire and by jet fans in order to evaluate the capability of the devices to confine the smoke. Jet fans in tunnel have been modelled and validated against different experiments in cold flow, in order to compare pressure and velocities. The fire has been later added and an entire tunnel has been simulated with jets fan activated, the results have been compared with experimental measurements for temperatures, velocities and volume flows. The simulations assessed the capabitity of FDS to simulate jet fans and fire predicting the pressure rise, velocity decay of the jet and the smoke confinement. FDS is also capable to correctly predict the throttling effect inside a tunnel considering the reduction of the volume flow rate across the tunnel due to the fire.

FDS has been later used also to predict the thermal loads on a concrete structure exposed to fire. A structural code developed at the University of Padua, Comes-HTC, has been used to simulate the response of concrete at high temperature. The code has been coupled with FDS in order to use a realistic set of boundary conditions for the structural calculation. To couple the two codes an interpolation approach has been proposed and verified for the interfacing of Cartesian grids and structured grids. The coupled approach has been applied to study a concrete slab exposed to different fire scenarios, evaluating the influence of the fire growth rate and the HRR per unit of area. The coupled analysis has been applied to study a rail coach on fire in a tunnel, the study focused both on the modelling of the fire scenario and on the response of the vault. The coupled approach has been developed to transfer the results from FDS to Comes-HTC, however in order to study the influence of the structure on the fluid a two way coupling has been tested for the slab exposed to fire. Another coupled approach has been proposed embedding the Comes-HTC model in FDS. The different approaches showed similar results, therefore the one way coupling is considered the most usable, due to its capability to coupled also non-corresponding geometries.

Acknowledgements

I would like to thank first my supervisor Prof. Brunello, who gave me the opportunity to study and discover the fire safety engineering, letting me investigate several topics in this wide engineering field. I would like to thank Prof. Pesavento for supporting my research even without being my official supervisor. Without his help and advises the coupled analysis for concrete structures would not be developed. I would also like to thank him for the long chats about thesis development and the research topics we want to investigate. I would like to thank Prof. Gawin for welcoming me in Łódź and supporting me during the period spent in Poland with his precious advises. I would like to thank Dr. Witek for his help in the first stages of the work in Łódź and for our long talks in the office. I would like to thank Dr. Sztarbała for his suggestion about the need of validation of the jet fan model in FDS, without him one chapter of this thesis would be missing. I want to thank also everyone who gave me any suggestion, advise or critic about my work, these feedbacks allowed me to improve my research and to make it better.

I want also to thank my fiancé, Marlena, for supporting my involvement in the work and for standing patiently my extra working hours when I was writing my thesis. She believed in me as researcher and partner, being next to me in our happy and though times. I want to thank my parents, Giuditta and Gianlucillo, my brothers, Andrea and Luca, and Umberto for supporting in my choices during these years and being close to me even if we were many kilometres far away. I want to thank also the family of Marlena, Witold, Beata, Wiktoria and Łukasz, for welcoming me and for making me feeling at home whenever I visit them. I want to thank all the friends I left in Italy and around the world, Stefano, Gabriele, Andrea, Giovanni, Giangi, Enrico Agostino, Hagar, David, Andrea, Paolo, Stefano, Simone, Matteo, Marco, Dario, Gava, Alberto, Benedetto, Jacopo, Andrea, Simone, Pera, Giulia, Enrico, Paola, Marco and Mirko. I also want to thank all the people I met in Łódź, Arek, Witek, Patryk, Piotrek, Ania, Kuba, Lidka, Ola, Igor, Magda, George, Matteo, Nico and Enrico.

Contents

Declaration of Authorship iii

Summary vii

Acknowledgements ix

1 Introduction 1
1.1 Tunnel ventilation test . . . 1
1.1.1 EUREKA project . . . 2
1.1.2 The Memorial Tunnel Fire Ventilation Test Program (MTFVTP) . . . 3
1.1.3 2nd Benelux Tests 2002 . . . 4
1.1.4 Other big scale test . . . 6
1.2 Smoke confinement and critical velocity . . . 7
1.2.1 Scaling process: from small scale to big scale . . . 10
1.2.2 Smoke confinement by means of jet fans . . . 11
1.3 Structural behaviour of concrete tunnels . . . 12
1.3.1 Temperature near the tunnels' ceiling in case of fire . . . 13
1.3.2 Structure failure and spalling . . . 16
1.3.3 Modelling of concrete at high temperatures . . . 20

2 Early validation cases 25
2.1 Introduction to FDS . . . 25
2.1.1 Governing equations . . . 26
2.2 Natural ventilation in a partially heated cavity . . . 28
2.2.1 Experiment description . . . 28
2.2.2 Numerical modelling and simulation results . . . 29
2.3 Natural ventilated fire in a large room . . . 34
2.3.1 Experiment description . . . 34
2.3.2 Numerical simulations . . . 35
2.4 Smoke movement in a medium scale tunnel . . . 39
2.4.1 Experiment description . . . 40
2.4.2 Numerical simulations . . . 41
Subcritical ventilation regime . . . 44
Supercritical ventilation regime . . . 47
2.5 Numerical investigation of Froude Scaling in tunnel geometries 51
2.5.1 Scaling theory . . . 51
2.5.2 Results comparison in different scales . . . 54
Subcritical ventilation regime . . . 54
Supercritical ventilation regime . . . 56
2.5.3 Effect of the wall properties . . . 57

3 CFD modelling of jet-fans **63**
3.1 Model of Jet-Fan in FDS . . . 63
3.1.1 Effect of the swirl in the jet fan modelling . . . 65
3.2 Tunnel without fire: Small scale test . . . 70
3.2.1 Description of the experiment . . . 70
3.2.2 Numerical simulations . . . 71
Effect of the tunnel's inlet geometry . . . 76
Effect of the turbulence model . . . 77
Effect of the nozzle geometry . . . 79
3.3 Tunnel without fire: Big scale test . . . 81
3.3.1 Description of the experiment . . . 81
3.3.2 Numerical simulations . . . 82
3.4 Tunnel with fire: Memorial tunnel test . . . 89
3.4.1 Description of the experiment . . . 89
3.4.2 Numerical simulations . . . 91

4 Fire-Structure interaction **103**
4.1 Coupling FDS with Comes-HTC . . . 103
4.1.1 Mesh interfacing . . . 107
4.2 Coupling verification . . . 112
4.2.1 Cylinder with burner . . . 112
4.2.2 Vertical wall exposed to fire . . . 116
4.2.3 Plume impinging a ceiling . . . 122
4.3 Concrete slab exposed to fire . . . 126
4.3.1 Fluid dynamic analysis . . . 126
4.3.2 Structural analysis . . . 130
4.4 Fire in a rail tunnel . . . 137
4.4.1 Fluid dynamic analysis . . . 138
4.4.2 Structural analysis . . . 144
4.5 Two ways coupling verification . . . 151
4.6 Coupled analysis with embedded approach . . . 155

5 Conclusions and future works **163**

A Velocity distribution for a jet fan with swirl **169**

Bibliography **171**

List of Figures

1.1 Introduction: Critical velocity and smoke backlayering . . . 10
1.2 Introduction: High temperature in tunnels 13
1.3 Introduction: Temperature and heat fluxes 16
1.4 Different failure modes in case of smalling presented in [37] 20

2.1 Natural ventilation in a partially heated cavity: Schematic view of the experiment 29
2.2 Natural ventilation in a partially heated cavity: Mesh independence study 31
2.3 Natural ventilation in a partially heated cavity: Velocity distribution along the middle line of the cavity 32
2.4 Natural ventilation in a partially heated cavity: Temperature distribution and Nusselt number 32
2.5 Natural ventilation in a partially heated cavity: Flow field in the cavity 33
2.6 Natural ventilated fire in a large room: Schematic view of the experiment 35
2.7 Natural ventilated fire in a large room: Heat Release Rate . . 36
2.8 Natural ventilated fire in a large room: Mesh independence study 37
2.9 Natural ventilated fire in a large room: Temperature time histories 38
2.10 Natural ventilated fire in a large room: Temperatures along the room's height 38
2.11 Natural ventilated fire in a large room: Species' concentrations 40
2.12 Natural ventilated fire in a large room: Velocity and temperature distribution in the room 41
2.13 Smoke movement in a medium scale tunnel: Schematic view of the experiment 42
2.14 Smoke movement in a medium scale tunnel: Mesh independence study 43
2.15 Smoke movement in a medium scale tunnel: Heat Release Rate curves 44
2.16 Smoke movement in a medium scale tunnel: Temperature time history with subcritical ventilation 45
2.17 Smoke movement in a medium scale tunnel: Temperature distribution along the tunnel with subcrtical ventilation . . . 46
2.18 Smoke movement in a medium scale tunnel: Velocity and temperature distribution in the tunnel for subcritical ventilation condition 46
2.19 Smoke movement in a medium scale tunnel: Velocity time history for subcrtical ventilation conditions. 46

2.20 Smoke movement in a medium scale tunnel: Radiative heat fluxes for subcrtical ventilation conditions. 47
2.21 Smoke movement in a medium scale tunnel: Temperature time history for supercritical ventilation conditions 48
2.22 Smoke movement in a medium scale tunnel: Temperature profiles along the tunnel for supercritical ventilation conditions 49
2.23 Smoke movement in a medium scale tunnel: Velocity and temperature distribution along the tunnel for supercritical ventilation conditions 50
2.24 Smoke movement in a medium scale tunnel: Velocity time history for supercritical ventilation conditions 50
2.25 Numerical investigation of Froude Scaling in tunnel geometries: Comparison of temperatures in the two scales under subcritical ventilation conditions 55
2.26 Numerical investigation of Froude Scaling in tunnel geometries: Comparison of velocities in the two scales 56
2.27 Numerical investigation of Froude Scaling in tunnel geometries: Comparison of temperatures in the two scales under supercritical ventilation conditions 57
2.28 Numerical investigation of Froude Scaling in tunnel geometries: Comparison of temperatures for differently insulated tunnels under subcritical ventilation conditions 59
2.29 Numerical investigation of Froude Scaling in tunnel geometries: Comparison of velocities for differently insulated tunnels 59
2.30 Numerical investigation of Froude Scaling in tunnel geometries: Comparison of temperatures for differently insulated tunnels under supercritical ventilation conditions 60

3.1 Model of Jet-Fan in FDS: Jet fan model and performance map 64
3.2 Effect of the swirl in the jet fan modelling: Velocity distributions across the rotor 67
3.3 Effect of the swirl in the jet fan modelling: Comparison of the velocities obtained with the two fans in free field 67
3.4 Effect of the swirl in the jet fan modelling: Comparison of the tangential velocity 68
3.5 Effect of the swirl in the jet fan modelling: Comparison of the velocities obtained with the two fans in tunnel 69
3.6 Effect of the swirl in the jet fan modelling: Comparison of the tangential velocity 70
3.7 Tunnel without fire: Small scale test: Schematic view of the experiment 71
3.8 Tunnel without fire: Small scale test: Pressure distribution near the wall 73
3.9 Tunnel without fire: Small scale test: Velocity decay along the jet's centreline 74
3.10 Tunnel without fire: Small scale test: Velocity profiles for different nozzle's positions 75
3.11 Tunnel without fire: Small scale test: Velocity contour on the tunnel's middle plane 76
3.12 Tunnel without fire: Small scale test: Velocity profiles at the tunnel inlet 77

3.13 Tunnel without fire: Small scale test: Comparison of different turbulence models simulated with mesh 1 78
3.14 Tunnel without fire: Small scale test: Comparison of different turbulence models simulated with mesh 2 79
3.15 Tunnel without fire: Small scale test: Comparison of different nozzle geometries simulated with mesh 1 80
3.16 Tunnel without fire: Big scale test: Schematic view of the experiment 82
3.17 Tunnel without fire: Big scale test: Tunnel's cross section . . 82
3.18 Tunnel without fire: Big scale test: Mesh independence study, velocity comparison 84
3.19 Tunnel without fire: Big scale test: Mesh independence study, pressure comparison 85
3.20 Tunnel without fire: Big scale test: Average velocity along the tunnel 86
3.21 Tunnel without fire: Big scale test: Flow field for cases 1.1, 1.2, 1.3 and 6.1 86
3.22 Tunnel without fire: Big scale test: Flow field for cases 2.1, 2.2, 4.2, 5.1 and 5.2 87
3.23 Tunnel without fire: Big scale test: Velocity along the tunnel obtained with different wall roughness 88
3.24 Tunnel with fire: Memorial tunnel test: Schematic view of the experiment 89
3.25 Tunnel with fire: Memorial tunnel test: Cross sections 90
3.26 Tunnel with fire: Memorial tunnel test: Heat Release Rate . . 91
3.27 Tunnel with fire: Memorial tunnel test: Mesh independence study, temperature and velocity comparison 93
3.28 Tunnel with fire: Memorial tunnel test: Mesh independence study, flow field comparison 94
3.29 Tunnel with fire: Memorial tunnel test: HRR sensitivity comparison of temperatures along the tunnel 94
3.30 Tunnel with fire: Memorial tunnel test: HRR sensitivity smoke front 95
3.31 Tunnel with fire: Memorial tunnel test: Temperature field after 50 s 96
3.32 Tunnel with fire: Memorial tunnel test: Temperature field after 110 s 97
3.33 Tunnel with fire: Memorial tunnel test: Temperature field after 290 s 98
3.34 Tunnel with fire: Memorial tunnel test: Temperature field after 590 s 99
3.35 Tunnel with fire: Memorial tunnel test: Velocities upstream the fire 99
3.36 Tunnel with fire: Memorial tunnel test: Velocities near the fire 100
3.37 Tunnel with fire: Memorial tunnel test: Velocities downstream the fire 101
3.38 Tunnel with fire: Memorial tunnel test: Volume flows upstream and downstream the fire 102

4.1 Coupling FDS with Comes-HTC: Coupling strategies 104
4.2 Coupling FDS with Comes-HTC: structures exposed to fire . 107

4.3 Mesh interfacing: Mesh interfacing approach 108
4.4 Mesh interfacing: Element selection in case of small FDS elements 110
4.5 Coupling verification: Cylinder with burner, schematic view and flow field 112
4.6 Coupling verification: Comparison of incoming heat fluxes, mesh 1 113
4.7 Coupling verification: Comparison of the heat flux distributions, mesh 1 114
4.8 Coupling verification: Comparison of incoming heat fluxes, mesh 2 114
4.9 Coupling verification: Comparison of the heat flux distributions, mesh 2 115
4.10 Coupling verification: Evaluation of the effect of the angular discretization 116
4.11 Coupling verification: Comparison of the convective heat transfer coefficient 117
4.12 Coupling verification: Vertical wall exposed to fire, schematic view and flow field 118
4.13 Coupling verification: Comparison of temperatures and the heat fluxes 118
4.14 Coupling verification: Comparison of the heat flux distributions, contours 119
4.15 Coupling verification: Comparison of the heat flux distributions, line plots and time history 119
4.16 Coupling verification: Comparison of the convective heat transfer coefficient distributions, contours 120
4.17 Coupling verification: Comparison of the convective heat transfer coefficient and water vapour density distributions, line plots 121
4.18 Coupling verification: Comparison of the water vapour density distributions, contours 121
4.19 Coupling verification: Plume impinging a ceiling, schematic view 122
4.20 Coupling verification: Flow field comparison 123
4.21 Coupling verification: Temperature and velocity comparison 123
4.22 Coupling verification: Comparison of heat fluxes 124
4.23 Coupling verification: Comparison of convective heat transfer coefficient and water vapour density 125
4.24 Concrete slab exposed to fire: Schematic view and HRR . . . 127
4.25 Concrete slab exposed to fire: Mesh independence study . . 128
4.26 Concrete slab exposed to fire: Comparison of flow fields . . 128
4.27 Concrete slab exposed to fire: Comparison of different burners' sizes 129
4.28 Concrete slab exposed to fire: Comparison of different fire growth rates 130
4.29 Concrete slab exposed to fire: Integral incident heat fluxes, effect of burner's size 131
4.30 Concrete slab exposed to fire: Temperature distribution in the slab, effect of burner's size 132

4.31 Concrete slab exposed to fire: Gas pressure distribution in the slab, effect of burner's size . . . 133
4.32 Concrete slab exposed to fire: Stress XX component distribution in the slab, effect of burner's size . . . 134
4.33 Concrete slab exposed to fire: Stress ZZ component distribution in the slab, effect of burner's size . . . 135
4.34 Concrete slab exposed to fire: Integral incident heat fluxes, effect of fire's growth rate . . . 135
4.35 Concrete slab exposed to fire: Temperature distribution in the slab, effect of fire's growth rate . . . 136
4.36 Concrete slab exposed to fire: Gas pressure distribution in the slab, effect of fire's growth rate . . . 137
4.37 Concrete slab exposed to fire: Stress XX component distribution in the slab, effect of fire's growth rate . . . 138
4.38 Concrete slab exposed to fire: Stress ZZ component distribution in the slab, effect of fire's growth rate . . . 139
4.39 Fire in a rail tunnel: Schematic view and HRR . . . 140
4.40 Fire in a rail tunnel: Mesh independence study . . . 141
4.41 Fire in a rail tunnel: Radiation angle independence study . . . 142
4.42 Fire in a rail tunnel: Length independence study . . . 143
4.43 Fire in a rail tunnel: Evaluation of the height's effect . . . 144
4.44 Fire in a rail tunnel: Flow field . . . 145
4.45 Fire in a rail tunnel: View of the structure and integral heat flux . . . 145
4.46 Fire in a rail tunnel: Maximum temperature and incident heat flux . . . 146
4.47 Fire in a rail tunnel: Maximum gas pressure and mechanical damage . . . 147
4.48 Fire in a rail tunnel: Incident heat flux distribution after 300 s 147
4.49 Fire in a rail tunnel: Temperature and Gas pressure in the structure after 300 s . . . 148
4.50 Fire in a rail tunnel: Stresses and Total damage in the structure after 300 s . . . 149
4.51 Fire in a rail tunnel: Incident heat flux distribution after 600 s 149
4.52 Fire in a rail tunnel: Temperature and Gas pressure in the structure after 600 s . . . 150
4.53 Fire in a rail tunnel: Stresses and Total damage in the structure after 600 s . . . 151
4.54 Two ways coupling verification: Coupling strategy . . . 152
4.55 Two ways coupling verification: Temperature comparison for different loop iterations . . . 153
4.56 Two ways coupling verification: Integral heat flux and Wall temperature for different loop iterations . . . 154
4.57 Two ways coupling verification: Temperature along the slab and displacement loop iterations . . . 155
4.58 Coupled analysis with embedded approach: Comparison of one dimensional and two dimensional models . . . 157
4.59 Coupled analysis with embedded approach: Comparison of two dimensional models, with and without mechanical damage . . . 157
4.60 Coupled analysis with embedded approach: Flow field . . . 158

4.61 Coupled analysis with embedded approach: Temperature in case of fire beneath the slab 159
4.62 Coupled analysis with embedded approach: Gas pressure distribution after 800 s 160
4.63 Coupled analysis with embedded approach: Temperature distribution after 800 s 161

List of Tables

1.1 Coefficients for the flame model of [32]. 14

2.1 Natural ventilation in a partially heated cavity: Wall's thermal properties 30
2.2 Natural ventilation in a partially heated cavity: Mesh data . 31
2.3 Natural ventilation in a partially heated cavity: Heat fluxes through the walls 33
2.4 Natural ventilated fire in a large room: Wall's thermal properties 36
2.5 Natural ventilated fire in a large room: Mesh data 36
2.6 Smoke movement in a medium scale tunnel: Mesh data . . . 42
2.7 Comparison of the different boundary conditions in the two scales 54
2.8 Thermal properties of the walls of the non insulated and insulated tunnels. 58

3.1 Average velocity with and without swirl 68
3.2 Operative conditions for different nozzle's positions 72
3.3 Mesh data 73
3.4 Operative conditions for different nozzle's positions 80
3.5 Operating conditions of the tunnel during the experiments . 83
3.6 Mesh data 84
3.7 Comparison of the numerical results with the experimental measurements 85
3.8 Position of the jet fans' batteries 90
3.9 Materials' properties 92
3.10 Mesh features for the mesh independence assessment 92
3.11 Mesh features 94

4.1 Angles used for the approximation of the orientation of the nodes in Comes-HTC 109
4.2 Resulting quantities for vector and scalar quantities obtained for different orientations 111
4.3 Mesh data 113
4.4 Material's thermal properties modelled in FDS 126
4.5 Mesh data 127
4.6 Material's thermal properties modelled in FDS 139
4.7 Mesh data 141

List of Abbreviations

AST	**A**diabatic **S**urface **T**emperature
CFD	**C**omputational **F**luid **D**ynamics
DNS	**D**irect **N**umerical **S**imulation
FDS	**F**ire **D**ynamic **S**imulator
FEM	**F**inite **E**lements **M**ethod
HRR	**H**eat **R**elease **R**ate
HRRPUA	**H**eat **R**elease **R**ate **P**er **U**nit of **A**rea
LES	**L**arge **E**ddy **S**imulation

Physical Constants

Stefan-Boltzmann constant	$\sigma = 5.670\,367(13) \times 10^{-8}\,\mathrm{W/m^2/K^4}$
Gravity force	$\mathrm{g} = 9.80(665)\,\mathrm{m/s^2}$

List of Symbols

A	Area	m^2
$\tilde{A}$	Resistant area after cracking	m^2
b_c	Length of a crack	m
b_{f0}	Radius of a fire source	m
c_p	Specific heat	$\mathrm{J\,kg^{-1}\,K}$
D^*	Characteristic diameter of the fire	m
D_h	Hydraulic Diameter	m
D_M	Mechanical damage	$-$
D_{TC}	Thermochemical damage	$-$
D_{tot}	Total damage	$-$
E	Young's modulus	Pa
$F_{f,u}$	Force induced by a fan	$\mathrm{kgm/s^2}$
F_t	Force induced by a fan in a tunnel	$\mathrm{kgm/s^2}$
Fr	Froude number	$-$
H	Tunnel's height	m
H_{eff}	Distance between fire and ceiling	m
L	Characteristic length	m
$L_{r,c}$	Depth of a crack	m
$\dot{m}_{H_2O}$	Water mass flux	$\mathrm{kgs/m^2}$
p (p^g)	Gas pressure	Pa
p_{atm}	Atmospheric pressure	Pa
p^c	Capillary pressure	Pa
p_w	Water pressure	Pa
P	power	$\mathrm{W\ (J\,s^{-1})}$
$\dot{q}''$	Heat flux per unit of area	$\mathrm{W/m^2}$
$\dot{q}''_{in}$	Incoming heat flux per unit of area	$\mathrm{W/m^2}$
$\dot{q}''_{out}$	Outooming heat flux per unit of area	$\mathrm{W/m^2}$
$\dot{Q}(HRR)$	Fire heat release rate	W
Q_f	Jet fan's discharged volume flow	$\mathrm{m^3/s}$
r	Radius	m
Re	Reynolds number	$-$
S	Saturation	$-$
S_{ssp}	Solid saturation point	$-$
u	Velocity	$\mathrm{m\,s^{-1}}$
u_a	Axial component of the velocity (Fan)	$\mathrm{m\,s^{-1}}$
u_t	Tangential component of the velocity (Fan)	$\mathrm{m\,s^{-1}}$
t	Time	s
T	Temperature	K
W	Work exchanged by a fan per unit of mass	$\mathrm{m^2/s^2}$
Z	Specie's mass fraction	$-$
α	Angle	rad
β	mass transfer coefficient	$\mathrm{m\,s^{-1}}$
γ	scaling factor	$-$

ξ	thermal thickness	$\mathrm{W/m^2/K}$
χ	thermal inertia	$\mathrm{Ws/m^4/K^2}$
ρ	Density	$\mathrm{kg/m^3}$
θ	Angle	rad
σ	Stress	Pa
ε	Emissivity	$-$
μ	Dynamic viscosity	$\mathrm{Pa\,s}$
ω	angular frequency	$\mathrm{rad\,s^{-1}}$

Dedicated to Marlena and to my family

Chapter 1

Introduction

Fires in tunnels is a wide and multidisciplinary topic due to the specific features that differentiate tunnels from other structures. Several studies about tunnels' fire safety have been carried out in many different fields of science and engineering. Smoke extraction and confinement have been widely investigated with numerical simulations and experiments, studying the effect of the ventilation on the smoke confinement and on the fire development. The possibility to suppress the fire with water has been investigated in order to understand the interaction between fire, smoke and droplets of water. Several studies have been carried out on the egress of the people trapped in the tunnel, in order to provide a safe exodus and minimize the fatalities. Concrete structures at high temperatures have been investigated with numerical methods and experiments in order to assess the risk of spalling and failure for the structure.

These topics are too wide to be studied in a single doctorate, therefore only two specific areas have been investigated.

1.1 Tunnel ventilation test

In tunnels' fire safety one of the most investigated topic is the ventilation, this can be used to control the level of pollution under security level [1, 2] or to extract or confine the smoke in case of fire. The smoke can be controlled with different strategies depending on the tunnel's features, such as length, slope, traffic and number of lines. The ventilation, in case of fire, has to maintain a tenable environment for the people trapped in the tunnel and exodus ways clear of smoke. In the engineering practice, guidelines and regulations are followed in order to provide the required safety level. Standards for tunnel safety have been released by NFPA [3], PIARC [4], European Union [5] and United Nations [6], besides these internationally recognised guidelines there are also national guidelines. In these regulations the different ventilation strategies are divided in two main groups: natural ventilation and mechanical ventilation.

Naturally ventilated tunnels don't require any mechanical device to control the pollution level or the smoke. The flow along the tunnel is induced by the movement of vehicles, piston effect, by the different atmospheric conditions at the portals and by stack effect combined with the tunnel's slope. These effects, except for the last, cannot be controlled in order to face different tunnel operating conditions, low-high traffic or fire. This ventilation strategy is obviously limited to short tunnels and their maximum length is bounded by the reference regulation.

Mechanically ventilated tunnels use ventilation devices to control the smoke and the air quality, therefore the tunnel's length can be extended up to many kilometres. Many different ventilation strategies have been developed to find the solution that provides high safety level and acceptable costs. Longitudinal ventilation induces a flow along the tunnel which pushes the smoke or the vitiated air out of the tunnel, using this as exhaust duct. Jet fans or Saccardo nozzles can be installed to push the smoke along the tunnel and keep a tenable environment upstream the fire. This approach is convenient for short tunnels because the installation of jet fans doesn't require the creation of a ventilation network. Longitudinal ventilation can be induced also with vertical shafts by generating a local circulation of the air and smoke extraction extract. Longitudinal ventilation can be applied only to tunnels with two or more tubes where the smoke can be exhausted in the direction of the cars exiting the tunnel.

Longer tunnels cannot be used as duct because of the high the pressure losses and because a large portion of tunnel is filled with smoke. In these cases the most common ventilation strategy is the transverse or semi-transverse ventilation. Additional ducts are created to supply fresh air and to extract the vitiated air or smoke. In a fully transverse ventilated tunnel there are both supply and extraction, while in semi-transverse ventilated tunnel only supply or extraction ducts are created. Fully transverse ventilation strategy is the most expensive because it requires the creation of a complex network of ducts for the exhaust and supply of air, however it is capable to keep the smoke confined near the fire. Transverse and longitudinal ventilation strategies can be combine together creating new hybrid approaches.

These ventilation strategies have been investigated with experiments, in small and big scale, and with numerical simulations. Big scale tunnel fire tests have been performed in the past in order to study the effectiveness of the ventilation on smoke confinement and the dynamics of fires in tunnels. From all those tests not everyone has a complete set of data that could be used to reproduce the experimental results with numerical models. In some older test the Heat Release Rate (HRR) has not been measured and only some information about the temperature are available. In this work special care has been paid to the experiments where tunnels were equipped with jet fans, since the topic is widely studied in chapter 3. Several small scale tests have been carried out in order to study the capability of the longitudinal ventilation to confine the smoke. But the difficulty in resizing the ventilation device required a simplification of the ventilation system, usually in these tests a uniform flow is provided at the tunnel's inlet. In large scale experiments the jet fans are used to confine the smoke, but due to the cost and the risk related with large scale tests, few experiments have been carried out. The experiments presented hereafter have been chosen because they include ventilation devices, jet fans, and comprehensive measurements which allows to simulate the whole tunnel with numerical methods.

1.1.1 EUREKA project

The first test campaign which gave many information about fire scenarios in tunnel, with several measurement, has been the EUREKA project [7].

In this project twenty one tests have been carried out in Repparfjord tunnel in Norway, using different fuels and different ventilation regimes. The project has been supported by different countries in Europe: Austria, Finland, France, Germany, Great Britain, Italy, Norway, Sweden and Switzerland. The main goal of the research was to investigate the safety of tunnels in case of fire, including different research topics:

- Fire dynamics in tunnels
- The effect of the surrounding structural parts on the fire
- Escape, rescue and fire extinguishing possibilities
- Reuse of the structure
- Accumulation of theory

During the tests different fire loads have been used such as cars, HGV, bus, metro car and wood cribs. The fire development has been monitored using oxygen consumption calorimetry allowing to quantify the HRR of the different fires. The tunnel was longitudinally ventilated with an average velocity ranging from 0 to 8 m/s. During the tests, the fire spread and the HRR have been investigated, highlighting the importance of the state of vehicle. The roof can act as screen for the radiative flux reducing the fire spread, the windows' break can speed up the fire growth because of the greater oxygen availability. In order to evaluate the thermal loads on the structure, temperatures beneath the ceiling have been measured for different fires. For cars and rail coach the temperature were about 800-1000 °C, but for a burning HGV the temperature under the ceiling rose up to 1300 °C, with an estimated HRR of 100 MW. This forced the national authorities to review their guidelines about the thermal input that has to be used to verify the tunnel structures.

1.1.2 The Memorial Tunnel Fire Ventilation Test Program (MT-FVTP)

The Memorial Tunnel Fire Ventilation Test Program is a large experimental campaign carried out in a abandoned tunnel in the West Virginia (USA) under the Paint Creek Mountain [8]. The Memorial Tunnel is a two lane tunnel with a length of 853 m, height of 7.86 m (4.33 with the ceiling in place) and a slope of 3.2%. Differently from the EUREKA project in the Memorial tunnel only pool fires have been used, with different nominal powers 10 MW, 20 MW, 50 MW and 100 MW, because the main goal of the tests was the assessment of the effectiveness of the ventilation system. Different ventilation strategies have been tested with different fire scenarios and suppression system. The ventilation regimes tested are listed hereafter:

- Full Transverse Ventilation
- Partial Transverse Ventilation
- Partial Transverse Ventilation with Single Point Extraction
- Partial Transverse Ventilation with Oversized Exhaust Ports

- Point Supply and Point Exhaust Operation
- Natural Ventilation
- Longitudinal Ventilation with Jet Fans

In the tests the heat release rate has been calculated basing on the fuel mass loss from the pan. Along the tunnel, temperatures, velocities, species' concentration and visibility have been measured at different locations.

First, the fully transfers ventilation has been tested, using the original ventilation system installed in the tunnel. The smoke is extracted in the upper part of the tunnel which is divided from the main body by a false ceiling. The ventilation duct was connected to the fan rooms located at the portals of the tunnel. Using the original ventilation configuration the first five ventilation strategies have been tested. Later, for the longitudinal and natural ventilation tests the false ceiling has been removed in order to hang the jet fans to the ceiling.

The tests performed under different fire and ventilation conditions gave back interesting results about effectiveness of the ventilation strategies. Semi-transversal ventilation strategy has been tested, when pure dilution of the smoke is performed the effectiveness of the ventilation system is quite small. Fully transverse ventilation system can better control heat and smoke when they can induce a longitudinal flow inside the tunnel. It is fundamental to have multiple extraction and supply zone in order to control the longitudinal flow, the single point extraction strategy couldn't handle properly the smoke flow along the tunnel. The most effective ventilation strategy requires both extraction and confinement, this can be done controlling the extraction and the supply of air. From the longitudinal ventilation test the capability of the jet fan to confine the smoke downstream the fire has been compared with the data coming from the small scale experiments. The critical velocity, capable to confine the smoke downstream the fire, has been already widely studied in small scale tunnels, but the MTFVTP depicted the longitudinal flow reduction caused by the fire, which is better know as throttling effect.

Besides the ventilation system, also foam suppression system has been tested in order to assess its performance with different fire size and different ventilation strategies.The test aimed to evaluate of the influence of longitudinal velocity on the suppression time. The test showed that the effectiveness of the foam was not diminished, even with the maximum longitudinal air velocity 4.2 m/s.

1.1.3 2nd Benelux Tests 2002

In 2002 in the Netherlands a series of large scale test has been carried out to study the tenability conditions for people trapped inside a tunnel in case of fire and the mitigation effects [9]. The effectiveness of mechanical ventilation, detection system and sprinklers has been widely investigated with a total of fourteen full scale tests. The tunnel is near Rotterdam and it is rectangular shaped with a length of 840 m, a width of 9.8 m and an height of 5.1 m. The slope changes along the tunnel and it has a maximum of 4.4% in the middle of the tunnel. The tunnel is equipped with six jet fans placed at the upstream portal of the tunnel, those are able to induce a longitudinal

velocity of 6 m/s. During the test different fuels have been tested in order to evaluate also the mutual interaction between fire and ventilation.

In the first series of test (1 to 4) pan filled with liquid fuel have been ignited using different sizes in order to provide different HRR. The ventilation system has been controlled providing different longitudinal velocities in order to study how the smoke propagates and mixes with the fresh air. In the second series of test (5 to 10) cars and covered trucks' loads were burned while the longitudinal ventilation was increased stepwise from 0 m/s to 6 m/s. The objective of this second series of tests was to monitor the tenability conditions inside the tunnel and to evaluate the influence of the ventilation of the fire's growth. In the last series of test (11 to 14) the sprinklers were activated with different fires: car, covered trucks' loads and uncovered trucks' loads. The sprinklers were activated with different delays in order to study the cooling effect on the fire, the inhibition of the fire's spread and the production of water vapour. When the sprinklers are activated the fire spread is delayed or inhibited, but sprinklers are not effective on fire in closed cars.

In the tunnel different quantities have been measured, the HRR has been calculated based on the mass loss rate of the burning material. Temperatures inside the tunnel were measured with thermocouple trees in different position and on the walls. The radiative heat flux was measured with heat fluximeter placed at different distances from the fire. The gas velocity was measured upstream and downstream the fire using hot wire anemometers and pitot tubes. Detection systems have also been studied in order to quantify the delay of the detection after the fire injection [10].

From the fire test it was possible to compare the critical velocities found in [11] with the measured velocity which were able to confine the smoke downstream the fire. The fire tests depicted the influence of the ventilation regime on fire growth and on the HRR. The ventilation has an important effect on the fire spread inside a vehicle, it can delay or speed up the fire propagation depending on the configuration of the fire load. Different results have been found for different vehicles on fire without giving an unique answer to the problem. With a burning car the ventilation delayed the fire spread since this was confined in the front part of the car without propagating to the rear part. In case of truck the fire was growing faster when ventilated, but the HRR peak increased only 1.2-1.5 times higher than the power of the non ventilated case.

From the measurements of different quantities inside the tunnel it was possible also to study the tenability conditions for the motorist. The conditions were based on different criteria such as radiative heat flux, convective gas temperature and optical density. Using these data, maps of tenability in the tunnel have been drawn, highlighting the regions with impeding and lethal conditions. The effect of ventilation on tenability conditions has been studied for the different fires, the supply of fresh air to the smoke allows to reduce the temperature of the gas downstream the fire. But the drawback of this strategy is loss of stratification of the smoke, which is mixed with fresh air and it leads to a reduction of visibility in the downstream zone. In case of sprinklers' activation the temperatures are reduced due to the cooling effect of water droplets, but the visibility is also reduced because of the de-stratification of smoke. Both for ventilated fires and suppressed fires it

is important to consider not only the direct effect of these systems on the tenability conditions, but also they interaction with the fire.

1.1.4 Other big scale test

In this chapter only three big scale experiments have been described, but much more can be found in the literature, [12, 13]. These tests have been selected because they provide a comprehensive set of measurements which can be later used for the validation of numerical models. There are other important experiments which are not directly related to ventilation with jet fans in case of fire, but which investigated the fire dynamics inside a tunnel and should be mentioned in this study.

In the Runehamar tunnel in 2003 four tests have been carried out to study the fire development in HGV cargo loads in a tunnel, the interaction of longitudinal ventilation with fire, fire spread between vehicles , the production of toxic gases and the heat exposure of the tunnel linings [14].The tunnel is 6 m high and 9 m wide and 1600 m long, the walls are made of rock apart for the section where the fires took place. The fire zone was placed 1.0 km from the upstream portal and the walls of the tunnel where covered by heat-resistant plates. The test aimed to reproduce the load of an HGV, therefore different material have been burned such wooden pallets, mattresses and tyres. In order to confine the smoke, the tunnel was longitudinally ventilated with two mobile fans able to provide an air velocity about 3.0 m/s. During the test some targets have been placed close to the fire in order to study the ignition and the fire spread to other vehicles. The measured power of the fire ranged from 50 MW up to 200 MW with a very fast development, during the tests temperatures rose up to 1300 °C.

In 2011 another series of experiments has been carried out in Sweden during the METRO project [15]. This project aimed to study the fire development inside train and metro coach, the egress of trapped passengers, smoke and fire control. In order to study the burning behaviour of a rail coach two large scale tests were performed reaching a maximum HRR about 75 MW and a maximum temperature under the ceiling about 1100 °C. Regarding the passenger egress in the METRO project, different tests have been carried out on small, medium and big scale. Particular attention has been paid to the evacuation of trains, underground stations and tunnels, with special care for senior citizen and persons with disabilities. In the project technical equipment for fire prevention, evacuation and rescue has been tested and classified in order to draw a state of the art for the problem. Ventilation tests have been performed in order to evaluate the possibility to confine smoke through jet fans located in different positions inside the tunnel. Smoke extraction has been studied together with pressurization process to limit the smoke spread. The ventilation process has been later simulated with numerical methods in order to reproduce the experiments and validate the numerical model. Another part of the project, which has been highly innovative, was the investigation about the consequence of explosions in underground stations, this was consequence of the terrorist threat. The METRO project investigated with experiment and numerical methods the effect of the explosion on the train and on the structure. From those investigation it has been possible to learn how to evaluate the risk for the structure after an explosion and how to proceed with the rescue operations.

The capabilities and limitations of the rescue personnel has been object of study using the full scale fire tests described before.

Those tests are only part of the several experiments carried out in the past. The interested reader can find an extended list of fire tests in small and large scale in [12, 13]

1.2 Smoke confinement and critical velocity

As seen in section 1.1 different ventilation strategies can handle smoke in case of fire, longitudinal ventilation confines the smoke in one part of the tunnel, while transverse and semi-transverse ventilation extracts the hot gases from the tunnel. In order to design the longitudinal ventilation system it is important to know the velocity able to confine the smoke downstream the fire. When the longitudinal velocity is too low and the smoke is capable to spread upstream the fire there is occurrence of backlayering. The critical velocity is defined as the minimum velocity capable to prevent the backlayering of the smoke in case of fire. Critical velocity is function of the HRR, position of the fire, the section of the tunnel and its slope.

The critical velocity has been investigated first by Thomas in [16] with mathematical modelling and experiment. Considering data coming from small and big scale tests he investigated the backflow of smoke, which can be confined when the inertial force of the incoming fresh is greater than the buoyancy force of the smoke. The ratio among these to forces is expressed by the Froude number, Fr:

$$Fr = \frac{Inertia forces}{Gravity forces} \tag{1.1}$$

According to Thomas the backlayering distance, defined as the length travelled by the smoke upstream the fire, is function of the Froude number:

$$\frac{X}{H} = f(Fr) = f\left(\frac{T_0 \rho_0 \, c_p u^3 A}{2\, g\, H\, \dot{Q}}\right) \tag{1.2}$$

Where u is the longitudinal velocity, ρ_0 is the air density, c_p is the specific heat, T_0 is the ambient temperature, A is the tunnel's cross section area, H is the tunnel's height and $\dot{Q}$ is the HRR. Thomas found out a linear relation between the back-layering distance and the reciprocal of the Froude number, as written in equation 1.2. If there is no back-layering so the smoke doesn't travel upstream the fire, according to equation 1.2 the critical velocity can be calculated as:

$$u_{cr} = k\left(\frac{g\, H\, \dot{Q}}{T \rho c_p\, A}\right)^{\frac{1}{3}} \tag{1.3}$$

Where k is a constant which can be calculated basing on experimental data. Similar results have been found out by Kennedy [17] who proposed a simple equation similar to equation 1.3:

$$u_{cr} = k\left(\frac{g\, H\, \dot{Q}}{T_f \rho c_p\, A\, Fr_{cr}}\right)^{\frac{1}{3}} \tag{1.4}$$

Where Fr_{cr} is the critical Froude Number and T_f is the downstream temperature induced by the fire.

$$T_f = \frac{\dot{Q}}{\rho c_p A \, Fr_{cr} u_{cr}} + T_0 \tag{1.5}$$

The equations presented above are based on the theory of a critical Froude Number which is calculated together with the constant k evaluated with experimental data. According to the measurements of Lee [18] the critical Froude number ranged between 4.5 and 6.7 while Kennedy proposed a value of 4.5.

This equation is valid in a reduced range of fires since for high values of HRR the critical velocity has an asymptotic behaviour. To study the backlayering in a wider range of fire powers, Oka and Atkinson introduced the non-dimensional velocity u^* and the non-dimensional HRR $\dot{Q}^*$ based on the Froude scaling theory[19].

$$u^* = \frac{u}{\sqrt{g\,h}} \tag{1.6}$$

$$\dot{Q}^* = \frac{\dot{Q}}{\rho c_p T g^{1/2} H^{5/2}} \tag{1.7}$$

Oka and Atkinson tested a wide range of HRR which corresponded in a real tunnel, with 5 m diameter, to fires from 2 and 150 MW. For each fire scenario the critical velocity, able to confine the smoke downstream the fire, has been measured. For high HRR the critical velocity is not following the relation 1.3, but it reaches an asymptotic value. Based on the experimental data, a new formulation for the critical velocity has been proposed:

$$u_c^* = \begin{cases} k_v \left(\frac{\dot{Q}^*}{0.12}\right)^{1/3}, & \text{if } \dot{Q}^* < 0.12 \\ k_v, & \text{if } \dot{Q}^* > 0.12 \end{cases} \tag{1.8}$$

Where the coefficient k_v is function of the geometry and of the position of the fire source and which varies between 0.22 and 0.38. From this equation it is clear that there is a limit to the critical velocity, which depends on the height of the tunnel, but not on the HRR. An explanation of the upper limit of the HRR has been partially given in [11] looking at the plume in the tunnel, when the flame impinges the ceiling then the critical velocity is not affected by the HRR. This study revealed the real trend of the critical velocity and the existence of a supercritical velocity independent from the HRR, but it couldn't give a satisfactory explanation of the reason why the critical velocity is bounded.

The effect of the tunnels' cross section couldn't be correctly explained by the equation 1.8, because only the height of the tunnel is considered, while the backlayering is a three-dimensional problem. To overcome this problem, as proposed by De Riz [20] and later assessed by Wu and Barak [21], the tunnel's height can be substituted with the tunnel's hydraulic diameter in order to consider the effect of the cross section. The hydraulic diameter is defined as the ratio among four time the area of the tunnel's section and the wetted perimeter. Starting from the same non dimensional analysis proposed by Oka [11], Wu and Bakar proposed an new equation

for the critical velocity:

$$u_c^* = \begin{cases} 0.40 \left(\frac{\dot{Q}^*}{0.20}\right)^{1/3}, & \text{if } \dot{Q}^* < 0.20 \\ 0.40, & \text{if } \dot{Q}^* > 0.20 \end{cases} \tag{1.9}$$

To explain the findings of Oka about the upper limit of the critical velocity the dynamics of the flame inside the tunnel has been investigated. Wu and Bakar divided the fire plume in three zones which can be summarized here:

- Persistent flame: portion of flame near the source with high temperature (T > 500 °C) and accelerating gas flow.
- Intermittent flame: above the persistent flame with medium-high temperature (250 °C < T < 500 °C) and near constant velocity.
- Buoyant plume: upper part of the plume with temperature (T < 250 °C) and velocity decreasing with height.

If the fire is small only the buoyancy plume reaches the ceiling, while the two other flame zones are low near the ground. When the HRR increases and the intermittent flame impinges the ceiling, the critical velocity approaches a constant value. According to [21] the constant velocity region generates a barrier which doesn't depend on the power of the fire, but this can be questioned because the smoke movement is controlled by the total pressure rather than the sole velocity. As argued in [22] the backlayering is stopped when the total pressure of the incoming flow is equal to the total pressure or the smoke, but at this time it is not fully understood why the pressure becomes independent from the HRR [12].

A review of the critical velocity and of the backlayerig distance in tunnels has been presented by Li in [23] where he proposed a formulation similar to equation 1.8 based on new experimental data obtained in small and large scale tests.

$$u_c^* = \begin{cases} 0.81 \left(\dot{Q}^*\right)^{1/3}, & \text{if } \dot{Q}^* < 0.15 \\ 0.43, & \text{if } \dot{Q}^* > 0.15 \end{cases} \tag{1.10}$$

This equation has been compared with the results coming from big scale test showing a great agreement with them. The equation can be applied also to tunnels with obstructions, which reduce the cross section of a factor ε (blocked area divided by total area):

$$u_{c,obst}^* = u_c^* \left(1 - \varepsilon\right) u_c^* \tag{1.11}$$

The reduction of the cross section increases the longitudinal velocity along the tunnel. In the section of the fire the velocity is higher than the critical one due to the section's contraction, while in the other parts of the tunnel, where there are no obstructions, the longitudinal velocity can be below the critical value. The different estimations of the critical velocity are compared together in figure 1.1a in order to show the difference between the proposed equations. If the longitudinal velocity is below the critical value the smoke is capable to flow upstream the fire. Figure 1.1b shows the backlayering during the Metro test [15] and the backlayering distance travelled by the smoke.

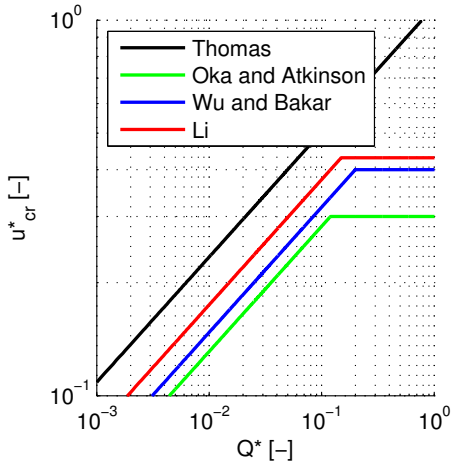

(A) Critical velocity

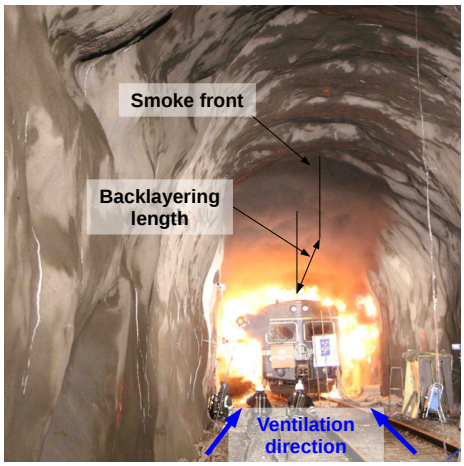

(B) Smoke movement in tunnel [15]

FIGURE 1.1: Critical velocities and smoke backlayering

1.2.1 Scaling process: from small scale to big scale

As seen in the previous section, the most of the data regarding the critical velocity are coming from small scale tests, because of the cost and of the difficulties related to the execution of full scale experiments. The information about critical velocity obtained in the laboratories are exported to real scale tunnels, therefore it is necessary to find a simple and reliable way to exchange results among scales. Starting from the governing equations of the fluid dynamic problem several non-dimensional numbers can be defined to describe the phenomena involved. In order to have two similar flow fields all the non-dimensional numbers should be preserved among the scales, but this is not feasible in practice so only some of them are kept among the scales. The two most important numbers for fire problems are the Froude and the Reynolds numbers, these represent the ratio among the forces that are driving the fluid:

$$Fr = \frac{Inertia forces}{Gravity forces} = \frac{u}{\sqrt{gL}} \tag{1.12}$$

$$Re = \frac{Inertia forces}{Viscous forces} = \frac{\rho u L}{\mu} \tag{1.13}$$

To transfer the results from one scale to the other these numbers should be the same in the two scales. The critical velocity in a real scale u_c can be calculated equalising the Froude numbers and knowing the characteristic lengths of the tunnels L and L_0 and the critical velocity in the small scale u_{c0}. In order to preserve also the Reynolds number the operative density of the fluid should be changed as follows.

$$\frac{\rho}{\mu} = \frac{\rho_0}{\mu_0} \left(\frac{L_0}{L} \right)^{3/2} \tag{1.14}$$

The fulfilment of the second equation 1.14 requires to change the density of the operating fluid in one of the two scales.

To scale the results in fire problems Quintiere [19] proposed three methods, summarized hereafter:

- Froude Scaling: only the Froude number is preserved, while the Reynolds number changes between the scales, ignoring the effect of the viscous forces on the fluid.
- Pressure Scaling: in order to preserve both numbers the operative pressure of the experiment is changed.
- Analogue Scaling: in order to preserve both numbers the density of the fluid is changed by using another one.

Among those three approaches the most common is the Froude scaling because it doesn't require to change the density of the operating fluid and it produces reliable results. The operative pressure in the experiment can be set at the ambient value and normal fuels and air can be used. The limit of the Froude scaling becomes evident when the fluid in the tunnel is not fully turbulent, but is laminar, in such case when the viscous forces become a major force in the flow the Froude scaling fails [24]. For the small scale tests presented in section 1.2 the scale reduction didn't change the flow from turbulent to laminar, therefore the results about critical velocity can be extrapolated to the real scale tunnel using the Foude scaling. A more detail verification of the Froude scaling for tunnel problems is presented in section 2.5.

1.2.2 Smoke confinement by means of jet fans

With small scale experiments the main research topic about longitudinal ventilation is the calculation of the critical velocity, which is later used for the design of the tunnel's ventilation. In a real tunnel the flow is pushed by jet fans which blow air or smoke at high velocity (30-40 m/s) inducing a longitudinal flow along the tunnel.

Jet fans are relatively simple machines, made by one rotor and in some solutions a stator. The work exchanged among the fan and the fluid can be written based on the Euler equation:

$$W = \omega(u_{t,2}r_2 - u_{t,1}r_1) \tag{1.15}$$

Where u_t is the tangential component of the velocity in the fan and ωr is the rotation speed of the fan. The impulse force induced by the jet fan when placed in a tunnel can be calculated as:

$$F_{f,u} = \rho(u_a - u_{tun})Q_f \tag{1.16}$$

where ρ is the flow density u_a is the velocity at the exhaust of the fan, u_{tun} is the velocity in the tunnel and Q_f is the discharged volume by the fan. The force of the jet fan is reduced because of the pressure losses caused by the recirculation of flow inside the tunnel, the net force applied to the tunnel is calculated as:

$$F_t = \rho(u_a - u_{tun})Q_f\frac{1}{k} \tag{1.17}$$

Where k is the effectiveness of the jet fan inside the tunnel or Kempf factor, which has been first introduced in [25] and it represents the portion of the

thrust of the fan that induce a longitudinal flow. The value k depends on the position of the fan inside the tunnel and on the jet fan configuration. The effect of the distance of the jet fan from the wall has been investigated by different authors in [25–27]. Those first experimental investigations considered a single jet fan which was tested with a uniform flow field at the tunnel's inlet. In real tunnels the presence of several jet fans generates a mutual influence between the fans, due to the non-uniform flow induced by the other devices. The jet fans' grouping and the orientation of the fan exhaust have been investigated with experimental test in [28, 29] evaluating the efficiency for several configurations.

All those test have been carried out with cold flow, but jet fans are commonly used also to confine the smoke in case of fire, providing a longitudinal velocity greater than the critical one. As found out by Oka and Atkinson in [11] the critical velocity is upper limited for large fires, but this doesn't assure that the ventilation designed for cold conditions can handle also the smoke confinement in case of fire. Large fires induce a pressure loss inside the tunnel and reduce the longitudinal flow generated by the fans, as seen in [8]. The reduction of the longitudinal velocity induced by the fire is known as fire throttling effect which has been studied first by Lee in [18] with experimental measurement in a small scale tunnel. Lee noticed that in case of a larger fire it is necessary to increase the fan speed and rise the pressure in order to keep the same velocity in the tunnel. Similar results have been found out in the Memorial tunnel when longitudinal ventilation has been tested, a fire of 10 MW reduced the air velocity about 10 % and a fire of 100 MW about 50-60 % compared to the cold conditions. The throttling effect of the fire has been later investigated with numerical methods in [30, 31], where the longitudinal velocity in the tunnel has not been imposed but calculated from the balance of the longitudinal forces inside the tunnel.

Throttling effect should be taken into account when the longitudinal ventilation is designed for the smoke confinement, since it induces an additional pressure loss which reduces the longitudinal flow compared to the cold case.

1.3 Structural behaviour of concrete tunnels

The second main topic of this work is the structural analysis of concrete structures exposed to fire. Most of the fires happened in the last decades caused fatalities and damaged the structure of the tunnels requiring huge cost for the refurbishment. In the Mont Blanc tunnel, between Italy and France, in 1999 a Belgian truck caught on fire leading to an extended fire which involved other 16 trucks, with 38 fatalities. In the Tauern Road Tunnel in Austria in 1999 an accident between several cars led to an extended fire which caused 12 fatalities and several injured. In 2000 in Kaprun, near Salzburg Austria due to an electric failure a funicular train caught on fire with 159 fatalities. Earlier, fires like in Great Belt Tunnel in 1994 and Channel tunnel in 1996 didn't cause fatalities but the tunnels were seriously damaged due to spalling on the walls of the tunnel. In the tunnels portions of material felt from the walls reducing the section of the tunnel and exposing other parts of the vault to fire. The temperatures measured in the fires were

in the range between 800 and 1100 °C and the fire lasted many hours due to the spread between vehicles.

1.3.1 Temperature near the tunnels' ceiling in case of fire

In order to protect the structures and the people trapped in the tunnel in case of fire it is important to study the fire resistance of tunnel's vaults, which are mainly made of concrete. The concrete elements can be tested at high temperature in order to assess their response to fire and their eventual failure. To reproduce the fire scenario it is necessary to expose the structure to high temperatures which represent a realistic thermal load in tunnel. Standard temperature curves have been developed during these years in order to reproduce different fire loads, figure 1.2a.

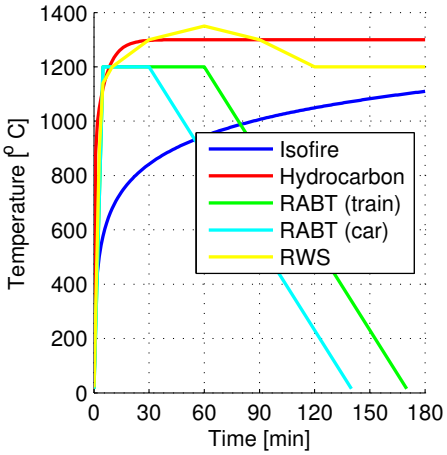

(A) Temperature curves

(B) Tunnel after fire

FIGURE 1.2: Temperature curves for tunnel fire and effect of the fire

A fire curve which was commonly used in buildings and is based on a cellulose fire is the BS 476 or ISO 834 fire curve. This curve has a logarithmic trend and it is a monotonic growing function, the temperature rises in the first 30 minutes from 20 to 842 °C but later the fire growth is slowed down and about 90 minutes are required to reach the 1000 °C. This fire curve doesn't have a descendent phase and it doesn't represent the decay phase of the fire. The cellulose fire, that is reproduced by the ISO fire curve, cannot represent fire loads induced by hydrocarbon fuels which have a faster growth and reach higher temperatures.

In the petrochemical industry a new fire curve, Hydrocarbon, has been drawn in the 70s in order to fulfil the lacks of the previous curves. The Hydrocarbon curve rises from 20 to 1000 °C in 7.5 minutes, reaches 1100 °C after 30 minutes and remains constant. Also this curve was unsuitable for tunnels where there is a strong interaction between the fire and the walls, due to the high temperature the hot surfaces re-radiate and reduce the heat losses through the vault rising the gas temperature. The curve has been changed in order to reach higher temperature that might occur in case of severe fires in tunnels, the modified HydroCarbon Modified curve (HCM) peaks 1300 °C and remains constant up to 180 s.

In Germany a curve has been developed to simulate the fire of a train and of a car giving a time curve. The temperature rises from 20 to 1200 °C in 5 minutes and later it remains constant up to 60 minutes for the train and to 30 minutes for the car, later the temperature returns to 20 °C in 110 minutes.

The most severe fire curve has been developed by the Ministry of Public Works, the Rijswaterstaat (RWS), and TNO in the Netherlands which simulated the temperature curve induced by a petrol tanker on fire (100 MW). The temperature rises in 5 minutes from 20 to 1140 °C and reach the peak of 1350 °C in 60 minutes later the curve cools down to 1300 °C up to 180 minutes.

The approach proposed here is fully prescriptive and doesn't consider the HRR of the fire, tunnels' geometry, ventilation strategy and ventilation velocity. A simplified approach to calculate the temperature of the gas impinging the structure has been proposed by Kurioka [32] considering a tunnel with longitudinal ventilation. In this model the flame is modelled as an hot flow of gas which is tilted by the longitudinal flow and can impinge the ceiling downstream the fire place. The model has been validated against some experimental data and it allows to predict the temperature distribution beneath the ceiling when the hot gas flow and/or flame impinges the ceiling. The maximum temperature impinging the ceiling can be calculated basing on the non dimensional HRR and on the Froude number:

$$\frac{\Delta T}{T_a} = \begin{cases} 1.77 \left(\frac{Q^{*2/3}}{Fr^{1/3}}\right)^{6/5}, & \text{if } \frac{Q^{*2/3}}{Fr^{1/3}} < 1.35 \\ 2.54, & \text{if } \frac{Q^{*2/3}}{Fr^{1/3}} > 1.35 \end{cases} \tag{1.18}$$

Due to the longitudinal velocity the flame is tilted downstream the fire place of a length L and the maximum temperature downstream the fire occurs at:

$$\frac{L}{H_{eff}} Fr^{1/2} = \alpha \left[\left(\frac{H^{3/2}}{b^{1/2} A_f^{1/2}} Fr Q^{*(2\eta-1)/5} \right) \right]^{\beta} \tag{1.19}$$

Where H_{eff} is the effective distance between the fire place and the ceiling. Since the interaction between the flame and the cross wind is different depending on the flame's region, the coefficients α,β,η are calculated basing on experimental observation and summarized in table 1.1.

TABLE 1.1: Coefficients for the flame model of [32].

Flame zone	α	β	η	ΔT_{max}
Buoyancy	-1/3	0.79	0.73	<250 K
Intermittent	0	0.92	0.60	250-550 K
Continuous	1/2	1.02	0.56	>550 K

The flame regions have been defined by Kurioka [32] in a similar way as proposed in [21] using the a threshold temperature to divide the zones. Another similar model has been developed by Li [33] who argued that the model proposed by Kurioka couldn't represent fire with high HRR since

the maximum temperature rises up to 750 °C. Starting from the results obtained in experimental works, Li proposed two different equations that can be used for small fire, which are not impinging the ceiling, and big fire, impinging the ceiling. To define the type of flame, the parameters DTR1 and DTR2 are defined as follow:

$$DTR1 = 17.5\frac{\dot{Q}^{2/3}}{H_{eff}^{5/3}} \tag{1.20}$$

$$DTR2 = \frac{\dot{Q}}{Vb_{f0}^{1/3}H_{eff}^{5/3}} \tag{1.21}$$

where b_{f0} is the radius of the fire source, the temperature rise can be calculated as function of the ventilation regime and of the fire power. A non dimensional velocity must be defined for the model as:

$$\frac{V^*}{V} = \frac{g\dot{Q}}{b_{f0}\rho_0 c_p T_0} \tag{1.22}$$

In case of transverse or semi-transverse ventilation system or in case of natural ventilation the longitudinal velocity is low. If the value of V^* is smaller than 0.19 the temperature rise is calculated as:

$$\Delta T \begin{cases} DTR1, & \text{if } DTR1 < 1350 \\ 1350, & \text{if } DTR1 > 1350 \end{cases} \tag{1.23}$$

While in case of longitudinal ventilation, when the V^* is greater than 0.19, the temperature rise is calculated as:

$$\Delta T = \begin{cases} DTR2,, & \text{if } DTR2, < 1350 \\ 1350, & \text{if } DTR2, > 1350 \end{cases} \tag{1.24}$$

From equations 1.20 and 1.21 the temperature rise is much higher that the one predicted by equation 1.18 and better fits the results from large scale experiments. In the present formulation the influence of the material's properties of the wall is not included despite it plays an important role in the heat losses due to conduction, this effect, ignored in the two models, could be one of the reason of the scattering of the experiential data found by Li in [33]. Despite the accuracy of the two models both of them depend from the same variables:

- HRR: Obviously higher is the power of the fire higher is the temperature inside the tunnel.
- Ventilation velocity: The longitudinal velocity is capable to cool down the gasses and to reduce the temperature near the fire source.
- Distance between the fire and the ceiling: This distance better represents, compared to the tunnel's height, the occurrence of impinging of the flame on the ceiling.
- Radius of the fire: The size of the burner has an important effect on the stretch of the flame towards the ceiling. Smaller burners have longer flames therefore warmer gasses impinge the ceiling.

The structures in tunnels in case of fire are exposed to extreme conditions, however the incident heat fluxes should be used to quantify the thermal loads instead of temperature. The net heat flux exchanged between the fluid and the walls is the balance of the incoming and outcoming heat flux. The incident heat flux is the sum of convictive and radiative heat flux impinging the structure:

$$\dot{q}''_{in} = T_g^4 \varepsilon \sigma + h T_g \tag{1.25}$$

Where T_g is the gas temperature in K, ε is the surface emissivity, σ is the Stefan–Boltzmann constant and h is the convective heat transfer coefficient. At high temperature the incident heat flux is driven by radiation so small difference in temperature implies huge difference in the fluxes as shown in figure 1.3.

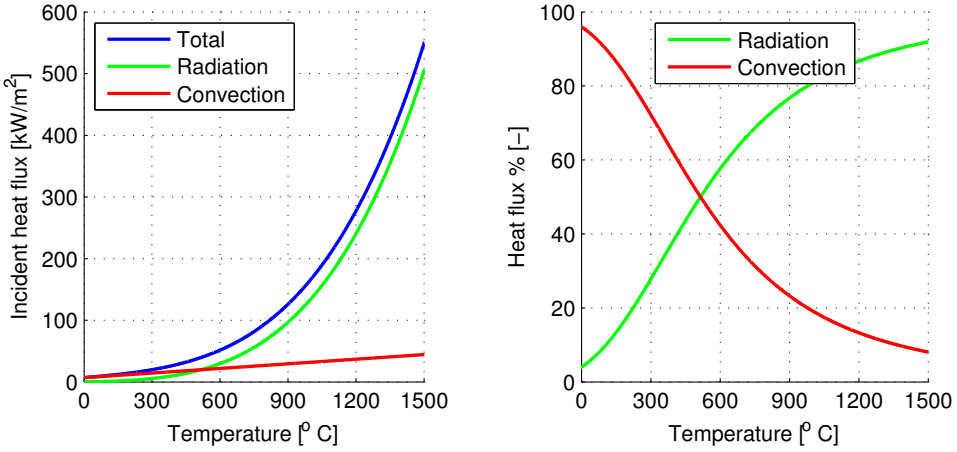

(A) Heat fluxes (B) Heat contributions

FIGURE 1.3: Incoming heat flux considering α equal to 25 W/m^2 and ε equal to 0.9.

In case of fire, the structure is exposed to heat fluxes rather than temperatures. The trend of the incident flux is much steeper than the temperature rise, the maximum temperature calculated with equation 1.23 is 1.8 times the maximum temperature calculated with 1.18, but the ratio between the heat fluxes is about 4.8.

1.3.2 Structure failure and spalling

Once the thermal input has been calculated as seen in the previous section the response of the structure and of the material must be investigated. Concrete is a common material in structures and it shows some important properties when exposed to fire: it is not flammable and it is highly insulating. But concrete shows also some weakness when the temperature rises because the mechanical properties deteriorate and the structure might fail in a explosive way due to spalling.

The loss of stiffness of concrete materials is consequence of the cracks' formation and propagation in the structure and it is commonly known as material's damage [34]. The damage leads to an irreversible reduction of

the resistant area so the modified effective stress that is acting on the material can be calculated starting from the nominal stress applied:

$$\tilde{\sigma} = \frac{A}{\tilde{A}}\sigma = \frac{1}{1-D}\sigma \tag{1.26}$$

where A is the initial resistant area of the material before damaging and $\tilde{A}$ is the resistant area after cracking, D_{tot} is the total damage which can range from 0 to 1 when the material undergoes to failure. The damage in concrete at high temperature is influenced by thermochemical and mechanical degradation as proposed by [35]. The thermochemical damage is consequence of microcracks induced by the different expansion of aggregates and cement paste at high temperature and of the decrease of strength due to the dehydration process. The thermochemical damage can be evaluated experimentally measuring the reduction of the Young modulus in a concrete sample, mechanically undamaged, at high temperature compared to the Young modulus at ambient temperature:

$$D_{TC} = 1 - \frac{E_0(T)}{E_0(T_a)} \tag{1.27}$$

The mechanical damage can be calculated considering the formation and spread of cracks inside the material due to the stresses applied to the structure. The mechanical damage model are usually formulated at ambient temperature, but damage can be calculated at high temperature considering the loss of stiffness at the generic temperature T:

$$D_M = 1 - \frac{E(T)}{E_0(T)} \tag{1.28}$$

The total damage is obtained composing the two equations 1.27 and 1.28:

$$D_{tot} = 1 - \frac{E(T)}{E_0(T_a)} = 1 - \frac{E(T)E(T)_0}{E(T)_0 E_0(T_a)} = 1 - (1 - D_{TC})(1 - D_M) \tag{1.29}$$

Therefore the effective stress on the structure as presented in equation1.26 can be calculated considering both the thermochemical degradation and the effect of the stress induced cracks:

$$\tilde{\sigma} = \frac{1}{(1 - D_{TC})(1 - D_M)}\sigma \tag{1.30}$$

When concrete structures are exposed to fire they can fail with lower loads compared to the same structure loaded at ambient temperature because the reduction of resistant area rises the stresses in the material. But the loss of strength is not the only threat for concrete structures because the material can fail in an explosive way due to spalling.

Concrete spalling is defined as "the violent or non-violent breaking off of layers or pieces of concrete from the surface of a structural element when it is exposed to high and rapidly rising temperatures". Spalling has been studied widely with both numerical and experimental analysis [36] in order to find the phenomena that are leading to the failure of parts of the structure. As proposed by Gawin et al. in [37] spalling is the consequence of several effects combined together.

- The gas pressure rises due to the evaporation of the water, the expansion and flow of gases inside the material. The phenomena responsible of the pressure peak are called "moisture clog" and "saturation plug". The pressure is usually in the range of 1-2 MPa with peaks of 4 MPa for ultra high performance concrete (UHPC) [38, 39].
- The heating and expansion of parts the structure which are constrained by the remaining parts still cold. The non uniform heating and expansion induces a compressive stress near the heated surface of the structure.
- The cracks inside the material reduce the section of the material and create stress concentration near the crack's tip.

These effects combined together lead the structure to spall, some spalling mechanism have been proposed by Gawin et al. in [37] in order to provide some simplified index to assess the risk for the structure, figure 1.4.

The first failure mode is consequence of the pressure-induced shear, the high gas pressure cumulated in the material generates a force that is proportional to the area of the crack and to the pressure. Parts of structure undergo to failure when the pressure induced force exceed the shear force of the material. The risk of spalling increases also with the damage of the resistant sections due to the reduction of the effective area on which the force is applied. The balance of forces can be written for a simple bi-dimensional case considering a crack of length b_c at depth $L_{r,c}$ from the surface applied on a material with tensional strength f_t.

$$(p_g - p_{atm})b_c = f_t L_{r,c} \tag{1.31}$$

The second failure mode is caused by the buckling of some layers of material which are behaving like columns with a bending force induced by the gas pressure inside the material. Due to the heating of the structure the outer layers tend to expand, this expansion is constrained by the colder material that is not warm yet. This non uniform temperature distribution induces a compressive stress parallel to the surface of the heated wall. Due to the damage of the material the first layers of material can be treated as columns under compressive stress, the limit stress that triggers the buckling and the spalling is:

$$\sigma_{th} = \sigma_E = \frac{\pi^2 E}{12}\left(\frac{b_c}{L_{r,c}}\right)^2 \tag{1.32}$$

The equation 1.32 doesn't take into account the effect of the bending induced by the pressure. The deflection of the column after the application of a constant pressure can be calculated as:

$$w_0 = \frac{5}{32}\frac{p_g - p_{atm}}{E}\left(\frac{L_{r,c}}{b_c}\right)^3 L_{r,c} \tag{1.33}$$

The initial bending caused by the pressure is enhanced by the compressive thermal stress. Two failure modes can occur in the beam, the tensile failure occurs when bending stress on the tensile side of the deformed beam is equal to the compressive thermal stress σ_{th}, in this case the limit pressure

inside the material can be calculated as:

$$p_g - p_{atm} = \frac{16}{15} E \left(\frac{b_c}{L_{r,c}}\right)^4 \left(1 - \frac{\sigma_{th}}{\sigma_E}\right) \tag{1.34}$$

The second failure mode caused by the buckling occurs when the sum of the compressive stresses induces by the bending force and by the thermal expansion reach the limit of the material leading to failure. By summing the two compressive stresses and considering the limit stress of the material it is possible to calculate a critical pressure inside the material.

$$p_g - p_{atm} = \frac{64}{5\pi^2}(\sigma_{th} - \sigma_E)\left(\frac{f_c}{\sigma_{th}} - 1\right)\left(\frac{b_c}{L_{r,c}}\right)^2 \tag{1.35}$$

The buckling mode for spalling consider the effect of the gas pressure and the constrained expansion of the material which is strongly related to the geometry of the structure exposed to fire.

Fracture mechanics mode has also been investigated in order consider the effect of the propagation of cracks inside the material. Cracks can propagate in the material due to the compressive stress induced by the constrained expansion. When the cracks propagate there is a generation of new surfaces and release of energy which change the stress field near the damaged zone. In the damaged material the first layers behave like columns compressed and bended by the gas pressure, as seen before. The probability of failure can be evaluated comparing the energy densities before and after the cracks' propagation. In the material the failure occurs due to two different cracks systems, one compressive splitting cracks and cracks parallel to the compressive stress induced by the transverse stress on the material. The region affected by the failure is a strip of material with several cracks, the energy released from the region is calculated as:

$$\Delta U = \int_V \delta U dV = \frac{\sigma_{th}^2}{2E} BaL_{r,c} \tag{1.36}$$

where σ_{th} is the compressive stress, a is the thickness of the fractured zone and B is the width of the compressed zone, the energy dissipated by the cracks is calculated as:

$$W_f = \frac{G_f Bha}{s} \tag{1.37}$$

From the equilibrium of the two energies 1.36 and 1.37 the critical compressive stress is equal to:

$$\sigma_{th} = \left(\frac{2E}{l_{r,c}} G_f \frac{h}{s}\right)^{1/2} \tag{1.38}$$

In this last failure mode is clear the effect of the local conditions of the material but in this mode the gas pressure doesn't have any influence on spalling. A graphical representation of the three spalling modes is presented in figure 1.4 As stated by Gawin the different modes of spalling are acting together on the material and the failure of the structure occurs when one of these modes becomes critical. However due to the large variability of structures and materials the prediction of spalling is still an open research topic. Further development are required in the modelling of concrete

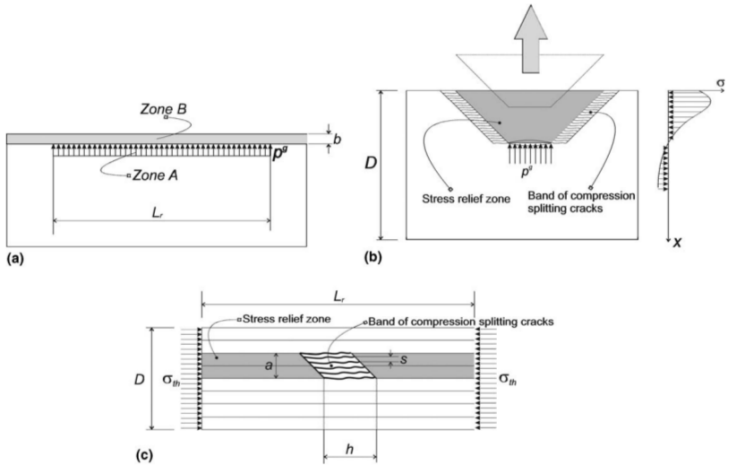

FIGURE 1.4: Different failure modes in case of smalling presented in [37]

on different scales: modelling the properties of different material's components, modelling the material at the meso-scale and finally modelling the structure in the large scale.

1.3.3 Modelling of concrete at high temperatures

In order to study the response of concrete structures at high temperature it is necessary to model the mechanical behaviour of the structure and the heat and mass transfer in the material. Concrete is a porous material which is made of a deformable skeleton whose pores are filled with water and dry air. The model here presented considers the material partially saturated therefore it considers always the presence of liquid and gas phases, also above the critical temperature. The model here presented bases on the original work of Schrefler and Gawin [40–42], which has been later extended in order to model porous media at high temperature [35].

Inside the material there are liquid water, water vapour and dry air, these species move due to concentration gradient (diffusive flow) and due to pressure gradient (Darcian Flow). The liquid water is present in the material as bound water (absorbed water) which is present in the whole range of water contents of the medium, and capillary water (free water) which appears when water content exceeds so-called solid saturation point S_{ssp} [43], below the critical point of water.

The conservation of liquid water and vapour together are expressed with a continuity equation, the equation allows to delete the phase change term which is common in for both phases. The second specie is the dry air which is flowing through the material, the conservation of the dry air is expressed by the second continuity equation. The third equation is the enthalpy balance for the material, considering that the heat is exchanged due to advection, phase change and conduction. Since the skeleton is considered as a deformable solid the linear momentum balance is written as fourth equation. The model solves all the equations together because of the strong coupling of the phenomena involved. Continuity equation of dry

air:

$$\phi\frac{\partial}{\partial t}\left[(1-S)\rho_{ga}\right]+(1-S)\rho_{ga}+\frac{\partial\phi_{hydr}}{\partial t}+\alpha(1-S)\rho_{ga}\frac{\partial}{\partial t}(\nabla\cdot\mathbf{u})+\nabla\cdot(\rho_{ga}\mathbf{v_g})+\nabla\cdot(\rho_g\mathbf{v_{ga}^d})=0 \tag{1.39}$$

Continuity equation of water:

$$\begin{aligned}\phi\frac{\partial}{\partial t}\left[(1-S)\rho_{gw}\right]+(1-S)\rho_{gw}+\frac{\partial\phi_{hydr}}{\partial t}+\alpha(1-S)\rho_{gw}\frac{\partial}{\partial t}(\nabla\cdot\mathbf{u})+\nabla\cdot(\rho_{gw}\mathbf{v_g})+\nabla\cdot(\rho_g\mathbf{v_{ga}^d})=\\ =-\phi\frac{\partial}{\partial t}(S\rho_w)-S\rho_w\frac{\partial\phi_{hydr}}{\partial t}-\alpha(S)\rho_w\frac{\partial}{\partial t}(\nabla\cdot\mathbf{u})-\nabla\cdot(\rho_w\mathbf{v_l})-\frac{\partial}{\partial t}(\delta m_{hydr})\end{aligned} \tag{1.40}$$

Enthalpy balance:

$$\begin{aligned}\rho C_p\frac{\partial T}{\partial t}+\left[C_{pw}\rho_w\mathbf{v_l}+C_{pg}\rho_g\mathbf{v_g}\right]\nabla T-\nabla\cdot(\lambda_{eff}\nabla T)-\delta h_{hydr}\frac{\partial}{\partial t}(\delta m_{hydr})=\\ =\delta h_{phase}\left[\phi\frac{\partial}{\partial t}(S\rho_w)+S\rho_w\frac{\partial\phi_{hydr}}{\partial t}+\alpha(S)\rho_w\frac{\partial}{\partial t}(\nabla\cdot\mathbf{u})+\nabla\cdot(\rho_w\mathbf{v_l})\right]\end{aligned} \tag{1.41}$$

Linear momentum equation:

$$\nabla\cdot\frac{\partial\sigma}{\partial t}+\frac{\partial\rho}{\partial t}\mathbf{b}=0 \tag{1.42}$$

where ρ is the average density of the different phases:

$$\rho=(1-\phi)\rho_s+\phi S\rho_l+\phi(1-S)\rho_g \tag{1.43}$$

The stresses acting on the material are calculated basing on the effective stress since the concrete has porous structure and it is filled with air and water.

$$\sigma'=\sigma+\alpha p^s I; \tag{1.44}$$

The solid pressure p^s represents the effect of the gas and liquid inside the porous media and it can be calculated as:

$$p^s=\begin{cases}p_g-p_{atm}, & \text{if } S<S_{ssp}\\ (S-S_{ssp})p_w+[1-(S-S_{ssp})](p_g-p_{atm}), & \text{if } S>S_{ssp}\end{cases} \tag{1.45}$$

Below the S_{ssp} only the gas phase is acting on the skeleton of the material, while above this limit both liquid and gas phases are inducing a solid pressure, because of a meniscus between the liquid and the vapour. Four equations are used to describe the concrete behaviour, but other three physical equations are required. The dehydration process of concrete which is function of temperature and can be measured for different materials with experimental tests [44]. The other two equations are the mechanical and thermochemical damage which have already been presented in the previous section in equations 1.27 and 1.28. For the model's closure the physical properties of the materials of water and of air are required, these are calculated basing on experimental tests carried out at different temperatures.

The model described above involves different species and different phases, to solve the problem the gas pressure, p_g, the capillary pressure, p_c, the temperature, T, and the displacement, u, are used as state variables. Special attention must be paid at the capillary pressure, used both below and above the solid saturation point, in presence of liquid and vapour the capillary

pressure is defined as:

$$p^c = p^g - p^w = -\rho_w \frac{RT}{M_w} ln\left(\frac{p^v}{p^{vs}}\right) \tag{1.46}$$

where p^g is the vapour pressure and p^w is the water pressure. This state variable has a physical meaning when in the material there is an interface between liquid and gaseous water. For fire problems when the material cross the critical temperature and the saturation is below the S_{ssp} the liquid water present in the material evaporates and becomes gas, which cannot condensate by varying the partial pressure. Above the critical point the only adsorbed water and water vapour is present, but due to the absence of the meniscus between the liquid and the vapour the equation 1.46 losses its meaning. The capillary pressure can be used also above the critical point of water as discussed by Gawin in [45] but a new definition is required. The capillary pressure above the critical temperature is a thermodynamic potential which can be calculated as:

$$p^c = -\rho_w \frac{RT}{M_w} ln\left(\frac{p^v}{f^{vs}}\right) \tag{1.47}$$

where f^{vs} is the fugacity of the water vapour corresponding to the saturation of adsorbed liquid water and ρ_w is the water density at the critical temperature. At the critical temperature the fugacity is equal to the critical pressure of water 22.09 MPa while above the critical point the fugacity is calculated assuming the vapour to behave like an ideal gas. This approach allows to span the whole range of temperature and to study the concrete at really high temperature.

In order to evaluate the capabilities of the model to correctly predict the behaviour of concrete at high temperature the model has been validated by Witek in [46] and by Pesavento in [47]. For a more complete description of the model presented in this section the interested reader should refer to [35, 42, 47–49]

een calculated the differe

Chapter 2

Early validation cases

The two main topics investigated in this thesis have been introduced in chapter 1: the analysis of longitudinal ventilation in tunnels and response of concrete structure exposed to fire.

For the analysis of longitudinal ventilation and fire scenarios computational fluid dynamics (CFD) is chosen to simulate the flow field in the tunnel. Several programs can solve the flow field by solving the equations of Navier-Stokes, but some of them are developed for a specific engineering field. In fire safety problems combustion, heat transfer, phase change are driving the flow and a great effort is required for the modelling and simulation of the fire scenario. Commercial codes like Fluent or CFX have been developed to be general purpose, while codes like FDS or Fire Foam have been specifically developed for the fire safety field. In this work FDS has been chosen because of the following reasons:

- the code has been specifically developed for fire safety problems.
- the code is Open Source and it allows to modify or add routines.
- the code is under continuous development with validation and verification.

In the next chapters FDS is used to investigate the longitudinal ventilation in case of fire in tunnels and to estimate the thermal input on concrete structures exposed to fire. Before starting to investigate these specific topics it is important to assess the reliability of the numerical results provided by FDS. In this chapter some experiments are selected to be reproduced with FDS showing its capability to correctly predict the experimental measurements.

2.1 Introduction to FDS

FDS is a CFD code developed by the National Institute of Standard and Technology (NIST) and Technical Research Centre of Finland (VTT), it has been first released in 2000 and it is still under development [50]. FDS solves the Naviest-Stokes equations with Large Eddies Simulation (LES) approach using a finite difference approach in time and space. The LES approach has been chosen since it allows to simulate transient problems, as contrary to RANS approach which simulates only steady state flows. The LES approach for the solution of the Navier-Stokes equations allows to simulate part of the flow field, while other parts are simply modelled. For the correct resolution of the Navier-Stokes equations, without any modelling of

the turbulence, the spatial grid size and temporal discretization should simulate all the eddies inside the flow with a huge computational cost, as done in Direct Numerical Simulations (DNS). From the research of Kolmogorov about turbulence [51] we know when the eddies dissipate their kinetic energy into thermal energy, so we can calculate the size of the smallest turbulent eddy, also known as Kolmogorov length scale:

$$\eta = \left(\frac{\nu^3}{\varepsilon}\right)^{1/4} \tag{2.1}$$

where ν is the kinematic viscosity and ε is the rate of viscous dissipation. After the definition of the Kolmogorov length scale in equation 2.1, the theory of the self similarity of the eddies can be applied in order to pass from DNS to LES. The small scale eddies are similar among them and they are not affected by the geometry of the domain, while large scale eddies are function of the fluid domain. The small scale vortex can be simulated with a sub-grid scale model, while the larger vortex are explicitly solved. This allows to solve the Navier-Stokes equation in large environment without using small grid size. With the LES approach the variable u(x) is decomposed in two parts:

$$u(x) = \bar{u}(x) + u(x)' \tag{2.2}$$

where $\bar{u}(x)$ is solved by the LES and $u(x)'$ is modelled. The term $\bar{u}(x)$ is calculated by applying a low-pass filter, parameterized by a width Δ as:

$$\bar{u}(x,y,z,t) = \frac{1}{V_c}\int_{x-\delta x/2}^{x+\delta x/2}\int_{y-\delta y/2}^{y+\delta y/2}\int_{z-\delta z/2}^{z+\delta z/2} u(x,y,z,t)dx'dy'dz' \tag{2.3}$$

2.1.1 Governing equations

After a brief introduction to the LES approach compared to DNS, the equations solved by FDS are presented hereafter. In fire problems the combustion process transforms fuel ($C_xH_yO_z$) and air (O_2, N_2) into combustion product (CO_2, CO, C, H_2O, N_2), modifying the composition of the fluid inside the flow field. The conservation of the total mass can be written as:

$$\frac{\partial \rho}{\partial t} + \nabla \cdot (\rho \mathbf{u}) = \dot{m}'_b \tag{2.4}$$

where the therm on the right hand side, $\dot{m}'_b$, represents the mass released or absorbed by sub-grid particles such as sprinklers droplets or fuel droplets. The sub-grid particles are not explicitly resolved but their mass production must be taken into account during the simulation. The conservation of the total mass is not sufficient to describe different species in the flow, therefore for different species or lumped species the mass conservation can be written as:

$$\frac{\partial \rho Z_\alpha}{\partial t} + \nabla \cdot (\rho Z_\alpha \mathbf{u}) = \nabla \cdot (\rho D_\alpha \nabla Z_\alpha) + \dot{m}'_\alpha + \dot{m}'_{b,\alpha} \tag{2.5}$$

For the single specie α some mass can undergo to chemical reaction with mass generation or loss $\dot{m}'_\alpha$. The diffusive flow inside the gas, $\nabla \cdot (\rho D_\alpha \nabla Z_\alpha)$, is driven by the concentration of the single specie. The sum of all diffusive

flows and of the mass generated and lost for every specie is equal to zero, therefore these two therms are not included in equation 2.4.

In FDS the equations of Navier-Stokes are solved using the approach proposed by Rehm and Baum [52] for flows with low Mach number, the gas pressure is decomposed as sum of background pressure $\bar{p}(z,t)$ and pressure fluctuation $\tilde{p}(x,y,z,t)$. The background pressure takes into account the stratification of the atmosphere, the temperature and the density variation while the pressure fluctuation drives the flow.

$$\bar{p}(z,t) = \rho T R \sum \frac{Z_\alpha}{W_\alpha} \tag{2.6}$$

After decomposing the pressure in two therms we can write the equation of the energy conservation where the background pressure $\bar{p}(z,t)$ is used instead of the pressure p. Due to this choice the derivatives in the directions x and y are zero since $\bar{p}(z,t)$ is not dependent on these variables.

$$\frac{\partial \rho h}{\partial t} + \nabla \cdot (\rho h_s \mathbf{u}) - \frac{D\bar{p}}{Dt} = \dot{q}_{HRR} - \dot{q}_S - \nabla \cdot \dot{q} \tag{2.7}$$

where the h_s is the sensible enthalpy $h_s = \int_{T0}^{T} c_p(T)dT$, $\dot{q}_{HRR}$ is the heat release rate per unit of volume, $\dot{q}_S$ is the heat released by the sub-grid particles and $\dot{q}$ is the sum of the conductive, diffusive and radiative heat fluxes:

$$\dot{q} = -k\nabla T - \sum_\alpha h_{s,\alpha} \rho D_\alpha \nabla Z_\alpha + \dot{\mathbf{u}}_{rad} \tag{2.8}$$

The formulation of the energy balance is suitable for flows with low Mach number since the pressure is constant in the domain unless for the atmospheric stratification. However the simplification assumes the speed of sound to be infinite and the flows with high Mach number, such explosions, cannot be modelled. The third equation is the balance of forces in the fluid or momentum equation which can be written for the mixture of gas, assuming they are in equilibrium.

$$\frac{\partial \mathbf{u}}{\partial t} - \mathbf{u} \times \omega + \nabla \left(\frac{\mathbf{u}^2}{2} + \frac{\tilde{p}}{\rho} \right) - \tilde{p} \frac{1}{\rho} = \frac{1}{\rho} \left[(\rho - \rho_0)\mathbf{g} + \mathbf{f}_b + \nabla \cdot \tau \right] \tag{2.9}$$

where $\mathbf{f}_b$ is the drag force induced by the sub-grid particles and τ is viscous stress tensor. As previously stated the LES approach models the small scale eddies with a simplified approach, while solves the eddies in bigger scale. The effect of the small eddies that are not solved cannot be neglected because they have an important effect also on the main flow, therefore subgrid stresses must be included for the closure of the problem. The effect of the stresses induced by the sub grid eddies is taken into account adding a turbulent viscosity in the tensor τ which is calculated with the Deardorff model [53].

The combustion in FDS is modelled as a infinitely fast reaction using the Eddy Dissipation Concept model proposed by Magnussen and Hjertager in [54]. The idea behind the model is that the reaction is driven by the availability of fuel and oxygen and by the mixing time, without taking into account the activation temperature. The heat released by the combustion,

$\dot{q}_{HRR}$ in equation 2.7, is calculated as:

$$\dot{q}_{HRR} = -\sum_{\alpha} \dot{m}_{\alpha} \Delta h_{f,\alpha} \tag{2.10}$$

where $\Delta h_{f,\alpha}$ is the heat of combustion of the reaction and $\dot{m}_{\alpha}$ is the mass per unit of volume that undergoes to reaction. $\dot{m}_{\alpha}$ can be calculated basing on characteristic mixing time and on the species' availability.

$$\dot{m}_{\alpha} = -\rho \frac{min(Z_f, Z_a/s)}{\tau} \tag{2.11}$$

where Z_f is the mass fraction of fuel and Z_a/s is the maximum mass fraction of fuel that can be burned per unit of volume. Z_a is the air mass fraction, s is the stoichiometric ratio, τ, is the time scale for the mixing of the species before the reaction [55]. In this section the numerical approach for the solution of the equations of Navier-Stokes implemented in FDS is briefly presented, the interested reader should refer to [56] for a more exhaustive description of the models implemented in FDS.

2.2 Natural ventilation in a partially heated cavity

In order to approach gradually the simulation of fire in tunnels the first validation doesn't involve any fire scenario, but investigate its effects on the flow field. A fire is a source of heat which induces a flow that, in absence of other forces, is driven by density gradient [57]. The buoyancy driven flow doesn't occur only in case of fire but when there is a source of heat which induces temperature and density variations in the fluid [58]. Buoyancy flows and natural convection have been studied in building to investigate the natural ventilation [59]. Because of the uncertainties induced by the fire, in the first validation the source heat are walls at different temperatures. A small scale experiment has been chosen instead of large scale one because of the limited uncertainties and the easier modelling. In case of small scale problems several quantities can be measured with greater accuracy and extensive validation can be carried out [60, 61].

2.2.1 Experiment description

The experiment used for the validation has been performed by Ampofo and Karayannis [62]. As shown in figure 2.1, a box 0.75 m high, (y-axis) 0.75 m wide (x-axis) and 1.5 m deep (z-axis), containing air at atmospheric pressure, was heated from one side (the left wall) and cooled from the other one (the right wall) to generate a circular flow patter in the air. This geometry was designed to provide a two-dimensional flow field at the vertical plane in the middle of the cavity: in fact, as pointed out by Penot and N'Dame [63], if the horizontal aspect ratio is greater than 1.8, the three dimensional effects can be neglected.

The vertical walls were kept at constant temperatures of 50° C and 10° C respectively by pumping water with a rate of 40 l/min inside water gaps separated from the air by a 6 mm steel plate. The horizontal walls were made by a 1.5 mm thick mild steel sheet, coated with a 100 mm polystyrene layer, insulating the cavity from the laboratory where the air temperature

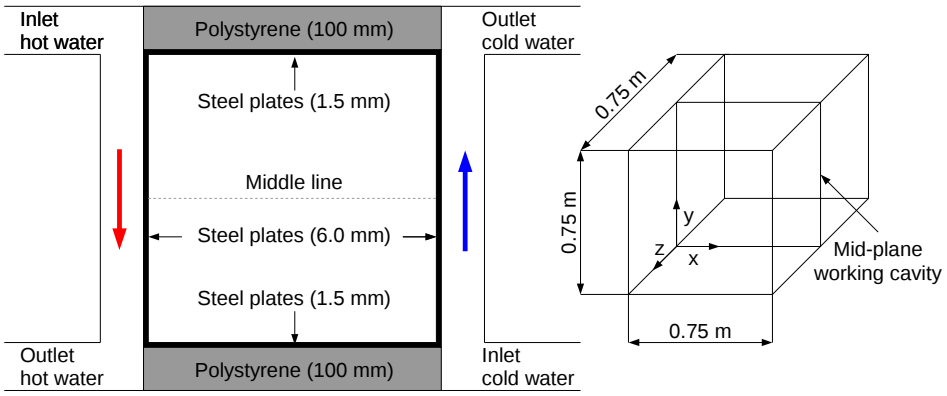

FIGURE 2.1: Schematic view of the experiment

was 30° C constant. The front and rear walls were made by a double glass panel and were used as guard cavities. In steady conditions, velocities and temperatures have been measured at different positions on the vertical middle plane (y = 0.75 m). A laser Doppler anemometer (LDA) was employed to measure the instantaneous velocities, while micro-diameter thermocouples were used to measure the air temperatures, as well as the surface temperatures of the walls. These data were used to compute the local Nusselt number along the surfaces:

$$Nu_{loc} = -\frac{H}{T_h - T_c}\frac{\partial \overline{T}}{\partial x_i}\bigg|_w \tag{2.12}$$

where H was the width of the cavity, T_h and T_c were the hot wall and cold wall temperatures, and the derivative was evaluated on the wall in the thermal boundary layer using the local surface temperature and the air temperature inside the conductive layer.

2.2.2 Numerical modelling and simulation results

In the cavity the flow is mainly circulating near the walls while the core has low velocity, as shown in figure 2.5b. The movement of the air driven by the density gradient and the heat exchange with the walls. To correctly reproduce this experiment with FDS it is necessary to simulate correctly the velocity profile and the heat exchange through the walls.

In FDS, to avoid too heavy calculations, the flow inside the boundary layer is not explicitly solved since it is usually fully contained in the first cells row. The near-wall velocities in the first cell are calculated by means of the correlations of Werner and Wengle [64], whereas the viscous stress is modelled using a logarithmic velocity profile. Near the wall, the tangential velocities are in phase with the instantaneous wall shear stress and the friction velocity is assumed to have a profile which is linear in the near wall region ($y^+ < 11.81$) and logarithmic elsewhere ($y^+ > 11.81$). The near wall velocity is calculated from the wall shear stress, integrating the friction velocity profile along the height of the first cell [56].

The convective heat transfer between a wall and the fluid is also modelled with a simplified approach: instead of solving the thermal boundary layer and using the local conduction in the first cell, a convective heat transfer coefficient h is used for the first cell; this coefficient is calculated by resorting to a combination of natural and forced convection correlations, which allow to obtain a good prediction of the heat transfer coefficient:

$$q_c = h(T_g - T_w) \tag{2.13}$$

$$h = max\left[C_1|T_g - T_w|^{\frac{1}{3}}; \frac{k}{L}Nu\right] \tag{2.14}$$

$$Nu = C_2 + C_3 \cdot Re^n \cdot Pr^m \tag{2.15}$$

where C_1, C_2 and C_3 are suitable coefficients depending on the geometry, Reynolds and Prandtl numbers, T_g is the gas temperature in the first cell, T_w is the wall temperature, k is the gas conductivity and L is a characteristic length [58, 65].

Since the aspect ratio of the cavity allows to neglect the three dimensional effects, a two-dimensional calculation has been performed, assuming a infinitely deep cavity. On the hot wall and the cold wall the temperature has been fixed at the nominal value according to [62], for the upper and lower surfaces, the wall described in [62] was modelled as conductive surface in FDS. The conductive model in the solid, embedded in FDS, is only one dimensional and it is not capable to simulate the fluxes along the solid coating of the box. The properties of the material, summarized in table 2.1 are not explicitly defined in [62] so they were assumed using the common value found in the literature.

TABLE 2.1: Wall's thermal properties

Material	Density [kg/m^3]	Specific heat [kJ/kg/K]	Conductivity [W/m/K]
Steel	7800	0.45	45
Polystyrene	50	1.3	0.033

All the walls of the cavity are supposed to have roughness equal to 0.0 m which is assumed to be a reasonable value due to the finishing of the surfaces. In FDS the numerical simulations are transient so in order to compare the measurements from the experiment which have been taken in steady conditions the result are averaged in time. The LES simulations ran for 500 s in order to obtain a steady condition. The initial conditions are prescribed according to [62], temperature 30 °C, velocity 0.0 m/s and relative pressure 0.0 Pa. The fluid inside the cavity is air, whose properties are defined as a function of the temperature using the default values implemented in FDS.

The next step before comparing the numerical results with the experiment is the choice of the correct mesh size. In this simulation due to the simplicity of the geometry square elements have been chosen using the same number of elements in the x and y direction, different grid's sizes have been compared in order to evaluate the best trade off among the computational cost and the accuracy of the calculation 2.2.

TABLE 2.2: Mesh data

Mesh	El. size [m] (x,y)	N. Elements
Mesh 1	0.01875 × 0.01875	1600
Mesh 2	0.009375 × 0.009375	6400
Mesh 3	0.00625 × 0.00625	14400
Mesh 4	0.00375 × 0.00375	40000

For the sensitivity analysis the net heat fluxes on the cold and hot walls 2.2a and the maximum and minimum velocities 2.2b are compared for different grid resolutions.

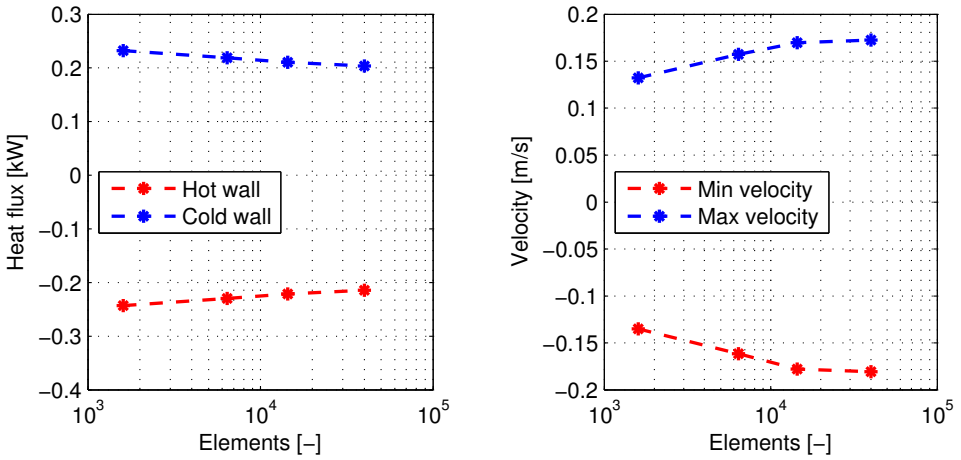

(A) Heat fluxes (B) Velocity

FIGURE 2.2: Mesh independence study

The mesh 3 and 4 have been considered adequate for the simulation of the cavity, while the mesh 1 and 2 are too coarse to correctly reproduce the flow near walls. In this particular scenario, the flow is confined near the walls therefore a good resolution is required in this tiny region. In order to evaluate the capability of FDS to simulate the flow field the velocities along the x and the y directions, u-velocity and w-velocity, have been compared along the middle line of the cavity and are presented in figure 2.3.

Figure 2.3 shows that the velocity pattern is well predicted, in particular the w-velocity near the wall is close the the experimental value considering that in FDS the boundary layer modelled basing on a simplified approach [64], figure 2.3b. The results for the u-velocity are more scattered but this can be acceptable also considering the magnitude of this velocity component, figure 2.3a. FDS has not been designed to solve the boundary layer as discussed before, but with a proper refinement it is possible to obtain good prediction of the velocity peak and of its distribution near the wall. The error of the FDS simulations has been calculated as the maximum difference between numerical and experimental w velocity along the mid-line. Maximum error for mesh 3 is about 21% which corresponds to a difference of 0.0479 m/s, while for mesh 4 the maximum error is about 19 % which corresponds to a difference of 0.0450 m/s. Both maximum errors are located near the cold wall at the velocity minimum position. In the experiment the

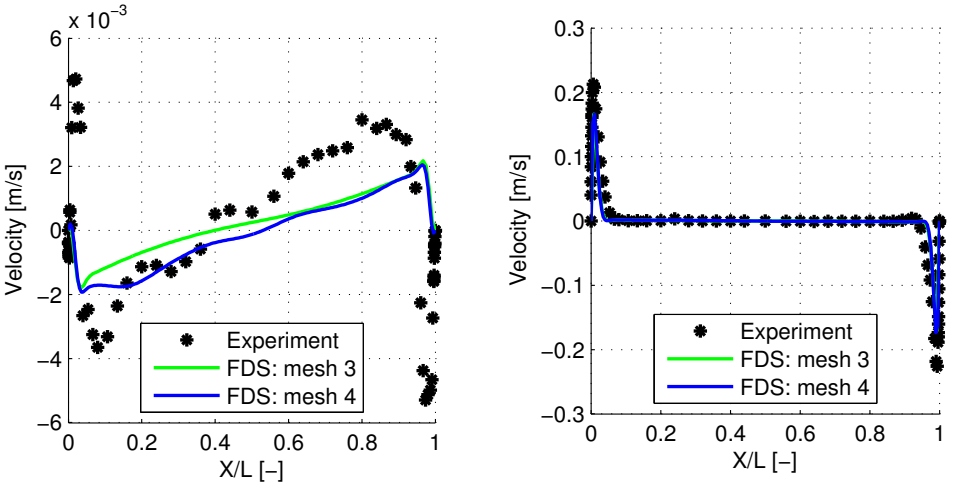

(A) U-velocity (B) W-velocity

FIGURE 2.3: Velocity distribution along the middle line of the cavity

temperature profile has also been measured for steady state conditions and numerical and experimental results are presented in figure 2.4a.

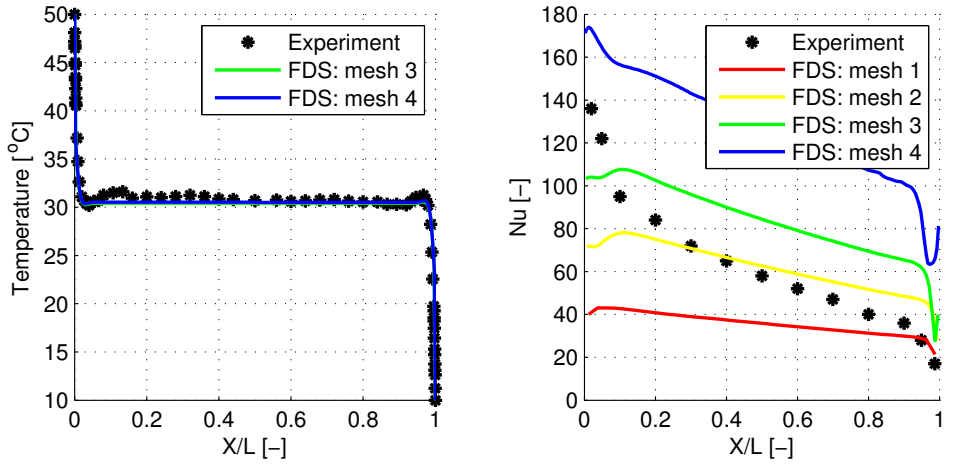

(A) Temperature (B) Nussel number

FIGURE 2.4: Temperature distribution and Nusselt number comparison between experiment and simulation.

The temperatures are correctly estimated along the cavity mid-line by meshes 3 and 4. The agreement between experiment and simulations decays when the temperatures are evaluated inside the thermal boundary layer, as depicted by the Nusselt number, presented in figure 2.4b. In [62] the temperature has been measured inside the conductive boundary layer near the walls, in this region velocity is negligible and the heat transfer occurs due to conduction. The scale of the conductive boundary layer is much smaller than the grid's size used for the spatial discretization in FDS. In the experiment the gradient of the temperature has been measured at 0.00025 m from the surface, while the element size in FDS is 0.00375 m for mesh 4. The other limit in the calculation of the near wall temperature is the near

wall modelling of FDS, which assumes that the whole conductive boundary layer is included in the first cell, therefore the heat transfer coefficient is calculated considering an approximated convective heat transfer coefficient [56].

Temperature and velocity fields in the whole cavity are presented in figure 2.5 in order to show the flow field not only along the mid-line, where the data have been compared with the measurements. The air flowing along the walls of the cavity exchanges heat with them and the temperature changes as function of the position. From the figure 2.5b it is clear that the central region of the cavity is not affected by the motion of the layers near the wall and velocity is close to the initial values. The temperature is stratified in the central region of the cavity where the curves at constant temperature are horizontal, figure 2.5a. In the region near the walls the velocity are higher and the temperature is changing as function of the position, near the vertical walls the flow accelerates and has a peak near the corner. As well the differences between the gas temperature and the wall temperature tend to reduce, while the gas flows along the heated or cooled surfaces. The effect of flow stratification and recirculation has been highlighted also by Ganguli et al in [66] showing that for tall cavities the heat transfer is mainly governed by conduction while for shorter cavities the flow recirculation enhances the convective heat flux.

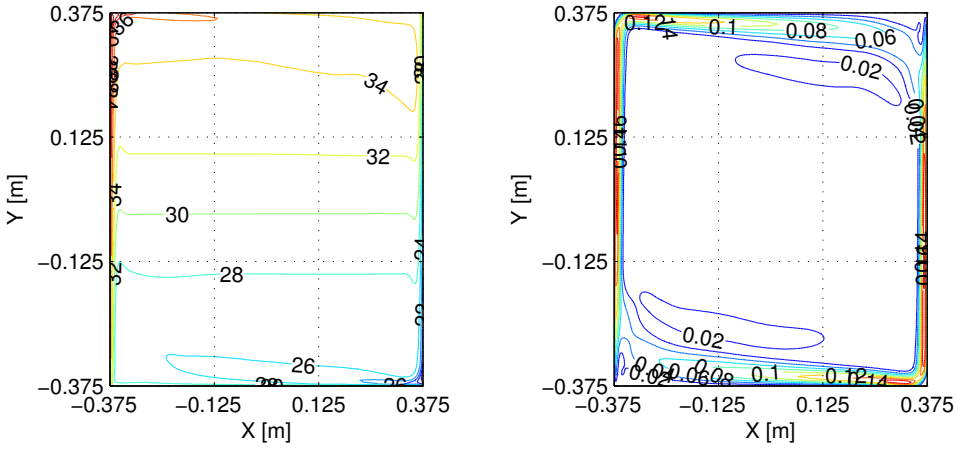

(A) Temperature (B) Velocity

FIGURE 2.5: Flow field in the cavity

The heat losses through the walls are compared in table 2.3 for the mesh 3 and 4 and the experiment. The heat losses are calculated in FDS considering a length of the cavity equal to 1.5 m as described in [62].

TABLE 2.3: Heat fluxes through the walls

Wall heat flux [kW]				
Case	Hot	Cold	Top	Bottom
FDS, Mesh 3	-0.2213	0.2105	0.0131	-0.0025
FDS, Mesh 4	-0.2144	0.2034	0.0124	-0.0017
Experiment	-0.0982	0.0977	0.0225	-0.0217

The heat fluxes show large discrepancies between the experimental and numerical results and the errors are greater that those found in the previous comparisons. Since in [62] there isn't a complete description on how the heat losses through the cavity have been calculated, the difference in the results can be consequence of different reference areas or different assumptions done in the calculation. The experimental and numerical results are reported for sake of completeness.

The simulations of the flow field in a small cavity studied in [62] show a good agreement with the experimental results regarding the velocity and temperature distribution in the main field. The region of the boundary layer shows the greater discrepancies between experimental results and simulations, this is consequence of the numerical grid which is not sufficiently refined to simulate the near wall flow. The other reason of the difference between the results is the near wall modelling in FDS, which is specifically developed for large scale simulations and not well suited for small scale problems. To overcome these problems the cavity should be simulated with a DNS approach, available in FDS, but this would require a huge numerical effort which is out of the scope of this work.

2.3 Natural ventilated fire in a large room

After the initial validation of FDS in a small square cavity, the fire is included in the next validation. In the literature many experiments have been carried out in fire compartments [67–75] providing measurements about the temperature field, the smoke stratification and the species concentration near the fire. In these cases different fuels can be used: solid, like furnitures, pallets, plastic materials, or liquid like pool fires. The second type of fires allows to estimate easily the HRR since the mass flow which evaporates and undergoes to combustion can be measured precisely with a scale, without the need of a cone calorimeter. Compartment fires have also the advantage of a better control on the boundary conditions since they are usually placed in large scale facilities, while for other fire scenarios, such as tunnels, the atmospheric conditions play a key role in the smoke movement. The experiment used for the second validation has been carried out at VTT by Rinne, Hietaniemi and Hostikka [68].

2.3.1 Experiment description

A large room of 500 m^3 has been built at the VTT research centre for experimental test on fire compartment. The room is 10.0 m long 10.0 m wide and 5.0 m high, the side walls are made of steel with a fibreglass insulation, while the ceiling is made of steel without any insulation. The room is naturally ventilated and a window 2.0 m by 2.0 m is open on one side of the compartment. The distance between the lower edge of the window and the floor is equal to 0.5 m. In the experiment different fuels have been tested, polymethyl-methacrylate (PMMA), wood, heptane and toluene, but in this validation for sake of brevity only the heptane fire has been simulated. In the selected fire scenario, 4.9 kg of liquid heptane have been burned in a square pan, 0.1 m^2 area, placed in the centre of the compartment, figure 2.6.

Inside the room several measurements have been taken in order to study the smoke movement and the conditions inside the compartment. The temperatures have been measured at different positions along two thermocouples trees placed near the fire. The concentration of oxygen, carbon dioxide and carbon monoxide have been measured near the open window at 3 m from the floor. The soot density has been measured with the light transmission through smoke. For the calculation of the HRR the mass loss of heptane has been measured and later multiplied by the heat of combustion of the fuel, 44.6 MJ/kg. A schematic view of the room and of the measurement devices is presented in figure 2.6.

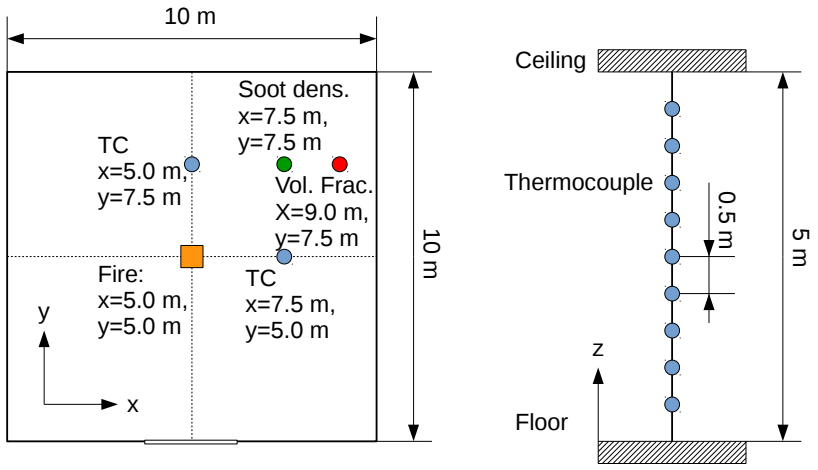

FIGURE 2.6: Schematic view of the compartment

2.3.2 Numerical simulations

The compartment described in [68] is simulated with FDS. Already in [68] some simulations have been carried out with a previous version of FDS, but due to the significant changes to the code new simulations are necessary. The domain is modelled considering the compartment and an additional domain next to the opening in order to don't impose a constant pressure at the window. As argued by Zhang et al in [76] the flow must be free to develop also outside the fire compartment and the domain's extension should be proportional to the HRR and to the opening size. Based on [76, 77] and on the hydraulic diameter of the window, equal to 2.0 m, the domain has been extend in the direction perpendicular to the wall of 2.0 m. The fire has been modelled with the standard combustion model implemented in FDS imposing the fuel mass loss which has been measured in the experiment. The reaction parameters for the heptane combustion are taken from [78], the soot yield is equal to 0.037 and the CO yield is equal to 0.010, the radiation fraction is equal to 0.4, by default in FDS.

The walls of the compartment are modelled as conductive surfaces and their properties are set according to [68]. The vertical walls are made of two layers, 0.002 m thick steel plate and 0.1 m thick fibreglass insulation, the ceiling is made of a 0.002 m thick steel plate and the floor is made of concrete. The data about the walls' materials are summarized in table 2.4.

TABLE 2.4: Wall's thermal properties

Material	Density [kg/m^3]	Specific heat [kJ/kg/K]	Conductivity [W/m/K]
Steel	7850	35	0.52
Concrete	2307	1.4	0.658
Fibreglass	50	0.843	0.04

The fire scenario lasted for 1860 s, until all the fuel was burned, therefore transient simulations have been carried to compare the results in transient regime.

For the grid selection a mesh independence study has been carried out comparing three different grids 2.5. For the selection of the grid's size in fire problems, Stroup proposed a simple method based on the fire size and on the ambient conditions [79].

$$D^* = \left(\frac{\dot{Q}}{\rho_\infty \, c_p \, T_\infty \, \sqrt{g}} \right)^{\frac{2}{5}} \tag{2.16}$$

The characteristic diameter of the fire D^*, equal to 0.437 in this case, is function of the HRR $\dot{Q}$ and of the specific heat, temperature, density of the air in the ambient. The ratio between D^* and the grid size δx should be between 4 and 16, in order to guarantee a proper resolution. However the mesh can not be selected only basing on this ratio and a grid sensitivity should be always performed.

TABLE 2.5: Mesh data

Mesh	El. size [m] (x,y,z)	N. Elements	$D^*/\delta x$
Mesh 1	0.200 × 0.200 × 0.200	75000	2.1850
Mesh 2	0.129 × 0.129 × 0.129	276480	3.3876
Mesh 3	0.100 × 0.100 × 0.100	600000	4.3700

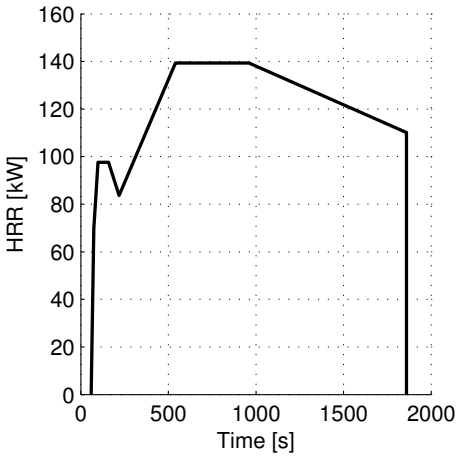

FIGURE 2.7: Heat Release Rate curve

According to [79] only mesh 3 should be used to simulate the fire scenario, but the results obtained with mesh 1 and 2 are also included in the

mesh independence study. In order to assess the proper grids size capable to simulate the fire scenario the temperatures are compared together for different meshes.

Since the HRR curve, figure 2.7, is not steady state the temperatures have been averaged in time only for the last part of the experiment starting from 1000 s, when the curve becomes more flat. The temperature profiles along the height of the room are presented at two different positions 1 and 2, respectively above the fire place, at x = 5.0 m y = 5.0 m, and at 2.5 m from the fire at x=7.5 m y=5.0 m.

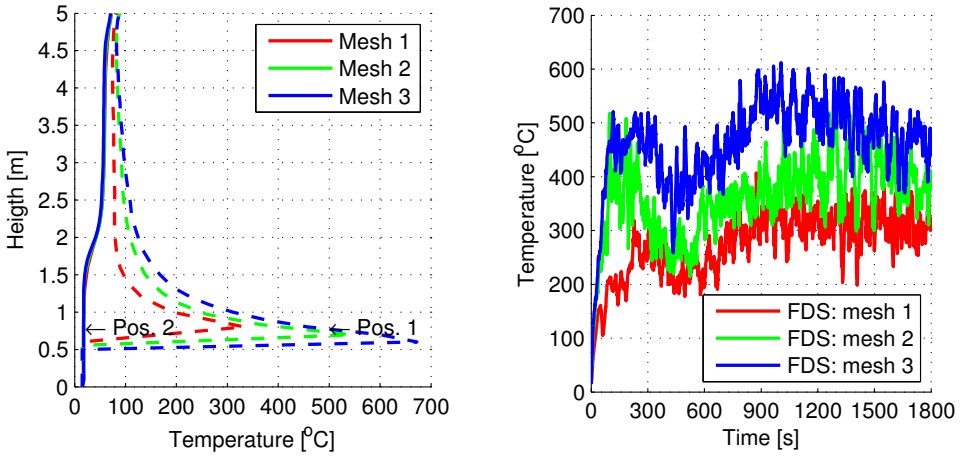

(A) Temperature profiles (B) Temperatures above the fire

FIGURE 2.8: Mesh independence study

The error on the temperature is higher above the fire due to the reaction process which requires refined mesh to be correctly simulated, while out of the fire region a meshes 1 and 2 are overlapping the results obtained with mesh 3. Above the fire the temperature is strongly underestimated by mesh 1, about 350 °C, and the whole temperature profile is lower. The temperatures obtained with mesh 2 are also lower than those obtained with mesh 3, but the error is about 100 °C, and the profiles are closer among them. To better understand the results obtained with different grids, the temperature histories are presented at 0.5 m above the fire in figure 2.8b. As highlighted by Pope and Bailey in [80] the coarser mesh underestimates the gas temperature giving unrealistic temperatures in the flame region. However the main goal of this validation is the estimation of the temperature in the room and not in the flame region therefore meshes 2 and 3 have been considered adequately refined for the simulation of the fire scenario.

Temperatures measured at different positions in [68] have been compared with the numerical results obtained with meshes 2 and 3. The temperatures have been measured at 2.5 m from the fire at different heights, figure 2.6. For sake of brevity these have been compared in figure 2.9 at three different heights instead of comparing all the registered positions.

The temperature profiles obtained with FDS follow the experimental results showing a great accuracy in all the positions presented. The maximum error between the numerical and experimental results is always within 10°C for the considered points. To give a better idea of the temperature distribution along the room's height, temperatures have been averaged for the

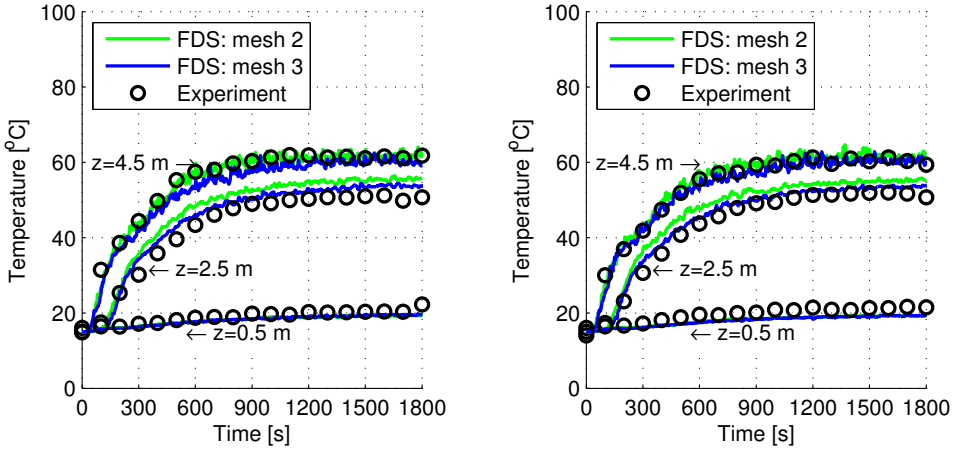

(A) x = 5.0 m y = 7.5 m (B) x = 7.5 m y = 5.0 m

FIGURE 2.9: Temperature profiles at different heights obtained at two different positions near the fire.

last part of fire, from 1000 s to 1800 s. The numerical and experimental results are presented in figure 2.10a showing a really good agreement in the temperature prediction inside the smoke layer; above 2.0 m, while the temperature a slightly underestimated in the lower part of the room. The discrepancies between the results in the lower region can be acceptable since the difference is always below 5 °C. Since the results along the two thermocouples trees are quite similar for sake of simplicity only one thermocouple tree is presented in figure 2.10a, at x = 5.0 m and y = 7.5 m.

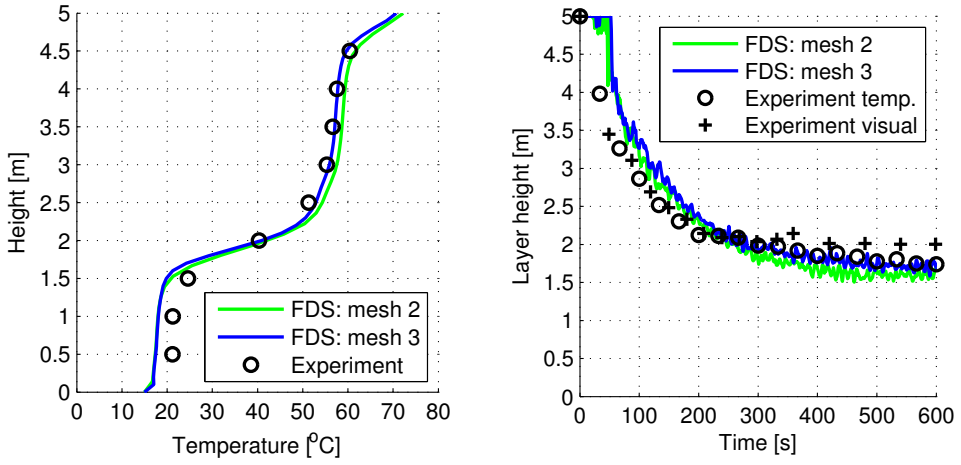

(A) Temperature (B) Smoke layer height

FIGURE 2.10: Temperature profiles and smoke layer height near the fire

The interface between the fresh air and the smoke, smoke layer height, is an important parameter for the safety assessment because it identifies a lower fresh zone without smoke and an upper warm layer. He in [81] proposed a method for the calculation of the smoke layer height which is based on the temperature along the height of the room and which is also implemented in FDS. In the experiment, image analysis has also been used

to calculate the interface between smoke and fresh air [68]. The results obtained with the two methods and the results of the simulations, which are based on the temperature distribution, are represented in figure 2.10b. Also in this case the numerical results are in good agreement with the experiment, as expected the agreement is better with the experimental results calculated with the method proposed by He. However for the visual method the maximum error is within 0.5 m.

After comparing the temperature field near the fire, the species' concentration are compared at one measurement point near the compartment wall, figure 2.6. The volume fraction of oxygen, carbon monoxide and carbon dioxide have been measured at x = 9 m, y = 7.5 m and z = 3.5. The numerical simulations presented in figure 2.11 show a good agreement with the measurements for the whole duration of the experiment. In the upper part of the room the smoke has a lower concentration of oxygen, due to the combustion process, figure 2.11a. The concentrations of combustion's products, CO, CO_2 and soot, are increasing in time, figures 2.11b, 2.11c and 2.11d. The results shows some minor discrepancies between the grids, however these are really small considering the volume fractions of the measured quantities. For O_2 concentration the concentration error is less than 3%, for CO_2 less that 0.001% and for CO less than 10 ppm. The soot density has been measured at x = 7.5 m, y = 7.5 m and z = 3.5, but because of a malfunction of the instrument, the measurements are available only for the last part of the experiment. From this last measurement it is not possible to compare experimental and numerical results, but this can give an idea of the soot density in the room which are at the same level in the experiment and in the simulation. The values of soot yield and CO yield have been taken from the literature, however the reaction's parameters are well suited for this experiment.

In order to give better idea of the flow field inside the room the temperature and velocity distribution are presented along the plane x = 5 m, which cut the open window and the fire place. The results of mesh 3 are time averaged as done for figure 2.10 from 1000 s to 1800 s. Figure 2.12 shows clearly the smoke stratification in the room as well as the flow of smoke escaping from the window and the fresh air entering. The flow field inside the room is weakly influenced by the air coming from the window, the temperature distribution on the two sides of the fire are similar between them. This explains also why in the two thermocouple trees the temperatures are almost overlapping despite their different positions.

2.4 Smoke movement in a medium scale tunnel

After two validations that gradually introduced to the simulations of fire scenarios and buoyancy driven flows the last early validation refers to a tunnel. As seen in the introduction 1 there have been many experimental investigations about fire and smoke confinement in tunnel. At this stage the large scale tunnel experiments have not been considered due to the computational cost and due to uncertainties about the tunnel's boundary conditions. In large scale tunnels the atmospheric conditions play an important role on the smoke movement, increasing the uncertainties of the experiment. On the other hand, many small scale tunnels have been used

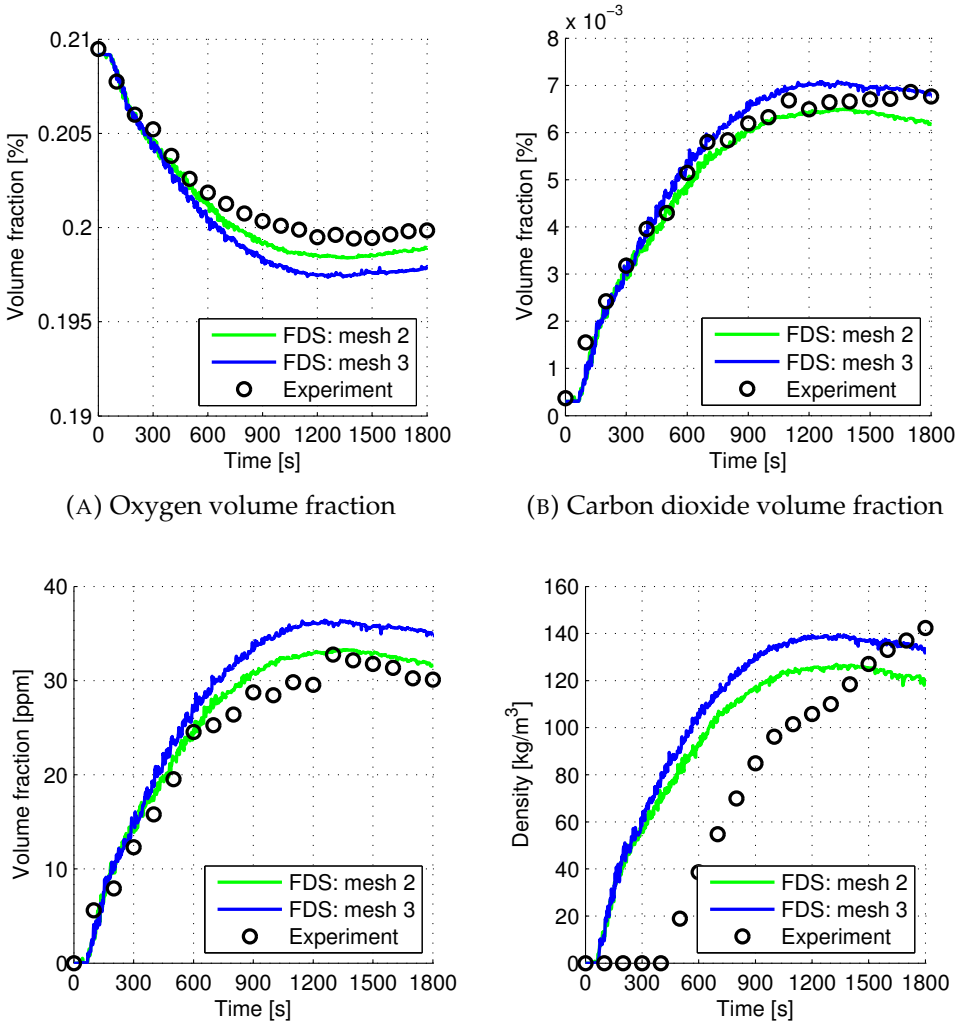

(A) Oxygen volume fraction

(B) Carbon dioxide volume fraction

(C) Carbon monoxide volume fraction

(D) Soot density

FIGURE 2.11: Species' concentration inside the compartment

to investigate the smoke confinement and the backlayering [82–84]. These experimental studies are mainly focused on the smoke confinement and on the study of the black layering therefore the most of the data are regarding temperatures. For a more complete validation it is necessary to compare as many data as possible between experiment and simulation, therefore a midscale tunnel studied by Blanchard has been chosen [85, 86].

2.4.1 Experiment description

In the work of Blanchard a midscale tunnel has been investigated under different ventilation regimes with and without water mist suppression. The tunnel is 43 m long, 1.9 m high and 2.5 m wide, without any slope. The cross section is circular, cut at the bottom in order to have a flat floor, the cross section is 4 m^2 and the hydraulic diameter is 2.16 m. The tunnel's walls are made of concrete 0.250 m thick and covered with a 0.050 m thick layer of mortar concrete, the thermal properties of the wall have been summarized

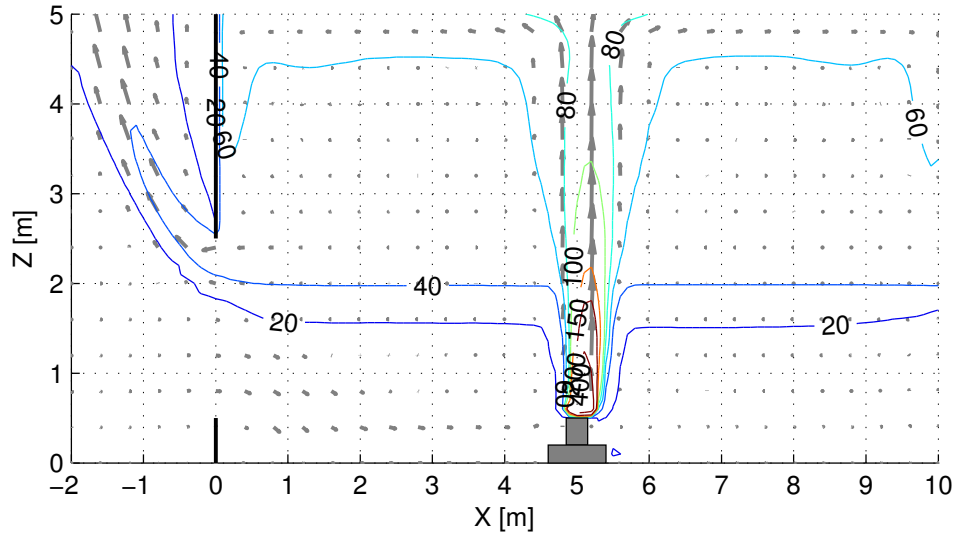

FIGURE 2.12: Velocity and temperature distribution along the middle plane of the room

in [85]. Liquid heptane has been used as fuel since it allows to estimate the HRR measuring the mass loss. A pan filled with the fuel is placed at 17.5 m from the tunnel's inlet and at 0.4 m high, the pan has an area of 0.5 m^2, 1.0 m long and 0.5 m wide. The experiment aims to study both sub-critical and super-critical ventilation conditions, therefore a smoke extraction system has been placed downstream the fire at the end of the tunnel. The fan is supposed to work with a constant volume flow rate and with different extraction flows in order to provide different longitudinal velocities. In the tunnel the last portion of the tunnel is joined to the fan inlet with a cone section in order to reduce the diameter of the tunnel to the size of the fan's inlet. The critical velocity for the tunnel has been calculated by Blanchard basing on different methods and considering a nominal HRR of 1.5 MW. Depending on the approached used for the calculation, the critical velocity ranged from 1.2 to 1.8 m/s, therefore the subcritical and supercritical velocities has been respectively set at 1.0 m/s and 2.2 m/s.

Inside the tunnel different quantities have been measured, temperatures and longitudinal velocities have been evaluated at different heights both upstream and downstream the fire. Heat fluxes have been measured with radiometers placed at different heights at 7 m upstream and 7 m downstream the fire. A schematic view of the tunnel cross section and of the measurement devices' location is shown in figure 2.13

2.4.2 Numerical simulations

Starting from the experiment's description, numerical simulations have been carried out with FDS in order to evaluate its capability to reproduce a fire in tunnel and to correctly simulate the smoke movement. In this new case the rounded geometry of the tunnel is approximated with many small square bricks because the Cartesian grid used by FDS is capable to draw only prismatic elements. As suggested in [76, 77, 86] the domain at the inlet of the tunnel has been extended 5.0 m in order to allow the flow to develop freely before entering into the tunnel. At the inlet region the pressure has been

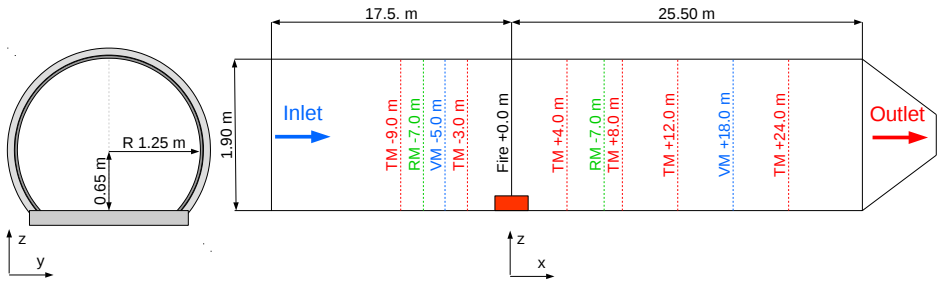

FIGURE 2.13: Schematic view of simulated tunnel with the position of the fire and of measurement devices.

imposed at the atmospheric value 101325 Pa and the temperature equal to 20 °C, at the outlet the velocity of the gas has been imposed in order to simulate the extraction fan, which is working with a constant volume flow rate. Two different regimes have been studied considering both sub-critical and super-critical ventilation. In the experiment the burned fuel was heptane, as in the previous case in section 2.3, therefore the reaction's parameters have been set according to [78], the soot yield is equal to 0.037 and the CO yield is equal to 0.010, the radiation fraction has been left as it is in FDS by default 0.40. The pan is modelled as a fuel source with an imposed mass flow rate, based on the experiential measurements, the HRR has been calculated multiplying this quantity by the heat of combustion of the fuel 44.6 MJ/kg. The tunnel's walls have been modelled as conductive surfaces with a tiny layer of mortar concrete 0.050 m and a thick layer of concrete 0.250 m.

A mesh independence study has been carried out for the subcritical ventilation regime in order to evaluate the correct size of the mesh capable to reproduce the experiment. Two grids have been tested with an element's size of 0.10 m and 0.05 m, the features of the two grids are summarized in table 2.6

TABLE 2.6: Mesh data

Mesh	El. size [m] (x,y,z)	N. Elements	$D^*/\delta x$
Mesh 1	$0.100 \times 0.100 \times 0.100$	300000	15.65 (12.65)
Mesh 2	$0.050 \times 0.050 \times 0.050$	2400000	31.30 (25.30)

The meshes are already quite refined, but small elements are necessary to correctly approximate the shape of the tunnel. In order to compare the numerical results obtained with the two grids the temperatures have been evaluated at different positions, upstream, above and downstream the fire, for the subcritical fire scenario. The temperatures are averaged in time from 180 s to 420 s and presented as function of the height, figure 2.14a. As expected the most critical section is the one above the fire, x = 0.0 m, while upstream and downstream the fire the difference between temperatures is always below 20 °C. The maximum error in the temperature distribution is close to the pool fire at z = 0.6 m, where the temperature obtained with the coarse grid is about 200 °C below the temperature obtained with mesh 2. The temperatures above the fire, over 1.0 m high, are again in good agreement between the two meshes. The temperatures above the fire, at 0.6 m

height, are compared for the two grids in figure 2.14b. The temperatures show strong fluctuations due to the high turbulence of the reaction region and this can explain the discrepancies found in figure 2.14a between the two meshes.

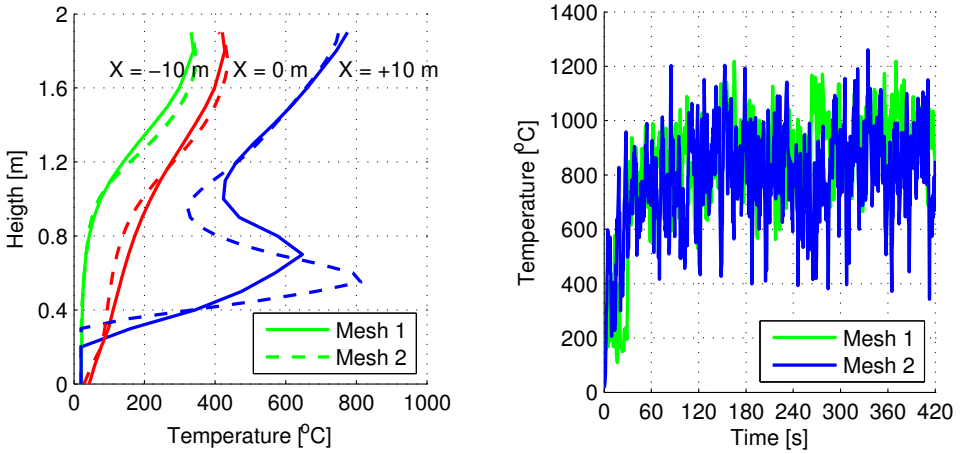

(A) Temperatures along the tunnels heigh

(B) Temperatures at x = 0 m, y = 0 m, z = 0.9 m

FIGURE 2.14: Mesh independence study for subcritical ventilation conditions

The largest differences in the results are confined to the fire region, while in the rest of the field different grids produce similar results. As seen in figure 2.14a, the different temperatures along the tunnel's height are not affecting the agreement between the grids in the rest of the tunnel. Therefore mesh 1 is chosen to simulate the fire scenario under the two ventilation condition.

After evaluating the proper grid size to use for the simulations, numerical and experimental results are compared together, both under subcritical and supercritical ventilation conditions. In [85] the subcritical ventilation has been obtained with a longitudinal velocity at the tunnel's outlet equal to 1 m/s, which allowed partial backlayering, while for supercritical ventilation the exhaust velocity is equal to 2.2 m/s.

The HRR for the two fires has been imposed according to the experimental, the HRR curves used for the simulations have been plotted in figure 2.15 for different ventilation regimes.

The HRR measured during the experiment is slightly higher that the nominal value, 1.5 MW, that has been used to calculate the critical velocity. As found by Carvel in [87], the longitudinal ventilation affects the HRR depending on the type of fire and on its size. In case of small or medium pool fires rising the longitudinal velocity the HRR decreases. In case of large pool fires the HRR increases rising the longitudinal velocity. For large pool the HRR is controlled by the availability of oxygen, ventilation controlled fire, therefore an increase of the ventilation supplies more oxygen to the fire rising the HRR. On the other hand small fires are fuel controlled thus there is no need of more oxygen and the higher velocity may enhance the cooling effect of the ventilation.

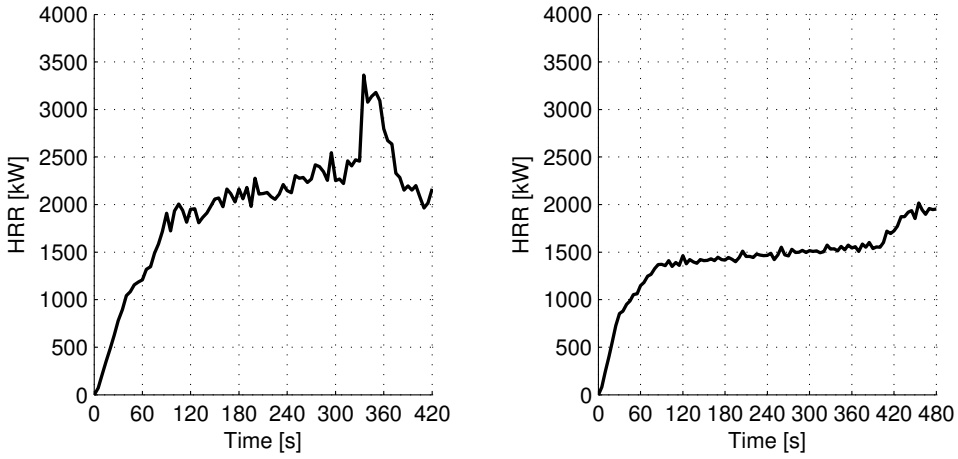

(A) Subcritical ventilation (B) Supercritical ventilation

FIGURE 2.15: Heat Release Rate curves

Subcritical ventilation regime

The results obtained with FDS for subcritical ventilation regime have been compared with the measurement obtained by Blanchard. In this first case the smoke flows back, up to the inlet of the tunnel with backlayering. To monitor the backlayering and the smoke flow, the temperatures and the velocities in the tunnel have been measured at different locations upstream and downstream the fire, figure 2.13. The temperature profiles during the simulation are first presented in figure 2.16.

Gas temperatures are slightly overpredicted by FDS, but the numerical values follow the trend of the experimental measurements. The temperature in the upstream region, figure 2.16a, and downstream, figure 2.16c, are overestimated by the code, and this can be consequence of the poor modelling of the mixing between the hot smoke layer and the incoming air [85]. In the upstream region, at x equal to -9.0 m, the maximum error in the temperature is about 80 °C in the upper part of the tunnel. While downstream, at x equal to +8.0 m, the maximum error can exceed 200 °C. Near the outlet of the tunnel the difference between measurements and simulations can be consequence of the boundary condition placed at the tunnel's outlet, figure 2.16d. In the experiment a cone connected the tunnel with the exhaust fan, but its geometry wasn't available. Therefore a uniform velocity has been imposed as condition at the tunnel's outlet and this could influence the velocity field. The temperatures along the tunnel have also been compared with the experimental results at different heights and times in figure 2.17, in order to evaluate the temperature evolution inside the tunnel. The results are in good agreement with the experimental measurement and they are also close to the numerical results presented in [85, 86]. The errors in the temperature are always below 100 °C, except for one point at x equal to 8.0 m where the temperature overestimation is about 150 °C. The temperatures in the fire region have not been measured during the experiment, but values about 1000 °C above the fire have been obtained also by Blanchard with numerical simulations.

The temperatures measured and simulated show in figure 2.16 an initial growth and later a quasi steady phase, so it is possible to consider a time

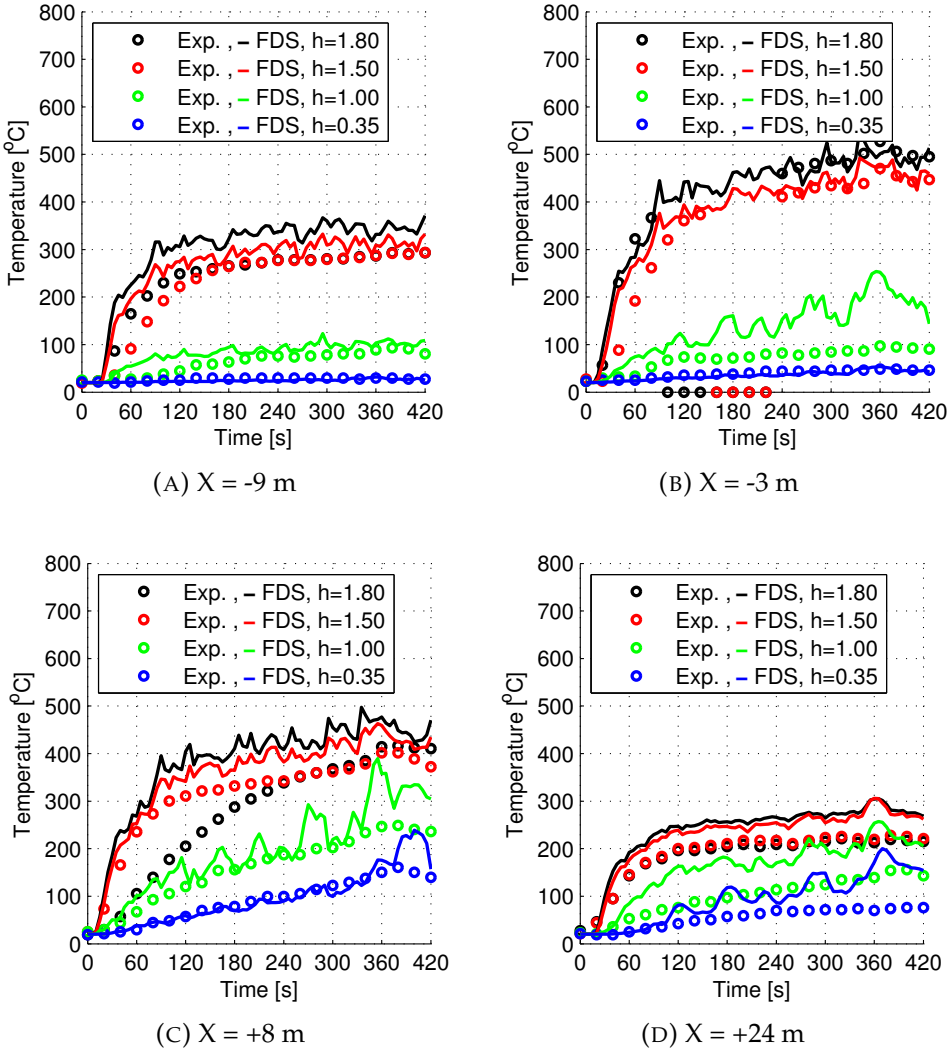

(A) X = -9 m

(B) X = -3 m

(C) X = +8 m

(D) X = +24 m

FIGURE 2.16: Temperature history for subcritical ventilation at different locations along the tunnel

averaged temperature in the tunnel in order to visualize the flow field, figure 2.18. The temperatures have been averaged in time from 240 s to 420 s, the end of the simulations. The contour shows clearly the backlayering of the smoke, this is not controlled by the ventilation and it is capable to flow upstream at the tunnel's inlet. Near the tunnel's outlet the boundary condition affects the temperature distribution, as already seen in figure 2.16d. The boundary condition is too close to the measured points and the simulation is not capable to correctly reproduce this tunnel's region. However the influence is confined to the final part of the tunnel about 3 m from the outlet, so the other results are not affected by this modelling approximation.

After the comparison of the temperatures, the velocities have been compared for the two measurement's locations, figure 2.13. Upstream the fire the velocity of the backflowing gas is well predicted, figure 2.19a, and the velocity in the lower zone of the tunnel is correctly estimated. Poorer agreement is found at 1.10 m and this can be consequence of a different stratification of the gas in the upstream region. FDS overpredicts the velocity

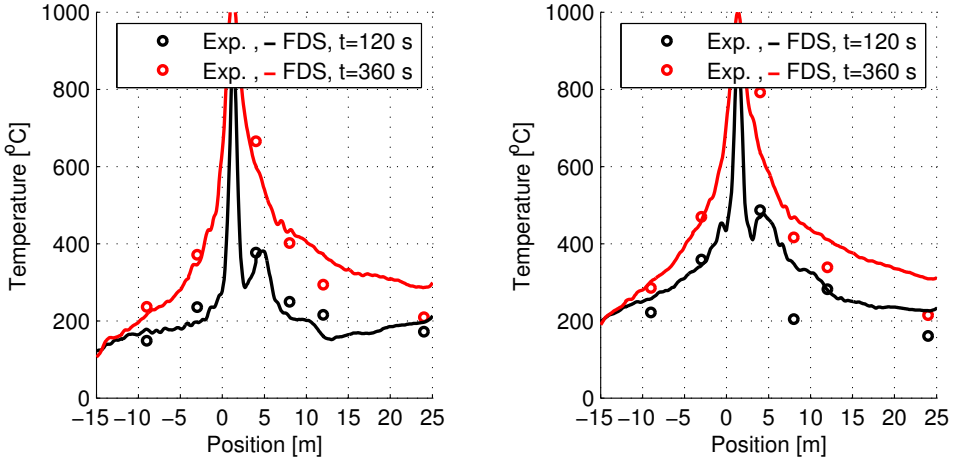

(A) h = 1.30 m (B) h = 1.50 m

FIGURE 2.17: Temperature profiles along the tunnel at different times and heights

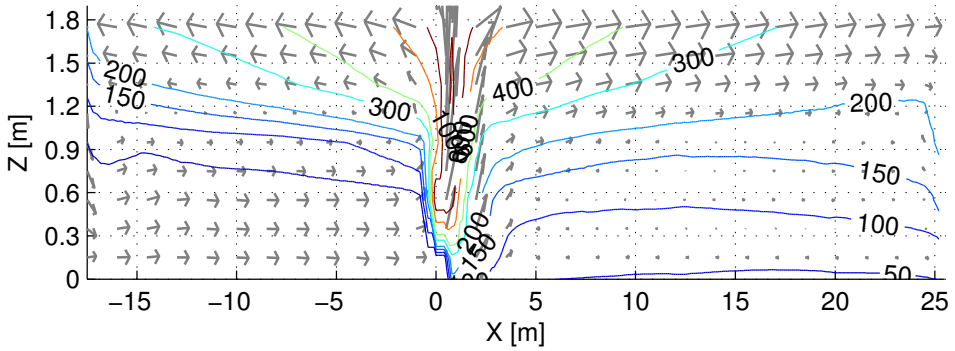

FIGURE 2.18: Velocity and temperature distribution along the middle plane of the tunnel

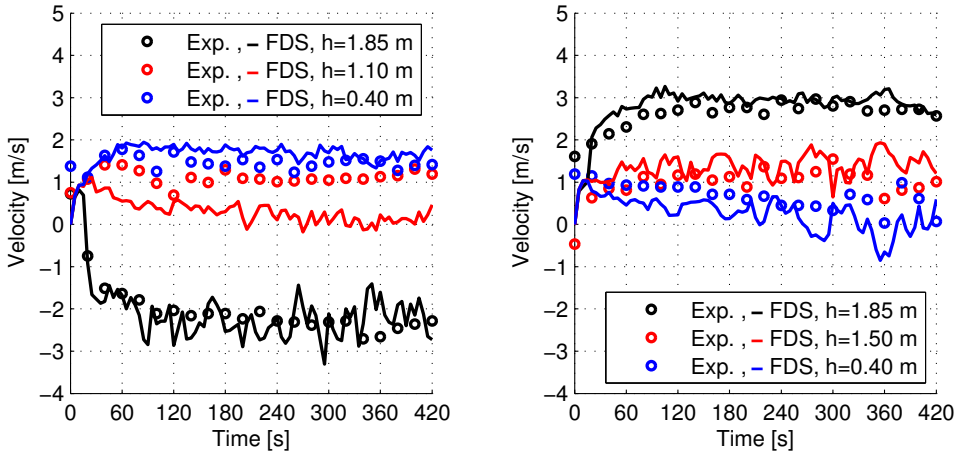

(A) X = -5 m (B) X = +18 m

FIGURE 2.19: Velocity profiles upstream and downstream the fire for subcrtical ventilation conditions.

with a maximum error about 1.0 m/s. In the downstream region, figure

2.19b, the velocities are well predicted by FDS along the height of the tunnel, with a maximum error always below 1.0 m/s. Downstream the fire the velocity gradient is correctly estimated, with higher velocity in the upper layer, where hot gasses are flowing, and lower velocities near the floor. In the downstream region the boundary conditions are far enough to not influence the velocity distribution along the tunnel's heigh. The last comparison, for subcritical ventilation conditions, has been done for the radiative heat fluxes, measured upstream and downstream the fire at 7.0 m 2.20. The radiative heat fluxes have been measured at different heights using a radiometer, while in FDS the radiative heat flux to a point has been calculated.

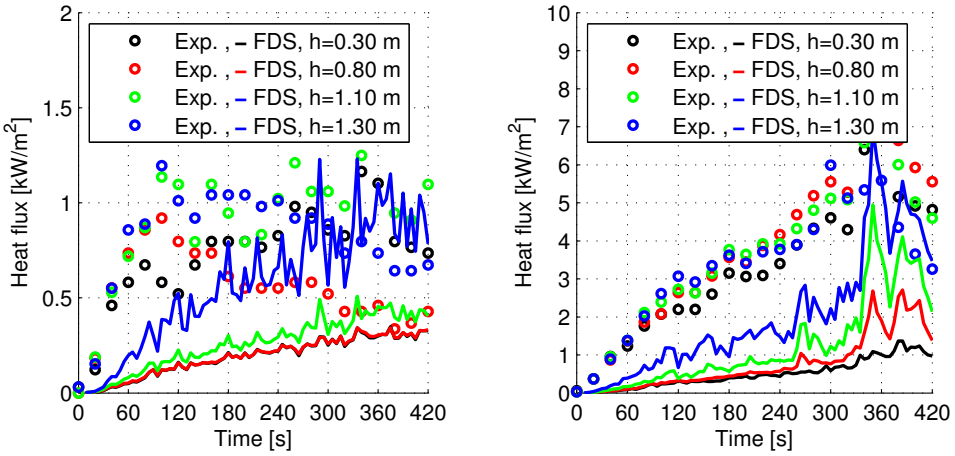

(A) X = -7 m (B) X = +7 m

FIGURE 2.20: Radiative heat fluxes upstream and downstream the fire for subcrtical ventilation conditions.

The results predicted by FDS are always underestimated compared to the experimental results, both upstream and downstream the fire. The poor agreement between the experiment and the simulation could be due to the poor quality of the measurement or due to an non proper modelling of the radiometer done with FDS. For both positions the heat fluxes are underestimated, but they show a trend similar to the experiment.

The comparison with several quantities measured in the experiment shows that FDS is capable to predict the backflow of smoke and the flow field in a tunnel in case of subcritical ventilation conditions. Some discrepancies have been found in the temperature's distribution, but there is a satisfactory agreement both with the experimental values and the numerical results proposed by Blanchard.

Supercritical ventilation regime

For supercritical conditions the velocity of at the outlet rose up to 2.2 m/s in order to prevent the backlayering, in this case only temperatures and velocities have been reported in [86]. The temperatures have been measured upstream and downstream the fire with three measurement section downstream, at 8, 12 and 24 m from the fire, and only one upstream the fire, at 3 m from the fire. The numerical and experimental results are presented in figure 2.21.

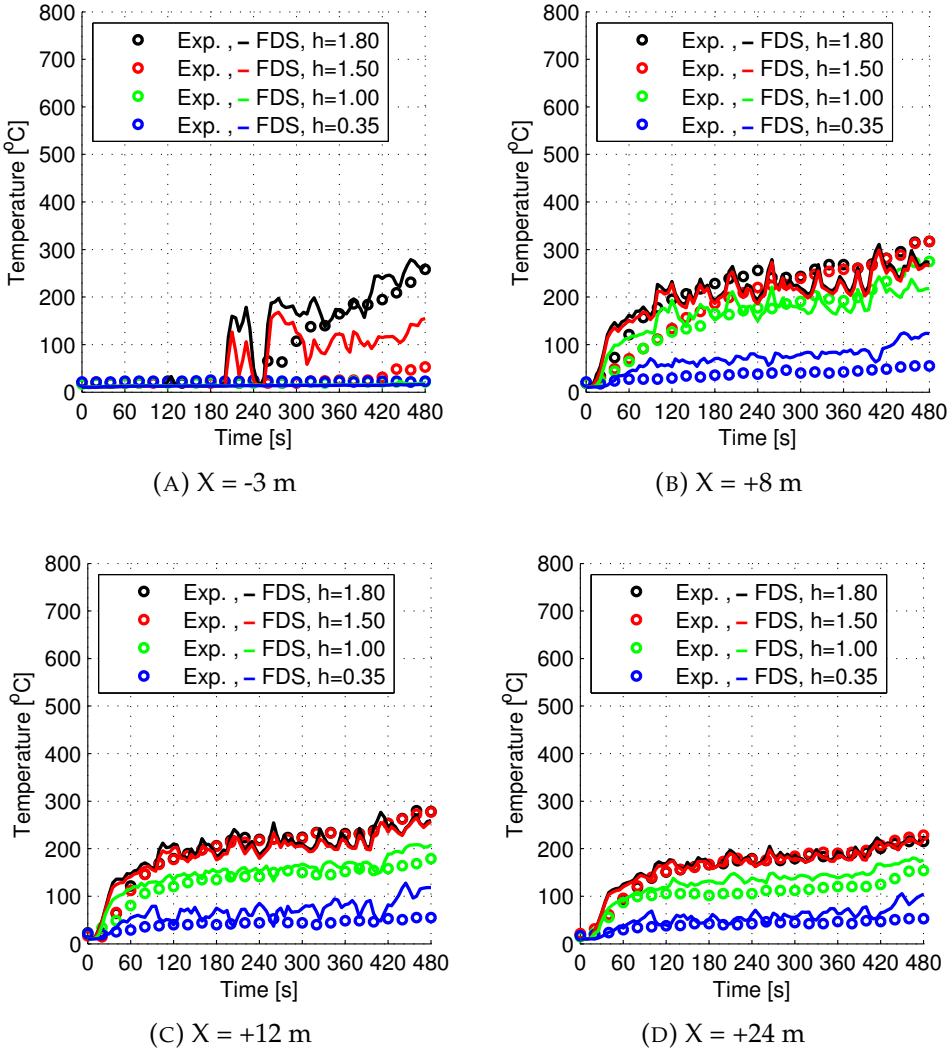

(A) X = -3 m

(B) X = +8 m

(C) X = +12 m

(D) X = +24 m

FIGURE 2.21: Temperatures for supercritical ventilation conditions at different locations along the tunnel

Figure 2.21a shows some smoke flowing upstream the fire, this backlayering is confined to the last part of the experiment and it is correctly predicted by FDS. The thickness of the smoke layer is overpredicted by FDS since the temperature at 1.5 m high is greater than the ambient value, while in the experiment there is not temperature rise at this height. The temperatures downstream the fire are all in good agreement with the experimental results and show a better agreement if compared with the subcritical ventilation case. The maximum errors between FDS and measurements are below 100 °C for the different locations. The backlayering was not expected in the experiment since this was designed to have longitudinal velocity greater than the critical one. The critical velocity has been calculated basing on different formulas for an HRR of 1.5 m while in the experiment the maximum HRR was about 2.0 MW. So the HRR based on [88] was underestimate if compared to the experimental results. Some smoke backlayering occurs already at 240 s, figure 2.21a, before the final HRR rise,

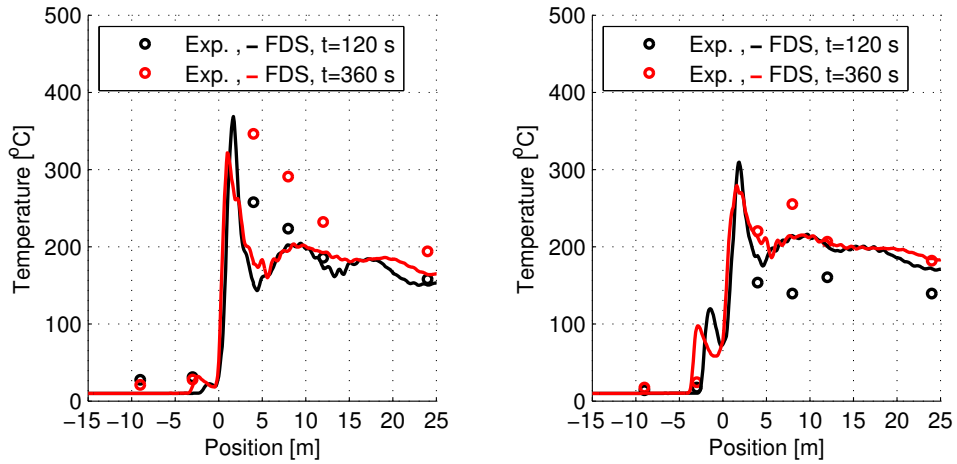

(A) h = 1.30 m (B) h = 1.50 m

FIGURE 2.22: Temperature profiles along the tunnel at different times and heights

occurring after 420 s. So considering an HRR of 1.5 MW, Q^*=0.198, the critical velocity calculated basing on [23] is about 1.9 m/s, but this velocity refers to the air velocity at the inlet of the tunnel as done in the experiment of Li. In this case the velocity was imposed at the outlet where the gas are warmer and less dense. For the last part of the simulation when there is smoke backlayering the velocity at the inlet section of the tunnel is about 1.8 m/s and the velocity at the tunnel's outlet 2.2 m/s. Even if at the tunnel's outlet the velocity is greater that the critical value, at the inlet the velocity is below the critical value and this allows the smoke to flow towards the inlet portal. In the downstream region the temperatures calculated with FDS are overlapping the experimental values and the boundary condition doesn't affect the temperature profiles near the tunnel's outlet, figure 2.21d.

The temperatures are compared along the tunnel at two different heights and different times steps, figure 2.22. The numerical results follow the experimental measurements apart for the region downstream the fire at 1.3 high. The temperature obtained with FDS in this case is below the experimental value with a maximum error about 200 °C. This error can be consequence of different smoke stratification downstream the fire considering the good agreement found between measurements and simulations in figure 2.21.

The temperatures in the tunnel, as done for the subcritical ventilation condition, are presented in figure 2.23, showing a limited region upstream the fire with backlayering and the downstream region filled with smoke. For this ventilation regime there is not a proper steady state phase as found before, but the temperature have been averaged in the last phase of the fire when the backlayering occurs, after 240 s. The temperatures are generally lower compared to those found in figure 2.18, this is consequence of the lower HRR and the higher cooling effect of the ventilation. The higher longitudinal velocity provides also a more uniform temperature distribution along the height of the tunnel in the downstream region. The temperatures

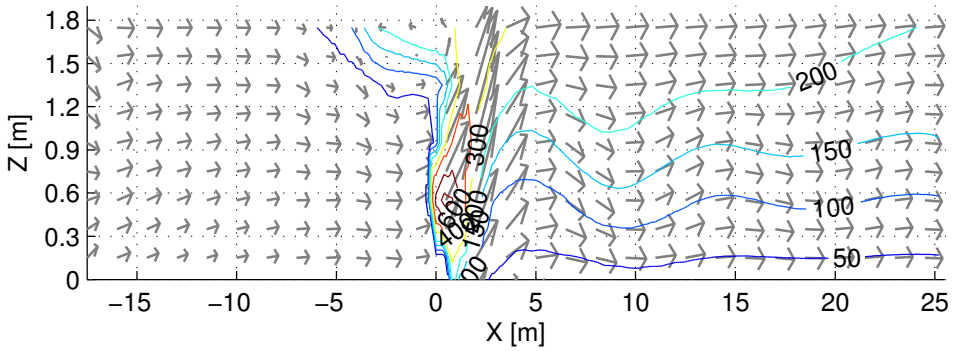

FIGURE 2.23: Velocity and temperature distribution along the middle plane of the tunnel

are quite regular also close to the outlet of the tunnel, so the boundary condition doesn't affect the temperature field as occurred with subcritical ventilation. This could be seen in figure 2.21d where the experimental values are in good agreement with the FDS simulations.

The comparison of the temperatures simulated with FDS and measured by Blanchard shows that FDS is capable to simulate the transient flow of smoke travelling upstream the fire. To complete the validation the velocities are compared with the experimental measurements, figure 2.24. The velocities have been measured at two sections in the tunnel, 5 m upstream the fire and 18 m downstream the fire.

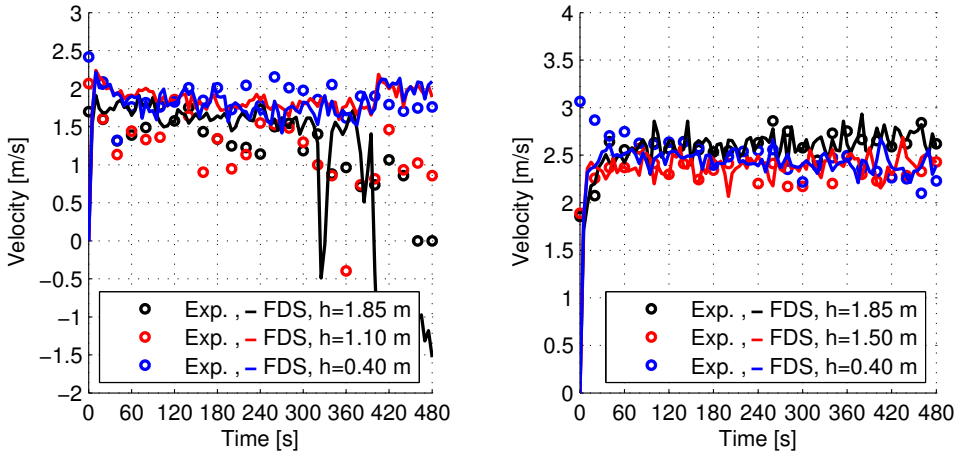

(A) X = -5 m (B) X = +18 m

FIGURE 2.24: Velocity profiles upstream and downstream the fire for supercritical ventilation conditions.

In the downstream region the results obtained with FDS are overlapping the experimental measurements, while in the upstream region the agreement is still good but FDS overpredicted the backlayering length. As seen in figure 2.23 the smoke flows back to -7.5 m in the FDS simulation, while in the experiment this distance should be smaller since the velocity at 5 m are still all positive.

Also for supercritical ventilation conditions FDS is capable to simulate the smoke confinement with a good estimation of temperature and velocity profiles. Some discrepancies occur in the prediction of the backlayering

length but the numerical simulation is capable to detect the correct time at which the backlayering starts.

2.5 Numerical investigation of Froude Scaling in tunnel geometries

In fire safety engineering, mainly in tunnel applications, the cost and the risk of real fires are not sustainable for a large experimental campaign, this is why most of the available data comes from model experiments, unless for some exceptions [7–9, 14, 15]. The model experiments are performed in order to scale a big event and to study it in a smaller size. When resizing a fire scenario some meaningful non-dimensional parameters must be preserved among the scales. The scaling approach is not unique and at least three different techniques have been proposed in the literature [19]: namely, Froude scaling, pressure scaling and analogue scaling.

Among them, the most popular is Froude scaling, since the manufacturing of the testing facility is easier when compared to the other approaches. Most available results about critical velocity and backlayering length [11, 21, 23, 89–92], have been obtained in experimental test rigs designed with the Froude scaling.

Until now the reliability of this scaling technique has not been completely assessed and only few studies have been done in this direction: [93] Quintiere compared the measurements coming from experiments in different scales, while Tilley [24] compared the results in different scales obtained using Computational Fluid Dynamics (CFD), but both cases didn't refer to fire scenario in tunnels. Without aiming at verifying the scaling process, Li [23] compared the critical velocities measured in different tunnels, both in small scale and big scale, finding a common trend in the results but also some scattering among them.

In order to fulfil this lack numerical simulations are performed in different scales. The results are later compared assessing the reliability of the Froude scaling. In order to provide more reliable results, the numerical simulations are based on the experimental tests carried out by Blanchard [85, 86]. This midscale scale tunnel is rescaled and simulated in the real size in order to compare results in the bigger scale with the predictions obtained from the small scale test.

2.5.1 Scaling theory

The scaling theory is commonly used to design a small scale experiment starting from a real scale one, as well as to transfer results from small scale test to bigger scale. An introduction to the scaling theory has been already proposed in section 1.2.1 for the scaling of critical velocity, in this section all the equations of the Froude theory are discussed in order to show how a tunnel can be designed in a new scale and results transferred. In this study the Froude scaling is chosen to resize fire scenarios in tunnels, since most of the model experiments are designed with this approach. With the Froude scaling the Reynold numbers are different in the two scales, however this approximation has small influence on the results [24].

In the scaling procedure shape of the tunnel remains the same in the two scales and all the lengths of the tunnels are in a constant ratio among them. The generic length of the rescaled tunnel L_2 can be obtained from the original one L_1 as:

$$\frac{L_1}{L_2} = \gamma \tag{2.17}$$

where γ is the scaling factor, which is later used to relate different quantities in different scales. In the Froude scaling the ambient pressure is not rescaled and is fixed to a constant value in all the scales. The fire load is resized changing the HRR, as:

$$\frac{HRR_1}{HRR_2} = \gamma^{5/2} \tag{2.18}$$

In case the ventilation conditions are imposed at the tunnel's portals, the velocities are changed in order to preserve the Froude number as:

$$\frac{u_1}{u_2} = \gamma^{1/2} \tag{2.19}$$

For transient problems, the characteristic timing of the simulation is also changed in order to fulfil equations 2.17,2.19:

$$\frac{t_1}{t_2} = \gamma^{1/2} \tag{2.20}$$

The heat losses through the walls need to be rescaled correctly among the scales.

$$\frac{\dot{q}''_{w,1}}{\dot{q}''_{w,2}} = \gamma^{1/2} \tag{2.21}$$

The walls' thermal properties therefore need to be changed in order to fulfil equation 2.21. This is done, as proposed by Ingason in [12], modifying the thermal inertia (χ) and the thermal thickness of the wall (ξ) defined as:

$$\chi = k\rho c_p \tag{2.22}$$

$$\xi = \frac{k}{\delta} \tag{2.23}$$

where k is the thermal conductivity, ρ is the density, c_p is the specific heat and δ is the thickness of the wall. Since in real tunnels the walls are many kilometres thick, while in model experiment these are just few centimetres thick, it is important to assess if there is heat transfer on the back side of the wall. If the thermal wave doesn't cross the tunnel's wall the thickness can be assumed to be infinite also in the small scale. The wall's thermal properties are rescaled according to:

$$\frac{\chi_1}{\chi_2} = \gamma^{3/2} \tag{2.24}$$

$$\frac{\xi_1}{\xi_2} = \gamma^{1/2} \tag{2.25}$$

Once the small scale test is designed starting from the previous equations,

the results from the small fire test can be exported to the original size. The Froude scaling allows to rescale the results of the small scale test and to make some prediction about the fire scenario in the real scale. The Froude scaling considers the gas to have an ideal behaviour, thus the temperature fields in different scales are the same after rescaling the position of the measurement. The temperature can be exported in a different scale both in the gas and on the walls of the tunnel.

$$\frac{T_1}{T_2} = \gamma^0 \tag{2.26}$$

The gas velocity inside the fluid domain can be transferred from the one scale to the other based on equation 2.19, including the estimation of the critical velocity. The smoke backlayering distance can be exported as well from the small scale to the big one using 2.17. The heat fluxes through the walls change among the scales in order to rescale correctly the heat losses, so they can be transferred from one scale to the other according to equation 2.21.

To assess the reliability of the Froude scaling it is necessary to compare similar fire scenarios, in similar tunnels. These should have similar geometry and materials, which satisfy 2.17, 2.24 and 2.25, similar ventilation conditions and fire load, scaled according to equations 2.18 and 2.19. In the literature many small scale experiment have been carried out, while just few large scales scenarios have been performed. Among these tests it is difficult to find similar cases because of the differences in the measured quantities and in the operating conditions, fire load, ventilation regime, tunnel's geometry. The differences between the experiments could combine with the differences induced by the Froude scaling preventing from assessing the reliability of the scaling technique. To overcome the previous difficulties numerical methods can be used instead of experiments [24], allowing to compare two fire scenarios which fulfil all the previous equations. The reliability of the numerical simulations can be assessed comparing the numerical results with the experimental measurements in the small scale, where several experiments are available. The validated tunnel can be later rescaled and the numerical simulations can be compared among each other in order to find the differences in the two scales. The small scale tunnel studied in [85, 86] is chosen for the validation and later for the rescaling because temperatures and velocities have been measured both in subcritical and supercritical ventilation regimes. The reliability of the FDS simulations in the small scale tunnel has been already assessed in section 2.4, showing a good agreement between numerical and experimental results.

In order to assess the reliability of the Froude scaling it is necessary compare two similar fire scenarios. The experimental work performed by Blanchard consists only of a midscale tunnel therefore a numerical simulation can be used to evaluate the fire scenario in the big scale. The numerical simulation allows to design a tunnel which fulfils all the equations proposed in the previous section and to compare the results in the two scales. As proposed in [86] the scaling factor is equal to 3 and this value allows to calculate all the features of the new tunnel. The shape is similar to the original tunnel, so the length is 129 m and the hydraulic diameter of 6.48 m. The materials of the walls are modified because their thermal inertia and the

thermal thickness are changed according to equations 2.24 and 2.25. Since in the small scale tunnel the thermal wave doesn't cross the insulating layer of mortar concrete, it is possible to consider only the first layer of material as semi-infinite, with a thermal thickness equal to zero in both scales. The HRR in the big scale is calculated based on the fire curve in the small scale, figure 2.15a. The intensity of the fire is increased according to equation 2.18, and the duration of the fire is changed because for transient problems the timing is rescaled according to equation 2.20. The ventilation conditions in the big scale tunnel are similar to the small scale one and the exhaust velocity is calculated using equation 2.19. For the large scale tunnel a preliminary mesh independence study has been performed to evaluate the adequate mesh size, comparing grids with elements of 0.30 and 0.15 m size. Due to the agreement between the results the coarser grid is chosen. The boundary conditions in the two different scales are summarized in table 2.7.

TABLE 2.7: Comparison of the different boundary conditions in the two scales

	Small scale	Big scale
Velocity exhaust [m/s]	1.0 (Subcritical), 2.2 (Supercritical)	1.73 (Subcritical), 3.81 (Supercritical)
Tunnel length [m]	43	129
Time [s]	420 (Subcritical), , 480 (Supercritical),	727(Subcritical), 832 (Supercritical)
Thermal inertia [kW^2 s / m^4 / K^2]	301.9	1569
Thermal thickness [W/ m^2 / K]	5.44 (0.0)	0.0

2.5.2 Results comparison in different scales

In this section the results in different scales under different ventilation conditions are compared using velocities and temperatures. The results are presented directly in the big scale tunnel, so values measured in the small scale tunnel are first rescaled to the bigger scale using respectively equations 2.19 and 2.26. Since not all the quantities presented hereafter have been measured in [86] and because of some differences between simulation and experiment only the numerical results are presented.

Subcritical ventilation regime

Tunnels in the two scales are first compared for subcritical ventilation condition, with exhaust velocity equal to 1 m/s in the small scale and 1.73 m/s in big scale tunnel. The HRR is imposed as boundary condition based on the experimental curve presented in figure 2.15a. The gas temperatures are first presented along the tunnel, figure 2.25, for sake of brevity these are averaged in time for the second part of the experiment when the fire reaches a steady condition, figure 2.16. The averaging interval is from 240 s to 420 s in the small scale and accordingly from 416 s to 727 s in the big scale. The temperatures are presented beneath the ceiling, T_{Ceil}, and averaged along the tunnel's height , T_{Ave}, to show the overall trend along the tunnel, figure 2.25a.

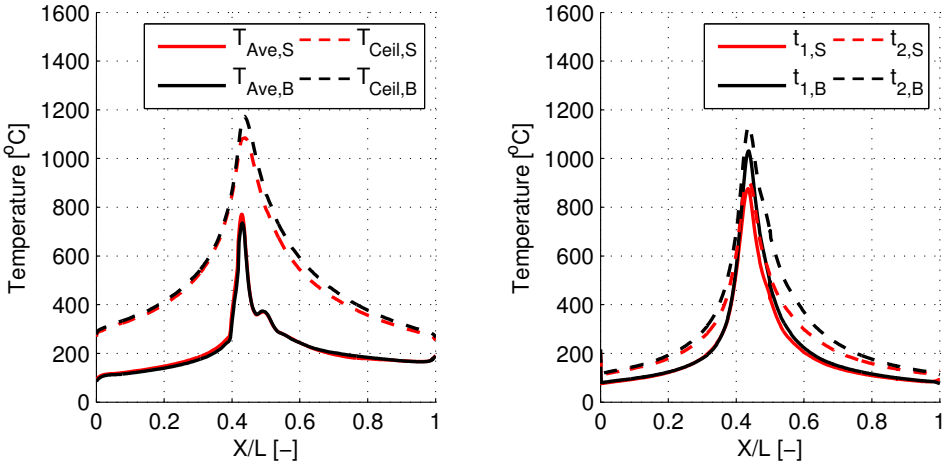

(A) Gas temperature (B) Wall's temperature

FIGURE 2.25: Comparison of the temperature in the tunnels in the two scales.

The mean temperatures along the tunnel show close trends in the two scales, while the gas temperatures beneath the ceiling show some differences. Near the fire the differences between the two scales are higher, but the effect is confined to the region near wall and the results in the remaining part of the tunnel are in good agreement. One of the most critical part of the Froude scaling is the correct scaling of the walls' thermal properties which cannot be done without introducing some approximations, as stated by Ingason in [12]. To evaluate these approximations the surface temperatures in the two scales are compared along the middle line of the tunnel at two different time steps, at the half and at the end of the fire, figure 2.25b. For the small scale tunnel the wall temperatures are evaluated at 210 s, $t_{1,S}$, and 420 s, $t_{2,S}$, while in the big scale the temperatures are evaluated at the corresponding time 364 s, $t_{1,B}$, and 727 s, $t_{2,B}$. The temperatures after the first half of the fire are in good agreement among them, while at the end of the fire these show some discrepancies near the fire region, with a maximum difference equal to 100 °C. As seen in figure 2.25b the effect of these discrepancies remains confined near the wall region.

The longitudinal velocities are presented along the tunnel's height upstream and downstream the fire, figure 2.26a. The velocity is averaged in time for the last part of the experiment as done for the temperature and compared for the position previously used for the validation, in the small scale 5 m upstream and 15 m downstream the fire. The position of the measurement is moved accordingly to the scale factor in the big scale, as well the velocity is rescaled from the small scale to the big one using to equation 2.19. The results show a good agreement between the two scales where there is a clear backlayering in the upstream part of the tunnel. The maximum difference between the results in the two scales along the two profiles is below 0.5 m/s. The thickness and the velocity of the smoke flowing against the ventilation direction are similar in the two scales.

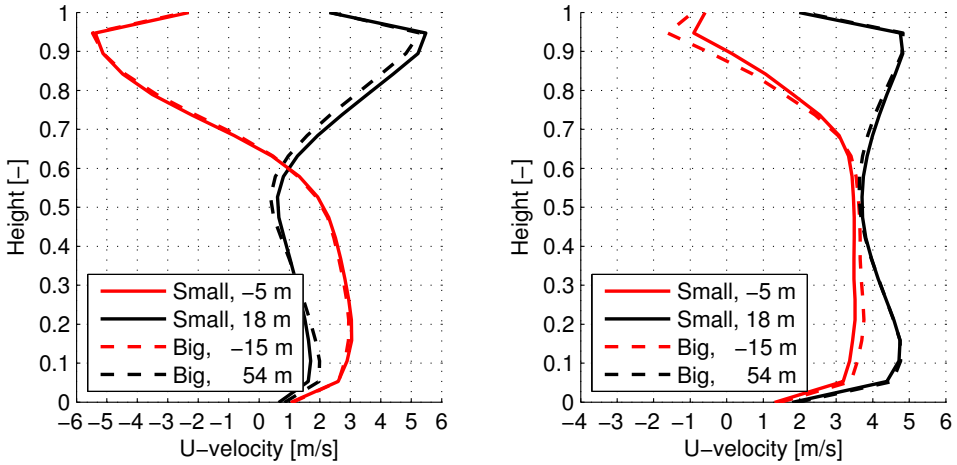

(A) Subcritical (B) supercritical

FIGURE 2.26: Comparison of the velocities in the tunnels in the two scales.

Supercritical ventilation regime

The approach proposed for subcritical ventilation conditions is employed with the higher outlet velocity. The exhaust velocity is increased to 2.2 m/s in the small scale tunnel and accordingly to 3.81 m/s in the big tunnel. The HRR is imposed as boundary condition starting from the experimental curve, figure 2.15b, and later rescaled in the big scale tunnel.

The gas temperature is averaged in time in the second part of the experiment because the fire scenario reaches a quasi steady phase. The time interval considered for the averaging is from 240 s to 480 s in the small scale and from 416 s to 832 s in the big scale. The temperatures averaged along the tunnel's height, T_{Ave}, and the temperature beneath the ceiling, T_{Ceil}, are presented in figure 2.27a for the two scales. The temperatures are generally lower compared to the previous case due to the lower HRR and due to the higher cooling effect induced by the ventilation. The results are in good agreement between the two scales and the maximum difference between the temperatures doesn't exceed 50 °C. Looking at the temperature beneath the ceiling it is evident that in both scales the backlayering length is correctly rescaled.

The wall temperatures are compared along the tunnel after half of the fire scenario and at the end, figure 2.27b. Temperatures are evaluated after 240 s, $t_{1,S}$, and 480 s, $t_{2,S}$, in the small scale and 416 s, $t_{1,S}$, and 832 s, $t_{2,B}$, in the large scale. The agreement between the results is better if compared with the subcritical ventilation condition, the temperature profiles show some differences just above the fire but these are smaller than 50 °C. With higher ventilation rate there are lower heat losses though the walls and the approximations introduced in the rescaling of the materials' properties induce smaller errors. The velocities are compared in the upstream and downstream region after rescaling the position of the measurement and the magnitude of the velocity from the small scale to the big scale. In figure 2.26b it is clear that the thickness and the velocity of the smoke flowing upstream the fire are similar in the two scales. The maximum difference

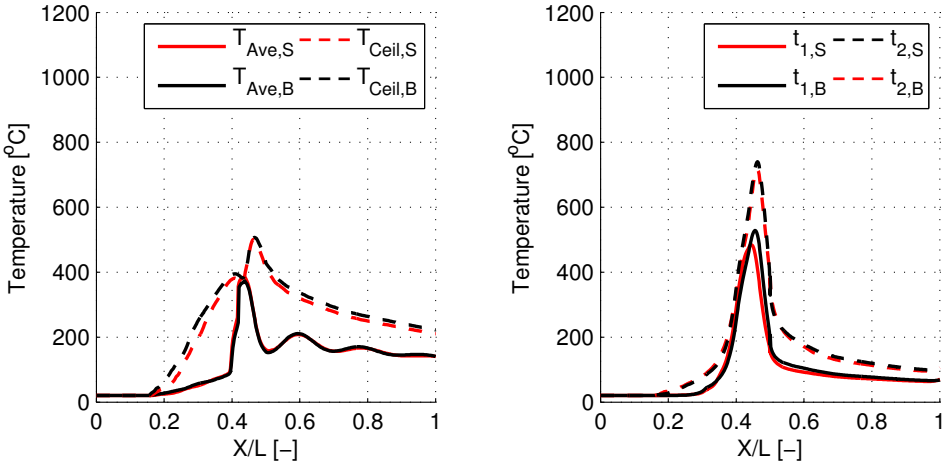

(A) Gas temperature (B) Wall's temperature

FIGURE 2.27: Comparison of the temperature in the tunnels in the two scales.

between the velocity profiles is below 1.0 m/s and it is located near the ceiling where the smoke flows upstream the fire.

In both fire scenarios the results in the big and in the small scale show a satisfactory agreement among them. Most of the differences are localized beneath the ceiling where the heat transfer through the walls has a major influence on the temperature and the approximations introduced with the scaling of the thermal properties reduce the agreement among the scales. The effect of the wall properties decreases increasing the exhaust velocity because a larger portion of heat is exhausted at the outlet of the tunnel. In case of supercritical ventilation regime a small backlayering occurs in part of the tunnel, the backlayering lengths predicted in the two scales have the same magnitude and the velocity profiles of the smoke flowing upstream are in good agreement.

The present comparison shows that if two tunnels are rescaled following the equations provided in section 2.5.1, the temperature and the velocity profiles can be exchanged among the scales. This is important when the critical velocity and backlayering distance are exported from small scale experiments to real scale tunnels. Attention must be paid to the wall properties since they affect the temperature field near the ceiling where the smoke stratifies. If the wall properties are correctly rescaled the error induced by the scaling is confined to the near wall region but in case of major different the error might influence the whole flow field.

2.5.3 Effect of the wall properties

Experimental results carried out in small scale tunnels are usually employed for the evaluation of the critical velocity and the smoke movement [94]. Results from a small scale tunnel can be rescaled and exported to a real scale scenario, if these are similar. In practical problems, not always real tunnels are made of the material prescribed by the Froude scaling. Tunnels often are coated with insulating layer or with concrete layer, but they can also be made only of rock. The thermal properties of the walls affect the heat

exchange between the hot gas and the tunnel's vault. It is thus important to assess how the different heat losses affect the flow field and if the results from a small scale tunnel can be still rescaled and used in the real scale.

To evaluate the influence of the thermal boundary conditions, one tunnel with highly insulating material and one with highly conductive are studied [33]. In the first case, the walls are coated with fibre boards, these are 0.03 m thick and their thermal properties are defined according to [95]. The second layer of the tunnel is assumed to be made of rock. In the second case, walls are completely made of rock, exchanging more heat compared to concrete or insulating material. The thermal properties of the rock depend on its composition, but some common values can be found in [96]. These two tunnels are similar to the big scale tunnel previously investigated unless for the wall's properties. The tunnels are simulated with FDS in case of subcritical and supercritical ventilation regimes using the same fire load and the same ventilation regime presented earlier.

The thermal inertia in case of insulated tunnel is much smaller compared to the other two cases due to the lower specific heat and conductivity of the material. In case of rock the thermal inertia is about two times higher than the reference case. The thermal thickness for the rock tunnel and for the second layer of the tunnel with insulating boards are 0.0, since the wall is supposed to be semi-infinite. All the thermal properties of the walls are summarized in table 2.8.

TABLE 2.8: Thermal properties of the walls of the non insulated and insulated tunnels.

	Rock tunnel	Insulated tunnel
Density [kg/m^3]	2500	240, 2500
Thickness [m]	Inf.	0.03, Inf.
Conductivity [W/m K]	1.5	0.048, 1.5
Specific heat [J/kg]	900	1000, 900
Thermal inertia [kW^2 s / m^4/ K^2]	3375	11.52, 3375
Thermal thickness [W/ m^2 /K]	0.0	9.38, 0

Temperatures and velocities are compared for subcritical and supercritical ventilation regimes in order to find the differences between these two new cases and the big scale tunnel presented earlier which is taken are reference case.

For subcritical ventilation condition the exhaust velocity is set equal to 1.73 m/s at the tunnel's outlet and the HRR is calculated rescaling the experimental curve, figure 2.15a. The temperatures also in this case are averaged in time from 364 s to 727 s and later presented beneath the ceiling, T_{Ceil}, and averaged along the height of the tunnel, T_{Ave}, figure 2.28a. Both temperature profiles obtained with the tunnel made of rock are in good agreement with the reference case, with maximum error about 30 °C. The temperatures in the tunnel with insulating boards are much higher, with an overprediction of the temperature in the whole tunnel greater than 100 °C. This result is confirmed by wall temperatures evaluated after half of the fire, t_1, and at the end, t_2, figure 2.28b. The rock tunnel shows some differences from the reference case, with a temperature underestimation along the whole tunnel and a maximum difference about 150 °C above the fire

place. The temperatures obtained from the insulated case are much higher in the whole tunnel, with an overestimation of the temperature greater than 200 °C in the whole domain.

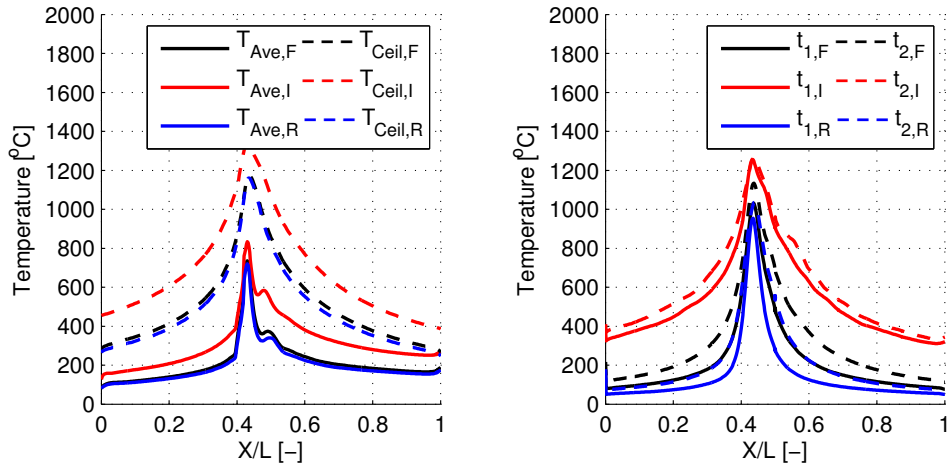

(A) Gas temperature (B) Wall's temperature

FIGURE 2.28: Comparison of the temperature in the tunnels with different thermal properties.

Longitudinal velocities upstream and downstream the fire are compared for the three cases in order to assess the magnitude of the smoke backlayering, figure 2.29a. The agreement found in the temperature profiles between the reference case and the rock tunnel is confirmed also by the velocity profiles, with a maximum error within 0.5 m/s. In case of highly insulated tunnel the velocity of the smoke flowing upstream is higher along the whole height of the tunnel, with a velocity overstimation greater than 1.0 m/s. The smoke layer in case of highly insulated tunnel is thicker than the reference case, because there is a larger part of the velocity profile below 0.0 m/s.

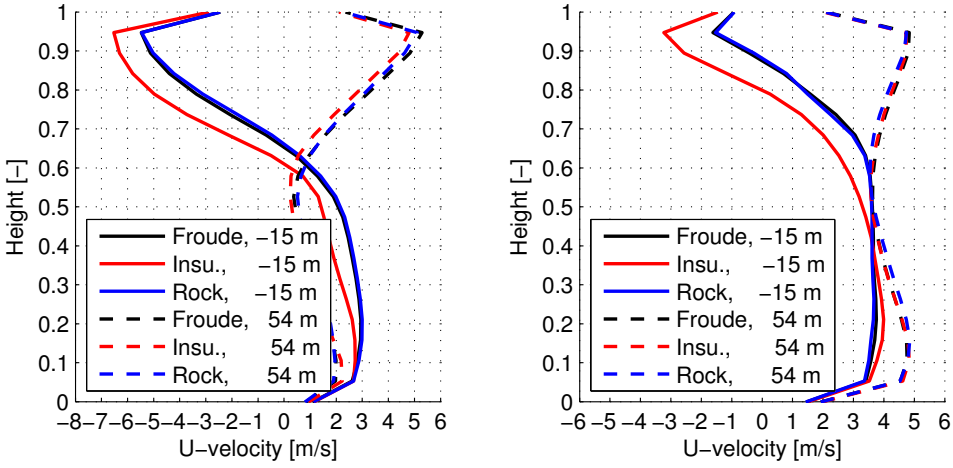

(A) Subcritical (B) Supercritical

FIGURE 2.29: Comparison of the velocities in the tunnels with different thermal properties.

For supercritical ventilation the velocity at the tunnel outlet is set at 3.81 m/s and the HRR calculated basing on figure 2.15b. Temperatures beneath the ceiling, T_{Ceil}, and averaged along the tunnel's height, T_{Ave}, are averaged in time from 416 s to 832 s, figure 2.30a. For the tunnel made of rock the temperature profiles are similar to the reference case and also the backlayering length is similar even if the wall properties are slightly different. The maximum error for the temperature beneath the ceiling is within 40 °C and it is located above the fire, the averaged temperature profiles are overlapping and the difference is smaller than 5 °C. In the highly insulated tunnel temperatures are higher and the smoke flows up to the upstream portal. Because of the different backlayering lengths the temperatures are more than 200 °C higher than the reference case in the part of the tunnel upstream the fire. The wall temperatures in this case show small differences between the rock tunnel and the reference case, with a maximum temperature underestimation about 100 °C above the fire place. While there is a strong overestimation of the temperature in case of insulated tunnel, which is greater than 200 °C along the whole tunnel, except near the inlet portal, figure 2.30b.

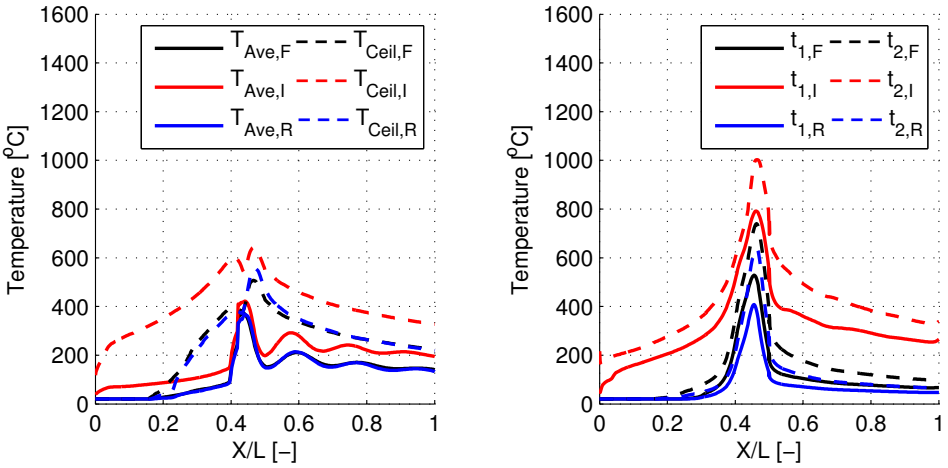

(A) Gas temperature (B) Wall's temperature

FIGURE 2.30: Comparison of the temperature in the tunnels with different thermal properties.

The different backlayering occurring in the tunnels can be depicted also comparing the velocity profiles upstream and downstream the fire, figure 2.29b. The smoke pattern in case of rock tunnel is similar to the reference case, with a maximum error below 0.3 m/s. For the highly insulated tunnel the velocity is higher with a maximum velocity overestimation of 1.5 m/s near the ceiling. The portion of tunnel with negative velocity is also larger so the smoke layer is thicker than the reference case. Under supercritical ventilation conditions some smoke is confined upstream the fire for the reference tunnel and the rock tunnel. In case of insulated tunnel the smoke flows up to the tunnel's inlet and the ventilation is not capable to confine the smoke. Therefore for the tunnel with highly insulated walls this ventilation regime is still subcritical.

Three different tunnels with different walls' thermal properties are compared in order to understand the influence of the thermal boundary conditions on the flow field in case of fire. The reference case has been designed with the Froude scaling from a small scale tunnel [86]. Two new tunnels are designed using the same geometry, fire load and ventilation conditions, but with different thermal properties of the walls. The materials are selected in order to provide an highly insulated case, tunnel coated with fibre boards, and a non insulated case, tunnel made of rock. Reducing the thermal inertia of the walls, with the tunnel insulation, the wall temperatures and the gas temperatures increase. The smoke, due to the higher temperature, is capable to float longer upstream the fire under the same ventilation conditions.

Critical velocities are usually obtained from small scale experiments and when these results are applied to the real scale tunnels not always the wall's properties are correctly rescaled. In case the walls in the real tunnel are less insulated than the reference case the temperature are lower and the backlayering is also less severe than expected, but in case the tunnel is more insulated than the reference case the critical velocity is underestimated. This can lead to unexpected backlayering and to warmer gases in the real scale compared to the small scale with higher risk and threat for the people trapped in the tunnel.

Chapter 3

CFD modelling of jet-fans

After the validation studies presented in Chapter 2, this chapter focuses on the modelling and simulation of jet fans with FDS. The study and validation of these devices is important because as seen in the introduction 1 longitudinal ventilation is frequently used in tunnels. Until now, most of the studies on smoke confinement with longitudinal ventilation focused on the critical velocity and back-layering distance, mainly with model experiments. In a small scale tests it is hard to use rescaled jet fans and longitudinal velocity is usually provided by a fan at the tunnel's portal. In real tunnels jet fans are used for the pollution control and for the smoke confinement in case of fire. However, full scale test where jet fans are installed and tested are not so often performed, so just few experimental data are available.

The limits of the experiments can be overcame using numerical simulations which allow to model ventilation devices and to consider their effectiveness on the smoke confinement. One dimensional methods model jet fans just considering the force they induce on the flow. CFD can simulate the flow field induced by jet fans, but attention must be paid to the modelling of the device. In the literature there are some validation studies about jet fans used for smoke confinement [97–100] or just for ventilation purpose [101, 102]. But in many cases jet fans have been simulated without a previous validation study [30, 103–107], lacking of reliability in the results. In order to assess the capability of FDS to simulate these ventilation devices, a comprehensive validation study has been carried out, including a small scale ventilation test, big scale ventilation and a fire test.

3.1 Model of Jet-Fan in FDS

In FDS it is necessary to model and simulate the jet fan in a simplified way, without including the flow field inside the machine but considering only the flows at the inlet and at the outlet. The simulation of the whole turbomachine is out of the scope of this work and it requires huge computational resources and detailed informations about the fan. The exact geometry of the machine is usually not known, since the blades' profiles and other geometrical features are not released by the manufacturers. Also the operative curve of the machine usually is not a given data, instead the nominal thrust, the nominal volume flow and the rotation speed are provided.

Because of these limitations a simplified model has been chosen to describe the fan's rotor as source of mass and momentum using the HVAC model of FDS while the casing of the fan is modelled as a solid boundary [30, 56, 102]. This approach models the rotor of the fan as section where the flow is intaken and discharged at high velocity [108], figure 3.1a. Through

the fan stage there is no accumulation of mass, so the mass inflowing is equal to the mass outflowing.

$$(\rho u)_{in} A = (\rho u)_{out} A \tag{3.1}$$

Where the density ρ at the inlet is function of the operative conditions of the fan while velocity u and the area A are features of the fan. Through the fan there are no heat losses and a small pressure rise occurs, less than 1000 Pa, therefore the density change is small and the axial velocity is constant across the the fan section. The force produced by the fan can be written as:

$$T = \dot{m}(u_{a,out} - u_{tun}) = A(p_{out} - p_{in}) \tag{3.2}$$

Where $\dot{m}$ is the mass flow through the fan, $u_{a,out}$ is the axial velocity discharged by the fan, u_{tun} is the average velocity in the tunnel and p is the pressure. The force described in equation 3.2 is the theoretical force of the fan, without the pressure losses inside the tunnel, this can be evaluated based on the data provided by the manufacturers. Turbomachines have a performance map which is similar to the one proposed in figure 3.1b, where the volume flow rate and the pressure rise are related among them as function of the machine rotation speed. Because of the lack of data about the performance curve of the jet fans, in the proposed FDS modelling the volume flow rate through the fan is imposed as constant and equal to the nominal value provided by the manufactures. This approach denies the changes of the volume flow and pressure, depending on the fan's operating conditions.

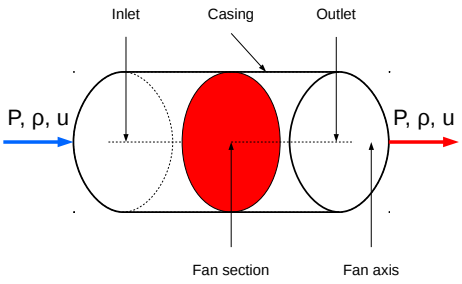

(A) Jet fan model

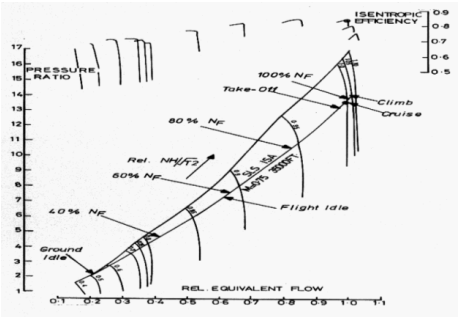

(B) Performance map

FIGURE 3.1: Jet fan model and performance map.

Another simplification required to model jet fans regards the secondary flows at the outlet of the machine, like swirl or radial components of velocity. Jet fans are relatively simple machines and not always after the rotor there is a stator which straights the flow and rise the static pressures at the outlet. Without the stator's blades, the flow at the outlet of the fan has a tangential component of the velocity which induces a vortex with a swirl motion. The swirl is hard to quantify since there are no informations about

the blades' geometry, but knowing the thrust produces by the fan, the geometry and the rotation speed it is possible estimate the velocity distribution. Starting from the Euler equation it is possible to calculate the work exchanged between the machine and the fluid:

$$\Delta H_{fan} = \frac{1}{\dot{m}} \int_{r_{hub}}^{r_{tip}} \omega r (u_{t,out} - u_{t,in}) d\dot{m} \tag{3.3}$$

where ω is the rotation speed of the rotor r is the radius and u_t is the tangential component of the velocity. The equation of conservation of energy across the fan can be written as:

$$\frac{p_{in}}{\rho} + \frac{u_{in}^2}{2} + \Delta H_{fan} - \Delta H_{loss} = \frac{p_{out}}{\rho} + \frac{u_{out}^2}{2} \tag{3.4}$$

where the ΔH_{fan} is the energy given to the fluid by the fan and ΔH_{loss} and the energy losses in the fan. The axial velocity across the section is assumed to be constant and the work exchanged by the machine with the fluid induces a pressure rise across the rotor. Combining together the equations of the thrust 3.2 and the equation of Euler 3.3 it is possible to write:

$$T = \int_A (p_{out} - p_{in}) dA = \rho \int_A \left(\eta \Delta H_{fan} - \frac{u_{out,t}^2}{2} \right) dA \tag{3.5}$$

where η is the machine's efficiency. Since the required thrust, the rotation speed and the nominal velocity are known it is possible to estimate a tangential velocity distribution downstream the rotor. This requires the estimation of the efficiency of the fan since the losses ΔH_{loss} are not known and the estimation of a vortex distribution, since the blades' geometry is also not known. For sake of simplicity a free vortex distribution is used to draw the velocity triangles across the fan:

$$\omega r (u_{t,out} - u_{t,in}) = const = \Delta H_{fan} \tag{3.6}$$

$$u_a = const = \frac{\dot{m}}{\rho A} \tag{3.7}$$

The equation 3.6 can be further simplified since the flow is assumed to enter axially into the rotor therefore $u_{t,in}$ is equal to zero. The equation 3.6 can be solved using equation 3.5 and it gives an estimation of the velocity triangles downstream the rotor, while the axial velocity is assumed to be constant along the span of the blade 3.7, figure 3.2b. This analysis allows to estimate the swirl component of jet fans without stator. In case of jet fan with rotor and stator the flow is straightened and the air flows axially out of the jet fan, so no secondary flows are included in the model. The effect of the swirl has been investigated comparing the numerical results obtained with and without swirl vortex.

3.1.1 Effect of the swirl in the jet fan modelling

When simulating a jet fan with CFD one of the main problem is the description of the jet fan's features. In common problems just few informations are

provided such volume flow or discharged velocity and thrust. The operating map of the compressor and the flow field downstream the fan are usually known only by the manufacturer and are not published. Therefore the modelling of the fan should be done starting from the nominal conditions and assuming that the machine operates always in the same point. When the jet fan has to be simulated also other informations are missing, the diameter of the hub is not known as well it is not known if the are static blades after the rotor.

Due to the lack of published experiments about the flow field near a jet fan, a numerical comparison has been carried out in order to evaluate the effect of the swirl on the performance of the jet fan. Two jet fans with the same discharged velocity and with the same geometry are simulated, one is supposed to have a stator that straight the flow at the outlet and the other is supposed to have only a rotor and the flow is exhausted with a swirl component. The jet fans have a diameter of 1.2 m and a hub of 0.48 m (D/d=0.4). The nominal volume flow discharged by the fan is 34.0 m/s and a nominal velocity of 35.81 m/s. The thrust of the fan is assumed to be 1300 N and the shaft is driven by an electric motor with 4 poles. The information about the thrust and about the rotation speed of the motor allow to defined the work exchanged by the fan assuming the efficiency of the machine equal to 95%. Once the specific work exchanged by the fan is calculated, assuming a vortex distribution along the span of the blade it is possible to calculate the velocity triangles and therefore the flow field downstream the fan. The velocity triangles can be imposed at the outlet of the rotor in order to generate the swirl component downstream the fan. The rotation speed of the rotor can be calculated using the number of poles of the motor and assuming a slip factor of the motor equal to 3%:

$$\omega = \frac{f(1-s)2\pi}{p/2} = \frac{50(1-0.03)2\pi}{4/2} = 152.36[rad/s] \tag{3.8}$$

Using equation 3.5 it is possible to calculate the work required to the fan to generate the pressure rise.

$$\omega r u_{t,out} = 1197[J/kg] \tag{3.9}$$

Knowing the specific energy exchanged along the span of the blade it is possible to calculate the velocity triangles at the outlet of the rotor, figure 3.2a.

The components of the velocity are imposed on the different elements at the outlet of the rotor in order to generate the flow field presented in figure 3.2a. After describing the design of the machine is it possible to simulate the two jet fans, one with only rotor and tangential velocity at the outlet and the other with rotor and stator without tangential velocity at the outlet. The jet fans are simulated in two different conditions, in free field and in a tunnel. For the simulation of the jet fan the numerical grid used in FDS is drawn based on [109] and on the results of the mesh independence study later presented in sections 3.2.2, 3.3.2. The span of the fan is dicretized with 16 elements, whose size is 0.075 m, in order to correctly approximate the geometry of the fan. A refined grid is used around the fan, extended 1.2 m from the fan axis and from 5.0 m upstream to 65.0 m downstream. Around the refined region the elements have a mesh size which is double

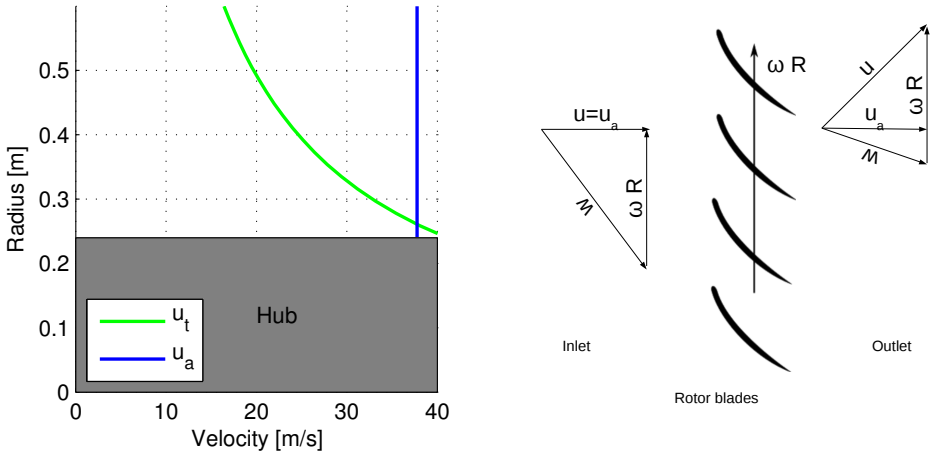

(A) Outlet velocity (B) Velocity triangles

FIGURE 3.2: Velocity distributions across the rotor.

than the elements near the fan, 0.15 m, this mesh is extended from 1.2 m to 3.6 m beside the fan. Around this second region there is another mesh which is further coarsened using elements with double size compared to the previous mesh, 0.30 m.

First, the fans are located in an empty domain which is extended near the fan 75.0 m downstream 15.0 m upstream and 6.0 m beside the fan. The velocity decay downstream the fan and the velocity profiles are compared in figure 3.3.

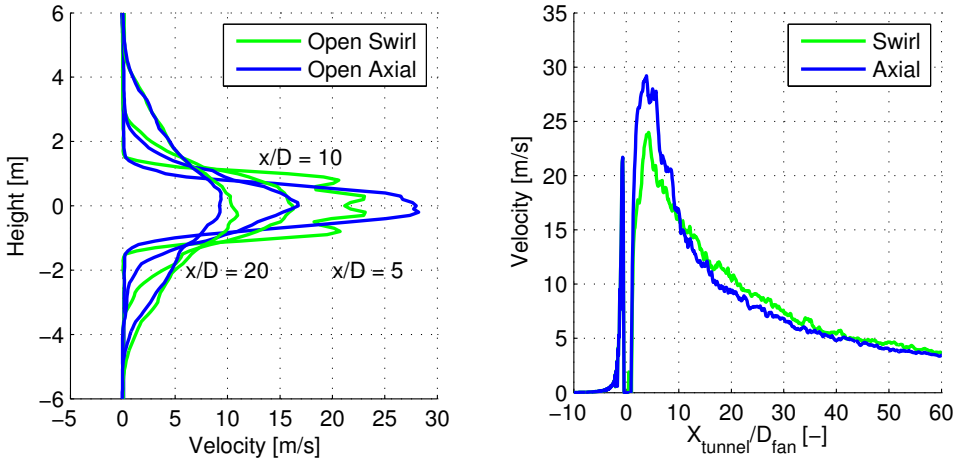

(A) Velocity profiles (B) Axial velocity decay

FIGURE 3.3: Comparison of the velocities obtained with the two fans in free field

The comparison of the velocities shows that the decays are similar in the two configurations far from the outlet, where the velocities are almost overlapping. At the outlet of the fan the velocity in case of jet fan without stator is smaller, 24.0 m/s, compared to the one axially oriented, 29.2 m/s, this is consequence of the different jet shape near the shaft of the jet fan, figure 3.3a. The tangential velocity distributions are compared along the

vertical plane parallel to the fan axis in order to evaluate the distribution of the swirl component in the flow field.

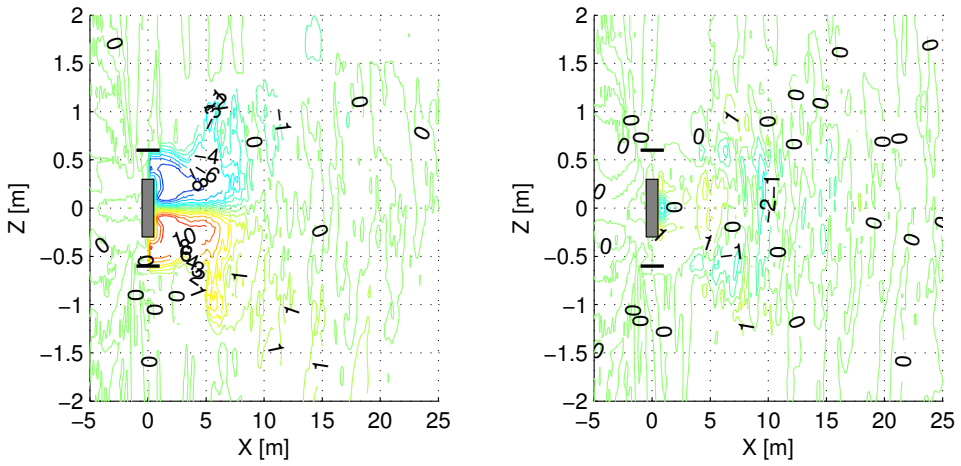

(A) Fan with swirl (B) Fan without swirl

FIGURE 3.4: Comparison of the tangential velocity

The comparison is limited only to the region near the fan since the tangential velocity is high near the fan exhaust 3.4a, but after few meter the tangential component drops to 0.0 m/s. The difference between the two models is evident only close to the fan and this explains why the swirl component doesn't have a strong influence on the axial velocity far from the fan, figure 3.3. The previous figures show the effect of the swirl locally near the fan, however the effectiveness of the fan should be evaluated comparing the entrainment ratios. This has been done comparing the average velocity at the outlet of the domain 75 m downstream the fan. The velocities are compared in table 3.1 including also the results of the next comparison, with jet fan in tunnel. In free field the average velocity obtained with an axial jet is slightly higher that the velocity induced by a fan with swirl component. The difference is small between the two values and the relative difference is about 3%.

TABLE 3.1: Average velocity with and without swirl

	Free field	Tunnel
Swirl	1.92 [m/s]	3.85 [m/s]
Axial	1.98 [m/s]	3.93 [m/s]

The comparison of the two jet fans with and without swirl component shows that the effect of the secondary flow is confined to the region close to the fan's exhaust. Far from the fan, as seen in figure 3.4, the tangential component of the velocity is negligible and the velocities along the axis are overlapping, figure 3.3b.

After the comparison of the jet fans placed in free field it is necessary to compare the two models inside a tunnel. The jet fans placed in the tunnel have the same features of those studied in the free field. The tunnel used for the simulation has a rectangular cross section, 12 m width and 9.6 m high and it is 90 m long. The fans are hanged beneath the ceiling without

a gap between the case and the wall in order to maximize the effect of the wall. The axial velocity profiles are evaluated along the jet fan axis and at different locations in order to evaluate the effect of the swirl on the velocity decay of the jet 3.5.

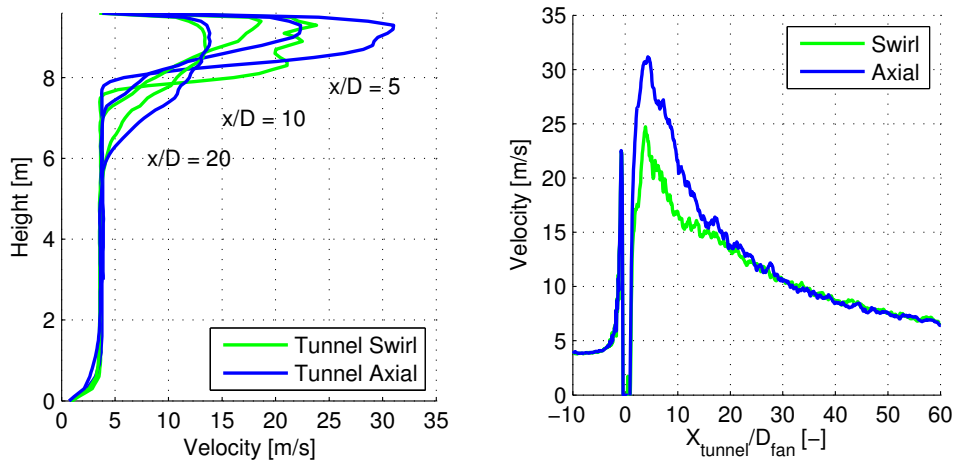

(A) Velocity profiles

(B) Axial velocity decay

FIGURE 3.5: Comparison of the velocities obtained with the two fans in tunnel

The comparison of the axial velocities with and without swirl show a strong influence of the secondary flow near the fan exhaust. The maximum velocity along the axis of the fan with swirl is lower, 24.7 m/s, than the maximum velocity induced by the fan with axial exhaust, 31.2 m/s. As seen in figure 3.4a, the velocity with swirl component decays faster at the fan outlet compared to the fan with axial exhaust. The velocity profiles show also a different decay of the velocity compared to the jet in free field, with a more compact jet downstream the fan. This can be related to the separation of the flow from the wall better known as the Coanda effect [27, 103, 104]. The tangential velocity profiles are compared along the vertical plane passing through the jet axis near the fan region. Figure 3.6a shows that the tangential component of the velocity is decaying after few meters and the flows are similar downstream the jet. The entrainment ratio evaluated for the two cases comparing the average velocity at the tunnel's portal is presented in table 3.1. In case the fan is located in a tunnel the difference of average velocity is small about 2% so the swirl is not strongly affecting the entailment ratio.

The numerical comparison carried out here investigated the need of modelling the swirl motion in the jet fans' simulation. The comparison is just numerical since no experimental data were available about this specific topic, but from the simulations it is clear that the effect of the swirl is located only near the jet fan exhaust. The axial velocity in the few meters downstream the fan is smaller in case swirl component is present. More downstream the velocity profiles obtained with the two models are overlapping and also the entailment ratio with the two models are really close. The swirl component has a secondary effect on the flow field induced by the jet fans, however the effect should be taken into account if when we

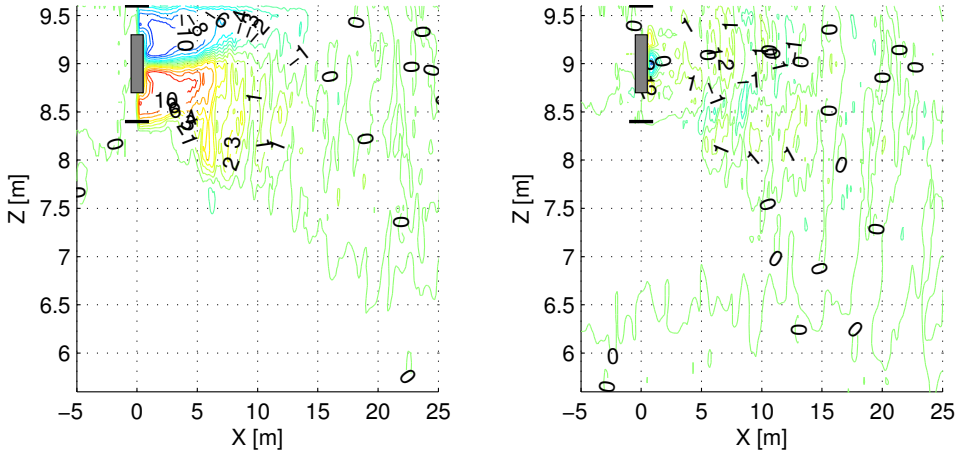

(A) Fan with swirl (B) Fan without swirl

FIGURE 3.6: Comparison of the tangential velocity

want to estimate the velocities near the fan's outlet. The effect can be neglected when we want to evaluate the entrainment ratio or the velocities far from the fan, x/D>20. Experimental data are required for a more reliable comparison of the two models, but due to the lack of data this remains still an open topic.

3.2 Tunnel without fire: Small scale test

Before considering the validation of a big scale scenario, where many uncertainties sum up together and where it becomes hard to control the boundary conditions, a small scale test has been validated. In the literature several experimental work with small scale test have been carried out in order to study jet fans, first Kempf [25] studied the effect of a fan in a tunnel using a nozzle has source of mass and momentum. This approach has been also applied by Pavesi and Martegnani [27–29] studying the velocity distribution induced by the jet fans inside the tunnel. Differently Jacques and Wauters [110] used a small scale jet fan to investigate the velocity field into a small scale tunnel. But due to the several measurements and the different cases investigated the work of Mutama [26, 111] has been selected for the validation.

3.2.1 Description of the experiment

A small scale wind tunnel has been designed to study the flow field induced by a jet fan in mines, the tunnel has been designed to work in cold conditions. The tunnel has a square section of 0.900 m by 0.900 m with and the main body is 7.314 m long, the walls are made of plexiglass 0.0095 m thick. At the tunnel's inlet a bellmouth entrance has been mounted to guarantee low pressure losses and a smooth flow, at the outlet an extraction fan has been mounted. The fan extracts a constant volume flow rate in order to evaluate the flow field for different longitudinal velocities. At the outlet

of the tunnel's main body a contraction piece joints the square section with the circular inlet of the extraction fan.

A real jet fan couldn't be housed inside the tunnel, thus a simple nozzle has been used as source of mass and momentum. The nozzle has a circular section of 0.100 m and it extends into the tunnel for 1.400 m, the nozzle can be connected to different endings with 0.100 or 0.150 m diameter. A fan was connected to the nozzle discharging an air velocity of 20 or 40 m/s for the smaller ending (0.100 m) and 21.8 m/s for the larger one (0.150 m). In order to study the effect of the vicinity of the fan to the wall the nozzle has been moved horizontally at different positions keeping the same height, taking measurements at four different positions. In the initial conditions the distance between the axis of the nozzle and the wall is 0.450 m, later the distance is reduced to 0.300 m 0.150 m and 0.075 m.

Pressure and velocities have been measured at different sections along the tunnel. The velocities have been measured with hot wire anemometers at six different section along the tunnel on the middle line crossing the tunnel. These measurements allow to evaluate the diffusion of the jet and the entrainment ratio in the tunnel. The pressure has been measured on the wall of the tunnel using static pressure holes connected with transducers. The measurements gave a distribution of the static pressure along the tunnel depicting the effect of the position of the nozzle. Differently from the experiments previously mentioned where only the velocity field was measured, Matuma presented both the velocity and the pressure distribution in the tunnel. The position of the pressure static holes and of the hot wire anemometers have been presented in figure 3.7 with a general scheme of the experiment.

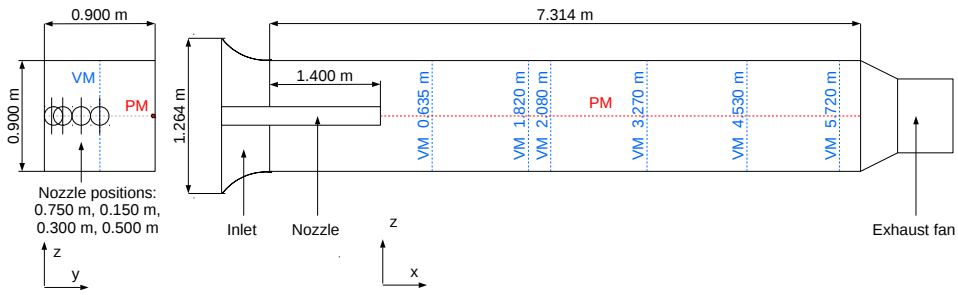

FIGURE 3.7: Experimental set-up used by Mutama [111]

3.2.2 Numerical simulations

In order to reproduce the experiment of Mutama, FDS has been used to model the tunnel and the nozzle. As seen previously two nozzles have been tested with two different velocities but for computational reasons only one has been chosen. The bigger (0.150 m) nozzle has been simulated since it allowed to use less elements for the spatial discretization, moreover the case with lower velocity (21.4 m/s) has been chosen since it allows larger time steps so lower computational cost. The nozzle has been modelled as a pipe connected at the inlet with an HVAC section where the air is discharged at the nominal velocity, the circular section of the nozzle has been approximated with several elements in order to have the same discharge area of the experiment. The tunnel walls have been modelled as no slip surfaces and

the velocity profile near the wall is calculated basing on [64]. The whole length of the tunnel has been modelled with FDS unless for the exhaust fan and the bellmouth inlet, at the inlet a pressure condition has been placed, while the velocity has been imposed at the outlet. The pressure couldn't be set at the outlet because this has been measured only near the wall and it was not known at the outlet section. The volume flow rate through the tunnel has been imposed as boundary condition, but the agreement of the pressure distributions ensures the correctness of the simulations. The volume flow at the tunnel outlet is reported in table 3.2 for the different nozzle's positions. The simulations in FDS are transient but since the results are presented in steady state conditions also the results from FDS have been time averaged.

TABLE 3.2: Operative conditions for different nozzle's positions

Fp Y_j/D_t	δ_j [m]	Vol. flow [m^3/s]	Vel. out [m/s]
0.083	0.075	0.5516	0.6810
0.167	0.150	0.4825	0.5956
0.333	0.300	0.4287	0.5292
0.500	0.450	0.4287	0.5292

A similar validation case has been found in [109] where the velocity decay of a jet is compared with the correlation proposed by Kümmel in [112]. In this case the numerical results are compared only along the centreline of the jet and no information is given about the pressure distribution or the velocity distribution downstream the jet. Moreover in [109] the jet is simulated in free field without considering the interaction of the wall with the jet. The validation however gives some interesting insights about the nozzle modelling and the mesh generation.

When jet fans are simulated the mesh cannot be drawn based on [79], so the informations contained in [109] have been used. The grid should have a good refinement inside the nozzle in order to correctly calculate the flow field, McGrattan et al. proposed different grids with 8 and 16 elements spanning the nozzle. The shape of the nozzle has been approximated using the Cartesian grid, but due to the approximation the area of the outflow is not the same of the experiment. The geometry of the pipe has been drawn considering the grid with 8 elements along the nozzle diameter and it has been kept constant also for the finer mesh. Assuming to keep constant the volume flow rate it is possible to calculate the error on the discharged velocity comparing the real section with the one approximated in FDS.

$$Err_v = \frac{u_{FDS} - u_{Exp}}{u_{Exp}} = \frac{A_{Exp} - A_{FDS}}{A_{FDS}} = -3.38\% \tag{3.10}$$

If the nozzle is drawn as square using the same diameter the error on the velocity would be much larger with an underestimation of the velocity of -21.50%, but this approximation is later investigated in section 3.2.2. For the turbulence model the default model, Deardorff's model, has been initially selected, also other models have been tested in order to evaluate their influence on the results. The domain has been cut in more meshes in order to use the parallel version of FDS with a refinement in the core region of the

jet. The mesh resolution for the two grids is presented in table 3.3. The refined zone is a region with square section of 0.450 m size around the nozzle, out of this refined region the elements have a double size compared to the elements in the refined region.

TABLE 3.3: Mesh data

Mesh	El. size jet-zone [m]	N. of Elements
Mesh 1	$0.02222 \times 0.018750 \times 0.018750$	306432
Mesh 2	$0.01111 \times 0.009375 \times 0.009375$	2451456

The two grids have been used to simulate different cases changing the position of the nozzle inside the tunnel and moving the refined zone near the jet core. Pressure distribution in the tunnel and velocity distribution for steady state conditions have been compared in order to validate FDS. The positions of the nozzle in the tunnel changed during the tests from the middle of the tunnel to the tunnel's wall as shown in figure 3.7.

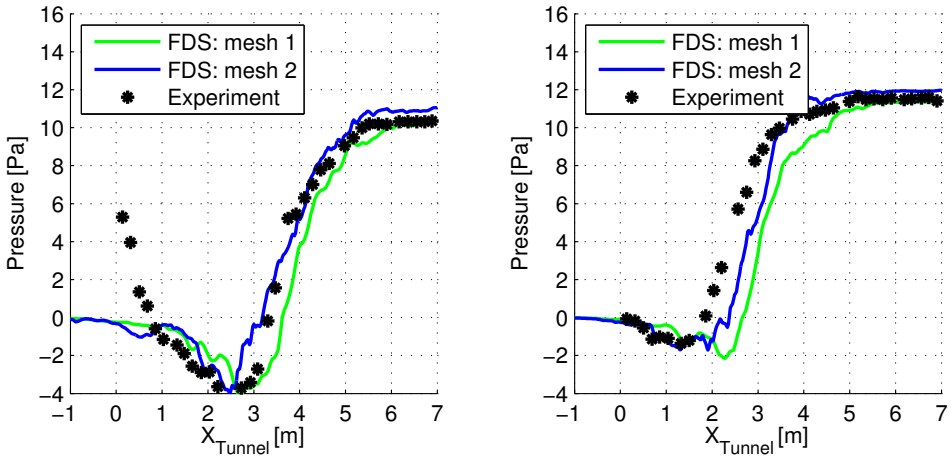

(A) Fp = 0.083 (B) Fp = 0.500

FIGURE 3.8: Pressure distribution near the wall

First, the pressure distributions obtained with FDS are compared with the experimental results, figure 3.8. The pressure has been measured only along the tunnel's wall at z equal to 0.450 m on the side opposite to the nozzle when it moves closer to the wall. The pressure distributions are presented for the two extreme positions Fp. 0.083 and Fp. 0.500 in figure 3.8, showing good agreement between the numerical and the experimental results. The pressure for different nozzle's position reaches almost the same value at the tunnel outlet, about 12.0 Pa for Fp equal to 0.5 and 10.0 Pa for Fp equal to 0.083, and show a flat trend near the outlet where the flow is uniformed. The differences in the pressure distribution for the two positions are mainly located in the region near the nozzle, x equal to 0.0 m, where the different recirculation paths induce different pressure losses. The nozzle closer to the wall shows higher depression near the outlet which indicates a possible flow recirculation, figure 3.8a. The position of the nozzle has also an influence on the pressure curve near the tunnel's outlet, the region with constant pressure is longer in case of jet in the middle of the

tunnel, while it reduces when the nozzle is close to the wall. The results show a good agreement for both grids which reach the same value of pressure at the tunnel outlet and correctly simulate the depression near the nozzle's outlet. The main difference between the experiment and the numerical simulations occurs when the pressure rises, FDS tends to delay the pressure ramp compared to the experiment.

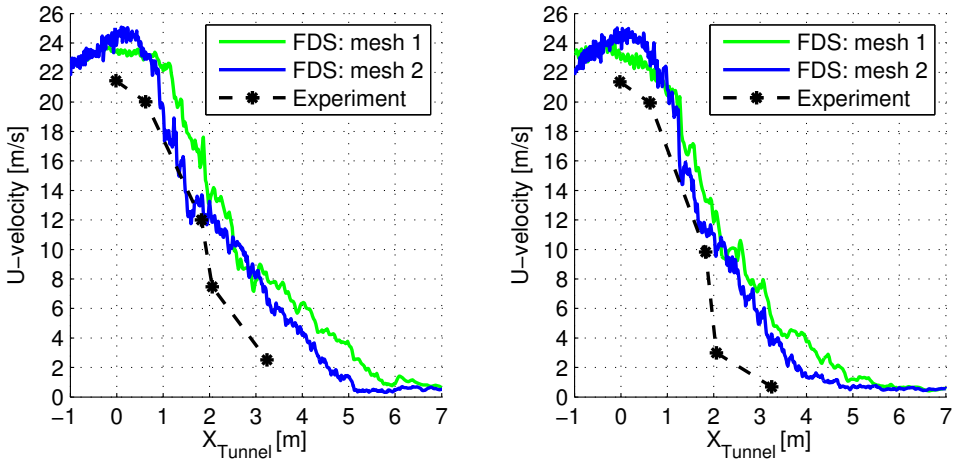

(A) Fp = 0.083 (B) Fp = 0.500

FIGURE 3.9: Velocity decay along the jet's centreline

To better understand the velocity field in the tunnel the velocity decay is presented for the different nozzle positions in figure 3.9. The experimental results have only four points, since the velocity is quite uniform after the initial decay and further points just give the average velocity in the tunnel. The structure of the jet for different nozzle's positions are quite similar among them and FDS follows the experimental data in both cases. The maximum velocity at the nozzle outflow is slightly overestimated by FDS and this can be consequence of the different jet contraction inside the nozzle. The decay of the jet is slightly underestimated by FDS, the centreline velocity obtained from the numerical simulations tends to drop to the constant value about 2.0 m later compared to the experimental results. This effect of delay in the jet decay explains the different pressure rise obtained in figure 3.8.

The longitudinal velocities have been measured at different sections along the tunnel and the results are presented for the different nozzle's positions in order to show the flow field along the tunnel. In figure 3.10 it is possible to see how the jet decays and how much backflow occurs in the section. For the jet in the central position with Fp 0.500 there is the smaller backflow compared to the other positions, while the maximum recirculation occurs when the jet is close to the wall Fp 0.083. The backflow induces a loss of efficiency for the nozzle because the flow is not pushed downstream in the tunnel, but generates a vortex near the fan dissipating pressure. Another consequence of the nozzle's position is the velocity decay along the jet centreline. For the nozzle close to the wall the jet tends to remain more compact and with higher backflow as already seen in section 3.1.1. This effect lead to higher losses due to friction on the wall and a lower

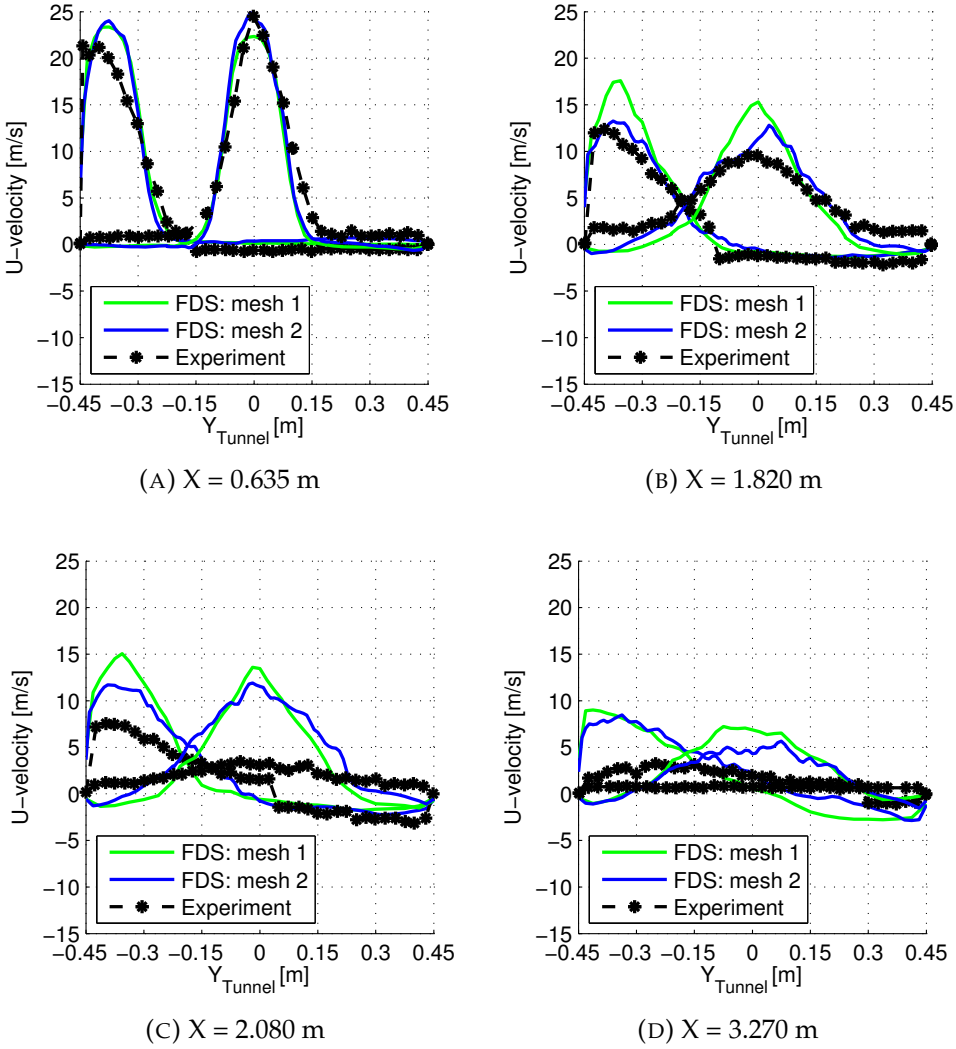

(A) X = 0.635 m

(B) X = 1.820 m

(C) X = 2.080 m

(D) X = 3.270 m

FIGURE 3.10: Velocity profiles for different nozzle's positions

efficiency of the fan as already stated by [25–27] For the two measurements at x equal to 2.080 m and 3.270 m FDS overpredicts the velocities of the jet, which is still compact in the simulation, while it is completely decayed in the experiment. The maximum errors are respectively about 7.0 m/s and 5.0 m/s for mesh 2 and about 10.0 m/s and 7 m/s for mesh 1. In these section there are the larger discrepancies between FDS and the experiment however these are confined to these section, while in the rest of the tunnel the agreement is still good.

The results presented for Fp. 0.083 and Fp. 0.500 give some more informations about the capability of FDS to predict the velocity decay of a jet, figure 3.9. The velocity becomes uniform later in the simulations compared to the experiment and this is clear in figure 3.10d, while for the sections close to the nozzle the results are better. Mesh 2 has a better capability to follow the velocity profiles measured in the tunnel, while the mesh 1 overestimates more the velocity in the last measurement sections. A finer mesh

should be tested to better simulate the velocity decay, but the computational cost of a finer grid couldn't be afforded and only these two meshes have been presented. FDS is capable to predict the velocity pattern of the jet and to predict the induced back flow. FDS is also capable to simulate correctly the faster decay of the jet when the nozzle is in the middle of the tunnel compared to the jet with the nozzle next to the wall.

Effect of the tunnel's inlet geometry

In the previous validation the tunnel's inlet has been simplified without considering the bellmouth inlet which was mounted in the experiment. In order to reduce the complexity of the model and the computational time, the effect of the inlet has been neglected and a normal open boundary condition has been used. To assess the effect of this simplification one more simulation has been carried out with an extended domain including the bellmouth inlet. The mesh used to simulate the new tunnel is based on mesh 1, table 3.3, and the nozzle has been placed at the centre of the tunnel, Fp 0.500. The inlet bell mouth has been designed in order to reduce the pressure losses and the turbulence at the inlet as much as possible. As explained by Mutama in [111] using a radius of curvature equal to the tunnel size 0.900 m the pressure loss coefficient at the inlet tends to zero, the inlet is 0.540 m long and has a cross section of 1.264 by 1.264 m.

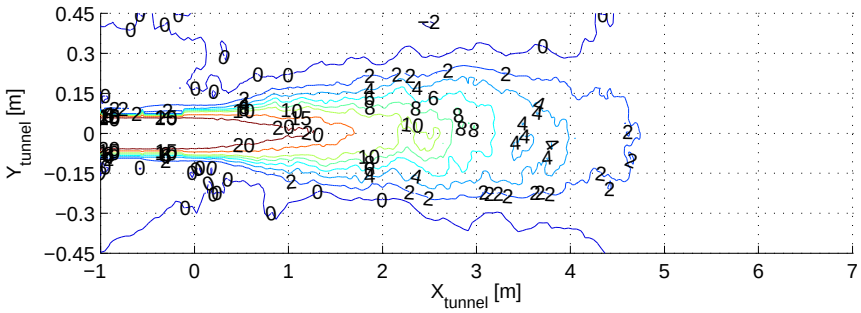

(A) Original domain

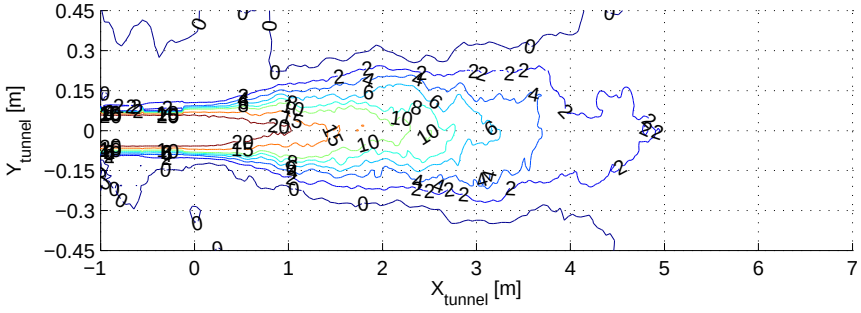

(B) Extended inlet domain

FIGURE 3.11: Velocity contour on the tunnel's middle plane

To evaluate the difference in the two models the velocity fields along

the middle plane at z equal to 0.450 m are presented for the nozzle simulated with bellmouth inlet and for the nozzle simulated with a simple open boundary condition, figure 3.11.

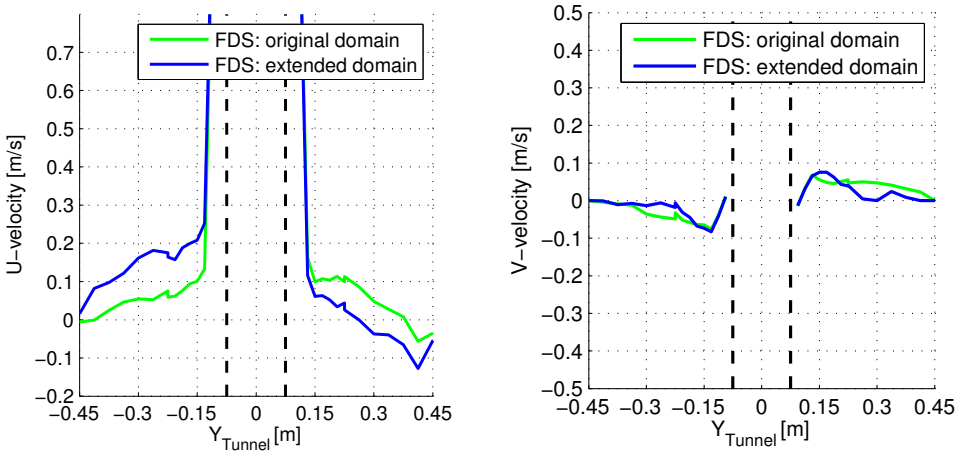

(A) u-velocity (B) v-velocity

FIGURE 3.12: Velocity profiles at the tunnel inlet

The velocity patterns look similar in the two cases, but to better evaluate the influence of the different inlet modelling the velocity at the tunnels inlet at x equal to -0.800 m are presented in figure 3.12. The longitudinal component of the velocity, u-velocity, figure 3.12a, for the two cases are almost overlapping as well as the tangential component of the velocity in the plane, v-velocity, figure 3.12b. The differences in the two patterns are really small, within 0.15 m/s for the u-velocity and 0.05 for the v velocity, and totally negligible if compared with the velocity of the nozzle. The figures presented here show that the modelling used in section 3.2.2 is appropriate for the simulation of this experiment.

Effect of the turbulence model

The geometry approximations are not the only factors that influence the velocity pattern induced by the nozzle in the tunnel. In the simulation of the nozzles or jet fans the flow shows huge recirculation zones and eddies which contribute to dissipate energy. As seen in Chapter 2 with a LES simulation the small eddies are not simulated, but modelled since they are weakly influenced by the geometry of the domain. Therefore a critical aspect of the simulation is the correct modelling of the viscous dissipations in the sub-grid scale. In FDS different sub-grid turbulence models are implemented but the code has been validated against several experiments only with the default turbulence model [109]. In particular the Deardorff model has been used for the validations presented in Chapter 2 showing a good agreement with the experimental results. It is necessary to assess if other turbulence model could better simulate jet fans, compared to the Deadorff model and to compare the results among them. The turbulence models tested in this section are:

- Constant Coefficient Smagorinsky Model

- Dynamic Smagorinsky Model
- Deardorff's Model (Default in FDS)
- Vreman's Model

These turbulence models have been simulated using mesh 1 and mesh 2 described in table 3.3 and for the nozzle configuration Fp 0.500. The velocity decay and the pressure profile along the tunnel's wall are used to compare the turbulence models, for sake of simplicity the results obtained with mesh 1 are first compared together, figure 3.13. In figure 3.13a the turbulence models show a similar trend, apart for the Constant Coefficient Smagorinsky Model which strongly delay the pressure rise on the wall due to the slower decay of the jet. The velocity along the centreline of the jet shows the same trend of the pressure with a good agreement among the turbulence models except for the Constant Coefficient Smagorinsky Model, which overestimate the velocities in the jet, figure 3.13b. A slightly better prediction of velocity and pressure is obtained with the Dynamic Smagorinsky Model which is closer to the experimental curve compared to Deardorff's and Vreman's models.

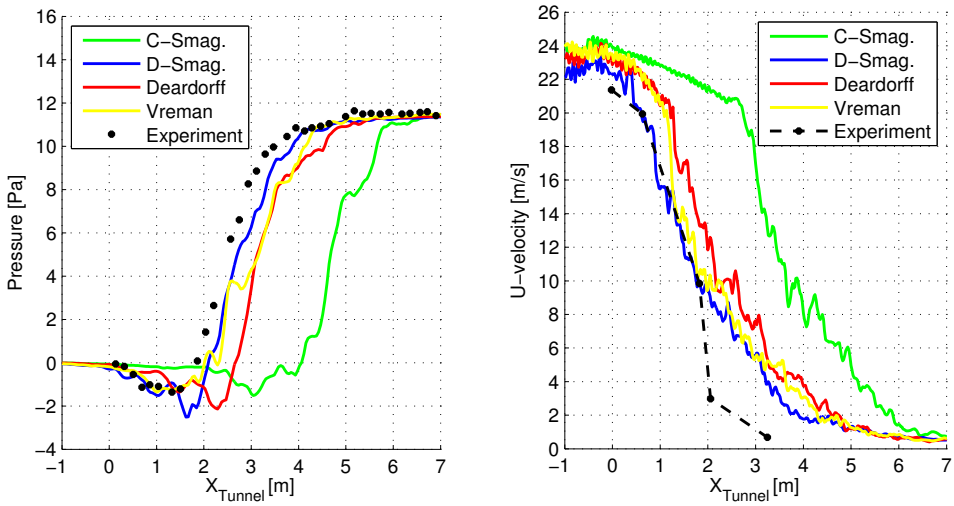

(A) Wall pressure (B) Centreline velocity

FIGURE 3.13: Comparison of different turbulence models simulated with mesh 1

For the simulation performed with mesh 2 the results are presented in figure 3.14 showing a much better agreement between the different turbulence models. The pressure along the wall shows only some minor differences between the curves and all the models correctly predict the pressure rise, also the Constant Coefficient Smagorinsky Model shows a much better agreement with the experimental results, figure 3.14a. The velocity decay highlights a good agreement among the models and the overestimation of the velocity is common among the different models, figure 3.14b. The results obtained with a finer mesh show that there is no influence of the turbulence model when the mesh is sufficiently refined.

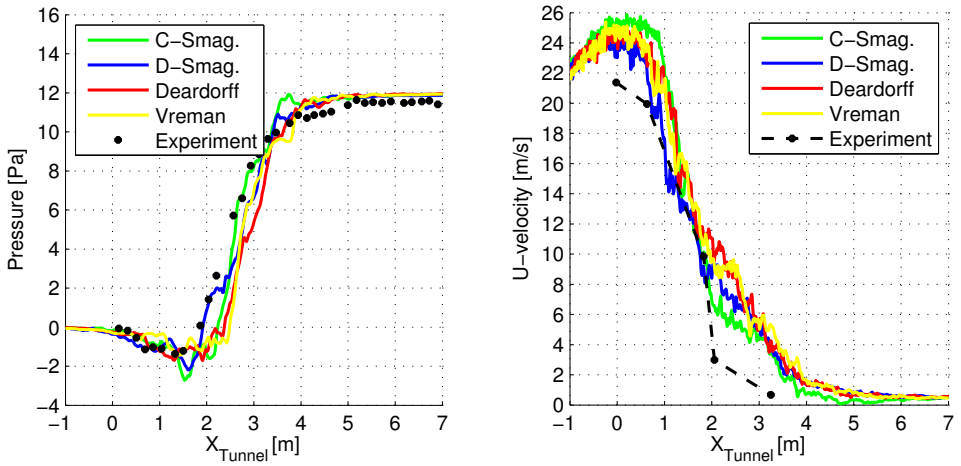

(A) Wall pressure (B) Centreline velocity

FIGURE 3.14: Comparison of different turbulence models simulated with mesh 2

With mesh 1 the results obtained with the Dynamic Smagorinsky Model are slightly better than the others, but this model has not been validated earlier in FDS, therefore it is not considered reliable in the simulation of fire scenarios. For the next validations, sections 3.3 and 3.4, as done in this section 3.2 the default Deardorff's turbulence model is used in the simulations.

Effect of the nozzle geometry

One limit of FDS in the geometry discretization is the need to use a Cartesian grid to mesh the domain. The Cartesian grid doesn't allow to draw rounded surfaces but only to approximate them with cuboid elements. The numerical grids commonly used in the engineering practice are quite coarse to reduce the computational time and simulate large domains [30, 102, 109, 113]. Therefore it is common to model a circular nozzle with few elements and with square shape, if the hydraulic diameter is kept constant between the nozzles, the edge of the square nozzle is equal to the diameter of the original nozzle. The area as seen in equation 3.10 changes in the two nozzles and therefore the velocity or the volume flow must change according to the changed area. In order to keep the same discharged volume and velocity, the hydraulic diameter should be reduced in order to have the same area of the circular nozzle.

Three tests in the small scale experiment have been performed in order to evaluate the error that is induced when simulating a square nozzle. First the nozzle is simulated keeping the same nominal velocity and hydraulic diameter and changing the volume flow. The second nozzle is designed keeping the same volume flow and hydraulic diameter of the experiment and changing the discharged velocity. The last nozzle is designed keeping the volume flow and velocity and changing the hydraulic diameter. For the comparison the nozzle is placed in the centre of the tunnel, with Fp. 0.500, and the coarser mesh, mesh 1 is used. The boundary conditions regarding the nozzles' features in the new cases are summarized in table 3.4, the other

boundary conditions not differently specified are the same of the original case.

TABLE 3.4: Operative conditions for different nozzle's positions

Case	Area$_N$ [m^2] (Err. %)	Diam$_h$ [m] (Err. %)	Vol. flow [m^3/s] (Err. %)	Vel. [m/s] (Err. %)
Original	0.0177 (-)	0.150 (-)	0.3780 (-)	21.4 (-)
Vol. flow	0.0225 (27.1)	0.150 (0.0)	0.4815 (+27.4)	21.4 (0.0)
Velocity	0.0225 (27.1)	0.150 (0.0)	0.3780 (0.0)	16.8 (-21.5)
Diameter	0.0177 (0.0)	0.1329 (-11.4)	0.3780 (0.0)	21.4 (0.0)

The pressure rise and the velocity decay are compared for the original nozzle and for the three square nozzles in figure 3.15. In figure 3.15a the velocity decays show similar trends when the velocity at the nozzle is the same of the reference case. The different discharged volume or the different hydraulic diameter don't affect the agreement with the results obtained with the original rounder nozzle. The difference is evident when the volume flow is the same of the reference case and the velocity is smaller, in this case there is a strong underprediction of the velocity profile and a faster decay.

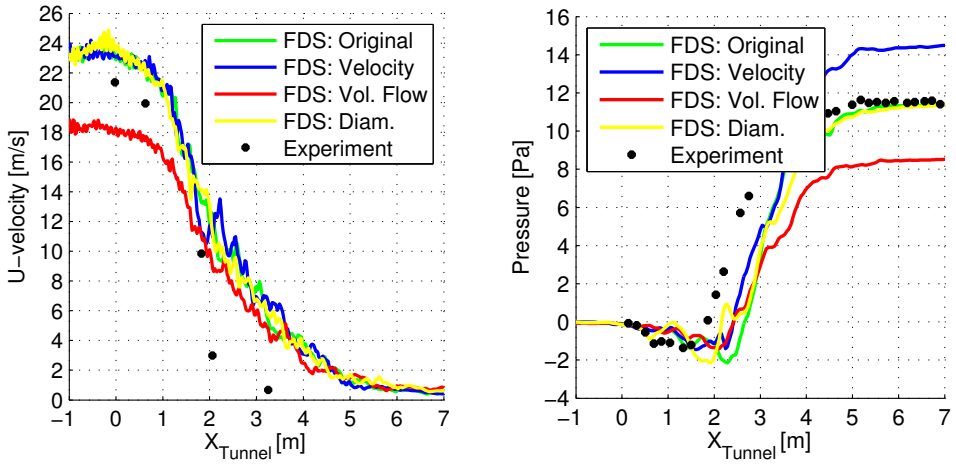

(A) Centreline velocity (B) Wall pressure

FIGURE 3.15: Comparison of different nozzle geometries simulated with mesh 1

The other important parameter in the simulation of jet fans is the pressure rise which induce the longitudinal flow along the tunnel. The pressure is more sensitive to the nozzle's approximation, in case the velocity is smaller and the volume flow is the same of the original case the pressure rise is underestimated about -25%. In case the velocity is the same of the original case and the volume flow is higher the pressure rise is overestimated about +27%. These errors have the same magnitude of the error induced in the calculation when defining the features of the nozzle, table 3.4. In case both velocity and discharged volume are the same of the reference case the pressure rise is similar to the original case. The hydraulic

diameter has a secondary influence both on the pressure rise and on the velocity decay.

When simulating jet fans in FDS it is important to consider the geometric approximations induced in the model because of the Cartesian grid. Jet fans should be simulated with a well refined grid in order to correctly approximate the rounded geometry of the fan. However if the computational power is limited and just few elements are available the best choice for the approximation of a rounded jet with a square shape is to use the same velocity and discharged volume changing the hydraulic diameter. This allows to correctly predict the pressure rise and the velocity decay, comparing simulations with the same grid resolution.

A refined grid in the fan region in not only necessary for a better approximation of the geometry in FDS, the grid resolution is important also for the correct simulation of the flow field downstream the fan. As discussed by Ang in [102] coarse grids in the fan region prevent to correctly simulate the flow field and the velocity decay, while as seen in this section 3.2 a refined grid is capable to correctly predict velocities and pressures.

3.3 Tunnel without fire: Big scale test

In the previous section pressure and the velocities measured in a small scale experiment have been compared with numerical simulations. However it has not been possible to simulate the intaken air into the tunnel when the nozzle is activated, since the volume flow has been fixed as boundary condition. In the engineering practice the most important information about the ventilation system is the average velocity induced by the fan which should be higher that the critical velocity in case of fire.

In order to evaluate the capability of FDS to simulate the flow induced by jet fans, a real scale tunnel without fire has been simulated and compared with the experimental measurements carried out by Colella in [31]. In the experiment only the average velocity across the tunnel is available, while velocity profiles and pressures have not been measured, however these have been already validated in section 3.2. In this new comparison also the results obtained by Colella with the commercial CFD code Fluent are presented together with the results obtained with FDS in order to highlight also the capabilities of the two codes for this specific problem.

3.3.1 Description of the experiment

The Norfolk road Tunnels is a two lines tunnel located in Sydney (AU), it is 460 m long and it has a zero slope. The tunnel has a rounded cross section which is symmetric with respect to the vertical middle plane, the tunnel is 7 m high and 12 m wide. The tunnel is equipped with six pairs of jet fans hanged beneath the ceiling and all of them have the same nominal operating conditions: volumetric flow rate of 34.2 m^3/s and discharge velocity of 34.7 m/s. The exact location of the fan has not been specified, but based on the information provided in [31] the fans have been located at: +20 m, +110 m, +190 m, +275 m, +350 m and +440 m from the inlet portal. The fans on the tunnel's cross section are located at 1.20 m from the vertical symmetry axis and at 6.10 m high, the position is referring to the axis of the fan.

The fan diameter is calculated based on the volume flow and the velocity reported in [31] and set equal to 1.12 m. A schematic view of the tunnel is provided in figures 3.16 3.17.

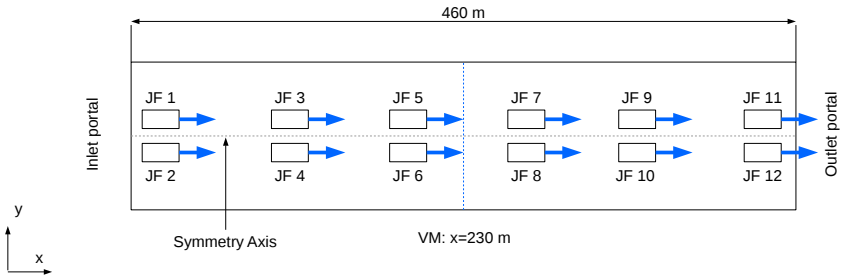

FIGURE 3.16: Experimental set-up used by Colella [31]

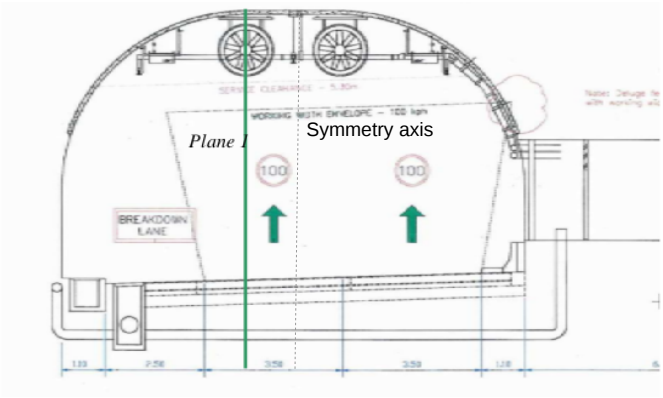

FIGURE 3.17: Cross section of the Norfolk road

The velocity inside the tunnel was measured with ultrasonic transducers at the centre of the tunnel about 230 m from the inlet portal. During the experiment several test have been performed, fans have been turned on and off with different strategies in order to evaluate the longitudinal velocity for the different configurations. Sixteen tests have been carried out but from them only nine are presented since the velocities in the other tests were measured too close to the fans. Therefore for the other seven tests the measurements weren't reliable to be later used for the validation. The scenarios simulated with FDS are listed in table 3.5.

The wind conditions at the portals of the tunnel have not been specified in the experimental report therefore it is not possible consider their eventual influence.

3.3.2 Numerical simulations

In order to simulate the whole tunnel and to reduce the computational cost of the simulations only half of the tunnel has been simulated as proposed by [31]. The fan is simulated as done earlier imposing the volume flow through the fan rotor, this is assumed to be constant and independent from the operating conditions. The fan is modelled without shaft since no informations are provided about the exact geometry of the ventilation device, apart from

TABLE 3.5: Operating conditions of the tunnel during the experiments

Case	fans 1,2 +20 m	fans 3,4 +110 m	fans 5,6 +190 m	fans 7,8 +275 m	fans 9,10 +350 m	fans 11,12 +440 m
1.1	OFF	OFF	OFF	OFF	OFF	ON
1.2	OFF	OFF	OFF	OFF	ON	ON
1.3	OFF	OFF	OFF	ON	ON	ON
2.1	ON	OFF	OFF	OFF	OFF	OFF
2.2	ON	ON	OFF	OFF	OFF	OFF
4.2	OFF	OFF	OFF	ON	OFF	OFF
5.1	OFF	ON	OFF	OFF	OFF	OFF
5.2	OFF	ON	OFF	OFF	ON	OFF
6.1	OFF	ON	OFF	ON	OFF	ON

the exhaust velocity and the volume flow. The tunnel is supposed to have a constant section as discussed in [31] since no other informations were available, and no obstacles in the model are included, apart of the fans. Due to the lack of informations about the atmospheric conditions at the portals it is assumed that there is no wind and that the conditions are the same at the upstream and downstream portal. The initial temperature in all cases is fixed at 20 °C and the atmospheric pressure at 101325 Pa. Based on the validation studies carried out in Chapter 2 the domain is extended out of the portals in order to allow the flow to develop freely without imposing non realistic pressure distributions. The length of the additional domain placed downstream the fans changes depending on the case, because if the fans are placed close to the tunnel's exit a longer domain is required. The extended domain at the upstream portal is 10 m long, 9 m wide and 10 m high, at the downstream portal the domain is the same apart for the cases with jet fans located at +440 m, where the domain is further extended 30 m instead of 10 m. Since no information about the roughness of the walls is available in [31], this is assumed equal to 0.02 m based on a typical tunnel friction coefficient, f=0.026 [102, 114]. Numerical simulations with FDS are in transient regime while the experimental data are assumed to be in steady state conditions, therefore the results of the simulations are averaged in time after reaching the steady state condition. In order to speed up the simulation the initial velocity is set equal to experimental value.

Before comparing the numerical simulations with the experimental results a mesh independence study has been carried out for the case 2.1. In the tunnel the region near the fan in meshed with a fine grid, while the region far from the fan has a coarser grid. The refined region is located from 4 m to 7 m high, from 0 m to 3 m from the symmetry axis and is extended 10 m upstream and 50 m downstream the fan. Out of this refined region the mesh is coarser and it has elements with size double than the elements in the refined region. The elements' size chosen in this phase allows to have 8 and 16 elements spanning the fan's diameter as suggested in [109], the features of the two meshes are listed in table 3.6.

The simulations are compared for steady state conditions and pressures and velocities are used for the comparison. Comparing the velocity along the fan axis it is clear that the decays of the velocity obtained with the two

TABLE 3.6: Mesh data

Mesh	El. size jet-zone [m] (x,y,z)	N. El. (case 2.1)
Mesh 1	0.200 × 0.150 × 0.150	192630
Mesh 2	0.100 × 0.075 × 0.075	1164430

grids are really close with a maximum difference of 1.7 m/s, figure 3.18a. As well the comparison of the velocity profiles shows that the flow field obtained with the two grids are really similar, 3.18b. The maximum error on the velocity peak is equal to 2.0 m/s and occurs at x/d_{fan} equal to 20.

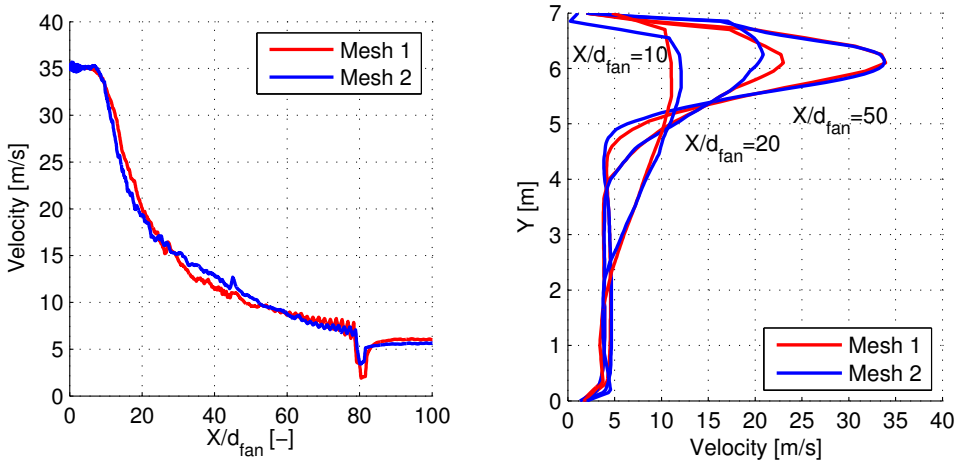

(A) Velocity decay (B) Velocity profiles

FIGURE 3.18: Comparison of the velocities obtained with mesh 1 and mesh 2

The comparison of the velocities shows a good agreement between the two grids, however the pressure rise induced by the fans must also be similar between the two meshes. The pressure is evaluated along the tunnel on the vertical plane crossing the jet fan, the pressure is averaged along the height of the tunnel in order to draw an average pressure profile, figure 3.19a. The pressure increases downstream the fan, the rise of pressure doesn't occur immediately after the fan but it is gradual as seen also in the previous validation, section 3.2. The pressure later decreases due to the friction losses with the walls and due to the losses induced by the fans that are turned off. The pressure profiles along the tunnel's height are compared at the inlet and outlet of the fan, figure 3.19b. The profiles show some discrepancies among them at the inlet region, where mesh 2 has higher depression than mesh 1. The maximum difference between the grids is about 150 Pa, but the difference between the average values is about 76 Pa. The difference in the pressures leads to different thrust calculated in FDS but this effect is secondary because the flow field obtained with different grids are generally in good agreement between them. The average velocity induced by the fans in the tunnel is 4.668 m/s for mesh 1 and 4.6838 m/s for mesh 2, the relative difference between the results obtained with different grids is -0.33%.

The comparison of mesh 1 and mesh 2 for the case 2.1 shows that it is possible to use a coarse mesh instead of a refined one to simulate the

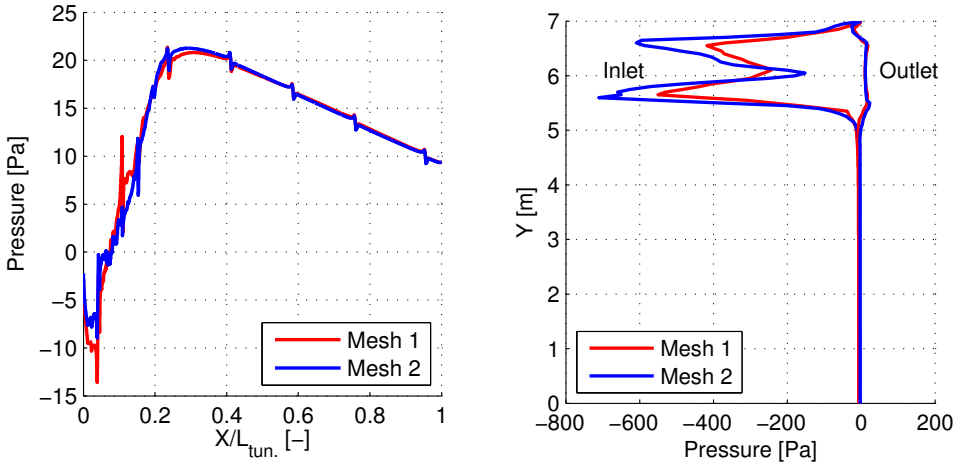

(A) Average pressure (B) Pressure profiles

FIGURE 3.19: Comparison of the pressures obtained with mesh 1 and mesh 2

ventilation scenarios in tunnel.

The average velocities obtained with FDS are presented in table 3.7 and in the figure 3.20. In table 3.7 apart of the results obtained with FDS also the results obtained with Fluent are presented and the relative error for the different ventilation scenarios. The comparison shows that for different fan configurations the velocity predicted by FDS is quite close to the experimental value, as well the agreement is always better in FDS than in Fluent, apart of the case 6.1. The maximum error between FDS and the measurements occurs in case 2.1 when the velocity is overpredicted about 1.2 m/s, however the result is close to the Fluent simulation. Therefore the discrepancy with the experimental result can be consequence of different boundary conditions, for example different wind velocity at the portals.

TABLE 3.7: Comparison of the numerical results with the experimental measurements

Case	Vel.$_{Exp.}$	vel$_{FDS}$	Err.$_{FDS}$ %	Vel.$_{fluent}$	Err.$_{fluent}$ %
1.1	1.94	1.39	-28.4	1.14	-41.2
1.2	4.16	4.10	-1.40	4.28	2.9
1.3	5.00	5.28	5.6	5.77	15.4
2.1	2.7	3.89	44.1	3.90	44.4
2.2	5.27	5.18	-1.7	5.66	7.4
4.2	3.33	3.74	12.3	3.83	15.0
5.1	3.33	3.85	15.6	4.06	21.9
5.2	5.83	5.29	-9.3	5.20	-10.8
6.1	6.1	5.53	-9.34	6.25	2.45

The comparison of the velocities in different ventilation conditions gives an overall idea of the capability of FDS to simulate longitudinal ventilation scenarios in tunnels. To better understand the flow field inside the tunnel, the pressure field and the velocity field induced by the jet fans are further

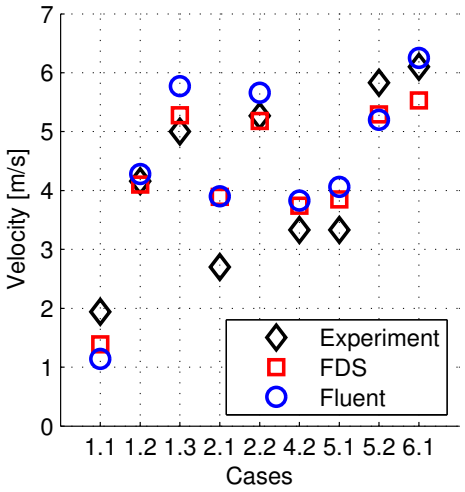

FIGURE 3.20: Comparison of average velocity in the tunnel between experimental and numerical results

investigated. The different ventilation scenarios are grouped together basing on the fans' locations. Cases 1.1, 1.2, 1.3 and 6.1 are presented together because the jet fans placed at 440 m are activated, the other cases are presented together because these fans are turned off.

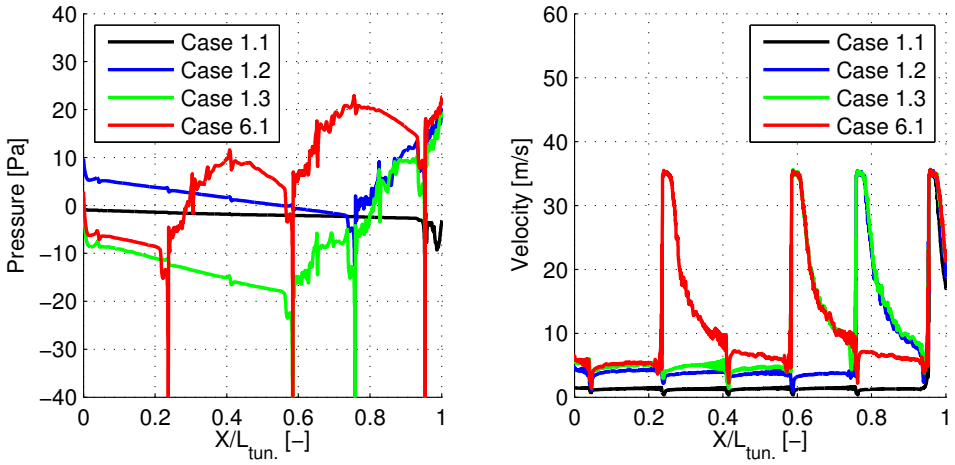

(A) Average pressure

(B) Velocity along the fan

FIGURE 3.21: Comparison flow field for the cases 1.1, 1.2, 1.3 and 6.1

As seen in the mesh independence study and in the previous section the fans induce a pressure rise which is not confined only to the fan section but it is extended also downstream. The pressure rise depicts the capability of the fan to generate longitudinal force and induce a longitudinal flow. In case the active jet fans are located near the outlet of the tunnel the average velocities are lower compared to the other cases with the same number of fans. For the cases 1.1, 1.2, 1.3 and 6.1 the active fans are located near the tunnel's exit the pressure partially rises inside the tunnel but the pressure profiles doesn't reach a plateau downstream the jet, figure 3.21. This means

that the jet fan doesn't transfer the whole thrust from the high speed jet to the main flow, but part of the force is dissipated out of the tunnel. If the pressure doesn't rise to the plateau value the pressure difference and the longitudinal force applied to the tunnel are lower than expected.

This effect is usually ignored in more simplified models where the jet fan is assumed to rise the pressure as a concentrated force on the cross section where the fan is located. The cases 1.2 and 1.3 have jet fans activated in the second half of the tunnel and not only near the exit, but the pressure inside the tunnel doesn't rise to a plateau. In cases 1.2 and 1.3 the velocity is not fully decayed before entering into the next fan, figure 3.21b.

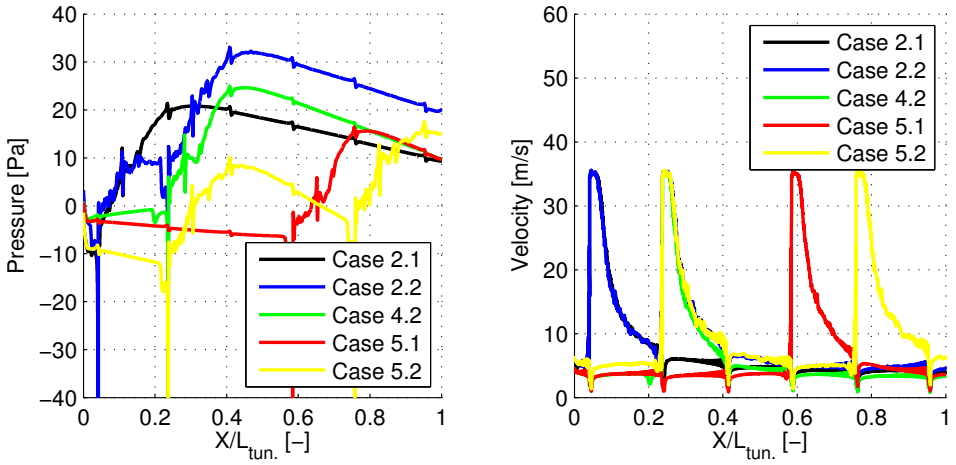

(A) Average pressure

(B) Velocity along the fan

FIGURE 3.22: Comparison flow field for the cases 2.1, 2.2, 4.2, 5.1 and 5.2

Evaluating the results coming also from the remaining tests it is evident that the longitudinal position of the jet fans plays a key role, figure 3.22. For these ventilation scenarios the pressure plateau is inside the tunnel, figure 3.22a, and this occurs after the velocity along the jet fan axis decays to the average value, figure 3.22b. The jet fans in the tunnel should be placed at a distance from the exit portal and from the next fan greater than the decay length of the jet velocity. If the fans have a shorter distance from the tunnel's exit then the jet is not fully mixed with the main flow and the pressure doesn't reach its maximum value. If the pressure rise is interrupted before the maximum, at the portals of the tunnel a lower pressure difference is applied so a lower velocity is induced along the tunnel.

In figures 3.21a 3.22a the pressure rises to a peak but after the plateau it decreases. The pressure is dissipated along tunnel by the pressure losses, localized and distributed. The distributed pressure losses are caused by the friction losses at the tunnel's walls. These losses are function of the roughness of the walls and of the velocity, that's why different ventilation scenarios have different slopes in the pressure profiles, since the longitudinal velocity change according to the fan configuration. Local pressure losses should be also included in the model, obstacles in the tunnel affect the flow field and generate additional pressure losses. Jet fans turned off, vehicles and every other obstacle should be taken into account in the model in order

to not underestimate the pressure losses. The portals should be modelled with additional zones which allow to simulate the flow near the portals instead of imposing the boundary conditions at the ends of tunnel. At the inlet portal the flow accelerates passing from a larger section to a smaller one, while on the exit portal the flow decelerates due to the section expansion. If the boundary conditions are placed at the portals' sections the flow contraction and expansion are neglected and the air flows normal to the portals' cross section.

The previous validation shows that FDS is capable to simulate correctly the average velocities inside a short tunnel which is ventilated with different jet fan configurations. The velocity in the tunnel is the result of a balance between the forces induced by the fan and the pressure losses along the tunnel. In order to highlight the effect of the distributed pressure losses, the tunnel has been simulated considering the walls of the tunnel as smooth. This approximation doesn't implies that the walls are free slip, but that the roughness of the walls is 0.0 m. A graph similar to figure 3.20 is presented in figure 3.23 in order to highlight the effect of the distributed pressure losses along the tunnel.

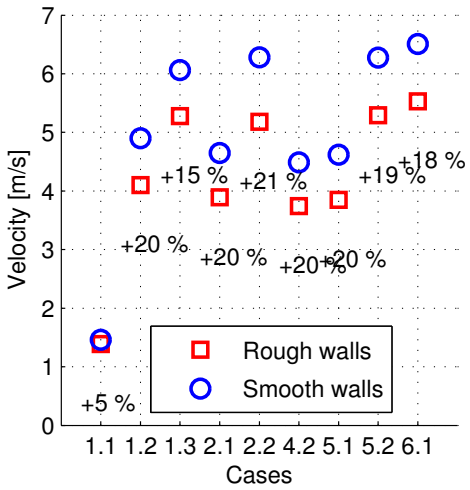

FIGURE 3.23: Evaluation of the influence of the roughness on the tunnel's longitudinal velocity

As expected the velocities in case of smooth walls are higher in every condition and this leads to an overestimation of the longitudinal velocity and of the safety level. The percentage error are also reported in the figure 3.23 with a minimum error about 5% and a maximum error about 21% depending on the fan configuration. The estimation of the pressure losses in tunnels is a critical aspect of the modelling because not only rough walls induces pressure losses, but every geometry change induce some further losses. These detailed informations about the tunnel's shape are not known at the design stage and the friction coefficient of the tunnel should be estimated with in-site measurements.

3.4 Tunnel with fire: Memorial tunnel test

In the section 3.3 jet fans in a short tunnel have been simulated in cold flow and the results have been compared with experimental measurements showing a good agreement among them. However no comparison has been done in case of fire, where the smoke is confined by the longitudinal flow induced by the jets. Smoke confinement by means of longitudinal ventilation has been widely investigated with small scale experiments and several CFD simulations have been performed by different authors [21, 115–120]. In these simulations the ventilation system is usually simulated as a constant source of fresh air with an imposed velocity. This has been done to reproduce the experiment where the fresh air is supplied by a fan at the tunnel's portal or to avoid the simulation of jet fans. In real tunnels the velocity at the portals in not imposed, but it is the results of a force balance, the fans are enforcing the air to flow along the tunnel with a pressure rise. The local and distributed pressure losses reduce the pressure difference between the portals and the longitudinal velocity, wind and atmospheric conditions at the portals reduce or enhance the flow depending on the specific conditions. The fire induces an additional pressure loss better known as throttling effect, which is proportional to the HRR [8, 30, 31]. To assess the capability of the ventilation system to confine the smoke, the longitudinal velocity shouldn't be imposed as boundary condition, but it should be the result of the calculation. Including the jet fan in the simulation, the complexity of the calculation and the uncertainties on the operative conditions of the tunnel increase. To assess the reliability of a CFD simulations where both fire and ventilation are simulated the numerical results should be compared with experimental results.

For the comparison, few experiment in full scale are available and these should list all the necessary informations about the ventilation system and fire scenario. Some large scale test have been presented in section 1.1 and due to the large amount of measured quantities during the fire test and thanks to the extensive report available, [8], the Memorial tunnel is chosen for the validation of the jet fans model in case of fire.

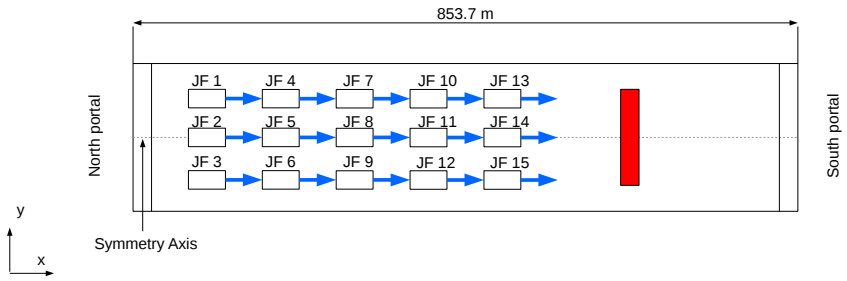

FIGURE 3.24: Schematic drawing of the fan and fire locations in the Memorial tunnel

3.4.1 Description of the experiment

The memorial tunnel test has been already introduced in section 1.1.2, now the features that are necessary to perform the simulation are presented in

detail. The tunnel has a straight geometry with length equal to 853.7 m and a slope of 3.2% from north to south portal. The geometry of the cross section is constant along the tunnel except for the portals where a section reduction is necessary to allocate the fans. The tunnel has a rounded ceiling with radius equal to 4.38 m and a rectangular geometry for the lower part of tunnel. The width of the tunnel is 8.76 m and the height 7.86 m in the tunnel's main body while at the portals the height is reduced to 4.33 m, the two sections of the tunnel are presented in figure 3.25.

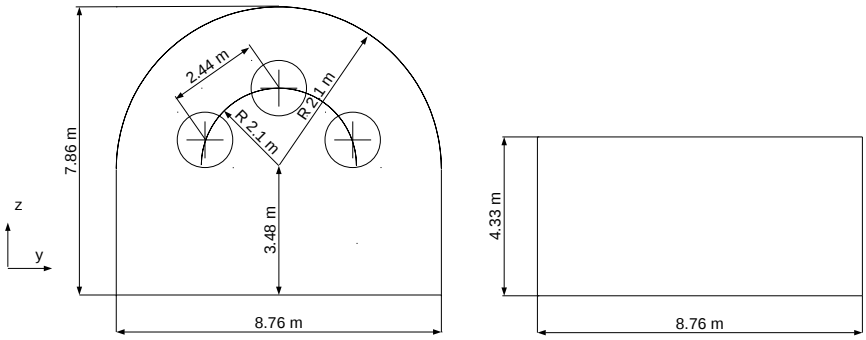

FIGURE 3.25: Cross sections of the memorial tunnel in the main body and at the portals

The tunnel is equipped with 15 jet fans which are hanged beneath the ceiling and oriented from the north portal to the south portal, against the natural flow of smoke. From the experimental report the jet fans are capable to discharge a volume flow of 42.95 m^3/s with a velocity of 34.19 m/s, the fan's inside diameter is 1.37 m. The fans are grouped five in batteries of three hanged at different longitudinal positions, the batteries' locations are summarized in table 3.8.

TABLE 3.8: Position of the jet fans' batteries

	Fan id	$x_{batt.}$
Batt. 1	1; 2; 3	95 m
Batt. 2	4; 5; 6	190 m
Batt. 3	7; 8; 9	285 m
Batt. 4	10; 11; 12	379 m
Batt. 5	13; 14; 15	474 m

The jet fans are turned on during the test at different times and only few of them are activated in order to evaluate different ventilation strategies.

Inside the tunnel pans filled with oil are located downstream the fans and they are filled with No. 2 fuel oil. In order to test different pool fires four pans are located in the tunnel at 615 m from the north portal, the pans are designed in order to provide different HRR: 10 MW, 20 MW, 30 MW, and 50 MW. Combining together the different pans it is possible to obtain fire scenarios up to 100 MW. The HRR is measured controlling the level of the fuel in the pan and refilling the pan in order to maintain a controlled level.

Tunnels' walls in the fire area are coated with a protecting layer of cemented vermiculite which insulate the tunnel and protect the structure. A

layer of 0.150 m is sprayed on the walls and a layer of 0.100 m on the floor. At the portal the atmospheric conditions are known in terms of temperature which is about 5 degrees, but no informations are available on the wind conditions and on pressure differences between the portals. Only the velocity is measured on the tunnel's cross section in order to evaluate the flow along the tunnel.

In the tunnel several measurements have been carried out, velocity, visibility, temperature and CO concentration. These have been measured at different locations providing a spatial distribution at different moments of the experiment. The location of the measurement devices is extensively described in the experimental report [8].

3.4.2 Numerical simulations

For the validation of the Memorial tunnel test numerical simulations with FDS have been carried out. The numerical model combines together the simulations of jet fans previously seen in sections 3.2 and 3.3 and the early validation of fire scenarios, chapter 2. The test 608 has been chosen for the validation and hereafter the boundary conditions of the case are presented. In this test only one pool fire is ignited to provide a nominal power of 20 MW, the real HRR has been measured in the experiment and it is used as boundary condition of the simulation, figure 3.26. The HRR of the pool fire is constant during the first part of the test, when the ventilation is turned off the HRR is about 7.5 MW, while when the jet fans are activated it rises with a maximum of 18 MW, figure 3.26. The experiment lasted about 36 minutes (2200 s), but for the validation only 600 s are considered since the fire is initially naturally ventilated and later longitudinally ventilated. During the simulation one experimental point is ignored after about 140 s, when the HRR drops to 0.0 MW. This is considered not realistic because the fire would extinguish and reignite by itself rising up to 18 MW.

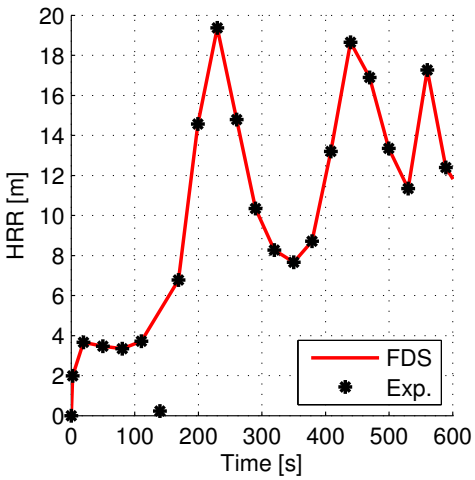

FIGURE 3.26: HRR measured during the test 608

The fuel used for the simulation is selected according to the experiment [8] in order to correctly reproduce the combustion of No. 2 fuel oil. Kerosene is chosen as fuel, with specific heat of combustion equal to 44.1 MJ/kg^{-1}, soot yield equal to 0.042 and CO yield equal to 0.012 according

to [78]. The jet fans are simulated based on the jet fan model previously presented, in the test 608, three jet fans are activated after 120 s of fire: fans 8, 11 and 14. These fans are placed along the tunnel's centreline therefore it is not possible to consider the tunnel as symmetrical because both the fans and the fire would be cut.

The walls are modelled as conductive surfaces in order to take into account the heat losses, two layers are included in order to consider the vermiculite coating and the concrete according to the information provided in [8]. The thermal properties used for the simulation are presented in table 3.9.

TABLE 3.9: Materials' properties

Material	ρ [kg/m^3]	C_p [kJ/kg/K]	k_{th} [W/m/K]	δ [m]
Vermiculite	500	1.2	0.065	0.15 (walls) 0.10 (floor)
Concrete	2100	1.4	1.2	2.5 m

The roughness of the walls is set equal to 0.025 m according to [102, 114]. The obstructions in the tunnel like cameras, measuring stations, jet fans not activated, pool fires not ignited are explicitly included in the model. The conditions at the portals are set according to the informations provided in the experiment, the temperature is equal to 5 °C, the pressure is set at the atmospheric value 101325 and no wind is included. The flow field is extended out of the portals with an additional domain which is 10 m long 17.6 m wide and 10.4 m high. In order to include the slope of the tunnel the gravity vector is tilted of 1.83°, slope 3.2%.

Due to the large uncertainties about the experiment and about the numerical set up few sensitivity analysis are presented hereafter before presenting the results of the validation. First, a mesh independence study is performed in with particular attention to the fire region. The comparison is limited only to the region near the fire since the refinement of the whole domain would require a too large computational power. Moreover the mesh independence study for the jet fan region has been already performed in the sections 3.3 and 3.2. For the mesh independence study only the last portion of the tunnel is simulated from 72 m upstream the fire to the exhaust portal. With this model the jet fans are not included in the simulation but a constant velocity 3.5 m/s is imposed upstream the fire. Three grids are compared in order to assess the correct size able to simulate the fire region, the features of the grids are presented in table 3.10. The mesh of the fire region is extended from -15.0 m upstream the fire to 25.0 m downstream the fire the remaining region is meshed with larger elements.

TABLE 3.10: Mesh features for the mesh independence assessment

Mesh	Fire zone [m] (x,y,z)	Far zone [m] (x,y,z)	N. El.
Mesh 1	0.267 × 0.275 × 0.260 m	0.533 × 0.550 × 0.520	228400
Mesh 2	0.167 × 0.1833 × 0.1625 m	0.333 × 0.367 × 0.3325	961152
Mesh 3	0.133 × 0.1375 × 0.130 m	0.267 × 0.275 × 0.260 m	1999360

The fire is similar to the one studied later in the validation, but in order to speed up the calculation and to study the effect of the mesh in steady state conditions a constant HRR of 15 MW is imposed as boundary condition. Since FDS performs only transient calculations, 300 s are simulated with the three grids, the results are averaged in time from 100 to 300 after the simulation reaches the steady state condition, so the results can be compared among them. These simulations are not really steady state since the walls heat up much slower than the gas but this effect is neglected since much longer simulations are needed to have steady state conduction in the heated walls. The temperature and the velocity profiles are presented in figure 3.27 at two position downstream the fire, after 10 and 20 m.

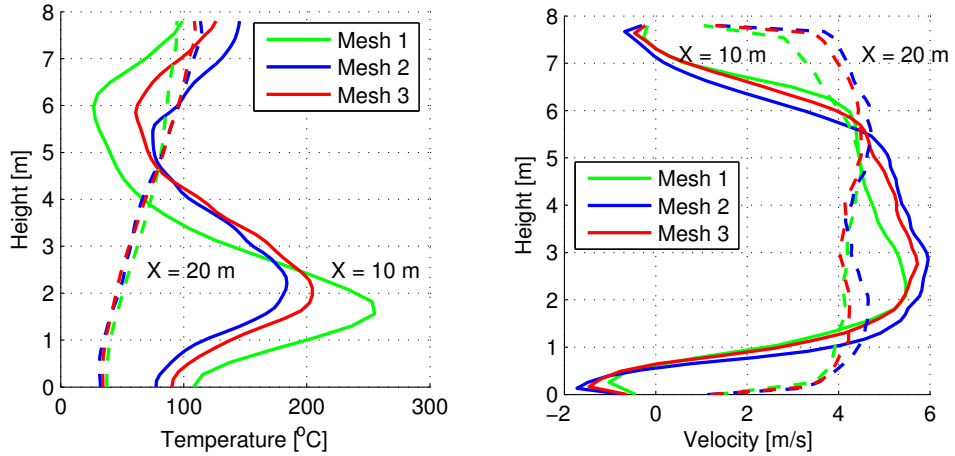

(A) Temperature (B) Velocity

FIGURE 3.27: Mesh independence study

The temperature profiles are closer for mesh 2 and 3 while for mesh 1 the agreement is poorer, the maximum errors are respectively 40 °C and 100 °C. Comparing the results obtained at the different position it is clear that the agreement improves moving far from the fire, the reaction zone as seen in previous analysis is always one of the most critical region to simulate and a fine mesh is usually required. Velocities show a smaller difference between mesh 2 and 3 than between mesh 1 and 3, with maximum errors respectively equal to 0.5 m/s and 1.0 m/s. The temperature distributions near the fire are presented for steady state conditions in figure 3.28 for the three different grids. The comparison of the plume region shows some small differences between grid 2 and 3, while the differences are larger between grids 1 and 3. The comparison among the simulations suggests that the meshes 2 and 3 are independent from the grid resolution. However mesh 2 cannot be chosen because it is not aligned with the mesh of the jet fans, therefore the mesh 3 is chosen.

Near the jet fans a refined mesh is used as well, the element's size is chosen in order to discretize the fan with 10 elements along the diameter. The refined region has a square section, with edge of 3.12 m, centred on the fan which is extended 5.0 m upstream and 35.0 downstream. This meshing strategy is based on the previous validations and it is considered reliable so has been excluded from the mesh independence study. The zones far from

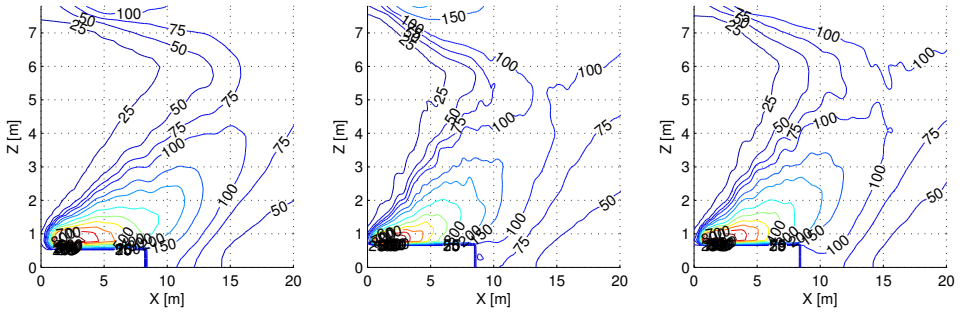

(A) Mesh 1 (B) Mesh 2 (C) Mesh 3

FIGURE 3.28: Comparison of results obtained from three different meshes

the fire and from the jet fans have a coarser mesh, the size of the element is doubled in order to reduce the computational power required and speed up the calculation. The features of the mesh that is later used for the simulation are listed in table 3.11.

TABLE 3.11: Mesh features

Mesh	El. size jet-zone [m] (x,y,z)	El. size fire [m] (x,y,z)	N. El.
Mesh 1	$0.200 \times 0.1375 \times 0.130$	$0.125 \times 0.1375 \times 0.30$	1199200

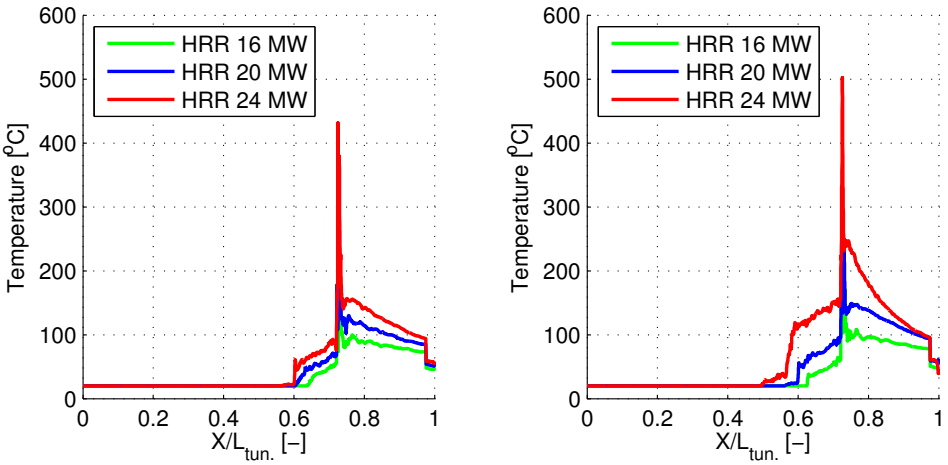

(A) After 150 s (B) After 300 s

FIGURE 3.29: Comparison of the temperatures for different HRR

After assessing the correct mesh size that should be used to simulate the fire another verification is done. During the experiment the HRR shows high fluctuations and its value is always lower than the nominal one. Therefore starting from the nominal power of 20 MW two other similar cases are simulated with a fire of 16 MW and a fire of 24 MW which are respectively 20% lower and higher than the nominal fire power. The comparison

aims to evaluate the sensitivity of the simulation from the HRR. In this second preliminary verification the jet fan are included in the model and the whole tunnel is simulated using mesh 1. For sake of brevity only 300 s are simulated, the fire is simulated with a constant HRR equal to the nominal power and the jet fans are turned on at the beginning of the simulation. The temperatures obtained with different fire powers are compared at different moments of the simulations in order to evaluate the smoke movement in the tunnel. The temperature is averaged along the tunnel's height and presented as function of the position along the tunnel's length. The temperature are presented after 150 s and 300 s in figure 3.29.

Increasing the power of the fire, the temperatures rise and the smoke can flow longer upstream the fire. After 150 s the temperatures obtained with 24 MW and 16 MW upstream the fire are 15 °C higher and lower than the reference case, 20 MW. While downstream the difference is greater, respectively about 30 °C higher and lower than the reference case. After 300 s the differences increase further and upstream the fire the temperatures obtained with 24 MW and 16 MW are respectively 60 °C higher and 30 °C lower than the reference case. Downstream the fire the temperatures are respectively 30 °C higher and lower than the reference case.

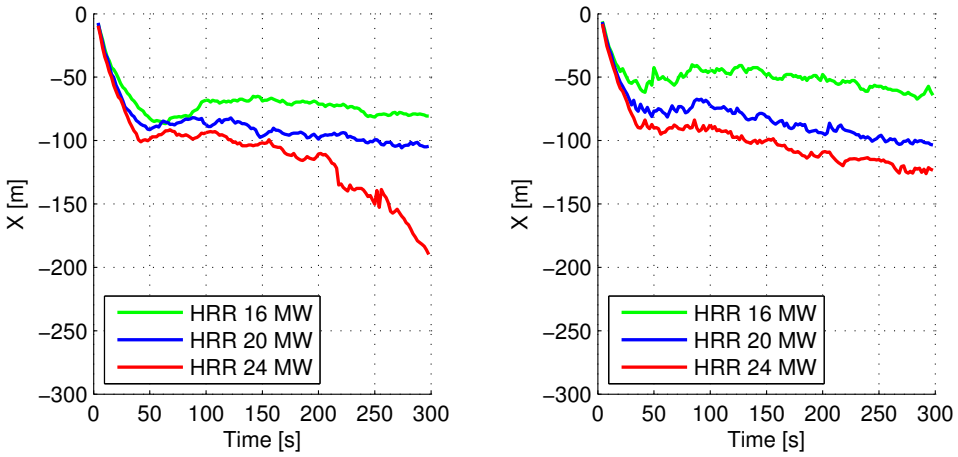

(A) Temperature 25 °C (B) Temperature 100 °C

FIGURE 3.30: Iso-temperature point traveling upstream the tunnel

The position of the smoke layer can be quantified monitoring the temperature along the tunnel beneath the ceiling, two different temperature levels have been monitored during the fire, 25 °C and 100 °C. The smoke travelling upstream the fire heats up the air and different fires have different backlayering lengths. From the figure 3.30 it is clear that higher HRR induces a longer backlayering length and the smoke flows faster against the ventilation flow. From figure 3.30a the temperature 25 °C is monitored and the difference between the curves increases in time. In particular for the stronger fire, 24 MW, the smoke travels upstream the fire in the last part of the simulation, while in the other to cases the smoke remains confined since the distance remains almost constant. Using the target temperature of 100

°C, figure 3.30a, the curves show a closer trend and the constant temperature point travels upstream the fire slower than the previous curves evaluated at 25 °C, figure 3.30a. The smoke backlayering length increases in time also in this case and the difference between the fires is always lower that 50 m. The present comparison shows that the HRR is a fundamental parameter for the simulation and the measured HRR curve is necessary for the correct simulation of the fire scenario. Using the nominal fire power, in this case 20 MW, there could be an overestimation of the backlayering length of several meters. Comparing the volume flows measured at the north portal after 300 s it is possible to estimate the influence of the fire through the throttling effect. For the nominal fire power 20 MW the volume flow is 88.9 m^3/s for the smaller fire 16 MW the volume flow is 136.5 m^3/s (+53.5%) and for the larger fire 24 MW the volume flow is 21.7 m^3/s (-75.6%). The volume flow is strongly affected by the HRR and the error of 20% on the fire power doubles the error in the volume flow. The comparison of temperatures volume flows and smoke movement show that small errors in the HRR induce large errors in the ventilation scenario and that the measured HRR is a fundamental boundary condition for the simulation.

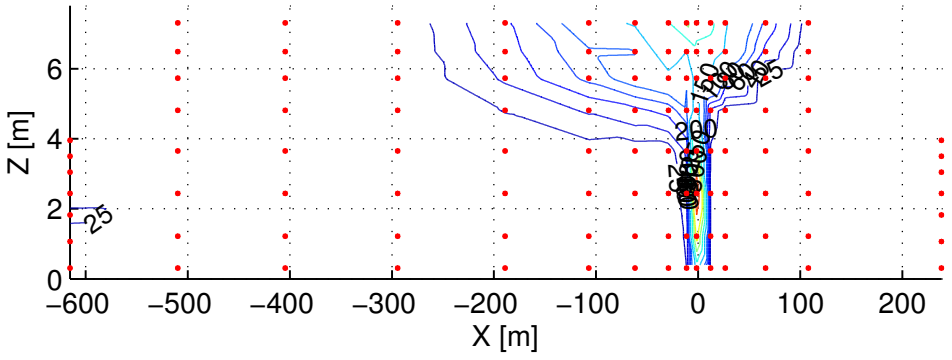

(A) Experiment

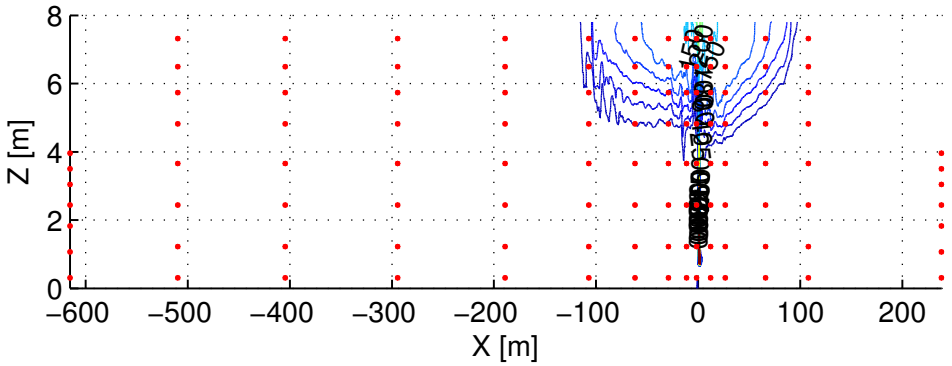

(B) FDS

FIGURE 3.31: Temperature field after 50 s

After the preliminary investigations which allow to evaluate the correct mesh size and the importance of using the correct HRR curve, the fire test 608 is simulated. First the temperature distributions along the tunnel are presented at different time steps. The experimental temperature field is obtained from the measurements at different stations along the tunnel on the

vertical middle plane. The positions of thermocouples used for the sampling are plotted in the temperature maps in order to provide an idea of the location of the measurement. The temperature measured after 50 s inside the tunnel are compared with the simulation in figure 3.31. At this moment the jet fans are still turned off and the fire is naturally ventilated, the spread of smoke in this case is faster in the experiment compared to the FDS simulation. In the experiment the smoke flows towards the north portal up to -256 m from the fire, while in the simulation just up to -114 m, referring to the iso-line at 25 °C. The reason of the discrepancy can be related to the atmospheric conditions, in FDS there is no wind at the portals while at the beginning of the experiment there is a longitudinal velocity from the south portal to the north portal, which enhance the flow of smoke upstream the fire.

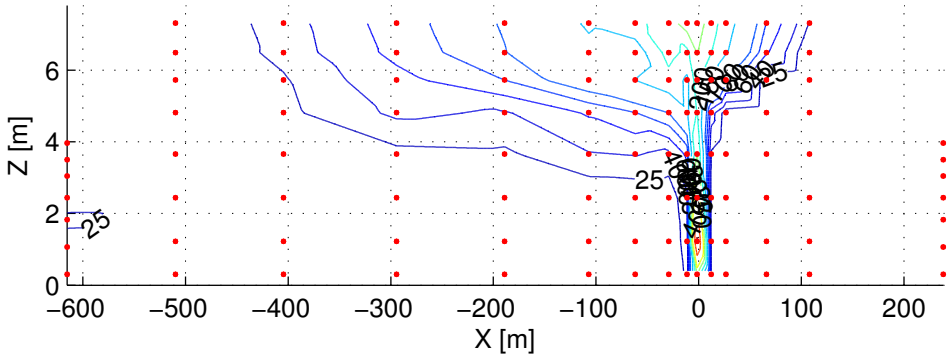

(A) Experiment

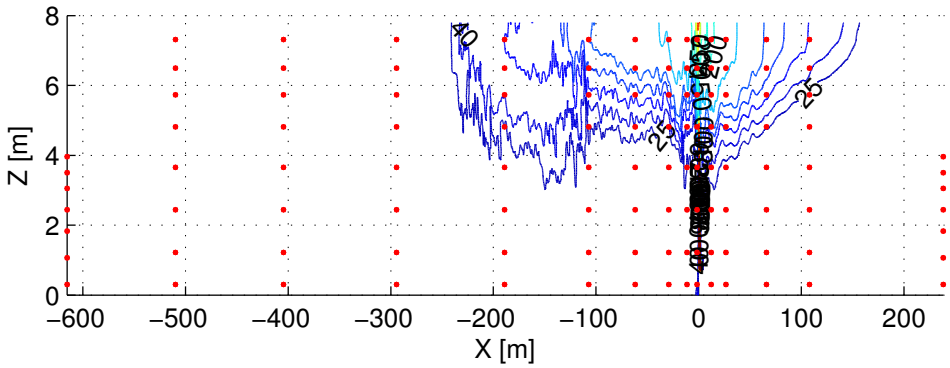

(B) FDS

FIGURE 3.32: Temperature contour after 110 s

The temperature in the tunnel are presented also after 110 s just before the jet fans' activation. At this moment the smoke should reach its maximum distance towards the north portal, because after the jet fans' activation the smoke starts to be confined. The temperature profiles also in this case show some discrepancies in the prediction of the backlayering lenght inside the tunnel. The smoke in the experiment is capable to flow upstream for a longer distance compared to the FDS simulation. In the experiment the smoke flows towards the north portal up to -429 m from the fire, while in the simulation just up to -245 m, referring to the iso-line at 25 °C.

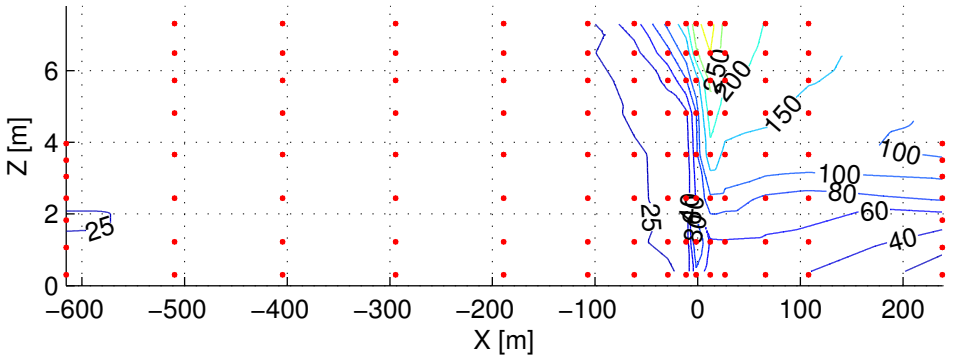

(A) Experiment

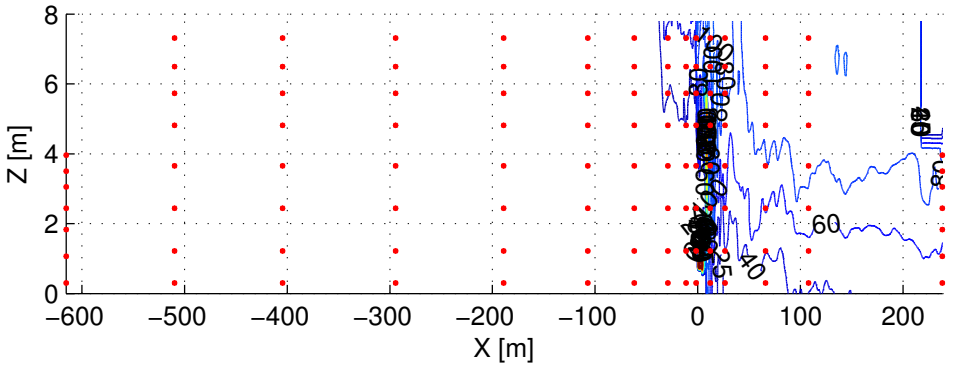

(B) FDS

FIGURE 3.33: Temperature contour after 290 s

After turning on the jet fans inside the tunnel the smoke stops flowing upstream the fire and start to be confined by the mechanical ventilation system. The comparison is done for quasi steady state conditions after 290 s. After the jet fans are activated the smoke is pushed towards the south portal and is confined in front of the fire. The temperatures in this case are in good agreement between the experiment and the simulation also the position of the smoke front is correctly predicted. Considering the smoke front at the temperature of 25 °C the front in the experiment is located at -95 m while in the simulation is closer to the fire at -36 m.

The last comparison is done after 590 s in order to evaluate the smoke confinement after about 10 minutes of fire under longitudinal ventilation, figure 3.34. The last comparison shows results similar to 3.33, the smoke is confined in front of the fire and the position of the smoke front as well as the temperature distribution obtained with FDS are in good agreement with the experiment. In the experiment the smoke is confined at -28 m from the fire, while in the simulation at -6 m.

The comparison of the temperatures obtained in the experiment and simulated in FDS shows that the model is correctly estimating the smoke confinement in case of fire when the conditions are steady. The error between the position of the smoke front is reducing during the simulation and in the last comparison the maximum difference is about 22 m. The smoke propagation when the ventilation is turned off is underestimated by FDS and the backlayering length is shorter. A possible cause of the discrepancy

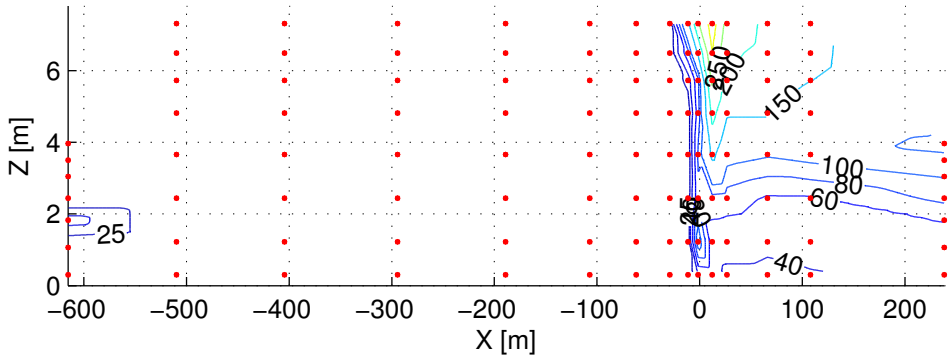

(A) Experiment

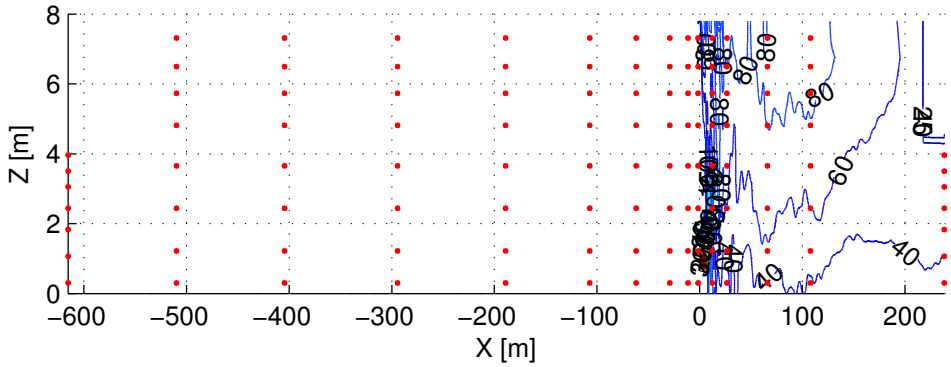

(B) FDS

FIGURE 3.34: Temperature contour after 590 s

between the model and the experiment can be the different pressure conditions at the portals which induce a longitudinal flow which is not modelled in the simulation.

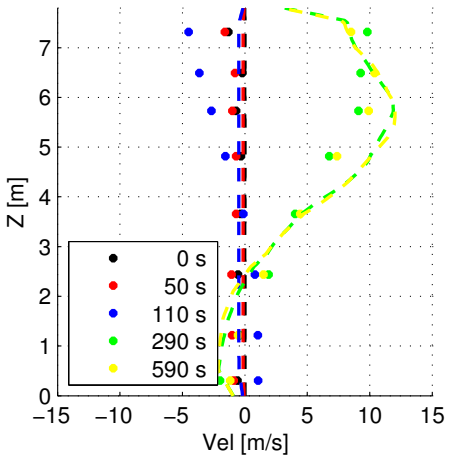

(A) Loop 209, X=-294.4 m

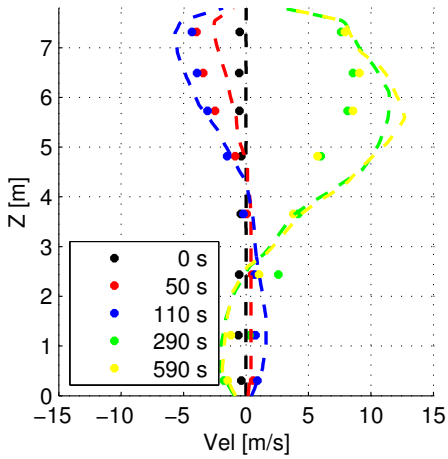

(B) Loop 207, X=-107.0 m

FIGURE 3.35: Comparison velocities upstream the fire

The goal of the validation is not only the analysis of the smoke confinement but also the validation of the velocity field. The velocities have been evaluated at different time steps and positions in order to assess if the modelling of the jet fan is reliable also in case of fire. The simulation's results are compared with the experiment at the time steps used before for the temperature comparison. In the velocity comparison also the initial conditions are plotted, after 0.0 s, showing the presence of a velocity from the south portal to the north portal. At the portals the initial velocity is 0.98 m/s so the smoke can flow faster towards the north portal. The velocities are compared at two sections upstream the fire, two near the fire and two downstream the fire.

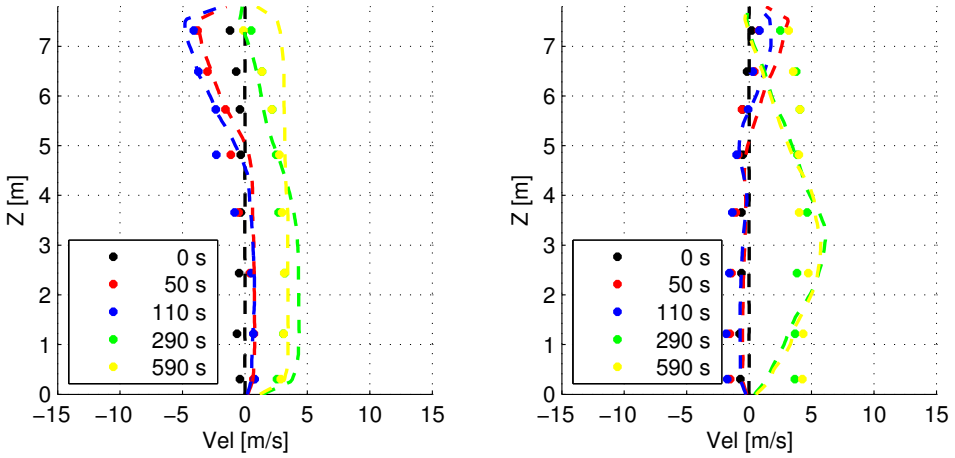

(A) Loop 304, X=-11.3 m (B) Loop 305, X=12.2 m

FIGURE 3.36: Comparison velocities near the fire

The velocities upstream the fire, at Loop 209 and at Loop 207, are presented in figure 3.35. The velocities are measured near the fans in order to depict the high speed flow downstream the fan, the Loop 209 is placed about 36 m downstream fan 8 and the loop 207 about 35 m downstream fan 14. The results obtained with FDS in the first stages of the simulation are smaller compared to the experiment. This is in agreement with the results seen about smoke confinement. When the fans are turned on the velocity and the shape of the jet obtained with FDS are similar to the experimental measurement. The velocity peaks predicted by the simulation are higher compared to the experiment, FDS overpredicts the velocity peak about 2.2 m/s at Loop 209 and about 4.2 m/s at Loop 207. The comparison of the profiles shows that FDS correctly simulate the shape of the jet downstream the fan. The velocity near the fire are compared at about 10 m from the fire upstream, Loop 304, and downstream, Loop 305, in figure 3.36. The velocities near the fire are more uniformed compared to the profiles upstream the fire 3.35. The velocity are generally lower but the agreement between the experiment and the simulation is good. The velocities at this location are close also in the initial stages of the simulation since this part of tunnel is immediately filled with smoke. For steady conditions the maximum error between FDS and measurement is 1.3 m/s at Loop 304 and 1.2 m/s at Loop 305. The last comparison is done for two positions downstream the

fire where the smoke and the fresh air are mixed together, figure 3.37.

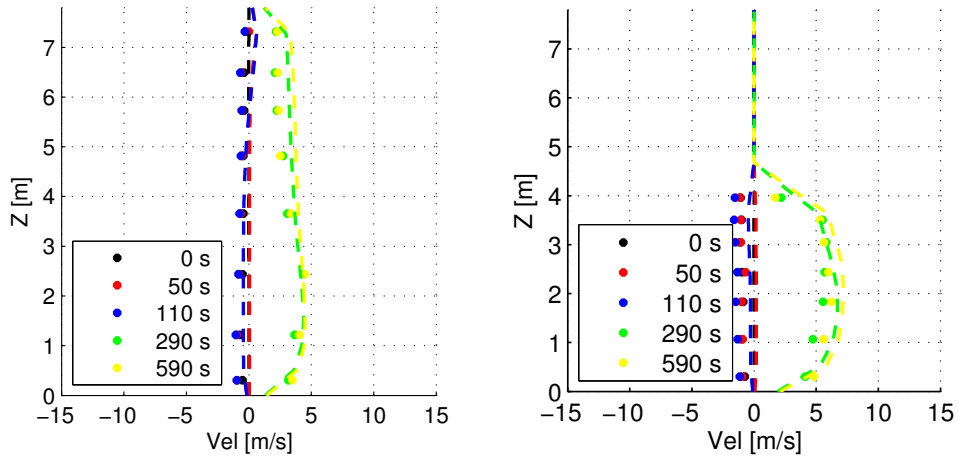

(A) Loop 301, X=107.9 m (B) Loop 202, X=238.4 m

FIGURE 3.37: Comparison velocities downstream the fire

The velocity downstream the fire are in good agreement for all the time intervals selected both at Loop 301 and at Loop 202, which is located at the downstream portal. For steady state conditions, the maximum error at these sections is smaller than 0.1 m/s at Loop 301 and equal to 1.2 m/s at Loop 202. The velocities in this region are more uniform than upstream the fire and this is consequence of the mixing of smoke and fresh air. In these sections FDS is capable to simulate the flows induced by the natural ventilation, in the first two time steps, and later to simulate the flow towards the south portal induced by the jet fans.

The comparison shows a good agreement in all the selected locations, in particular the velocity profiles at the south portal and near the fan are in good agreement with the experiment. The last comparison between experiment and simulation is done for the volume flow, as seen in the previous validation, in section 3.3, the average velocity along the tunnel is well predicted by FDS without fire. In case of fire the volume flow is reduced due to the throttling effect, the effect has been investigated with numerical simulations and experiments, but a comparison of experiment and simulations is still missing. The volume flows measured at different locations upstream and downstream the fire are presented as function of time in figure 3.38.

The volume flow is initially negative because of the flow of smoke from the south portal towards the north portal. The flow is driven by the atmospheric conditions at the portals and by the slope of the tunnel in the first phase. After the activation of the jet fans the air starts to flow from the north portal to the south portal. When the fire and the ventilation reach steady state conditions the volume flow also reaches an asymptotic value. In FDS the results show some fluctuations of volume flow, which are not so evident in the experiment, however as seen before the volume flow rate is highly influence by small variation of HHR. At the north portal after 590 s FDS slightly overpredicts the volume flow rate compared to the experiment, respectively 180 m^3/s and 135 m^3/s. The volume flows upstream and downstream the tunnel are smaller in the experiment compared to the

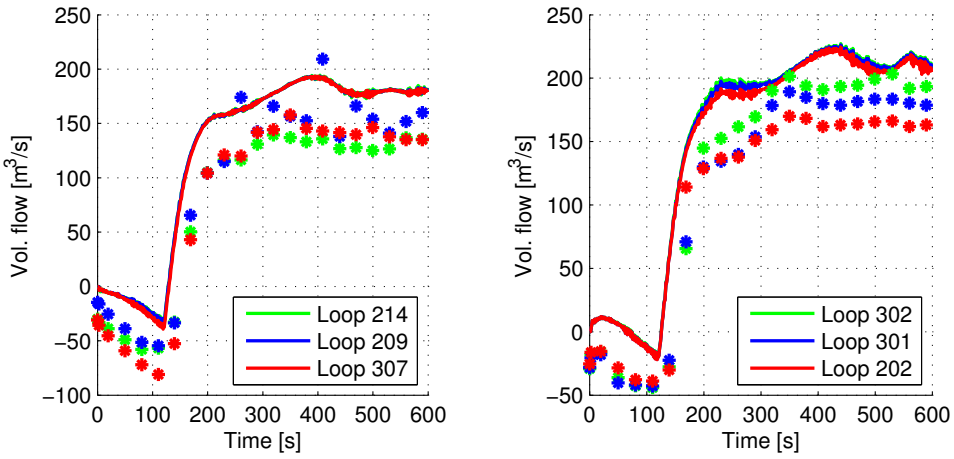

(A) Loop 301, X=107.9 m (B) Loop 202, X=238.4 m

FIGURE 3.38: Volume flows upstream and downstream the fire

simulation also in the initial phase. Therefore it is supposed that the wind, blowing from the south portal, reduces the volume flow during the whole simulation.

The comparison of several experiments with numerical simulation allows to assess the capability of FDS to simulate longitudinal ventilation devices both in cold flow and in case of fire. The model proposed here of a ducted jet simulated in FDS is capable to reproduce the velocity profiles, volume flows through the tunnel, pressure and temperatures. Moreover comparing the results obtained in sections 3.3 and 3.4 it is clear that FDS is capable to correctly simulate the throttling effect predicting the volume flow both with and without fire.

Chapter 4

Fire-Structure interaction

For the assessment and verification of the safety level of structures exposed to fire in the literature can be found several curves which reproduce the temperature history induced by a fire, figure 1.2a. Usually these curves are obtained from experiments where the structure is exposed to the worst case fire scenario, section 1.3.1. This approach allows for designing safe structures without relating the structural verification to the possible fire scenario. For a more realistic analysis it is necessary to go beyond such approach and provide thermal loads for the structural analysis directly related to the fire scenario. This can be done by resorting to experimental data, which are usually different from the case study, or resorting to numerical methods.

For the simulation of a fire several approaches are available, among them the most accurate, and computationally expensive, is CFD. This allows to solve numerically the flow field induced by the fire and to predict the thermal loads acting on the structure. These can be later used combined with the mechanical loads' distribution for the structural verification.

Initial attempts to perform coupled analysis with CFD and FEM for steel structures have been done by Zhang [121] and Silva [122–124] transferring the results obtained from the CFD simulation in a pure thermo-mechanical solver. Potentially, this approach can be used also for concrete structures, but it is necessary to consider more sophisticated models to describe the behaviour of the material [35, 41, 42] taking into account heat and mass transfer. For the simulation of concrete at high temperature the research code, Comes-HTC, developed at the University of Padua by Gawin, Pesavento and Schrefler [35, 42, 47–49] has been chosen because it allows to model concrete as partially saturated deformable porous material. The model has already been described in section 1.3.3, where the main equations of the model have been presented.

Two initial attempts to perform a structural analysis starting from a real fire scenario have been done in [125, 126], but through an uncoupled analysis in the first case and without taking into account the radiation and the mass exchange with the environment in the second work. Due to the lacks of the fire modelling in the previous approaches, it is necessary to develop, a new tool able to consider all the most relevant phenomena involved. In particular, for the structural analysis a set of boundary conditions is imposed for heat and mass transfer starting from the CFD simulation.

4.1 Coupling FDS with Comes-HTC

In this section a coupled approach is presented for the analysis of concrete structures at high temperatures. Fluid and structural simulations can be

coupled together with two strategies: one way coupling (i.e. weak coupling) and two way coupling (i.e. strong coupling).

With a one way approach the results from the fluid dynamic simulation are transferred to the structural calculation as new boundary conditions. But the results obtained with the structural calculation are not transferred to fluid dynamic calculation as new boundary conditions. With this approach the calculation is not iterated and the structural analysis can be done at the end of the fire simulation. The one way coupling neglects the influence of different modelling of the structure on the fluid simulation.

With a two ways coupling the results of the structural simulation transferred to the fluid dynamic calculation as new boundary conditions. The flow field is simulated again and the new results are transferred to the structure with a loop calculation, until the coupled simulation converges. This approach is obviously more accurate than the simple one way coupling, but it requires to iterate the calculation and to exchange the boundary conditions between fluid dynamic and structural analysis several times, increasing the complexity and the time of the calculation. This complex approach can be necessary in case the results of the structural analysis strongly affect the fluid dynamic simulation, therefore the fluid dynamic simulation need to be updated with new boundary conditions.

To better understand the difference between one way and two way coupling for thermal problems, in figure 4.1 fluid dynamic and structural analysis are linked together with the two approaches.

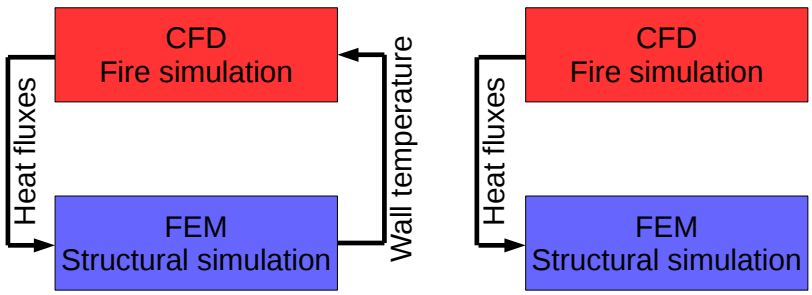

FIGURE 4.1: Coupling strategies: two way coupling and one way coupling

For fire structure interaction problems the two way coupling is required mainly in the following cases:

- Large deformations which significantly modify the fire scenario and the geometry of the structure around the fire.
- Complex temperature distributions in the solid which cannot be obtained with the CFD code and which later affect the flow field near the fire.

In case of concrete the displacement of the structure are usually small and the fluid domain is not affected by the structure's deformations, unless to

model the collapse of the structure or massive spalling. In case of more flexible structures, such as steel structures, the geometry can significantly change due to the fire and the fire scenario must be changed accordingly in order to consider the large deformations. In CFD models and in particular with FDS the heat transfer through the wall is calculated in a simplified way. The heat transfer model is one dimensional and pure conductive, so the heat flux can cross the wall, but not spread tangentially. This approximation can be a strong limitation in case of highly conductive bodies, but for more insulating materials it may be acceptable.

For the coupling of FDS with the structural FEM code Comes-HTC a one way coupling strategy has been chosen. This approximation was necessary because of the numerical issues related with the interfacing of different meshes used in the two codes, but also because of the small deformations and good insulation of concrete structures. The two way coupling is also discussed in section 4.5 for one specific case where the different meshes can be directly linked together.

The CFD calculation provides a set of boundary conditions, necessary for the FEM simulation, directly related to the specific fire scenario. Comes-HTC involves both heat and mass transfer in a deformable medium, therefore it requires four boundary conditions for the problem closure.

- Pressure of air or mass flow of dry air for the mass conservation of dry air.
- Pressure of water vapour or mass flow of water for the mass conservation of water.
- Temperature or heat flux for the enthalpy balance.
- Displacement or force for momentum balance.

The pressure of the dry air is assumed to be constant on the structure's surface because in case of fire, excluding explosions, there are no significant pressure fluctuations which could affect the structural calculation. In case of fire the pressure of the gas inside the material, water and dry air, can rise up to 1 MPa or more depending on the concrete and on the heating [38, 39] so fluctuations of few Pa in the fluid domain can be neglected in the calculation.

The water vapour inside the fire region is depending on the humidity of the ambient and on the process of combustion. A generic combustion reaction can be written as:

$$C_x H_y O_z + \nu_{O_2} O_2 \rightarrow \nu_{CO_2} CO_2 + \nu_{H_2O} H_2O + \nu_{CO} CO + \nu_S Soot \qquad (4.1)$$

Among the others, the combustion produces water vapour therefore the density of water vapour in not constant on the structure's surface. The water is tracked in the FDS simulation and evaluated near the wall in order to provide a map of water vapour density.

The incident heat flux induced by fire is not uniform on the structure and it depends on the geometry and on the fire scenario. The heat fluxes obtained with the FDS simulation draw a map in space and time which is imposed as boundary condition to the structural analysis.

The mechanical loads, excluding explosion in case of fire, are not calculated starting from the CFD simulation, since the pressure variation in

the tunnel are not significant for the structure deformation. The mechanical loads should be defined in case of tunnels basing on the soil or rock conditions near the tunnel. In case of other structures the mechanical loads are usually calculated basing on the specific problem, but usually not related to the fire scenario.

For the coupled analysis the boundary conditions, based on the FDS simulation, are the heat flux on the structure and the mass flux of water vapour. Robin type (third type) boundary conditions are imposed in order to consider both the input coming from the CFD simulation and the output coming from the structural analysis. For the heat flux calculation the net heat flux between solid and fluid is calculated as:

$$\dot{q}'' = \dot{q}''_{in} - \dot{q}''_{out} = \varepsilon(\dot{q}''_{inc,rad} - \sigma T_w^4) + h(T_g - T_w) \tag{4.2}$$

where the $\dot{q}''_{inc,rad}$ is the incident radiative heat flux, T_w is the wall's temperature T_g is the gas temperature, h is the convective heat transfer coefficient and ε is the surface emissivity. The incoming heat flux is mainly dependent on the flow field near the fire, while the wall temperature are depending both on the structure and on the fluid conditions. In order to define a Robin boundary condition the incident heat flux is calculated with FDS and the wall temperature is calculated in Comes-HTC. The incident flux acting on the generic point of the structure can be calculated as:

$$\dot{q}''_{in} = \varepsilon \dot{q}''_{inc,rad} + h(T_g) \tag{4.3}$$

The calculation of the incident flux can be obtained in a simplified way using the concept of Adiabatic Surface Temperature, AST, proposed by Wickström in [127]. This quantity is one of the output of FDS and it can be calculated based on the equation:

$$\varepsilon \dot{q}''_{inc,rad} + h(T_g) = \varepsilon \sigma T_{AST}^4 + h T_{AST} \tag{4.4}$$

The incident heat flux and the convective heat transfer coefficients h are calculated in FDS simulations and they are imposed with a Robin type boundary condition as in equation 4.2.

For the water vapour mass transfer a similar approach is proposed in order to impose a mass transfer distribution which is not uniform on the surface. A Robin type boundary condition is implemented and the mass flux of water on the surface of the concrete can be written as:

$$\dot{m}_{H_2O} = \beta(\rho_{H_2O,g} - \rho_{H_2O,w}) \tag{4.5}$$

where β is the mass transfer coefficient, $\rho_{H_2O,g}$ $\rho_{H_2O,w}$ are the water vapour densities in the gas near the surface and on the surface of the structure. The water vapour density near the surface is evaluated with FDS, while the water vapour density on the wall is calculated in Comes-HTC. Once the incoming heat flux, the convective heat transfer coefficient and the water vapour densities are evaluated on the elements of FDS these quantities need to be transferred to the structural calculation.

The coupled approach has been applied to different structures exposed to fire. Concrete slab exposed to fire is studied in order to understand the effect of different fire scenarios on the response of the structure, figure 4.2a,

while tunnel vault is studied in order to evaluate the response of the structure in case of a rail coach on fire, figure 4.2b.

(A) Concrete slab

(B) Tunnel

FIGURE 4.2: Structures exposed to fire studied with the coupled approach

The geometry of the structure is important for the coupling due to the different meshing strategies in FDS and Comes-HTC. Rectangular geometries are correctly represented in FDS and Comes-HTC, like a slab, while FDS is not capable to draw rounded surfaces, like tunnels.

4.1.1 Mesh interfacing

The main issue encountered in the coupling of FDS with Comes-HTC is the interfacing of different grid strategies. In FDS the Cartesian mesh doesn't allow to draw rounded surfaces, but these are approximated with several square elements, figure 4.3. Therefore the orientations of the square elements in the FDS model are different from the orientations of the elements in Comes-HTC, as well the areas of the structure exposed to the fire are different. In case of a rounded surface, such as a tunnel vault, in FDS the area exposed to fire is equal to the area of the rectangle circumscribed around. In a circular tunnel with exposed surface of $2\pi \times R$ the corresponding exposed surface in FDS is $8 \times R$. The coupling procedure is designed to transfer the integral incident flux calculated in FDS to the structure, without creating sinks or sources of energy. Because of the geometric approximations the specific heat fluxes might show some discrepancies between the programs.

The coupling between the FDS and Comes-HTC is done for two dimensional geometries, the boundary conditions are transferred from CFD to FEM only along one tiny line of elements, figure 4.3. The two dimensional approach for the simulation of concrete structure, such tunnels, has been already proposed in previous works [125, 128] therefore it has been considered reliable.

The problem of interfacing FDS with a FEM code has been already tackled by different authors Paajanen et al. in [129] and by Silva in [122, 123]. These authors combined together the AST obtained in FDS and the resulting value was later used in the FEM simulation. In this work a slightly different approach is chosen since Comes-HTC requires heat fluxes rather than temperatures as boundary condition. The incident heat fluxes are first

calculated for every solid cell in FDS based on the equations 4.4 4.3.

$$\dot{q}''_{in} = \varepsilon \dot{q}''_{inc,rad} + h(T_g) = \varepsilon \sigma T^4_{AST} + hT_{AST} \tag{4.6}$$

In order to evaluate the incoming heat flux $\dot{q}''_{in}$ the AST and the convective heat transfer coefficient h are exported from FDS. Once the incoming heat fluxes draw a spatial map which is function of position and time these can be combined together in order to define the boundary condition for the FEM calculation.

The idea behind the coupling strategy is to transfer the whole energy produced in FDS to the structure and to generate the smallest error in the flux distribution. Given a generic node of Comes-HTC on the surface the incoming heat flux must be calculated using the heat fluxes of the nodes that are close to this. The elements of FDS are selected based on their position and on their orientation. The idea is to combine together elements which are close to the target node and to build an artificial element whose orientation is similar to the orientation of the target node.

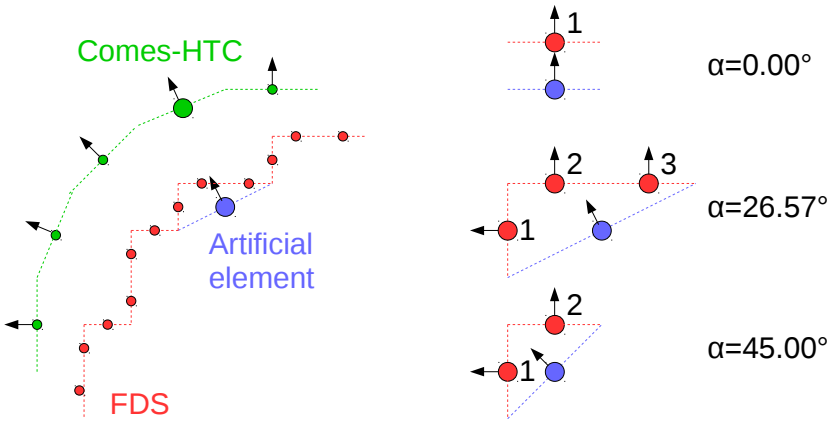

FIGURE 4.3: Mesh interfacing approach proposed for the coupling of FDS and Comes-HTC

As seen in figure 4.3 the node of Comes-HTC is linked to an artificial element which has a similar orientation and which is made by three other elements differently oriented. The incoming heat flux on the Comes-HTC node $\dot{q}''_{in,art,Comes-HTC}$ is equal to incoming heat flux on the corresponding artificial element $\dot{q}''_{in,art,FDS}$. The coupling allows to create an artificial element which is made by other FDS elements. The heat flux crossing the face of the artificial element is equal the sum of the fluxes of the single elements. The specific heat flux evaluated on the artificial element built in FDS can be calculated with an energy balance equation:

$$\dot{q}''_{in,art} A_{art} = \frac{1}{n_{sel}} \sum_{el=1}^{n_{sel}} \left(\dot{q}''_{in,el} A_{el} \right) \tag{4.7}$$

where the A_{art} is the area of the artificial element, A_{el} is the area of the element in FDS $\dot{q}''_{in,art}$ is the resulting heat flux on the artificial element while $\dot{q}''_{in,el}$ is the heat flux on the FDS element.

Given a generally oriented node in Comes-HTC several elements have to be combined together in order to rebuild an artificial element whose orientation is the same of the target node. The large number of elements might require to consider elements far from the target point and this precludes from having a local information, unless many small elements are used. Therefore the orientation of the nodes in Comes-HTC needs to be approximated to some reference values. The angle selected for the orientation's approximation in Comes-HTC are reported in the table 4.1

TABLE 4.1: Angles used for the approximation of the orientation of the nodes in Comes-HTC

Angle (α)	0.00 °	26.57 °	45.00 °	63.43 °	90.00 °
Min. El.	1	3	2	3	2
Tan(α)	0.0	0.5	1.0	2.0	∞

These angles are selected because they allow to use few elements in FDS to rebuild an artificial element with the selected orientation. The maximum number of elements required to rebuild the target orientation is three and this allows to keep a local information about the heat flux distribution.

In order to show how the angles selected can be rebuilt with the FDS elements we consider a mesh in FDS with cubic elements, or at least with square elements on the cross section that is later coupled with Comes-HTC. If the elements are square these, combined together, draw an artificial element with a specified orientation, the heat fluxes that pass though the elements selected are summed together and passed to the artificial element. Equation 4.7 can be simplified if the areas of the FDS elements and of the artificial one are in constant ratio among them.

$$\dot{q}''_{in,art} = \frac{1}{A_{art}} \sum_{el=1}^{n_{sel}} \left(\dot{q}''_{in,el} A_{el} \right) \tag{4.8}$$

The equation 4.8 has also another meaning, the heat flux obtained on the artificial element is the sum of the projections of the heat fluxes on the single elements along the direction normal to the artificial element. This second interpretation of the equation 4.8 is later verified for some selected cases. For the different angles the equation 4.8 is simplified basing on the assumptions of square elements in FDS. Starting from the easiest case α equal to 0.00 ° and considering one FDS element the formula becomes:

$$\dot{q}''_{in,art} = \dot{q}''_{in,1} = \dot{q}''_{in,el} cos(0.00^\circ) \tag{4.9}$$

As expected the heat flux on the artificial node is corresponding to the heat flux on the element. The same is obtained for α equal to 90.00 °, therefore the case is not repeated. In case the element has an angle α equal to 26.57 ° three elements have to be selected to rebuild the geometry.

$$\dot{q}''_{in,art} = \frac{1}{\sqrt{5}} \left(\dot{q}''_{in,1} + \dot{q}''_{in,2} + \dot{q}''_{in,3} \right) = \dot{q}''_{in,1} sin(26.57^\circ) + \frac{(\dot{q}''_{in,2} + \dot{q}''_{in,3})}{2} cos(26.57^\circ) \tag{4.10}$$

The area of the artificial element is different from the sum of the areas of the single element, this is consequence of the non corresponding elements,

figure 4.3. The resulting heat flux obtained here is the sum of the projections of the heat fluxes along the normal direction to the artificial element. The same approach can be used for the angle α equal to 63.43 ° since two elements with the same orientation and one normal to them are selected. In case the element has an angle α equal to 45.00 ° two elements are selected to compose the artificial element.

$$\dot{q}''_{in,art} = \frac{1}{\sqrt{2}}\left(\dot{q}''_{in,1} + \dot{q}''_{in,2}\right) = \dot{q}''_{in,1} sin(45.00°) + \dot{q}''_{in,2} cos(45.00°) \tag{4.11}$$

Also in this case the sum of the area of the single elements is not equal to the area of the artificial element and this induce an higher specific heat flux on the artificial element. The combination of fluxes done in this way is different than a simple arithmetic average and this is done in order to transfer the integral incoming flux on the element in FDS also in the node of Comes-HTC. Using an arithmetic average to calculate the incident heat flux:

$$\dot{q}''_{in,art} A_{art} = A_{art} \sum_{el=1}^{n_{sel}} \left(\dot{q}''_{in,el}\right) \neq \sum_{el=1}^{n_{sel}} \left(\dot{q}''_{in,el} A_{el}\right) \tag{4.12}$$

Once the incoming heat flux $\dot{q}''_{in,art}$ is evaluated for the specific element this has the correct orientation, which is similar to the original orientation of the Comes-HTC node. The incoming heat flux can be associated to the node of Comes-HTC and later used as boundary condition for the structural calculation. The specific heat flux is imposed instead of the integral flux because the node of Comes-HTC and the artificial elements don't have the same area.

$$\dot{q}''_{in,Comes-HTC} = \dot{q}''_{in,Art} \tag{4.13}$$

In case the FDS elements are smaller than the area associated with the Comes-HTC node, more elements should be selected in order to not neglect their contribution to the node. Usually the elements selected in FDS are those within a certain distance from the target node. The reference distance used to select the elements of FDS is equal to half of the distance between the target node and the one next to it. Therefore if more elements are selected, the procedure of fluxes combination needs to be repeated on for all the elements within the reference distance. In figure 4.4 three examples are shown for the element selection. Considering in blue the node of Comes-HTC and in red the elements of FDS selected, in the first case there are only elements within the reference distance. In the others more elements are selected in order to take into account all the contributions of the heat fluxes.

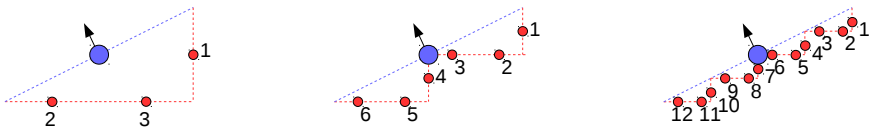

FIGURE 4.4: Element selection in case of small FDS elements

This approach has been used for the incident heat flux, but this is not the

only quantity exchanged between FDS and Comes-HTC, also the convective heat transfer coefficient and the density of water vapour are transferred as new boundary conditions. The heat transfer coefficient is calculated in FDS using equation 2.14 and it is function of the local temperature and of the local Reynolds number. Since the convective heat transfer coefficient is a scalar value it shouldn't be treated as the heat flux, vector, and the coefficient on the artificial element can be calculated with a simple arithmetic average:

$$h_{art} = \frac{1}{n_{sel}} \sum_{el=1}^{n_{sel}} (h_{el}) \tag{4.14}$$

There is obviously an error in the calculation of the average due to the different gas temperatures and different velocities, but this approximation is acceptable because the convective heat transfer has a small contribution in the high temperature problems. In the calculation of the net heat flux, equation 4.2, the convective heat transfer coefficient obtained with FDS is only used to evaluate the outcoming convective heat flux. Moreover velocities and gas temperatures in cells close to each other are usually similar, while the incident heat fluxes can be really different due to the contribution of the radiation. Elements with different orientations and view factors can have different incoming heat fluxes, even if they are next to each other.

The same approach proposed for the convective heat transfer coefficient is used for the water vapour density calculation. The water vapour density on the artificial element is evaluated with an arithmetic average of the values close to it. This is possible because from FDS there is no mass transfer through the walls so it is not possible to make a mass balance as done for the heat flux.

$$\rho_{H_2O,g,art} = \frac{1}{n_{sel}} \sum_{el=1}^{n_{sel}} (\rho_{H_2O,g,el}) \tag{4.15}$$

The last result transferred from FDS to Comes-HTC is the mass transfer coefficient β. This is calculated basing on the convective heat transfer coefficient through the equation:

$$\beta = \frac{h}{Le} \tag{4.16}$$

Where Le is the Lewis number and it is assumed 1000 for water vapour [58]. The approach presented in this section needs to be verified with different numerical tests before being used for practical problems.

In table 4.2 the resulting heat flux obtained on the artificial element and the other scalar quantities, convective heat transfer coefficient, water vapour density are calculated for the different orientations.

TABLE 4.2: Resulting quantities for vector and scalar quantities obtained for different orientations

Angle (α)	0.00 °	26.57 °	45.00 °	63.43 °	90.00 °
$\dot{q}''_{in,art}$	$\dot{q}''_{in,1}$	$\frac{\sum_{el=1}^{3}(\dot{q}''_{in,el})}{\sqrt{5}}$	$\frac{\sum_{el=1}^{2}(\dot{q}''_{in,el})}{\sqrt{2}}$	$\frac{\sum_{el=1}^{3}(\dot{q}''_{in,el})}{\sqrt{5}}$	$\dot{q}''_{in,1}$
h_{art}	h_1	$\frac{\sum_{el=1}^{3}(h_{el})}{3}$	$\frac{\sum_{el=1}^{2}(h_{el})}{2}$	$\frac{\sum_{el=1}^{3}(h_{el})}{3}$	h_1
$\rho_{H_2O,art}$	$\rho_{H_2O,1}$	$\frac{\sum_{el=1}^{3}(\rho_{H_2O,el})}{3}$	$\frac{\sum_{el=1}^{2}(\rho_{H_2O,el})}{2}$	$\frac{\sum_{el=1}^{3}(\rho_{H_2O,el})}{3}$	$\rho_{H_2O,1}$

4.2 Coupling verification

In order to verify if the process of coupling proposed in section 4.1.1 is correct there is the need to perform some verification tests. These are mainly performed in FDS and don't involve directly the Comes-HTC calculation. The cases presented hereafter are mainly focused on the incident heat flux and on the integral heat flux. These examples presented don't involve complex structures or flux distributions, rather they are simple in order to understand the results and the capabilities of the interpolation process.

4.2.1 Cylinder with burner

The first verification test is a cylinder with a burner placed in the centre, the case is selected since it should provide an axis-symmetric fire load and the incoming heat fluxes should be uniform along the tangential direction, figure 4.5a.

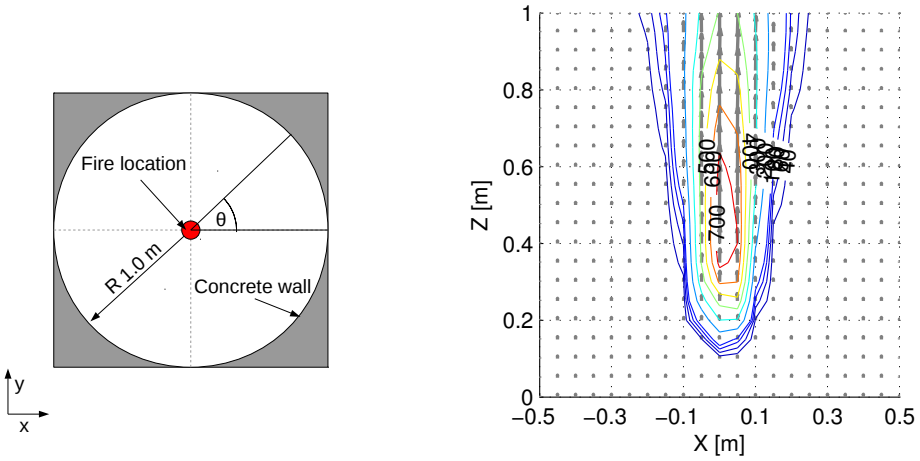

(A) Cylinder view (B) Flow field

FIGURE 4.5: First verification case, cylinder with axis-symmetric fire

The cylinder is 1 m high and with 1 m of diameter, the walls are modelled as conductive surfaces and the material is concrete. The properties of the material are set according to the Eurocode 2 [130]. The cylindrical vessel has a fire with a HRR of 55 kW, the burner is placed in the centre or the circular section at 0.2 m from the bottom. The top and bottom surfaces of the domain are open in order to allow the air to flow across the cylinder. In order to show the effect of the grid size on the coupling, two grids are used in FDS, mesh 1 has cubic elements with element's size 0.05 m, while mesh 2 has cubic elements with element's size 0.025 m, table 4.3. The grids used for the structural part is a concrete ring with equally spaced elements in the tangential direction, the distance between the two adjacent nodes is 0.0980 m. The coupling between FDS and Comes-HTC is evaluated along the cylinder at 0.5 m from the bottom.

Using mesh 1 the heat fluxes are presented as function of time in figure 4.6. The heat fluxes at different angular positions in FDS are presented in figure 4.6a showing that the distribution is not uniform on the walls. For

TABLE 4.3: Mesh data

Mesh	El. size jet-zone [m] (x,y,z)	N. El.
Mesh 1	$0.050 \times 0.050 \times 0.050$	8000
Mesh 2	$0.025 \times 0.025 \times 0.025$	64000

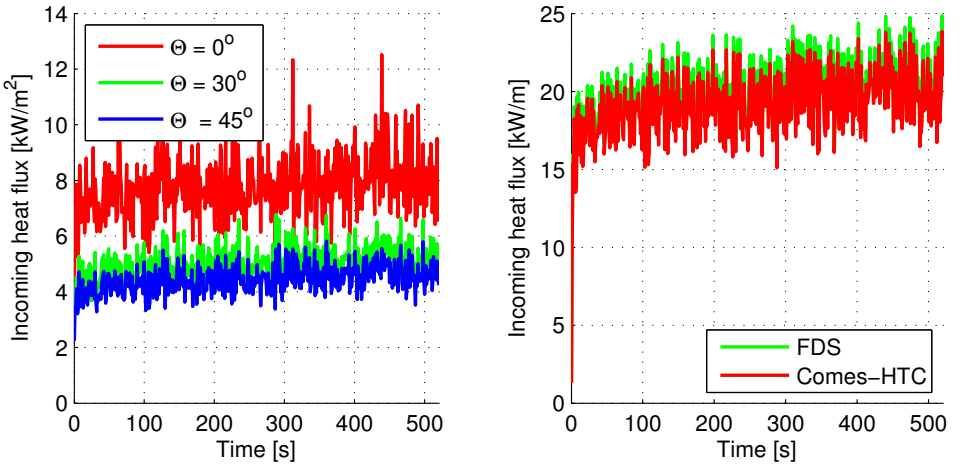

(A) Fluxes in FDS at different angular positions

(B) Integral flux in FDS and Comes-HTC

FIGURE 4.6: Comparison of incoming heat fluxes in FDS, mesh 1, and in Comes-HTC

angle θ equal to 0.0° the incident flux is higher than for the other two angles and this is consequence of the different surface orientations. After the interpolation process the integral heat fluxes $\dot{q}$ are presented as function of time both for FDS and Comes-HTC, figure 4.6b, these are calculated as:

$$\dot{q} = \sum_{el=1}^{tot_{el}} \left(\dot{q}''_{in,el} A_{el} \right) \tag{4.17}$$

where the sum of the heat fluxes is extended to the whole surface on which the data are exchanged. The two curves are overlapping on each other and this ensures that the interpolation process proposed before is capable to transfer the power produced in FDS to Comes-HTC. After comparing the integral flux, the angular distribution of heat fluxes is presented for steady state conditions, figure 4.7. The incident fluxes are averaged in time in order to present them as function of the position. In FDS the incident heat flux distribution shows many peaks and an highly irregular trend, consequence of the different view factors of the orthogonal elements, figure 4.7a. The heat flux distribution after the interpolation process is more smooth and damps the scattered fluxes coming from FDS. Figure 4.7b shows the distribution of heat fluxes as function of the angular position. The distribution is not axis-symmetric because the heat fluxes are higher near θ equal to 0°, 90°, 180° and 270°. However the distribution after the interpolation process is smoother than the original one coming from FDS.

The second verification has been carried out for the same case with mesh 2. The heat fluxes obtained with the new mesh are similar those found

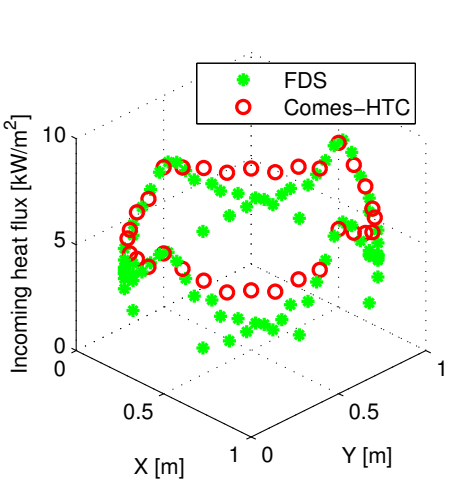

(A) Spatial flux distribution

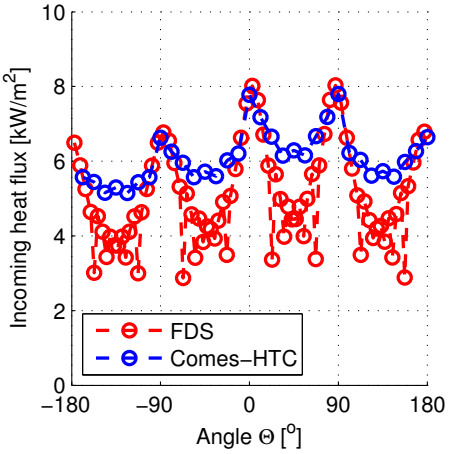

(B) Fluxes as function of the angular position

FIGURE 4.7: Comparison of the heat flux distribution between Comes-HTC and FDS, mesh 1

with the coarse one, figure 4.8. The heat fluxes in figure 4.8a have the same order of magnitude of those in figure 4.6a, as well the incident flux is higher for θ equal to 0° compared to the fluxes with θ equal to 30° or 45°. The integral heat flux transferred from FDS to Comes-HTC are in good agreement between the two codes therefore no energy is lost in the interfacing process.

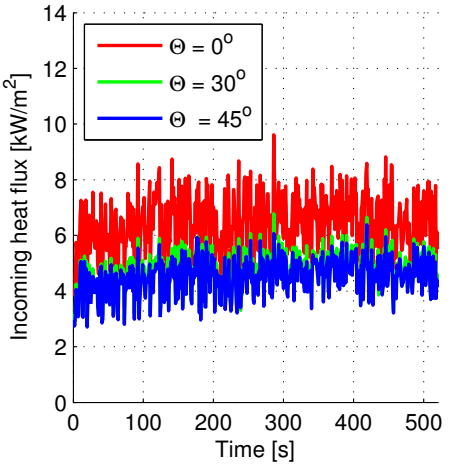

(A) Fluxes in FDS at different angular positions

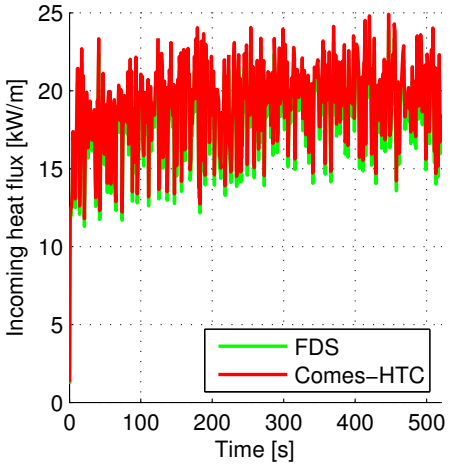

(B) Integral flux in FDS and Comes-HTC

FIGURE 4.8: Comparison of incoming heat fluxes in FDS, mesh 2, and in Comes-HTC

The most interesting results obtained with the mesh refinement comes from the heat flux distribution obtained after the interpolation process, figure 4.8. Comparing the heat fluxes obtained with mesh 2 and those obtained with mesh 1 it is clear that the first is capable to damp the fluctuation of the fluxes coming from FDS visibly better than the second one. In figure

4.9b the incident heat fluxes after the interpolation process have a smooth distribution along the angular direction and the fluxes are axis-symmetric as expected for this case.

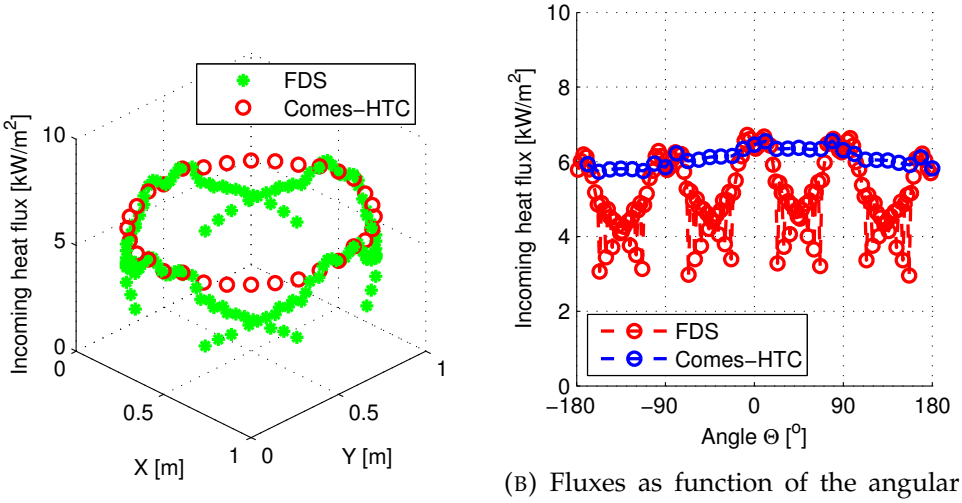

(A) Spatial flux distribution

(B) Fluxes as function of the angular position

FIGURE 4.9: Comparison of the heat flux distribution between Comes-HTC and FDS, mesh 2

This first comparison shows that regardless the meshing strategy the integral heat flux $\dot{q}$ is correctly transferred from FDS to Comes-HTC. The energy conservation is the necessary parameter to avoid non physical results with the creation of sources and sinks of energy. The comparison shows also that the finer mesh can smooth much better the irregular results obtained with FDS. This is important also in practical problems since for a correct interfacing of FDS and Comes-HTC large grids should be avoided in order to prevent irregular heat flux distributions.

In order to verify if the angles selected for the discretization of the nodes' orientation are sufficient, a test has been done adding two other angles which require some more elements for the construction of the artificial element. The angles are 71.57°, atan(3), and 18.43°, atan(1/3), the heat fluxes for the artificial element can be calculated combining three parallel elements and one normal to them. The equation for the resulting heat flux calculated for the angle θ equal to 18.43° is:

$$\dot{q}''_{in,art} = \frac{1}{\sqrt{10}}\left(\dot{q}''_{in,1} + \dot{q}''_{in,2} + \dot{q}''_{in,3} + \dot{q}''_{in,4}\right) = \\ = \dot{q}''_{in,1} sin(18.43°) + \frac{(\dot{q}''_{in,2} + \dot{q}''_{in,3} + \dot{q}''_{in,4})}{3} cos(18.43°) \quad (4.18)$$

The same approach can be used for the angle θ equal to 71.57°. The angular distribution of the heat fluxes is presented for the two meshes in figure 4.10. The comparison is done only for the heat fluxes in Comes-HTC, since the fluxes in FDS remain the same. The effect of the new angles is evident only near the peak of flux, where θ is close to 71.57°+k 90° or 18.43°+k 90°, out of these regions the distribution of flux remains unchanged. For the

two meshes the new angles increase the incident fluxes near 71.57°+k 90° and 18.43°+k 90°, but there isn't an evident improvement of the heat flux distribution. In particular for mesh 2, figure 4.10b, the distribution quality deteriorates, while for mesh 1 there is no evident improvement. The comparison ensures that the number of angles selected and reported in table 4.1 is sufficient for the correct interpolation of the fluxes obtained in FDS.

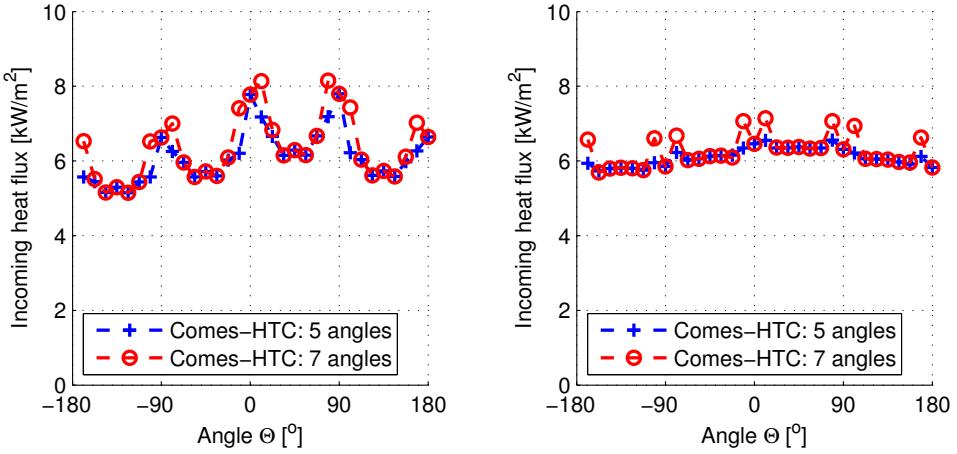

(A) Mesh 1 (B) Mesh 2

FIGURE 4.10: Evaluation of the effect of the angular discretization

After the comparison of the heat fluxes the convective heat transfer coefficient is also presented as function of the tangential angle for the two mesh presented before. The heat transfer coefficient as the density of water vapour are interpolated using equations 4.14, 4.16. In figure 4.11a the results of mesh 1 are presented, the convective heat transfer coefficient shows some fluctuations but follows the trend of the FDS calculation. With the mesh 2, figure 4.11a, the fluctuations from the FDS calculation are smaller and after the interpolation process the peaks of convective heat transfer coefficient are smoothed.

The comparison of the convective heat transfer coefficients shows that the approach is reliable and induces small errors in the calculation. It is important to stress that the heat transfer coefficient is only used to calculate the convective part of the outcoming heat flux in equation 4.2. In this verification example the axis-symmetric distribution of heat was expected because of the geometry and of the fire source placed in the centre of the vessel. The results show that with a refined mesh it is possible to obtain a result close to the theoretical model, which allows both to transfer the integral heat flux from FDS to the structure as well to provide an uniform heat flux distribution along the tangential direction.

4.2.2 Vertical wall exposed to fire

The second verification case is a vertical wall exposed to fire, the wall is tilted with different angles keeping a constant distance between this and the centre of the fire, figure 4.12a. Theoretically the heat flux impinging the wall is not affected by the orientation of the wall, if the distance is not

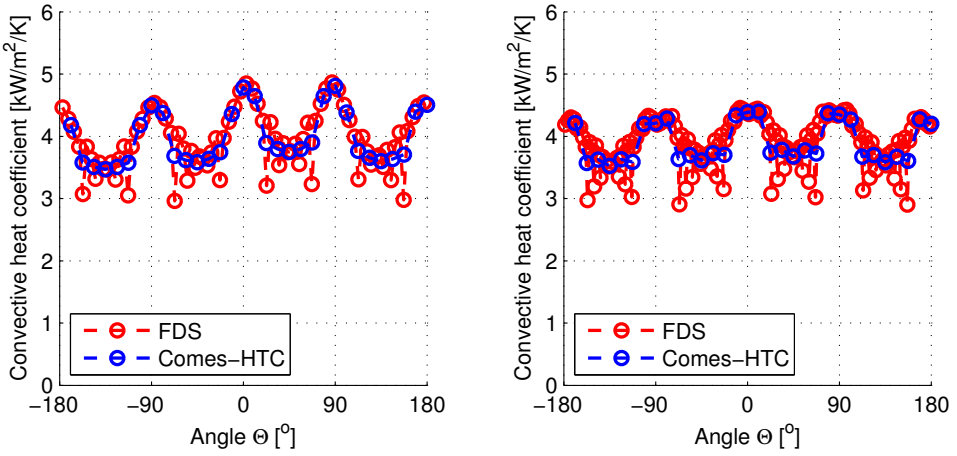

(A) Mesh 1 (B) Mesh 2

FIGURE 4.11: Convective heat transfer coefficient along the cylinder

changed. The vertical wall is placed at 0.5 m from the centre of the fire with different orientations. First the wall is placed parallel to the FDS grid setting the reference angle to 0.00 °. The wall is later reoriented starting from the reference position with a new angle of 26.57 ° and later reoriented again with an angle of 45.00 °. The fire is produced by a burner with radius 0.2 m and with a constant HRR of 280 kW using n-heptane as fuel. The simulated domain is 2 m high and 3 m deep and wide, this allows the fire to develop freely and to not be strongly affected by the boundary conditions, figure 4.12a. The mesh used for the discetization of the domain is the same in the different cases using cubic elements with 0.05 m size. The flow field along the plane parallel to the y axis and crossing the fire is presented in figure 4.12b, in order to show the flow field near the fire and the wall. The flame is burning next to the wall and the gas temperature on the wall is about 200 °C, while in the core of the flame it rises up to 800 °C.

Incident heat fluxes, convective heat transfer coefficient and water vapour density are compared for the three different orientations using the equations reported in table 4.2. Before comparing the thermal loads on the walls, the gas temperature along the centreline of the fire are compared for the three wall's orientations, theoretically since the distance between fire and wall are the same the temperature curves should overlap. Figure 4.13a shows that there are some discrepancies between the different cases along the flame height, the flame with θ equal to 0° overpredicts the temperatures compared to the other two cases with different orientations. However the maximum temperature along the flame is correctly simulated by the three cases.

After comparing the flow field the integral incoming fluxes are compared for the different wall's orientations. The orientation of the plane shouldn't affect the energy dissipated through the wall therefore in figure 4.13b the time history of the integral flux is presented for different cases. The heat flux is calculated on a reduced area in order to avoid the influence of the boundary conditions. The integral flux is calculated for the elements that are closer than 1.0 m from the point with minimum distance

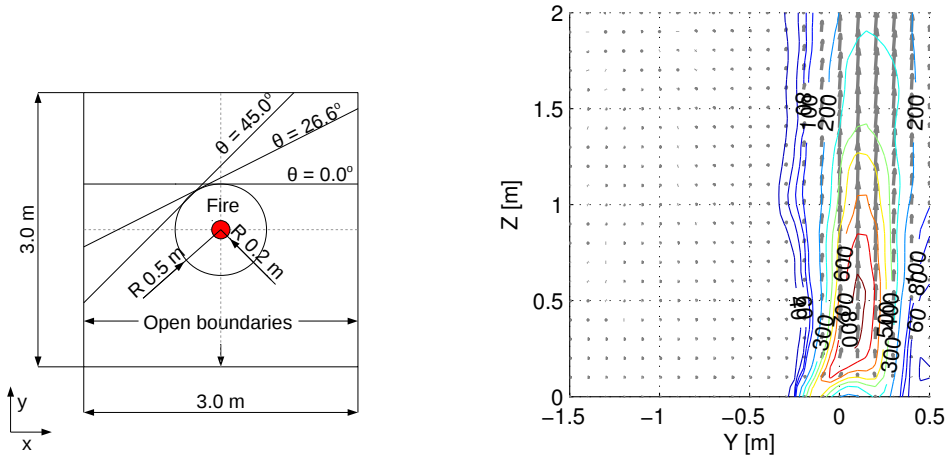

(A) Top view of the room (B) Flow field

FIGURE 4.12: Second verification case, vertical wall exposed to fire

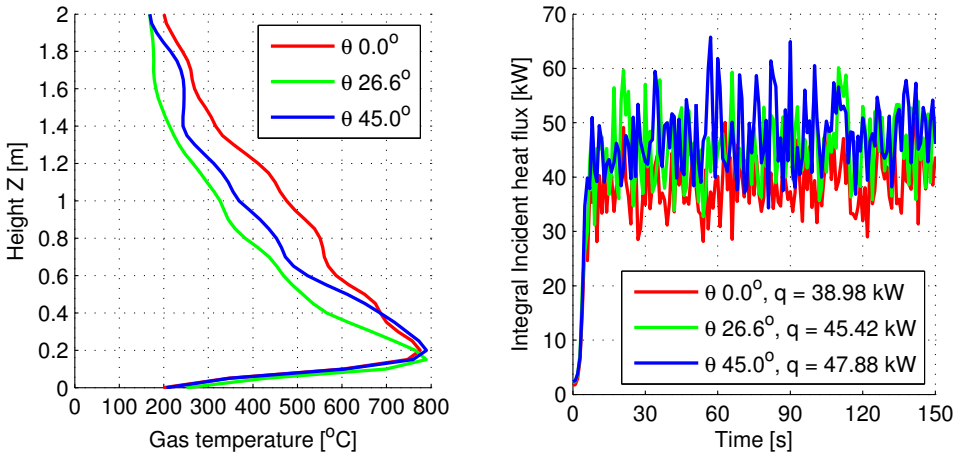

(A) Flame temperature (B) Integral heat flux

FIGURE 4.13: Comparison of temperature and heat fluxes for the different cases

from the fire. The integral fluxes show oscillations during the fire and the average values shows some discrepancies among them, with a maximum error about 20%. The discrepancies among the integral fluxes can be affected also by the different temperature fields near the wall.

After comparing the integral flux it is important to compare also the heat flux distribution, the incident heat fluxes are averaged in time and evaluated along the walls in figure 4.14. The contours show a similar distribution in the three cases with a highly heated zone near the fire and less heated far from the fire source. The heat flux distributions show the same shape with an iso-line at 30 kW/m^2 stretched along the vertical direction.

For a better understanding of the discrepancies between the incident heat fluxes presented in figure 4.14, these are reorganized in figure 4.15. The heat fluxes as function of the x coordinate are presented in figure 4.15a

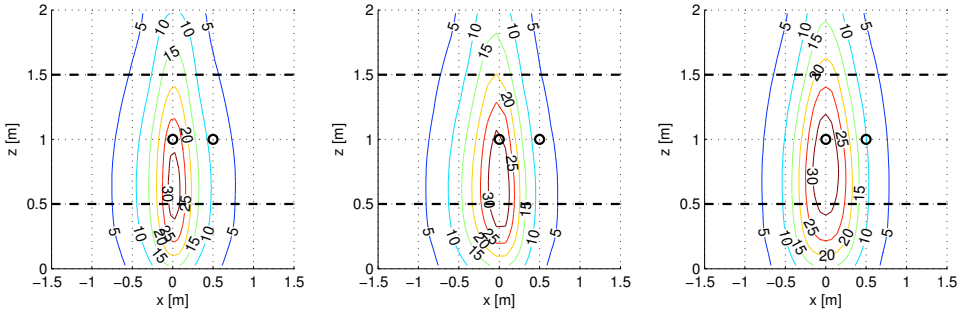

(A) θ = 0.00 ° (B) θ = 26.57 ° (C) θ = 45.00 °

FIGURE 4.14: Comparison of incident heat flux distribution for different wall's orientations

for to different heights z, equal to 0.5 m and 1.5 m. The figure shows that the heat fluxes are in good agreement among them considering the geometry approximations and also the discrepancies of the gas temperature. The most of the discrepancies are located in the peak region where the heat flux distributions have different maximum values. At z equal to 0.5 m the peak of heat flux is 31.91 W/m^2 for θ equal to 0.00 °, 34.64 W/m^2 for θ equal to 26.57 °, and 31.34 W/m^2 for θ equal to 45.00 °. While at z equal to 1.5 m the peaks of heat flux are respectively 19.02 W/m^2, 20.56 W/m^2 and 23.80 W/m^2. The heat fluxes as seen in figure 4.13b show huge fluctuations during the simulations due to the turbulent nature of the flame. The time histories of the incident heat flux, evaluated at two different points, are presented in figure 4.15b. The points are selected one at x equal to 0.0 m, at the minimum distance from the fire, and the other to be at 0.5 m, both are at z equal to 1 m. The heat fluxes show high fluctuations, but the trends are in good agreement among the three oriented walls.

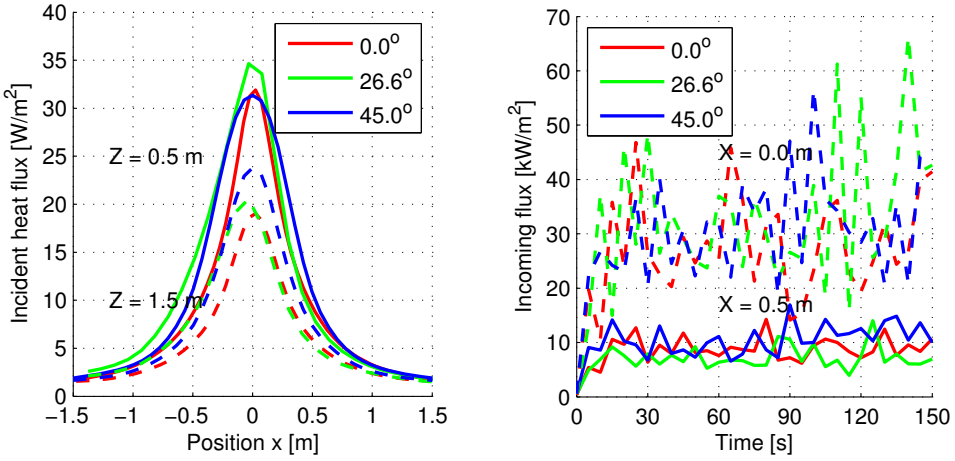

(A) Fluxes function of x coordinate (B) Fluxes function of time

FIGURE 4.15: Comparison of incident heat fluxes as function of position and time

After the comparison of the incident heat fluxes it is important also to

compare the convective heat transfer coefficient and the water vapour density. The convective heat transfer coefficient is presented on the walls after being averaged in time, figure 4.16. The coefficient is interpolated in space using an arithmetic average, as described in table 4.2, the results show a good agreement among the different walls. Most of the differences in this case are located far from the fire, in particular the iso-line 2 $W/m^2/K$ for θ equal to 0.00 ° is located near the boundaries of the wall while for the other orientations the line is closer to the fire.

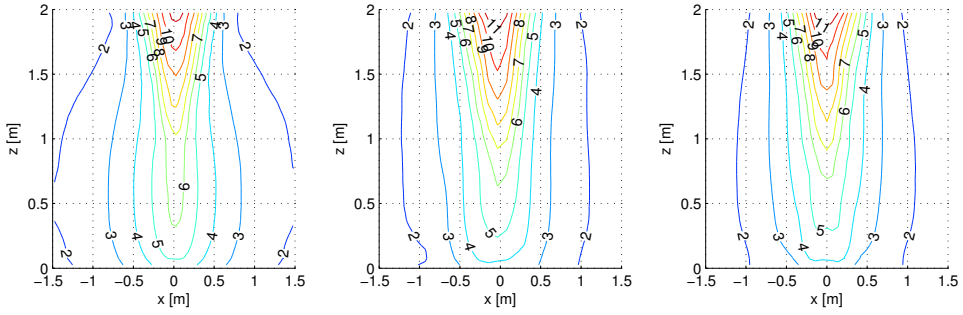

(A) θ = 0.00 ° (B) θ = 26.57 ° (C) θ = 45.00 °

FIGURE 4.16: Comparison of convective heat transfer coefficient distribution for different wall's orientations

The convective heat transfer coefficients along two lines are presented in figure 4.17a. The coefficients for the different cases show similar trends with some differences, the peaks of convective heat transfer coefficients are 6.21 $W/m^2/K$ for θ equal to 0.00 °, 5.69 $W/m^2/K$ for θ equal to 26.57 ° and 5.37 $W/m^2/K$ for θ equal to 45.00 ° at z equal to 0.5 m. For z equal to 1.5 m the peaks are respectively 8.93 $W/m^2/K$, 9.79 $W/m^2/K$ and 9.47 $W/m^2/K$. Some discrepancies occur also far from the flame but these have a low influence on the final result due to their small value. Moreover the effect of the boundaries should be better investigated using larger domain, but in order to speed up the calculation it has been necessary to reduce the size of the simulated domain.

The last comparison is done for the water vapour density, in this case the flame is close enough to the wall to induce a higher water density in the region near the flame. Water density distributions are presented on the walls in figure 4.18 showing a trend similar to the convective heat transfer coefficient. The maximum density for the different distribution is located near the top of the wall at x equal to 2.0 m. This is consequence of the flame shape and of the hot gas expansion which flows close to the wall as seen in figure 4.12b. The most of the discrepancies are located also in this case far from the flame at the iso-line 0.02 kg/m^3, while at x equal to 0.0 m the water density show a good agreement among the cases. To better understand the differences in the water density distributions, these are plotted as function of the position x for two different heights at z equal to 0.5 m and 1.5 m. The results show some minor discrepancies but the overall agreement is satisfactory. The peaks of water density located near the flame are 0.0698 kg/m^3 for θ equal to 0.00 °, 0.0649 kg/m^3 for θ equal to 26.57 ° and 0.0613 kg/m^3 for θ equal to 45.00 ° at z equal to 0.5 m and 0.1137 kg/m^3, 0.1316 kg/m^3 and 0.1251 kg/m^3 for z equal to 1.5 m.

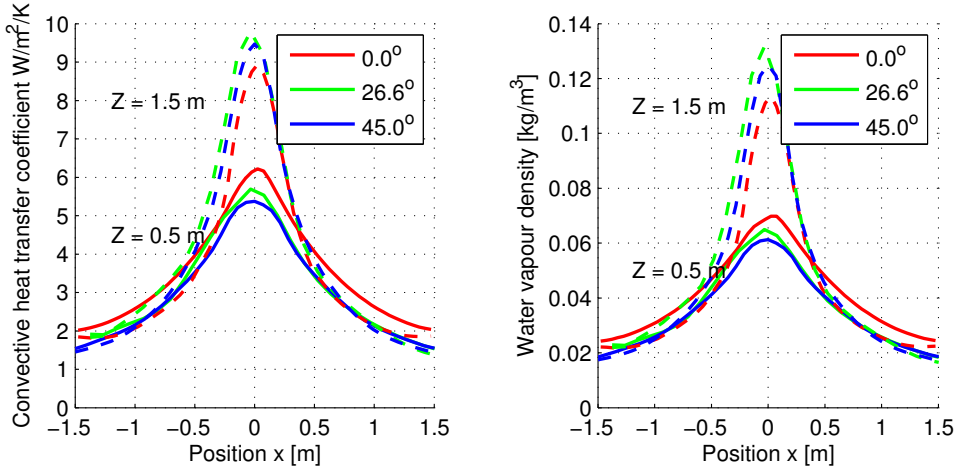

(A) Convective heat transfer coefficient (B) Water vapour density

FIGURE 4.17: Comparison convective heat transfer coefficient and water vapour density

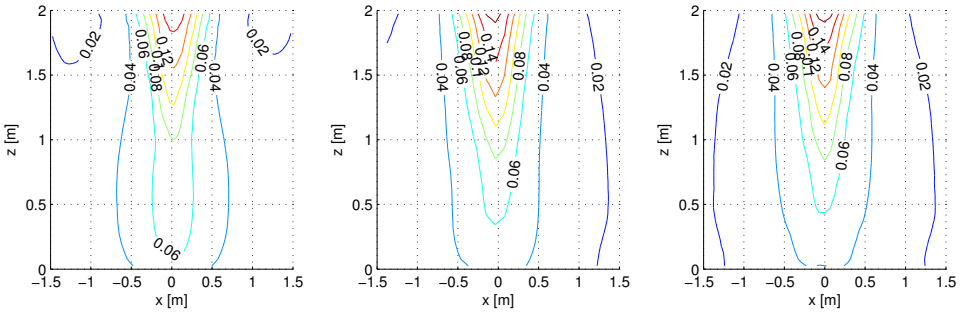

(A) θ = 0.00 ° (B) θ = 26.57 ° (C) θ = 45.00 °

FIGURE 4.18: Comparison of water vapour density distribution for different wall's orientations

The results presented in this section show that the three variables transferred from FDS to Comes-HTC are interpolated with a reliable approach. The verification case shows that for different orientations of the walls the variables in terms of integral value and distribution show some minor differences. The agreement between the cases is affected also by the different flow fields. The differences in the flow and temperature distributions partially prevent from comparing three cases that are exposed to the same fire. However the spatial distribution and the time history of the heat fluxes are in good agreement between them. The convective heat transfer and the water density show just some minor discrepancies near the peak. The discrepancies far from the peak can be related to the vicinity to the domain's boundaries, therefore they are considered acceptable. In this verification case the vertical plane is mainly heated up by radiation since there is no direct impingement of the flame on the wall and the hot gasses flow tangentially along the wall. Another verification case is needed to evaluate the effect of the flame impingement on the wall.

4.2.3 Plume impinging a ceiling

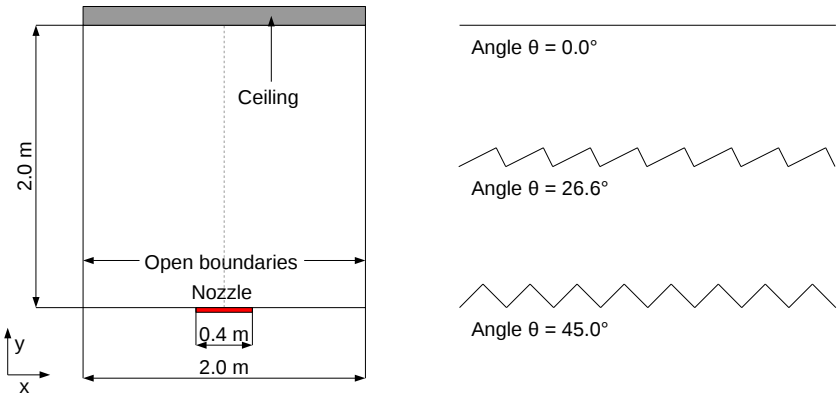

FIGURE 4.19: Third verification case, Plume impinging a ceiling.

The last verification case is a ceiling heated by a plume of hot gasses. Thanks to the capability of FDS to tilt the gravity vector it is possible to change the orientation of the domain and to draw the ceiling with different meshing strategies, figure 4.19. The domain is tilted with three angles which are 0.00 °, 26.57 ° and 45.00 °. With this approach the horizontal ceiling is smooth in the first case, θ equal to 0.00 °, while it is sawtoothed in the other two cases , θ equal to 26.57 ° and to 45.00 °. In order to simplify the calculation the domain is two dimensional therefore the ceiling is assumed to be infinitely long. Instead of a burner a jet of hot gas is used as heat source, the jet has a nominal temperature of 1200 °C and is discharged from a nozzle, 0.4 m wide, with a velocity equal to 3.0 m/s. The velocity has been reoriented in the cases with θ equal to 26.57 ° and to 45.00 ° in order to blow hot gases towards the vertical direction. The meshes used for the three different cases have the same element's size 0.05 m, in order to compare together similar flow fields. The heated ceiling is placed at 2.0 m above the burner, placed at the floor level at 0.0 m, on the sides of the domain open boundary conditions are located at 1.0 m from the centre of the nozzle. In order to evaluate the different flow fields produced with the tilted domains the temperatures and the velocities are compared in figure 4.20. The pictures show the same portion of the domain where the nozzle blows hot air towards the ceiling inducing two vortexes on the sides of the jet. The temperature field show some differences between the three cases in particular the eddies on the two sides of the jet are slightly different when the domain is tilted. The different velocity field can be consequence of the location of the domain's boundaries that are not corresponding due to the tilting of the domain.

In figure 4.21a the temperatures averaged in time are plotted along the middle-line of the flame in order to show the effect of the tilting angle. The temperature near the floor are the same, but in the middle, between ceiling and floor, some differences occur, the temperatures converge again to the same value under the ceiling. The velocity component parallel to the x axis is presented beneath the ceiling, figure 4.21b. When the ceiling is

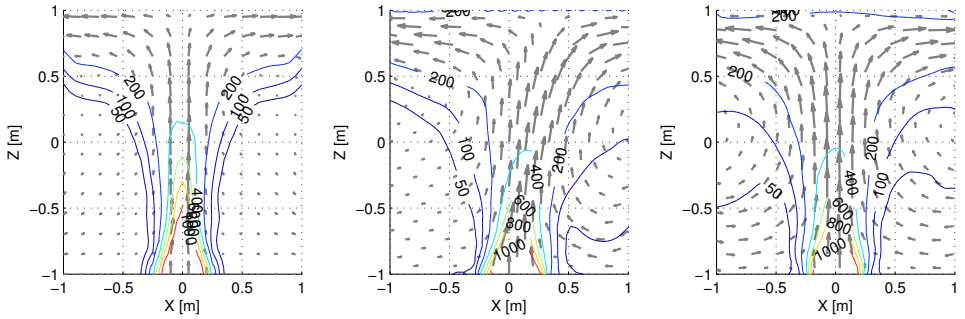

(A) θ = 0.00 ° (B) θ = 26.57 ° (C) θ = 45.00 °

FIGURE 4.20: Temperature and velocity field beneath the ceiling for different tilting angles of the domain

tilted with a different angle the component of the velocity, which are later used to calculate the convective heat transfer coefficient, are also modified. The smooth wall simulated with θ equal to 0.00 ° shows higher velocities compared to the other cases where air flows along a non regular geometry.

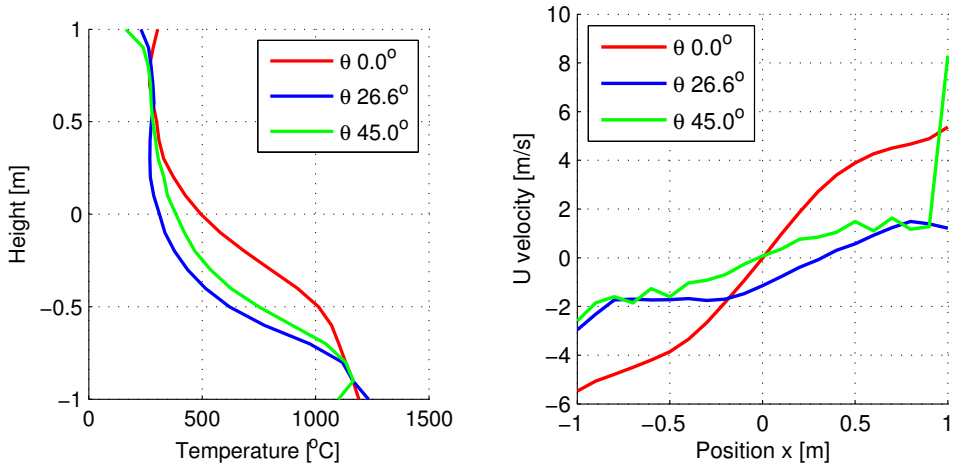

(A) Temperature (B) U velocity

FIGURE 4.21: Comparison of temperature and velocity

The comparison of the flow fields shows some minor differences among the different orientations, but the differences are limited. It is thus possible to compare the variables that are later exported from FDS to Comes-HTC. First the incoming heat fluxes are compared for the different ceiling's orientations in figure 4.22, the integral heat fluxes are presented as function of time in figure 4.22a and later averaged in time and presented as function of the position, figure 4.22b.

The heat flux time histories show several fluctuations due to the high turbulence of the hot gas plume. The heat fluxes are in steady state condition after few seconds and the oscillations are related with the plume's puffing. The spatial distribution of the heat fluxes can highlight the difference between the three cases filtering the time fluctuations seen in figure 4.22a. From figure 4.22b the heat flux distributions are in good agreement

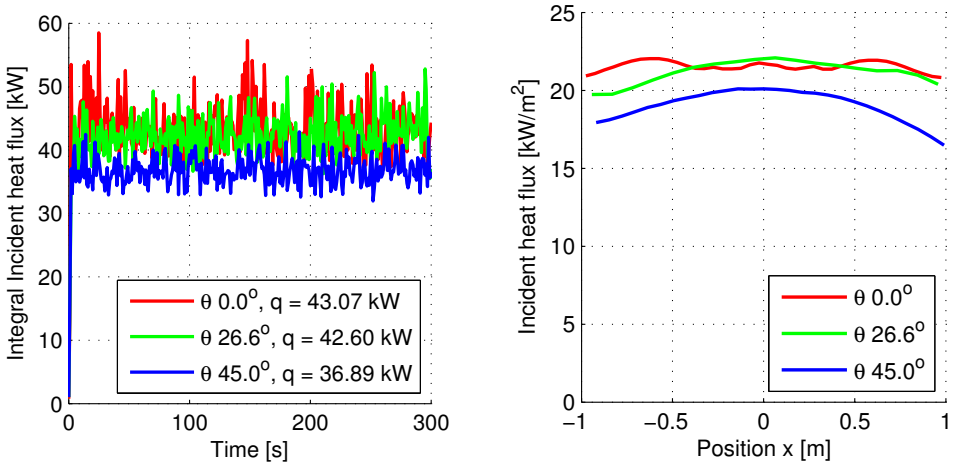

(A) Time history (B) Spatial distribution

FIGURE 4.22: Comparison of incident heat fluxes on the walls for different orientations

among them with a flat distribution along the ceiling, the different cases have different peaks, in case of θ equal to 0.00 ° the peaks are not on the centreline of the plume, while in cases θ is equal to 26.57° or 45.00° the maximum is located above the plume. The maximum heat flux obtained with θ equal to 45.00°, 20.08 kW/m^2, is underestimated compared to the other cases, 22.03 for θ equal to 0.00° and 22.09 forθ equal to 26.57° . The lower heat flux for the case with θ equal to 45.00° is depicted also in figure 4.22a where the integral flux is always lower than the other cases, with an error equal to 14.3 %. While for θ is equal to 26.57° the integral heat flux shows a good agreement with the reference case with θ equal to 0.00°.

The convective heat transfer coefficient is investigated comparing its distribution along the ceiling for steady state conditions, figure 4.23a. The figure shows a strong underestimation of the convective heat transfer coefficient by the cases with θ equal to 26.57° or 45.00° compared to the reference case with θ equal to 0.00°. The convective heat transfer coefficient is strongly related with the velocity field near the wall, due to its definition with equation 2.14. The differences in the velocity field previously depicted by figure 4.21b affect the convective heat transfer coefficient distribution along the wall. With θ equal to 0.00° the high velocity on the sides of the plume increased the convective heat transfer coefficient, therefore the minimum of the coefficient is located above the plume, for the other two cases the velocity is almost uniform and also the coefficient has a flat distribution. The higher heat transfer coefficient in the reference case has also an influence on the incident heat flux distribution, because as seen in figure 4.22b the maximum flux is not located above the plume but on the sides. The poor agreement of the convective heat transfer coefficient couldn't be improved since the velocity field near the wall is strongly affected by the geometry modelling, to have a better distribution of the coefficient more radical modification are required to FDS in order to draw rounded surfaces.

The last comparison is done for the water vapour density, figure 4.23b, the hot plume produces also water vapour which flows along the ceiling,

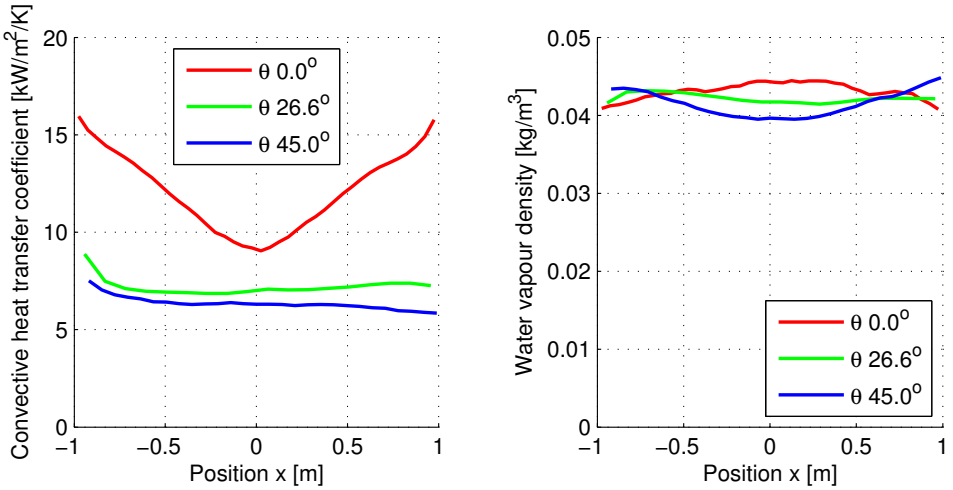

(A) Heat transfer coefficient

(B) Water vapour density

FIGURE 4.23: Comparison of convective heat transfer coefficient and water vapour density

the density in the different cases shows a good agreement and the spatial distributions are in a close range. The main difference is on the shape of he density distributions, with θ equal to 0.00° the maximum is located above the plume, while in the other two cases near the centre there is a minimum of density. These differences are directly related with the the flow field beneath the ceiling but the agreement among the cases is considered satisfactory.

The comparisons of different fire scenarios assesses that the approach proposed in section 4.1.1 can be reliably used to interface a Cartesian mesh with a structured mesh also for non-corresponding geometries. From the verification cases it is clear that the incident heat flux is well transferred for the different orientation. Minor differences occur also because of the different flow fields compared together. From the verification case of the cylinder with burner, in section 4.2.1, it is clear that the heat flux distribution is affected by the grid resolution in FDS and that a finer grid allows to obtain a heat flux distribution that is closer to the theoretical result. The largest differences have been found for the convective heat transfer coefficient, which is calculated basing on the velocity near the walls. In the cylinder and on the vertical wall the hot gasses flow along the channels made by the geometry discretization and the velocity is mainly parallel to the channels. In the last verification when the plume impinges the ceiling the gas flows crossing the steps made by the mesh. The different flow regimes induce different convective heat transfer coefficients. The agreement among walls with different orientations is good if the velocity is parallel the the channels made by the grid, while it is poorer if the velocity is perpendicular to them. The water density vapour is well predicted in all cases where it has been evaluated, showing some minor differences which don't affect the overall agreement between different cases.

4.3 Concrete slab exposed to fire

After the introduction to the coupling and the verification of the proposed approach the coupled tool applied to a structural verification on a slab exposed to fire. This first case is rather simple since it considers a two dimensional concrete slab exposed to fire. This first application aims to show the effects of the specific fire scenario, in terms of HRR per unit of area and of fire growth rate, on the response of the structure. Different fire scenarios are simulated keeping the same maximum HRR and the same distance between the burner and the slab. Different fire scenarios can produce different heat fluxes distributions and the coupled tool proposed here is capable to evaluate their influence on the structure's response.

4.3.1 Fluid dynamic analysis

The fluid domain investigated is presented in figure 4.24a. A 1.2 m wide burner blows n-heptane with a specified mass flow rate, the HRR curve for the reference case is presented in figure 4.24b with a linear ramp from 0 s to 450 s up to 600 kW/m and later a constant HRR up to 900 s. The combustion process is ideal since the smoke production is out of the scope of this analysis, the soot yield and the CO yield are set equal to 0.0, while CO_2 and H_2O are calculated based in the stoichiometric balance. The distance from the burner to the slab is 1.8 m. The slab, 2.0 m wide and 0.2 m thick, is made of C60 concrete and in FDS the thermal properties of the slab are set according to the Eurocode [130]. For the concrete it is assumed an humidity of 40 % and a water content of 19.69 kg, the properties of the material such conductivity and specific heat are presented as function of temperature in table 4.4, the density of concrete is set constant at 2300 kg/m^3. The concrete slab is assumed to have emissivity equal to 0.9.

TABLE 4.4: Material's thermal properties modelled in FDS

Conductivity	
Temp. [°C]	k [W/m/K]
0.0	2.0
200.0	1.553
400.0	1.191
600.0	0.915
800.0	0.724
1000.0	0.619

Specific heat	
Temp. [°C]	C_p [kJ/kg/K]
20.0	0.936
100.0	0.936
101.0	1.240
115.0	1.240
200.0	0.98
400.0	1.045
1000.0	0.977

The main focus of the simulation is the interaction between plume and slab, but an additional fluid domain must be added near the slab in order to allow the flow to develop freely. The domain is 4.0 wide and 4.0 m high and at every open boundary the gas pressure is imposed equal to the atmospheric pressure.

The initial fire scenario is modified in order to obtain different HRR per unit of area and in order to obtain different fire growth rates. In order to change the HRR per unit of area and the shape of the flame, the burner is resized. The burner in the reference condition has a HRRPUA of 500 kW/m^2, new fire scenarios are simulated with different burners' size, 0.4 m

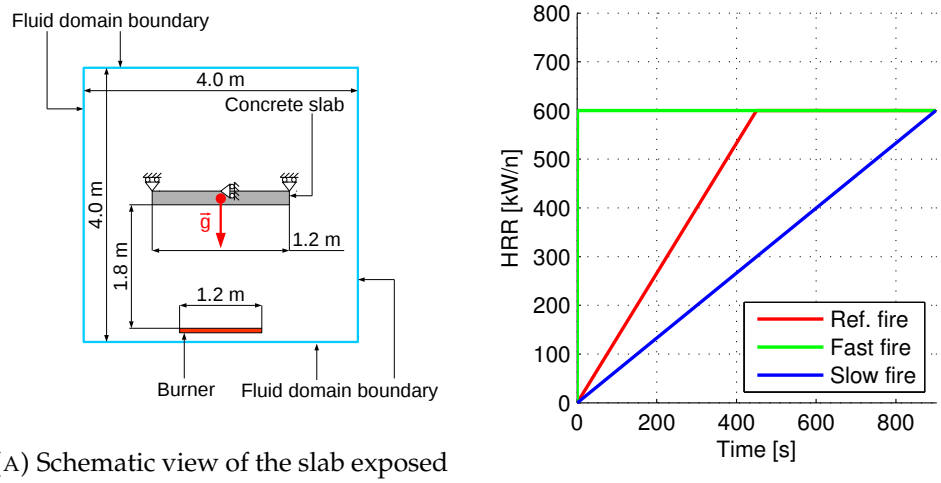

(A) Schematic view of the slab exposed to fire

(B) HRR

FIGURE 4.24: Fire scenario investigate with the coupled approach

and 2.0, with a HRRPUA of 1500 kW/m^2 and 300 kW/m^2. The fire growth rate for different burner's size is the same of the reference case, presented in figure 4.24b. In order to change the fire growth rate the shape of the HRR curve is modified. Two new fire curves are simulated, a fast growing fire and a slow growing fire as reported in figure 4.24b, in these scenarios the size of the burner is kept the same as the reference case 1.2 m wide. Before comparing the different fire scenarios a preliminary sensitivity analysis has been carried out. For the reference case different meshes are compared together in order to assess the correct grid's resolution. The grids are regular and made by square elements whose features are listed in table 4.5

TABLE 4.5: Mesh data

Mesh	El. size [m] (x,y)	N. of El.	$D^*/\delta x$
Mesh 1	0.200× 0.200	400	3.9
Mesh 2	0.100× 0.100	1600	7.8
Mesh 3	0.067× 0.067	3600	11.7
Mesh 4	0.050× 0.050	6400	15.6

In order to compare the different grids, the temperatures above the flame and AST along the slab are compared together, figure 4.25. The temperatures are averaged in time from 450 s to 900 s and these are evaluated along the centreline of the plume in the middle of the burner, figure 4.25a. The two finer grids, mesh 3 and mesh 4 are in good agreement among them, while the other two grids tend to underpredict the temperature along the plume. The AST are compared on the lower face of the slab and these are in good agreement for the last two grids, mesh 3 and 4, while the coarser meshes underpredict the heat fluxes on the walls. The mesh required to simulate correctly the incident fluxes on the walls produced by the plume is much finer than the grids usually employed to simulate the smoke movement, as seen in the previous chapters 2 and 3.

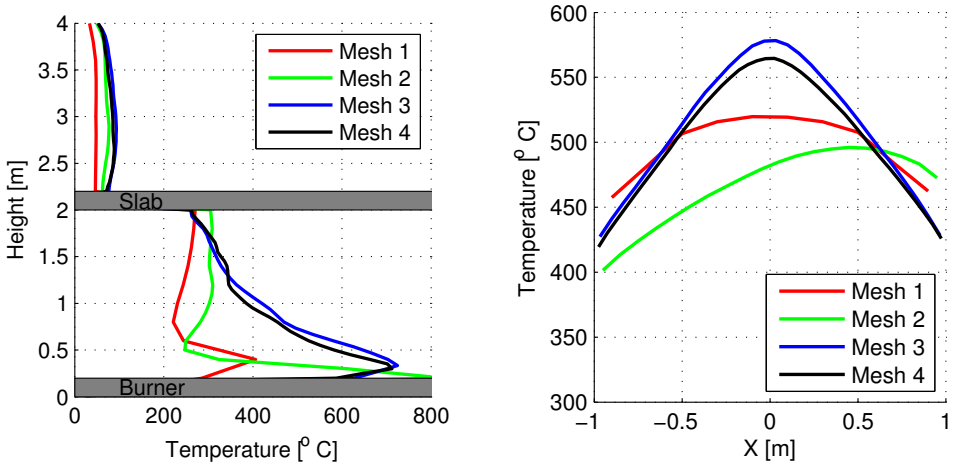

(A) Gas temperatures (B) AST

FIGURE 4.25: Mesh independence

From the mesh independence study the mesh 3 is chosen for all the cases, also when the size of the burner and the fire growth rate are changed. After the mesh independence study the flow field induced by the fire is presented in figure 4.26b. The plume is impinging the slab and the hot gas flows on the sides and rise again out of the domain. As seen from figure 4.25b the incident heat flux is maximum in the middle of the slab, therefore the maximum wall temperature is expected in the middle of the slab.

After comparing the different grids and showing the flow field obtained with mesh 3, the different cases are compared among each other. First, the effect of the burner size is investigated and the temperature fields in the two cases, with narrow and large burners, are presented in figure 4.26. In the comparison is included also the original burner, whose size is 1.2 m, the temperature fields show clearly that a smaller burner is capable to generate a more stretched flame which induces higher temperatures near the ceiling.

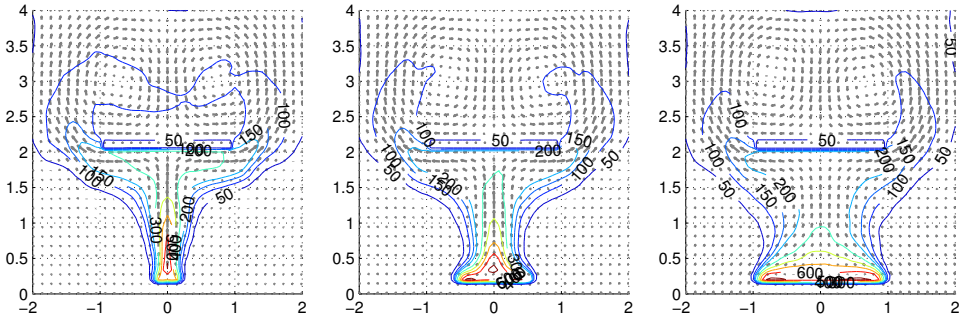

(A) Narrow burner (B) Medium burner (C) Wide burner

FIGURE 4.26: Comparison of flow fields obtained with different burner's size

For the three burners the temperatures along the centreline of the plume are presented in figure 4.27a. The temperatures near the burner are quite similar between them, but increasing the size of the burner and reducing

the HRR per unit of area the temperature also decreases along the centreline of the flame. This effect is not so evident from the contours, figure 4.26, but it is well depicted by the figure 4.27a. Beneath the slab the temperature of the smoke is more than 100 °C higher for the narrow burner if compared to the wide one. Regarding the incident heat fluxes on the walls, the AST are compared along the length of the slab on the face exposed to fire. In figure 4.27b the effect of the burners size is clear with higher temperatures for the narrow burner and lower temperatures for the wide one. The narrow burner induces higher temperatures not only in the centre but all along the slab, if compared with the other fires. The heat flux impinging the structure is higher for narrower burner compared to the wider one. The different flame shapes affect the distribution of the heat fluxes on the slab, a wide burner generates a more uniform heat flux distribution compared to a narrow burner.

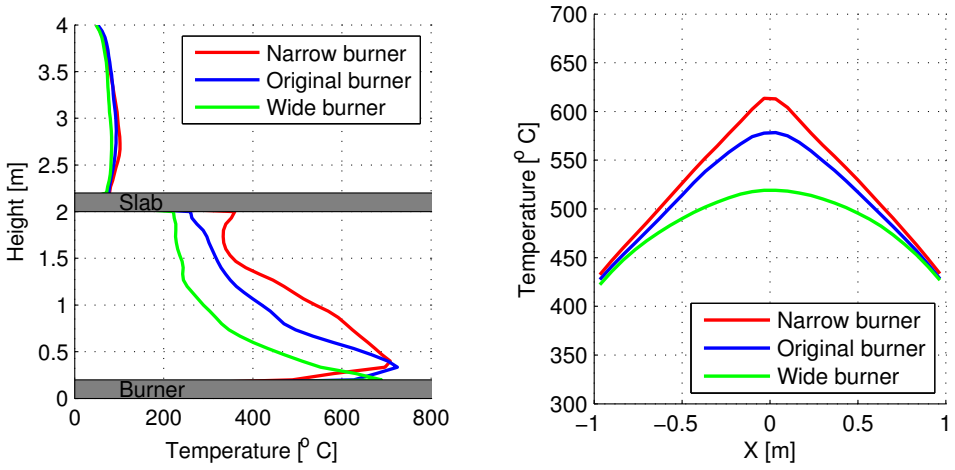

(A) Gas temperatures (B) Adiabatic surface temperatures

FIGURE 4.27: Comparison of different burners' sizes

The effect of the fire growth rate can be depicted by time history of the temperatures and by the net heat fluxes. The gas temperature beneath the centre of the slab at 1.8 m height is plotted as function of time together with the temperature on the slab's surface, evaluated in FDS, in figure 4.28a. The different fire growth rates induce temperature fields and this influences directly the wall temperature. The different wall temperatures are caused by different heat losses through the walls, figure 4.28b. When the fire has a fast growth rate, the net heat flux has a peak in the beginning of the fire scenario because the high incoming flux caused by the fire is not balanced by the outcoming flux from the wall. In case the fire grows slowly the temperature on the wall is closer to the temperature of the gas and the incoming and outcoming fluxes can better balance together. If the incoming and outcoming fluxes are similar the net heat flux is smaller. The effect of the different fire growth rates can be depicted by the slope of the wall temperature. Increasing the net heat flux through the wall the slope of the wall temperature increases, while decreasing the net heat flux also the wall's temperature slope decreases.

The fire scenarios have an influence on the flow field which affects the

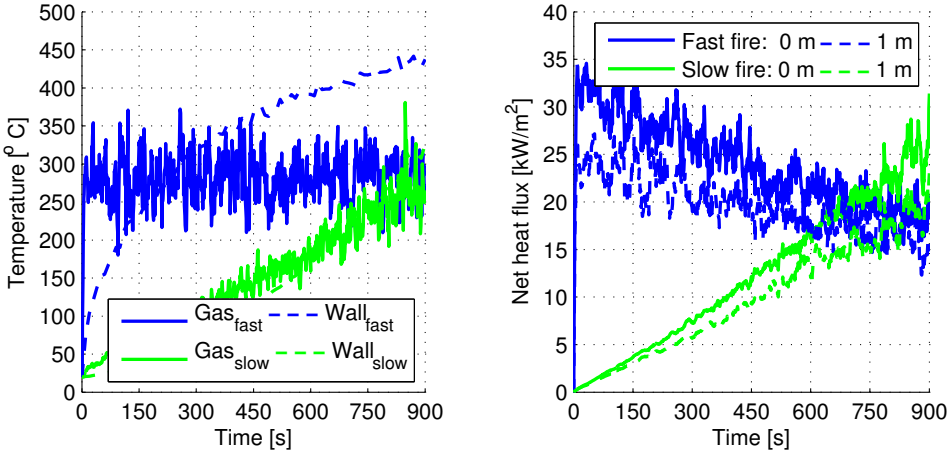

(A) Temperatures (B) Net heat flux

FIGURE 4.28: Comparison of different fire growth rates

thermal inputs on the structure. The fire scenarios can be modified in time, with different fire growth rates, or in space with different flame's shape. The coupled analysis is capable to show the effects of different flow fields on the structure.

4.3.2 Structural analysis

After comparing the fire scenarios the response of the concrete structure exposed to fire is investigated. The structure is a simple slab which is constrained according to figure 4.24a, where the slab is free to bend keeping its position above the fire. The slab is mechanically loaded using the weight of the slab as distributed volume load, the gravity vector is oriented as in figure with a magnitude of 9.81 m/s^2. The material chosen for the analysis is a C60 concrete not reinforced with an initial content of water of 21.64 kg/kg, relative humidity of 46 %, a saturation of 25 %, pressure of 101325 Pa and temperature of 20 °C. The structure in not pre-stressed and no displacements are imposed at the beginning of the simulation. The mesh used for the structural calculation is drawn in order to link directly the elements of FDS with the nodes of Comes-HTC. The elements are stretched along the width of the slab in order to reduce the computational load of the calculation. The elements used for the calculation have 8 nodes and 3 gauss points along each element's axis. The distance between two nodes on the surface of the slab is 0.0667 m, the same of the size of the FDS element. The coupling links the two closer elements of FDS to the target node of Comes-HTC since the geometries in the two codes are corresponding. The upper and lower surfaces of the slab are linked with FDS, but the two sides of the slab are not coupled because of the huge difference in the size of the elements which could arise numerical stability issues. The mesh and the boundary conditions are the same for all the fire scenarios.

First the effect of the burner size on the concrete structure is evaluated, as seen before in figure 4.27b the heat flux impinging the structure is greater with a narrow burner than with a wide one. For sake of simplicity in the following comparison only the scenario with narrow and wide burners are

presented, the scenario with the original burner is neglected since it lays between the two extreme cases. The integral incoming heat flux for the two fire scenario is presented in figure 4.29, comparing the output from FDS and the input in Comes-HTC.

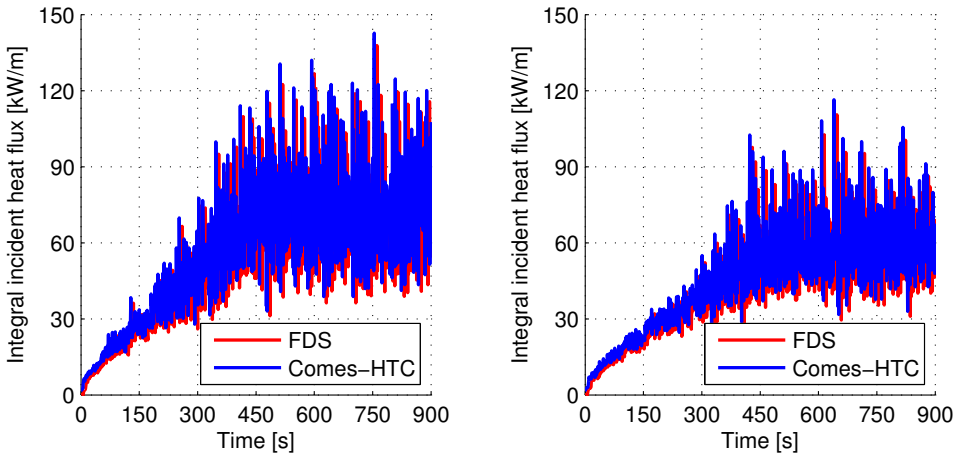

(A) Narrow burner (B) Wide burner

FIGURE 4.29: Integral incident heat fluxes on the slab

The integral incident heat flux before and after the interpolation process are overlapping for the two fires. The narrower burner produces an higher integral incident heat flux compared to the other burner, 4.29. In order to evaluate the influence of the fire scenario on the structure stresses, temperature and gas pressure are presented. The comparison is done at the end of the simulation after 900 s, 15 min, of intensive heating. The temperatures inside the slab after 900 s, figure 4.30, show clearly that the temperature peaks are different in the two cases, but in both cases are located at the centre of the slab on the lower face. The narrow burner heats up the slab up to 397.6 °C, while the wide one reaches only 270.7 °C. The figure shows also that the structure is mainly heated from the lower face, but there is a temperature rise also on the upper face. This is consequence of the hot gasses that are flowing around the structure and warming up the whole slab. The curves with constant temperatures on the slab are almost parallel to horizontal line, meaning that the main gradient of temperature is along the vertical direction and the heat flux flows normal to the heated face. The wide burner induce temperature fronts which are flat due to the uniform heating along the width, while the slab heated by the narrow burner has some deflection in the temperature profiles near the lower face of the slab due to the more localized heating, figure 4.27b.

The gas pressure in the structure is consequence of the gas movement inside the material combined with the expansion and evaporation. When the structure is heated up the first layers tend to dry out, while in the inner layers the gas cannot escape. Due to the cumulation of moisture and heating the pressure rises inside the structure and generates a pressure peak. The gas pressure is one of the factors which are argued to trigger the spalling, since it opens the pores of the material, as discussed in section

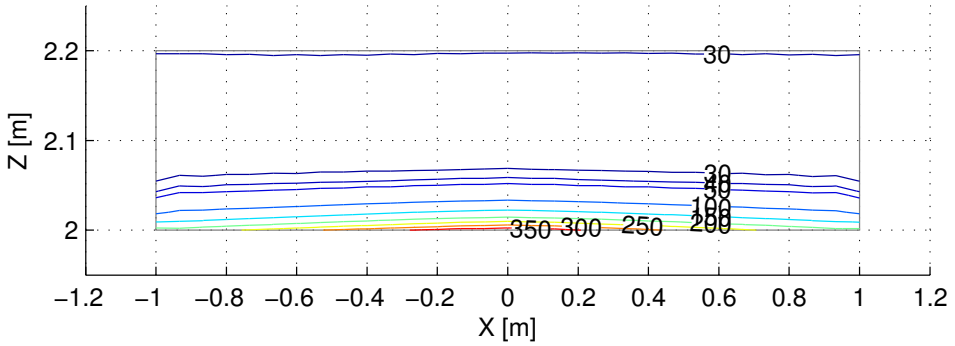

(A) Narrow burner

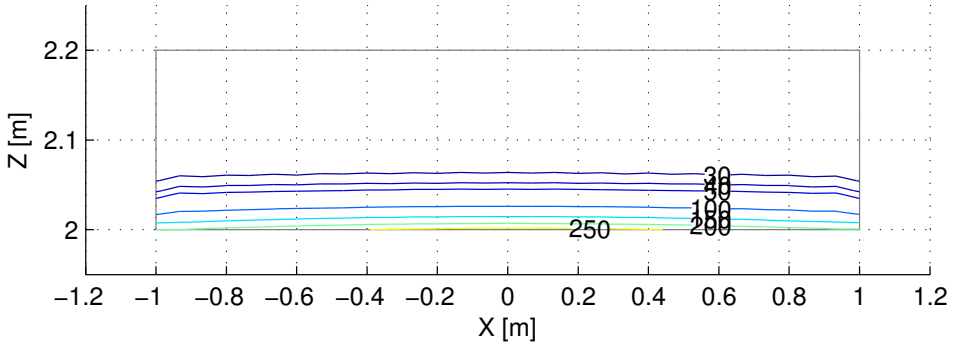

(B) Wide burner

FIGURE 4.30: Temperature distribution in the slab.

1.3.2. The gas pressure as expected is higher for the fire scenario with narrow burner, while is lower for the other wide one. The maximum pressure is below 1 MPa in both cases, 0.3495 MPa for the wide burner and 0.4583 MPa in case of narrow burner. These values are small if compared with the stresses induced by the mechanical loads, but are in agreement with the experimental data found for similar concrete, [36, 39]. The C60 concrete has an higher permeability compared to HPC therefore the gas is capable to flow out of the material reducing the pressure peak in the structure.

The last comparison is done for the stress distribution inside the material, the slab is not affected by the thermal loads but also loaded by its own weight. The mechanical load on the slab without any thermal expansion should strain the lower part of the slab and compress the upper layer. Due to the heating of the slab the structure is expanding proportionally to its temperature. The temperature distribution as seen in the figure 4.30 is not uniform, therefore thermal induced stresses rise inside the slab. The combination of stresses induced by the mechanical load, by the thermal expansion and by the solid pressure is presented in figure 4.32.

The component XX of the stress is negative, compression, on the upper face of the slab as expected by the stress distribution induced by the mechanical load. But the stress is negative also on the lower part of the slab, where the stress induced by the mechanical load is supposed to be positive. The thermal expansion of the heated concrete is constrained by the rest of the structure which has lower temperature, therefore in the lower

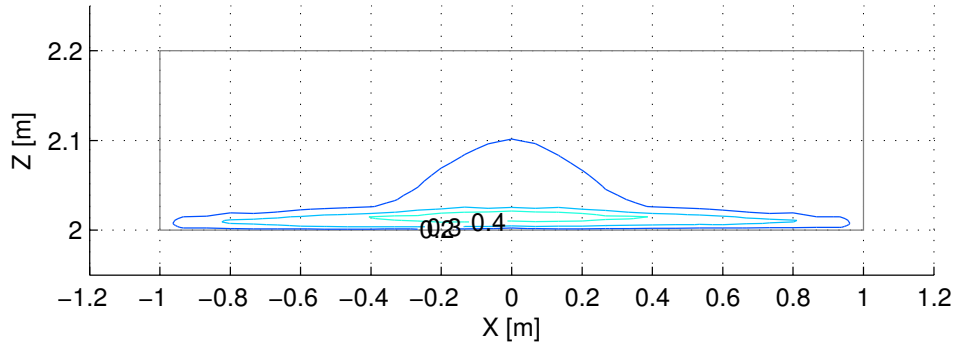

(A) Narrow burner

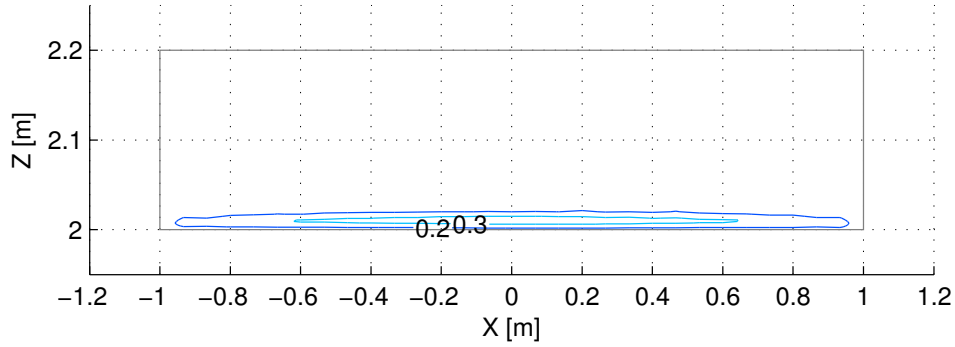

(B) Wide burner

FIGURE 4.31: Gas pressure distribution in the slab.

layer of the slab the concrete is put under compression due to the constrained expansion. The first layers of the slab exposed to fire are under compression and this stress condition is also one of the conditions that trigger the spalling of the material, because of a buckling load. The maximum compressive stress are -30.77 MPa for the wide burner and -34.80 MPa for the narrow one. The stress distributions are more similar between the two scenarios than the previous quantities, this can be consequence of the mechanical load and of the temperature gradient. The thermal induced stress is not depending on the maximum temperature itself rather on the temperature spatial gradient. The last comparison between these two fire scenario is done for the stress component parallel to the Z axis, sigma ZZ.

Also for this stress component the distributions for the two fire scenarios are similar between them. There is a compressed region in the core of the slab, but there is a negative stress on the lower layer which are the most exposed to fire. The traction stress tends pull away the first layer of material, the traction is consequence of the mechanical and thermal loads but also of the gas pressure which tends to open the pores of the material. The maximum traction stresses are 5.17 MPa for the wide burner and 5.06 for the narrow one. The maximum XX compressive stress occurs near the heated surface of the slab where also the traction stress ZZ has its maximum positive value. The combination of pressure and stresses presented for this comparison shows that the lower layers of the slab have an higher risk of spalling, and most likely above the fire where the thermal load is maximum

A similar comparison is done also for the slabs exposed to fires with

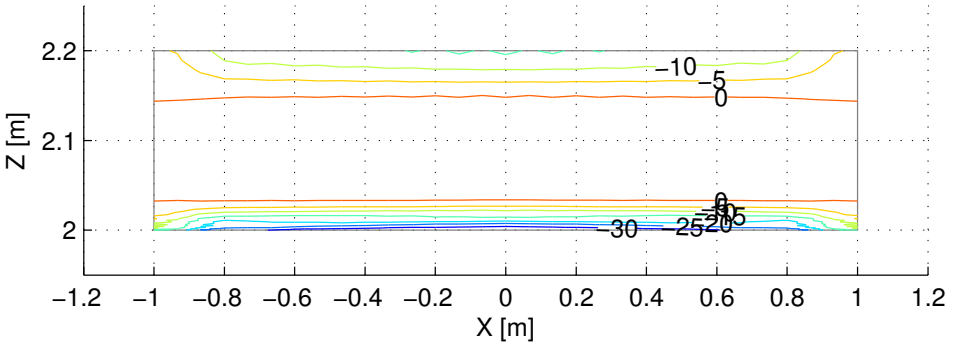

(A) Narrow burner

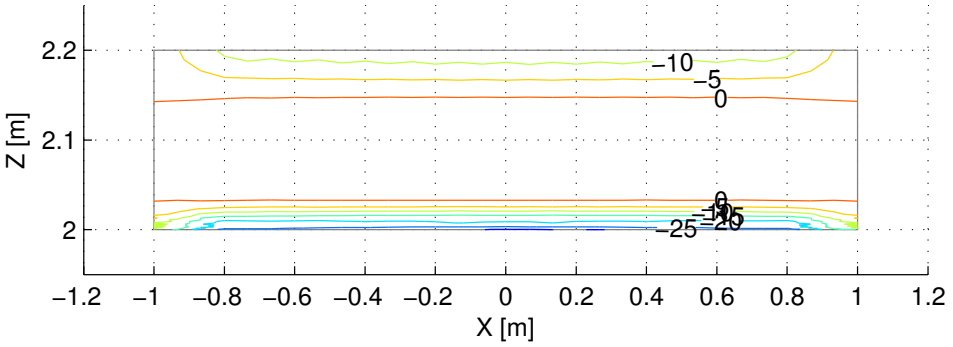

(B) Wide burner

FIGURE 4.32: Stress XX component distribution in the slab.

different growth rates. The integral incident heat fluxes are compared first as verification of the coupling as done before, figure 4.34.

The integral heat flux is transferred correctly from FDS to Comes-HTC and the coupling doesn't generate any sink or source of energy. The heat fluxes in the figure 4.34 follow the same trends of the HRR of the two scenarios with a constant heat flux and a linearly growing heat flux. The energy absorbed by the slab is equal to the integral of the integral heat flux, the area under the two curves in figure 4.34, so for the fast growing fire the energy impinging the slab is almost double than the energy for the slow growing fire. The effect of the fire growth rate is evident on the temperature distribution inside the slab compared after 900 s of fire, figure 4.35.

The maximum temperatures are different in the two cases 380.4 °C for the fast fire and 270.2 °C for the slow rate fire, for both cases the maximum is located at the centre of the slab on the lower face. The iso-curves of temperatures are parallel to the horizontal face of the slab due to the strong heating from the bottom. The heat flux flows mainly across the slab along the vertical direction. For all the fire scenarios investigated, the temperature distributions are similar even if the maximum temperatures are different. With the coupled approach FDS Comes-HTC the heat flux distribution on the wall is not uniform as seen in figure 4.28b, but the effect of the local heating is mainly evident near the heated surface.

The gas pressure also obtained with these two scenarios is compared at the end of the fire. The pressure peak is higher in case of fast growing fire with a peak value of 0.46 MPa, while in case of slow fire the pressure

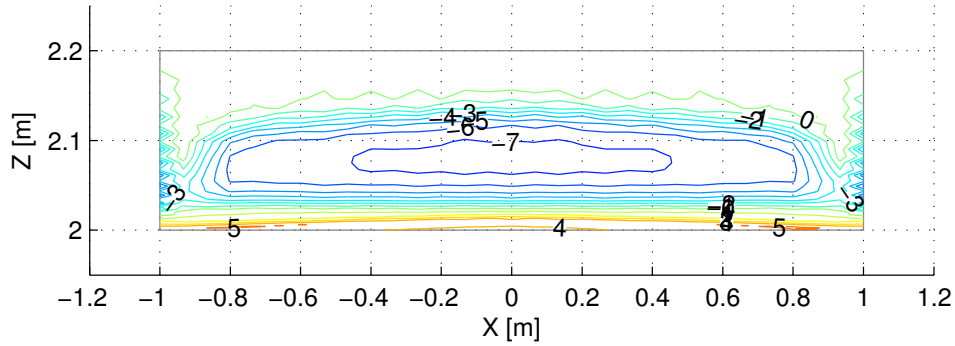

(A) Narrow burner

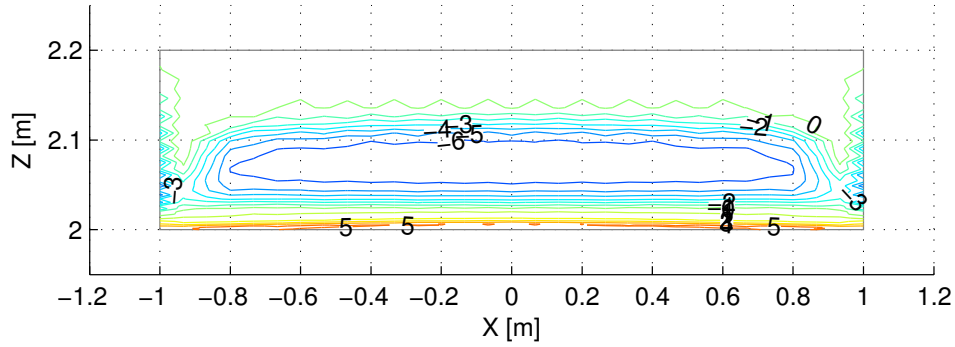

(B) Wide burner

FIGURE 4.33: Stress ZZ component distribution in the slab.

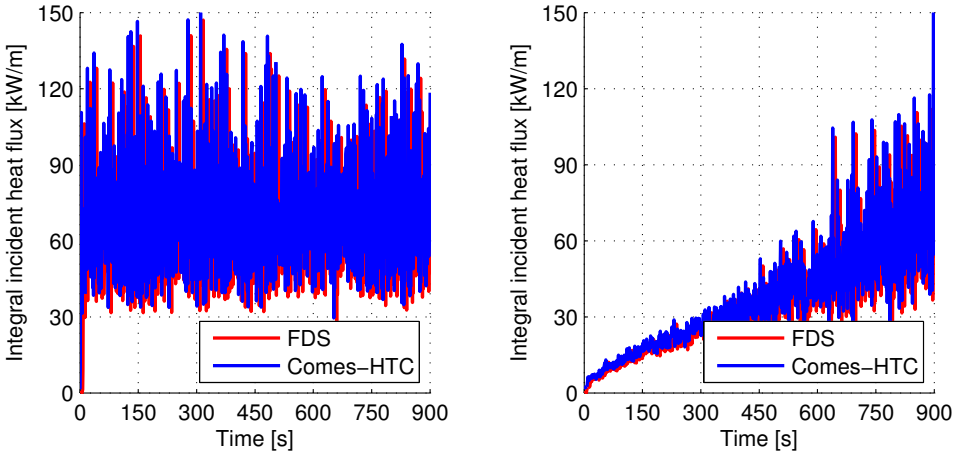

(A) Fast growth rate

(B) Slow growth rate

FIGURE 4.34: Integral incident heat flux on the slab.

rise up to 0.36 MPa. The pressure rise with a fast fire is entering deeper in the structure with a more extended pressure front, while the slow fire is just rising the pressure in the front layers exposed to fire. The higher energy provided to the structure, with narrow burner and fast growing fire, makes the pressure peak travelling faster inside the slab and rising to higher values. The last comparison for the two fire scenarios is done for the stresses

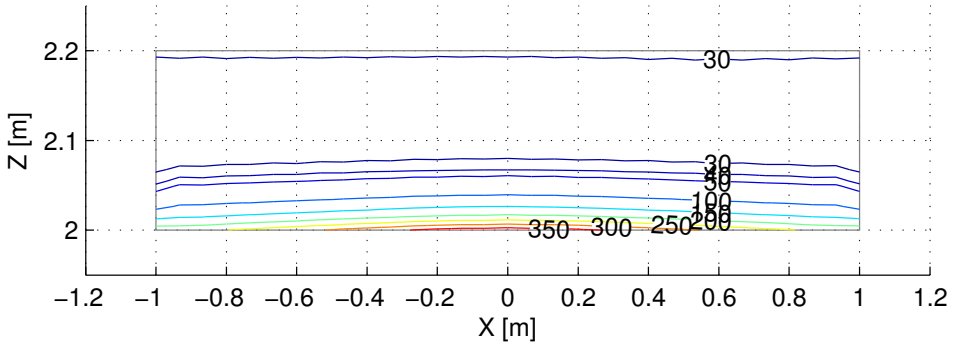

(A) Fast growth rate

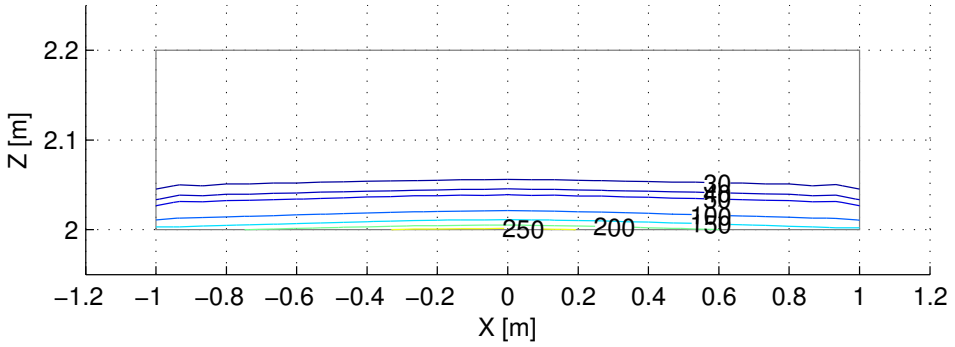

(B) Slow growth rate

FIGURE 4.35: Temperature distribution in the slab.

inside the material along the two axis XX and ZZ. The stress component parallel to the slab width is XX and is shown in figure 4.37

The stresses are similar among them, the upper layer and the lower layer of the slab are compressed, while the core is strained, figure 4.32. The mechanical load is the same of the previous case but the first layers exposed to fire are under compression. The maximum compression stresses are -31.98 MPa for the fast growing fire and -33.20 MPa for the slow growing fire. The compressed layer can break as a column subject to a buckling load, this kind of failure is also made more likely by the traction load in the other direction ZZ, figure 4.38. Near the heated layer of the slab there is a positive stress which pulls the outer layer away from the structure. The maximum traction ZZ stresses are 4.96 MPa for the fast growing fire and 5.60 MPa for the slow growing fire. The two stress component if combined together are both promoting the loss of material from the slab.

All the slabs, even if they are differently heated, show similar mechanical behaviours, the response of the structure in terms of stress is weakly influenced by the fire scenario. On the lower face of the slab there is always a compression stress parallel to the heated face and a traction stress in the opposite direction. Temperature and gas pressure, on the other hand, are strongly affected by the energy that is absorbed by the structure. In case of localized fire or fast growing fire the temperatures are much higher on the face exposed to fire, as well the high temperature fronts are deeper into the thickness of the slab. The high temperatures induce a pressure peak due to the movement of gas, evaporation and thermal expansion, therefore the

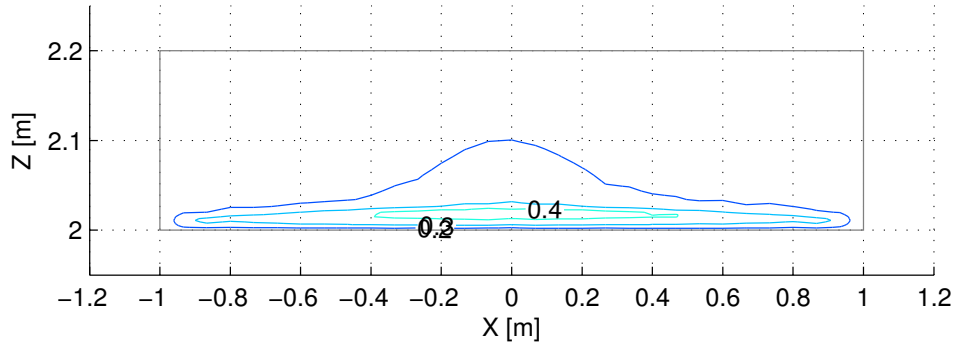

(A) Fast growth rate

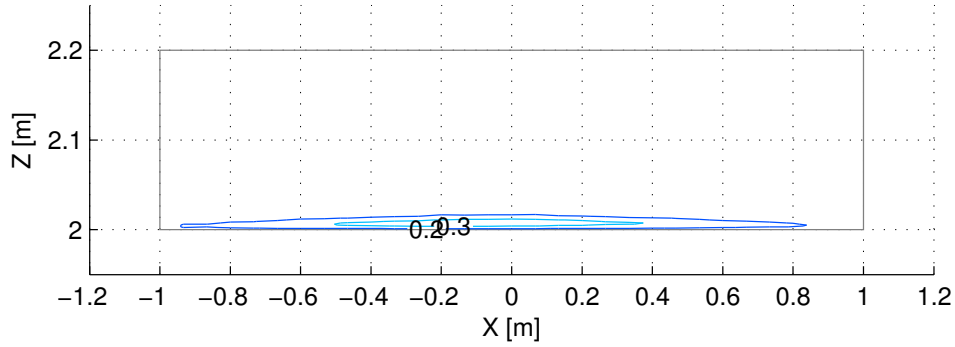

(B) Slow growth rate

FIGURE 4.36: Gas pressure distribution in the slab.

pressure peak is strongly affected by the fire scenario. In case of narrow burner and fast growing fire the pressure peak has higher magnitude and it is located deeper into the material.

The present comparison assesses the capability of this coupled analysis to evaluate the response of the concrete structure starting from different fire scenarios. As previously discussed the fire scenarios are designed starting from a common case which has a maximum power of 600 kW/m and an HRR per unit of are of 500 kW/m^2. Changing the HRR per unit of area or changing the fire growth rate there is not only an effect on the flow field but also on the whole structure exposed to fire.

4.4 Fire in a rail tunnel

After the comparison of a simple geometry which allows to test the capabilities of the coupled analysis, this is applied to a fire scenario in tunnel. The fire scenario is a rail coach on fire inside a rounded tunnel. The tunnel is several kilometres long so it cannot be modelled for the whole length. Since the aim of the study is to investigate the structural response of the tunnel's vault, only one portion of the tunnel is modelled with FDS. The study of a rail coach on fire aims to assess the effect of a real fire on the heat flux distribution and on the response of the structure itself. In the engineering practice some conservative temperature curves are used as thermal inputs

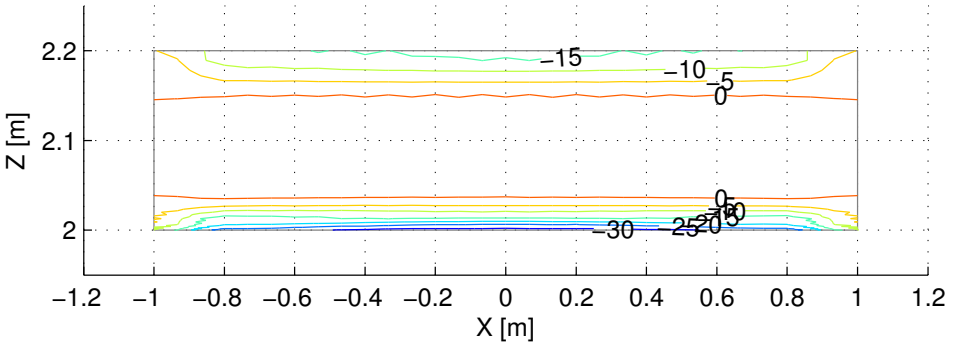

(A) Narrow burner

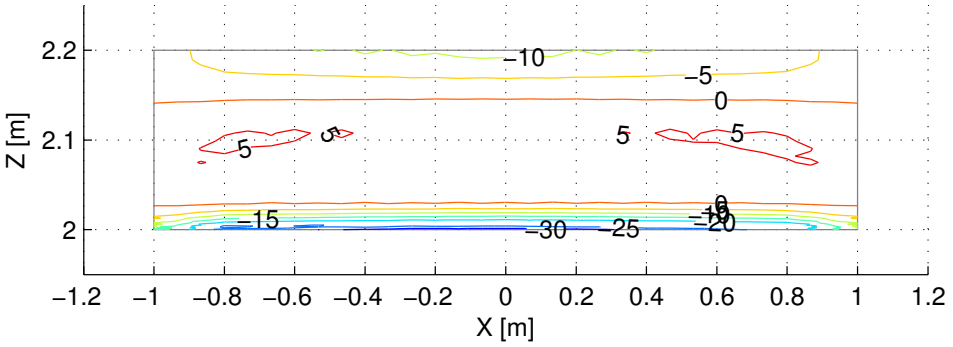

(B) Wide burner

FIGURE 4.37: Stress XX component distribution in the slab.

for the structural verification, section 1.3.1. These curves are applied uniformly on the structure since no information about the real distribution of the heat fluxes is available.

4.4.1 Fluid dynamic analysis

The tunnel investigated has a rounded cross section with different curvature radius, 9.6 m wide and 7.2 m high. The tunnel is 55 km long and due to the lack of information provided about the slope it is assumed to be horizontal. The tunnel is made of concrete so the walls are modelled as conductive surfaces, the properties of the concrete are defined according to the Eurocode [130] supposing to have a relative humidity of 80 % in the material and water content of 48.78 kg/kg. The density is constant equal to 2300 kg/m^3 and the specific heat and the conductivity are function of temperature, table 4.6. The wall is assumed to have emissivity equal to 0.9.

The tunnel is equipped with a fully transverse ventilation system, but due to the lack of informations about the location of the exhaust portals and due to the lack of informations about the extraction rate, the ventilation cannot be modelled properly. Also the uncertainty about the position of the fire with respect to the exhaust vent prevents from including the ventilation into the model, the portion of the tunnel simulated with FDS is assumed to be naturally ventilated. The case is non realistic for the smoke propagation,

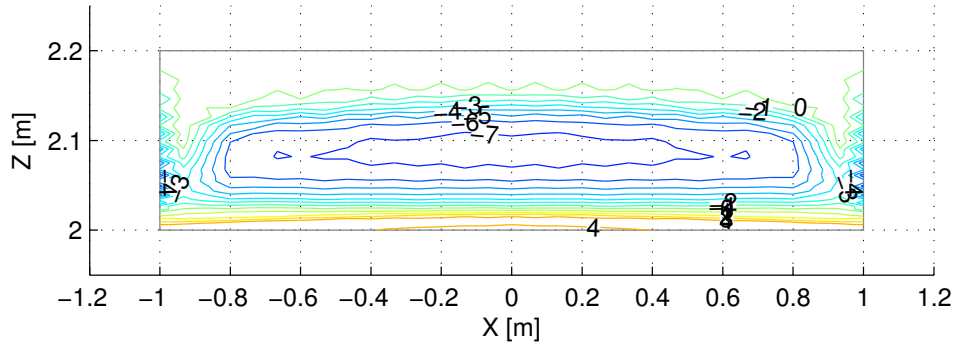

(A) Narrow burner

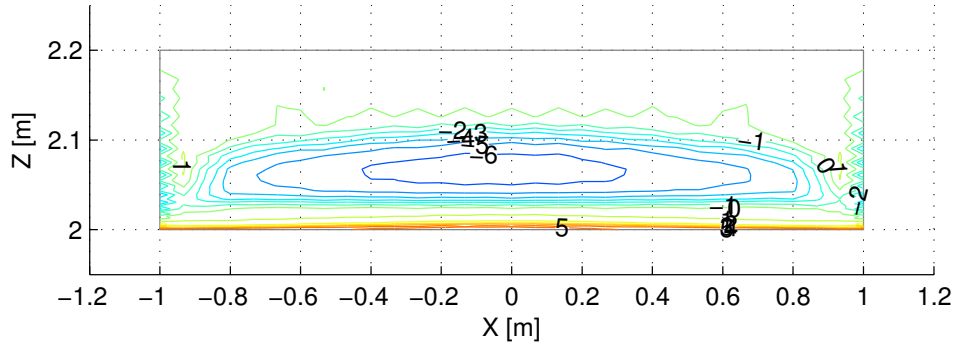

(B) Wide burner

FIGURE 4.38: Stress ZZ component distribution in the slab.

TABLE 4.6: Material's thermal properties modelled in FDS

Conductivity	
Temp. [°C]	k [W/m/K]
0.0	2.0
200.0	1.553
400.0	1.191
600.0	0.915
800.0	0.724
1000.0	0.619

Specific heat	
Temp. [°C]	C_p [kJ/kg/K]
20.0	0.9
100.0	0.9
101.0	1.47
115.0	1.47
200.0	0.98
400.0	1.045
1000.0	0.977

but the absence of ventilation should provide the worse case scenario, since the smoke is not exhausted from the tunnel and is not mixed with fresh air.

The fire load is a rail coach on fire, this is assumed to be 20 m long 3.2 m wide. The fire load is placed at 3 m high in order to consider an average height of the fire load inside the coach, which is supposed to be about 6 m high. In order to have a conservative estimation of the heat fluxes, the roof of the coach is not modelled, since this could act as radiative screen for the wall. The fire is not modelled as a unique burning block, but several smaller blocks are ignited in order to provide a more realistic approximation of the fire scenario. The HRR of the rail coach is designed starting from experimental tests carried out in real scale. Ingasson proposed a review of the these fire tests [12, 94] showing a wide spread in the maximum HRR value,

from 7 to 77 MW, and in the time required to the fire to reach the peak, from 5 to 80 minutes. The experimental data are referring to rail coach fire tests, [131–134], and to metro coach fire test, [132, 133, 135] The difference in the experimental values is caused by the high variability of the fire load, the ventilation condition and the fuel configuration. Also the construction features of the coach have an important influence on the fire scenario, if the coach is highly ventilated due to the windows' break the fire grows much faster. The fire scenario chosen for the simulation of the rail coach is the one tested in [135] because it is the most threatening for the structure and the tunnel has similar geometry to the case study, 6.1 m wide and 6.9 m high. The HRR curve used to simulate the fire scenario is presented in figure 4.39b. The fire curve has a initial phase where the fire grows slowly and later it ramps up to 60 MW in 600 s, it remains at the constant power of 60 MW for 600 s until 1200 s and later it decreases to 0 MW in the last 2400 s.

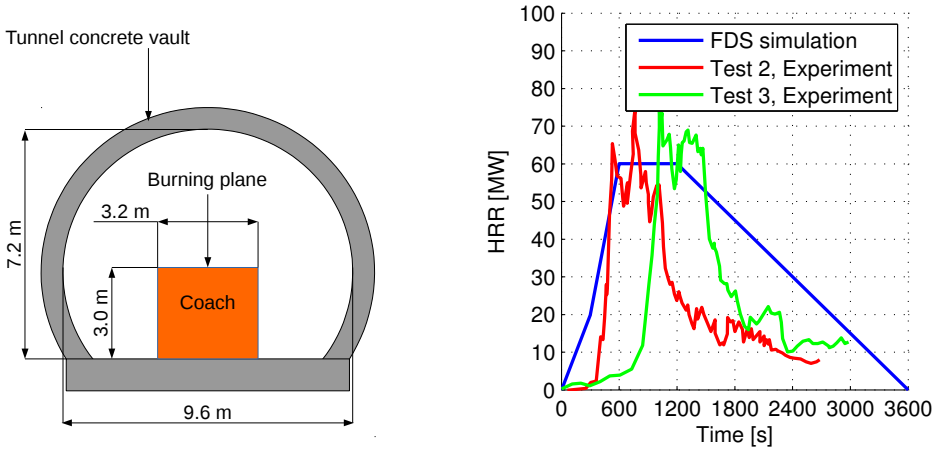

(A) Tunnel's cross section (B) HRR

FIGURE 4.39: Fire scenario investigate with the coupled approach

The combustion reaction is defined according to the paper of McGrattan [117] who investigated a rail fire in tunnel where a large spill of tripropylene caught of fire. The soot yield is set equal to 0.20 according to [117] this value is quite high and provides a conservative estimation of the smoke production. The CO yield is set equal to 0.05 which is an average value for plastic materials taken from [78] and the heat of combustion is set equal to 44.3 kJ/g.

As already mentioned the fire scenario is modelled considering a small portion of the whole tunnel where the coach on fire is simulated. The length of the simulated tunnel is 72 m and at the endings of the tunnel the pressure is imposed at the atmospheric value.

Before presenting the results of the simulations some preliminary analysis are performed in order to assess the reliability of the model presented. Due to the lack of experimental data referring to the specific case, the following parameters need to be investigated:

- Grid spatial discretization and radiative spatial discretization.
- Length of the tunnel's portion that is simulated with CFD.

- Height of the fire load.

The first point is related to the numerical discretion of the fire scenario, as seen before the grid's size is a key parameter for the simulation of the thermal load on structures. Three different mesh have been simulated considering a reduced portion of tunnel, in order to speed up the calculation, the effect of the tunnel's length is later investigated. The modelled portion of tunnel is just 24 m long in order to include the rail coach which is burned with a constant HRR of 60 MW for 500 s. The features of the mesh tested are listed in table 4.7.

TABLE 4.7: Mesh data

Mesh	El. size [m] (x,y,z)	N. of El	$D^*/\delta x$
Mesh 1	$0.200 \times 0.200 \times 0.200$	207360	24.66
Mesh 2	$0.150 \times 0.150 \times 0.150$	491520	32.88
Mesh 3	$0.100 \times 0.100 \times 0.100$	1658880	49.32

The temperatures above the fire are compared together along the height of the tunnel at the centre of the coach. Figure 4.40a shows that the temperature rises above the coach where the combustion occurs, the temperature profiles are in good agreement among them and show minor differences along the height of the tunnel. The mesh is already quite refined therefore the results are supposed to provide reliable results. The AST are compared as well along the ceiling at the tunnel's middle line, figure 4.40b. In the second comparison there are some more discrepancies between the grids, in particular the coarser mesh overpredicts the AST if compared to the others. Mesh 2 and 3 are in good agreement among them, therefore the mesh 2 is selected for the other simulations. For every mesh $D^*/\delta x$ is higher than the suggested value, 16, but for this specific case a much finer mesh is required to simulate the incident heat fluxes.

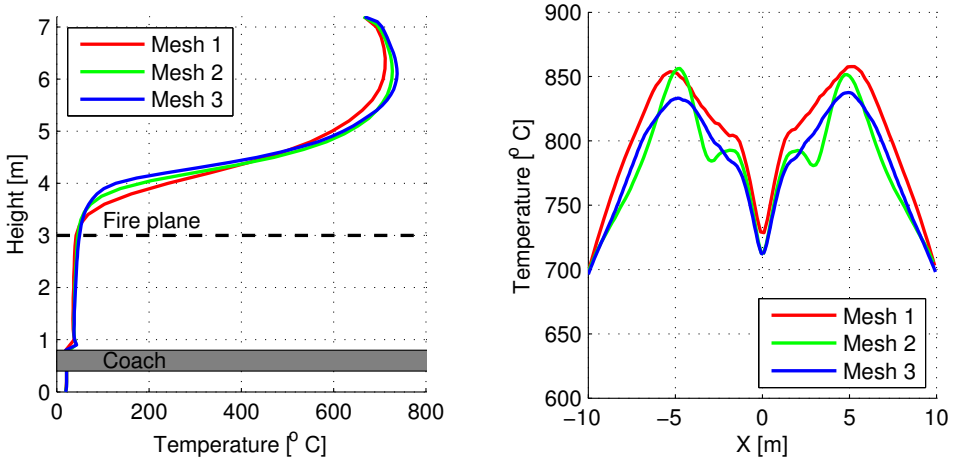

(A) Gas temperature (B) Adiabatic Surface Temperature

FIGURE 4.40: Temperature comparison for the mesh independence study

After evaluating the correct mesh size, the number of angles necessary to simulate the radiative heat flux is evaluated. Using mesh 2 and the short

domain with a length of 24 m the scenario is simulated with different radiation angles. This parameter is set by default to 100 in FDS so 300 and 1000 angles are used in two other simulations in order to assess the influence of the parameter. As done for the mesh independence study the gas temperature above the fire and the AST along the ceiling of the tunnel are compared together for the different simulations, figure 4.41.

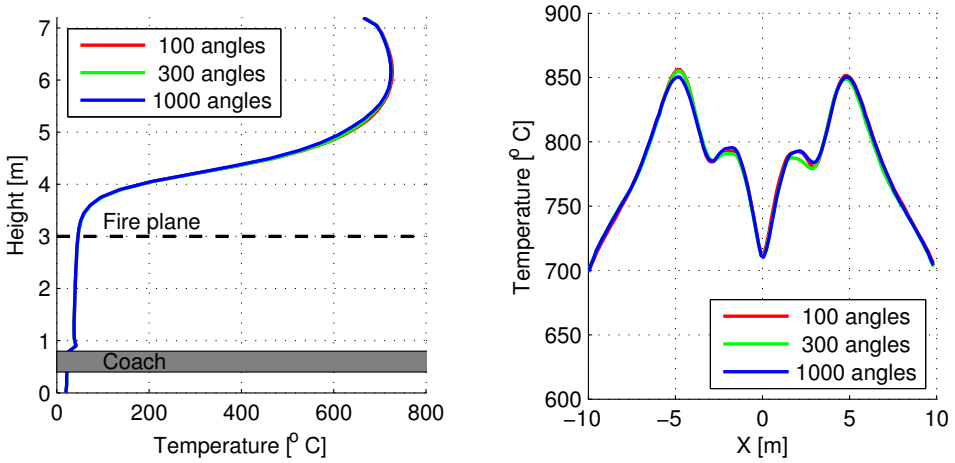

(A) Gas temperature (B) Adiabatic Surface Temperature

FIGURE 4.41: Temperature comparison for the radiation angle independence study

For different radiation angles the results are overlapping, gas temperatures and AST beneath the ceiling don't show any significant difference. The default number of angles as suggested by McGrattan [50] is sufficient for a correct radiation resolution so 100 angles are used for the next simulations.

In the present model due to the length of the real tunnel it is not possible to simulate the whole structure, moreover this is out of the scope of the present simulation. However the boundary conditions have a strong influence on the flow field near the fire. From the open portals fresh air flows towards the fire region, while in case of real fire the smoke, propagating in the tunnel, heats up the air that undergoes later to combustion. There is also an effect of re-radiation of the heated walls on the others which is neglected if the boundary conditions are placed to close to the fire. In order to evaluate the minimum length of the tunnel which should be simulated in order to not have a strong influence of the boundary conditions, tunnels with different lengths are simulated. The fire scenario is the same that has been previously presented, just two portions of tunnel are added on the sides in order to provide an additional domain where the flow can develop. The tunnel initially has been simulated with 24 m length, which was the minimum length capable to include the whole coach in the domain, later 72 m and 120 m are simulated. The domain is equally divided on the two sides of the tunnel and the results are presented as done before for gas temperature and AST.

The gas temperature in the centre of the coach shows some minor differences, which are always smaller than the differences in the AST, figure

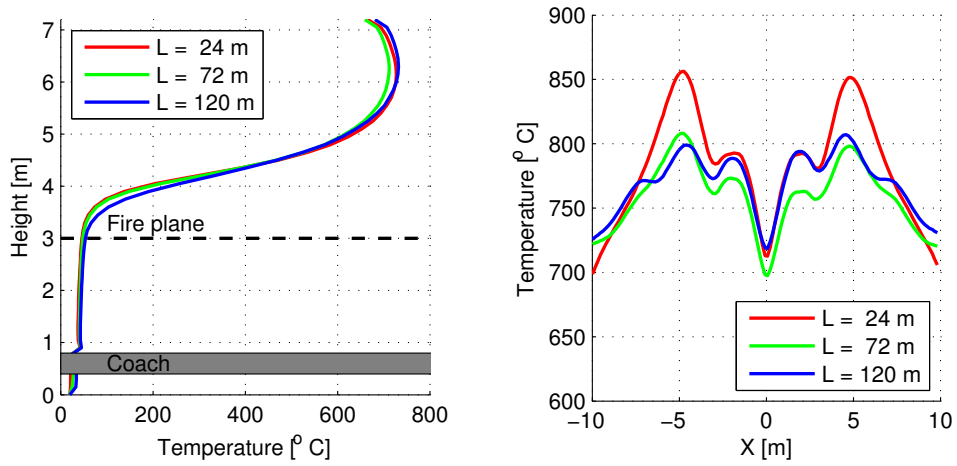

(A) Gas temperature (B) Adiabatic Surface Temperature

FIGURE 4.42: Temperature comparison for the length independence study

4.42. The comparison shows that with a short domain the AST in the fire region are overestimated if compared with the two other longer tunnels, figure 4.42b. These are in good agreement between the tunnels 72 and 120 m long. The initial length of the model is unsuitable to simulate the fire scenario, but with an extension of the domain the boundary conditions don't affect the result of the calculation.

The gas temperature obtained in figure 4.42a are lower than the experimental values measured in [135]. One reason of the difference could be the insulation of the walls. The tunnel used for the test was insulated with U Protect Wired Mat 2.0 which reduces the heat losses through the vault and consequently rises the temperature in the tunnel. As seen in section 2.5.3 the wall's thermal properties have a strong influence on the temperatures inside the tunnel, since they limit the heat losses and the cooling of the gas. One other aspect that may be different between the test and the simulation is the distance between the fire load and the ceiling. The free space between the fire source and the ceiling is another important parameter influencing the thermal load on the walls. The tunnel's vault confines the gas in a small volume where the temperature can rise higher and the hot surfaces re-radiate on the gas which is further heated. This effect has been seen clearly in the Runehamar tunnel test [14] where temperature reached 1300 °C because of the high insulation of the walls, covered with protecting boards, and because the fire load is placed right beneath the ceiling. The effect of the distance between the fire and the ceiling has been investigated by Li in [33] showing that the temperature beneath the ceiling increases when the distance decreases. The fire load previously studied is therefore placed at different heights and the temperatures are compared for three different cases, figure 4.43. The fire load is placed at 3.0 m in the original case and later moved to 4.5 and in the last case to 6.0 m. The temperature profiles along the tunnel's height show that the distance between fire load and ceiling is a key parameter for the thermal load calculation on the walls. The maximum temperature for a fire placed at 3.0 m height is 727

°C, while for 4.5 and 6.0 the maximum temperatures are 1048 °C and 1034 °C, figure 4.43a. The AST obtained with higher fire loads are higher than the initial case, which has a peak of 856 °C, for burner placed at 4.5 and 6.0 the maximum temperatures are 1121 °C and 916 °C, figure 4.43b. From the comparison of the AST the fire load placed at 6.0 m induces lower temperatures compared to the fire load at 4.5 m. When the fire load is too high the combustion cannot occur only above the coach but the fuel burns also out of the coach. This effect is clearly depicted by the shape of the temperature profile, which is higher on the sides than in the centre.

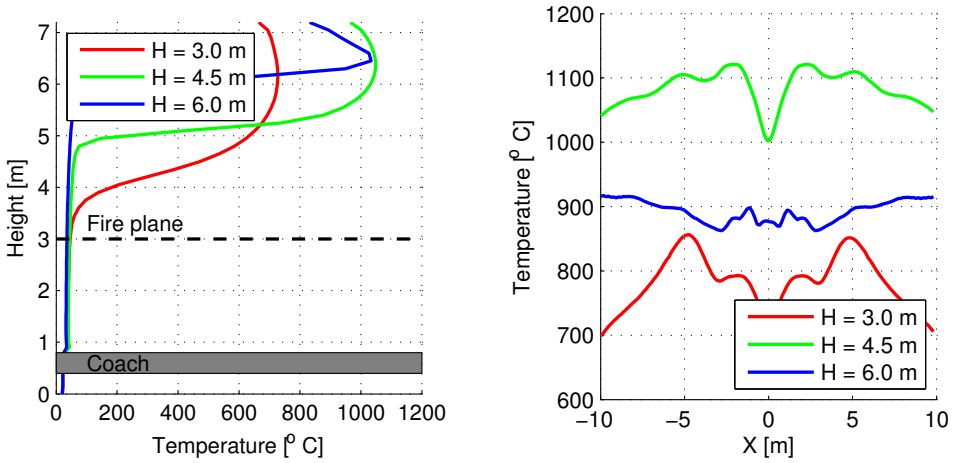

(A) Gas temperature (B) Adiabatic Surface Temperature

FIGURE 4.43: Temperature comparison for the evaluation of the height's effect

The evaluation of different numerical parameters allows to correctly set up the simulation that is later used to define the boundary condition for the structural problem. In order to show the temperature distribution in the tunnel the flow field is presented along two planes. The temperature above the rail coach rises up to 800 °C and from figure 4.44 it is possible to see the flow field induced by the fire.

The fresh air that undergoes to reaction comes from the bottom of the coach and flows up into the fire region, figure 4.44a. The smoke flows along the tunnel in a symmetric way upstream and downstream the fire generating two large eddies. The flow field depicts the influence of the fire modelling, using many small obstacles to model the burning objects the air can reach the centre of the fire with a larger reaction zone. Similar approach has been used to simulate solid objects burning in [136, 137] in order to provide a more realistic modelling of the fire.

4.4.2 Structural analysis

The fire scenario proposed in the previous section is used to calculate the boundary conditions for the structural analysis of the tunnel's vault. The structure is modelled considering only half of the vault since the temperatures and the thermal load are symmetrical on the cross section of the tunnel, figure 4.44b. The tunnel's vault is not modelled for the whole depth of

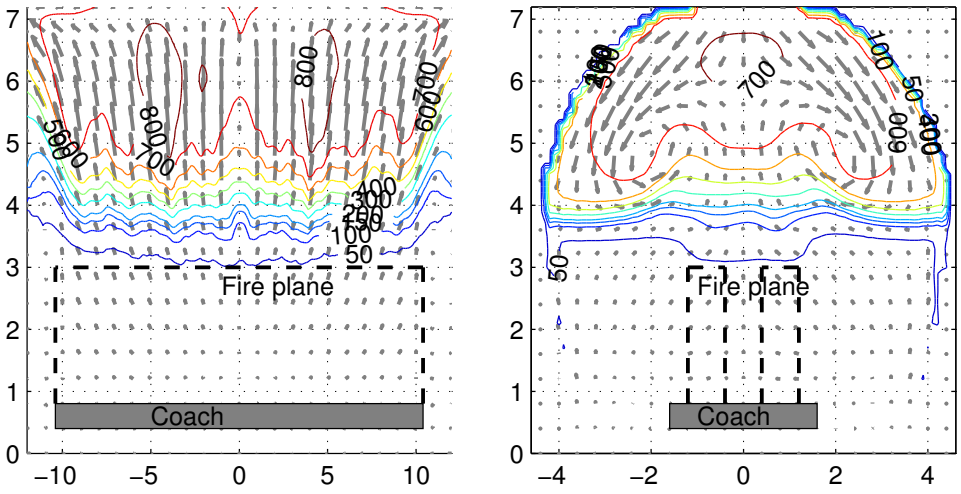

(A) Tunnel longitudinal section (B) Cross section

FIGURE 4.44: Temperature field in the tunnel near the coach

the structure but only for 0.3 m considering that the high temperature front is not crossing such distance. The tunnel is made of C60 concrete with a relative humidity of 80%, this high value is considered to be reasonable if the tunnel is located in wet soil. The water saturation of the material is 56% at the initial stage of the calculation, the temperature is 20 °C and the gas pressure is 101325 Pa. The tunnel is mechanically constrained as in figure 4.45a in order to simulate the symmetry boundary conditions. The outer part of the vault is supposed to be self standing therefore only the gravity force is added as mechanical load.

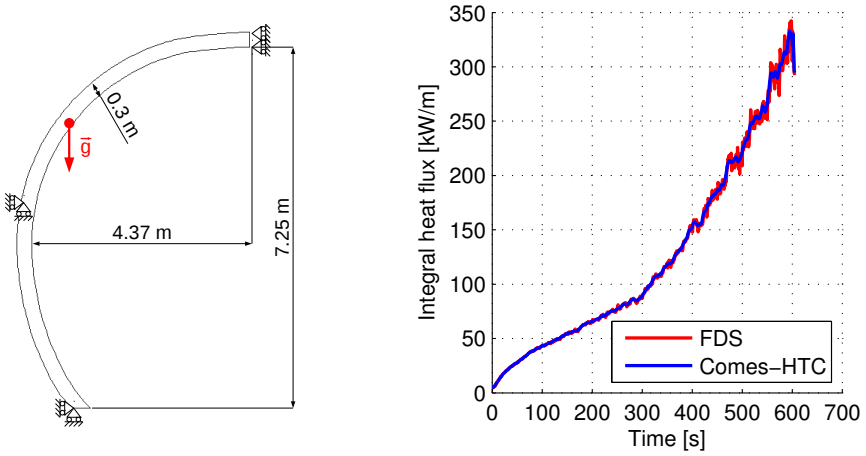

(A) Structure's geometry (B) Integral incident heat flux

FIGURE 4.45: Tunnel geometry and heat flux balance

As seen in the structural analysis of the slab exposed to fire, one of the main issues of the coupling is the correct transfer of the energy released in FDS and imported in Comes-HTC. In case of the slab the geometries are corresponding and there is no error in the fluxes interpolation, however in

this fire scenario the tunnel is rounded and the geometry of the vault is approximated with many square elements. The interpolation process has a key role in the coupling of the two codes, therefore the integral incident flux obtained in FDS and in Comes-HTC are compared together in order to verify the correctness of the calculation. From figure 4.45b it is clear that the integral heat flux is correctly transferred from FDS to Comes-HTC.

After verifying the correct interpolation of the integral heat flux the overall response of the structure is presented as function of time. The maximum temperature is monitored every time step in order to see the heating up of the vault. At the initial stages the temperature grows up slowly considering the initial phase of the HRR, but after 300 s the temperature starts growing faster, figure 4.46a. The rise of the temperature follows the maximum heat incident heat flux on the section, this is plotted in figure 4.46b. The incident heat flux has a steep rise after 300 s leading to a fast heating of the structure. After 600 s the incident flux reach a steady value since the HRR reaches a plateau in this phase.

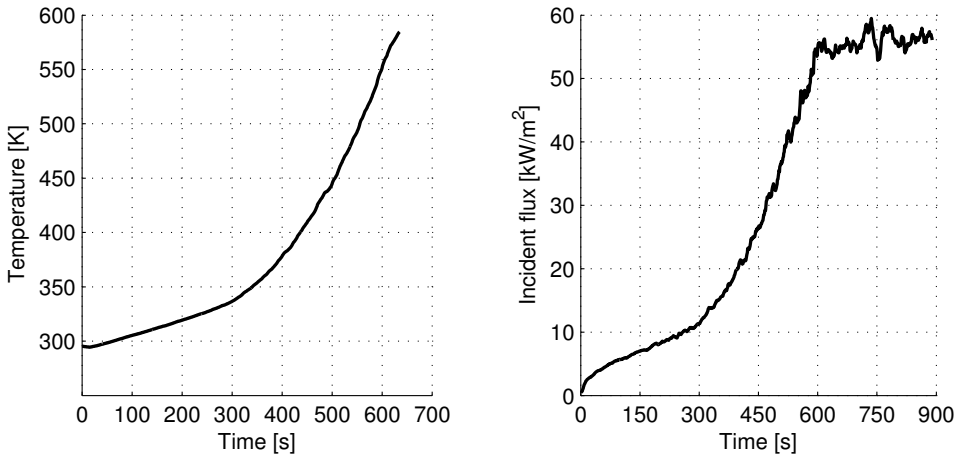

(A) Structure's geometry (B) Integral incident heat flux

FIGURE 4.46: Time history of the tunnel on fire

The maximum gas pressure in the structure is monitored during the fire, showing a flat trend in the initial phase of the fire, while when the temperature rises, after 300 s, also the pressure grows. The curve shows also some peaks after 600 s when the maximum pressure is over 1.6 MPa, this sudden pressure rise can be consequence of a low damaged material which still has low permeability and is strongly heated [138]. The pressure later drops due to the damaging of the structure and the increase of the intrinsic permeability, allowing the gas to flow out of the structure. The presence of more peaks can be explained by the pressure rise in different points on the structure.

The maximum mechanical damage is presented as function of time for the whole structure, this grows regularly and doesn't show the oscillations that occur for the gas pressure. The damage is zero in the first phase of the simulation, it starts to grow only after the structure heats up, after 470 s.

After presenting the overall response of the structure the analysis focus on the response of the structure after 300 s and 600 s. Unfortunately numerical issues rose in the simulation therefore the results are limited at 638 s.

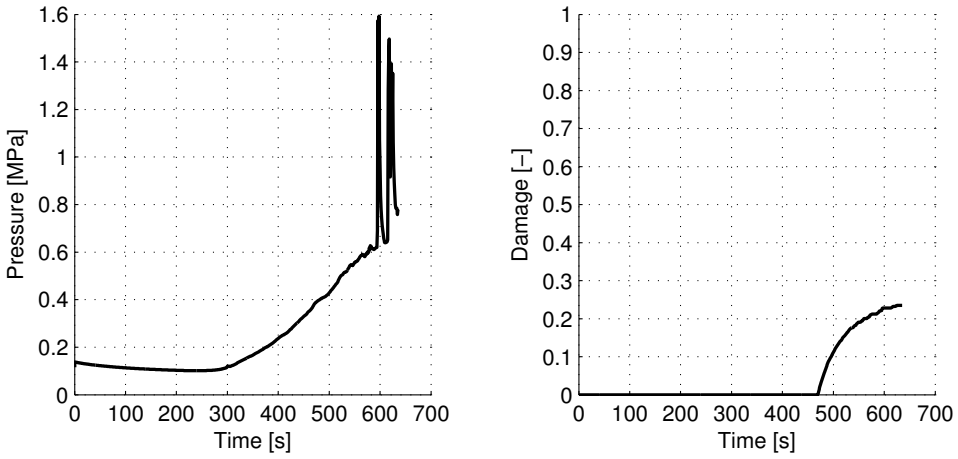

(A) Gas pressure (B) Mechanical damage

FIGURE 4.47: Time history of the tunnel on fire

However these are sufficient to highlight the capability of the coupled tool to set a map of boundary conditions which is directly related with the fire scenario. After 300 s of fire, the heat flux distributions obtained with FDS and for Comes-HTC are presented in figure 4.48a. The maximum flux is located near the top of the ceiling, while the values are lower near the bottom of the structure. The heat flux distribution is presented also as function of the angle θ which is centred on the symmetry axis at the height of 3.4 m, figure 4.48b. The plot shows that the flux distribution obtained after the interpolation is smoother than the original one in FDS and both distributions have the same trend.

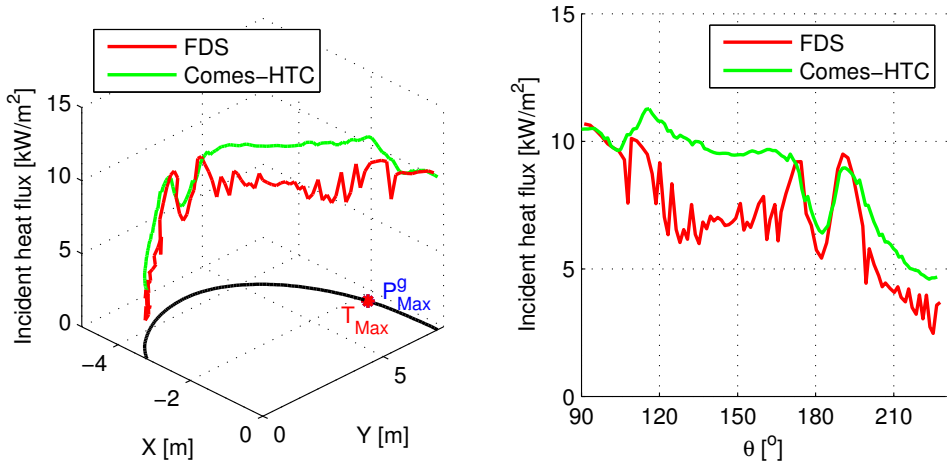

(A) As function of the position (B) As function of θ

FIGURE 4.48: Incident heat flux distribution after 300 s

The temperature inside the structure is presented at three location as function of the structure's depth. The points are chosen in order to show the different thermal loads on the structure, one on the side of the structure at θ equal to 180° one on the top of the structure at θ equal to 90° and one located

where the maximum temperature occurs, θ equal to 116°. The maximum temperature reaches 61.96 °C, this value is still low and is consequence of the HRR which doesn't grow fast in the first stages of the fire. On the side the maximum temperature is 42.91 °C and on the top 53.10 °C. The gas pressure rise is also really small, since the values are almost at the ambient value, the structure is still cold and the water is not evaporated yet. The pressure rise is mainly driven by the gas expansion. The maximum values of pressure are 0.1116 MPa, 0.1013 MPa and 0.1037 MPa respectively in the location of the maximum pressure, on the side and on the top of the vault.

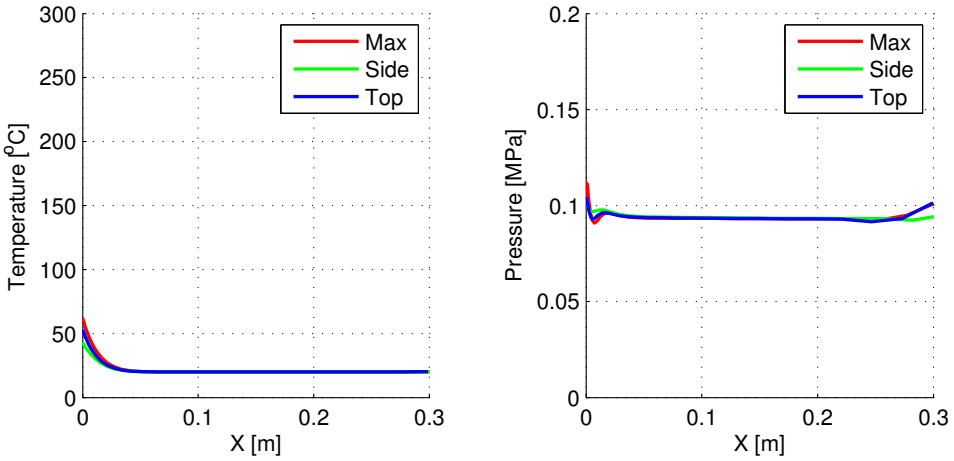

(A) Temperature (B) Gas pressure

FIGURE 4.49: State of the structure after 300 s

The structure is affected by the thermal load and by the mechanical load induced by its own weight. The stresses obtained on the side of the vault and on the top are presented along the thickness of the structure. The stresses are calculated parallel to the vault and normal to the vault in order to take into account the effect of the curvature. The tangential stress, parallel to the tunnel's surface, is negative on the side exposed to fire, the maximum compressive stress is -11.85 MPa on the side and -14.39 MPa on the top. As seen in the previous analysis the thermal expansion constrained by the rest of the structure induces a compressive stress in the heated layers. The damage in the material is presented as well for the three sections previously selected. After 300 s, the damage is still small with a maximum of 0.0443, the damage at this stage of the simulation is consequence of the thermochemical degradation of the material, because as seen in figure 4.47b the mechanical damage is still 0.0. Since the temperature is the only parameter driving the mechanical damage in the material the most damaged section occurs in the same section where the temperature is maximum.

These results show that the structure after 300 s is still cold with low pressure and stresses, but the temperature rises in the next seconds and after 600 s the maximum temperature is about 276.71 °C. The pressure shows also a steep rise and sudden peaks occur in the structure. The thermal load in this phase is much higher due to the greater HRR with a maximum of 54.73 kW/m^2. The incident flux in case of fire is not uniform on the structure and the maximum it is localized near the top where the flames impinge

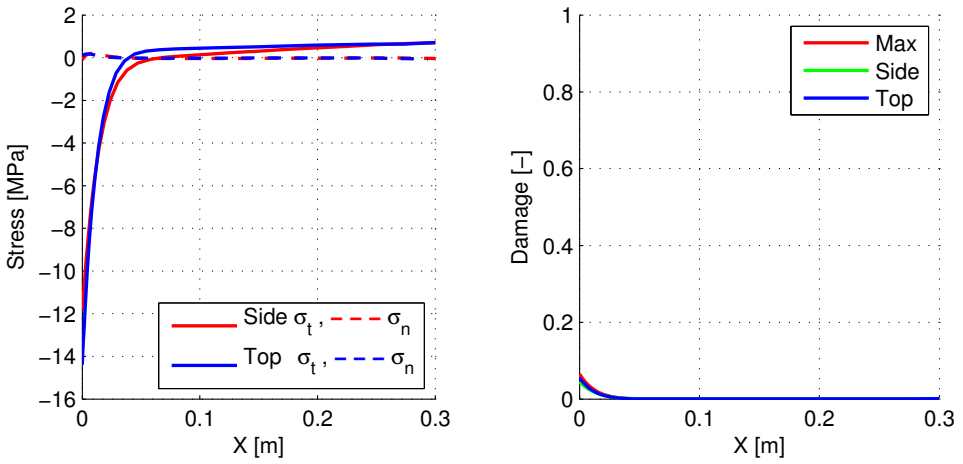

(A) Stresses (B) Total damage

FIGURE 4.50: State of the structure after 300 s

the ceiling, figure 4.51a. In the lower part of the structure, near the floor, the heat flux is minimum, 13.53 kW/m^2, therefore the ratio between the maximum and the minimum flux on the section is 4.04. The heat fluxes presented as function of the angular position are similar in the two programs and both decrease moving from the ceiling of the tunnel to the floor, figure 4.51b.

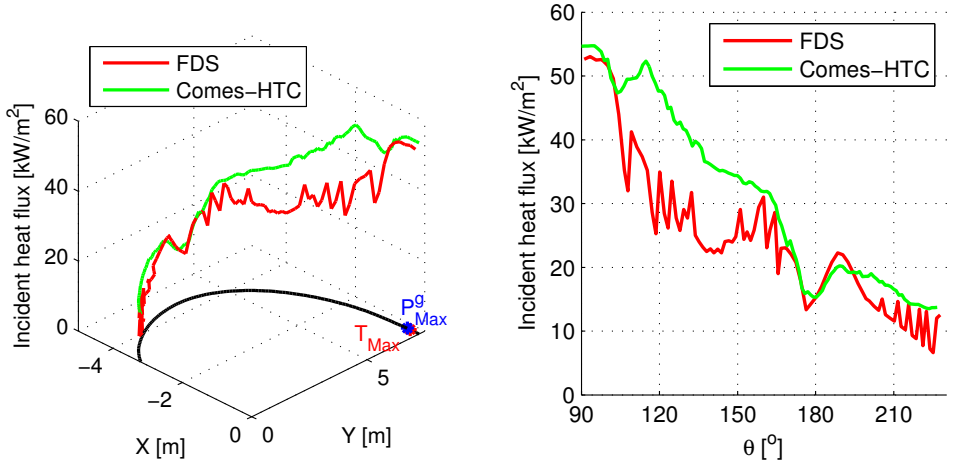

(A) As function of the position (B) As function of θ

FIGURE 4.51: Incident heat flux distribution after 600 s

The temperature inside the structure is presented in three sections, on the side of the slab on the top and where the maximum temperature occurs. The temperature are plot as function of the depth inside the vault. After 600 s the temperatures in the material are much higher on the whole vault, in the maximum heated point the temperature rises up to 276.71 °C, but the whole upper part of the tunnel is much warmer since also on the top the temperature is 276.16 °C. The maximum heated point is close to the top of the structure with a angle θ equal to 94°. The smaller heat flux on the lower

part of the tunnel doesn't rise the temperature to the level of the upper layer and on the side the temperature is 116.65 °C. The high temperature also induces large evaporation of moisture which expands and rise the gas pressure in the structure. After 600 s the pressure is over 1.0 MPa on the upper part of the tunnel, with a maximum pressure equal to 1.0675 MPa and a maximum pressure on the top of the tunnel equal to 1.0444 MPa. On the side of the slab the lower temperature and the smaller heat flux induce a smaller pressure rise with a peak equal to 0.2597 MPa.

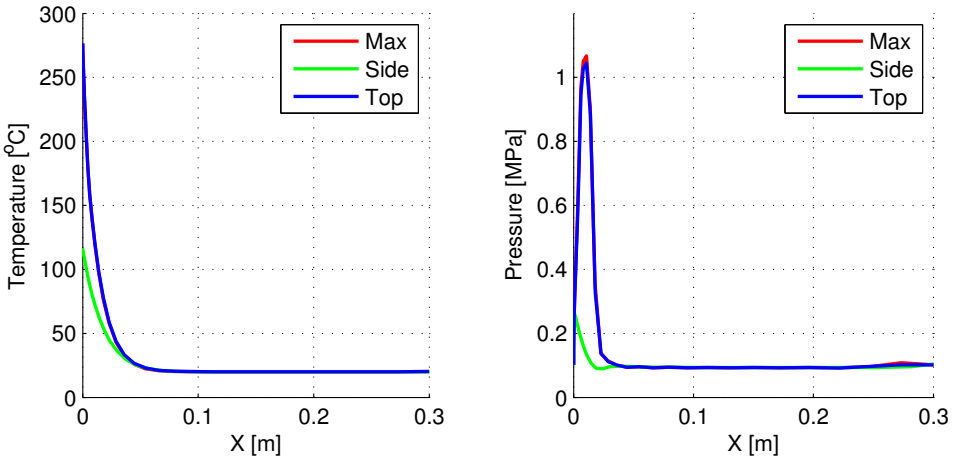

(A) Temperature (B) Gas pressure

FIGURE 4.52: State of the structure after 600 s

The structure is warmer after 600 s and the pressure rises in the material opening the pores of concrete. The stresses in the structure along the vault of the tunnel and normal to it are presented in the sections on the top and on the side of the tunnel, figure 4.53a. The maximum compressive stress that was already evident after 300 s rises in magnitude and on the top of the structure reaches -52.74 MPa, while on the side it rises up to -35.57 MPa. The compressive stress on the top of the structure is consequence of the strong heating of the wall and the constrained expansion of the first layers. On the side the effect of the weight of the structure is added to the effect of constrained expansion. In the other direction, normal to the surface, the stress is positive on the top of the structure, the traction stress tends to pull out the material increasing the risk of failure due to spalling. The maximum stresses on the side of the structure and on the top are 1.31 MPa and 4.60 MPa. The lower part of the structure is much less threatened by spalling than the top part. The effect of the heating and the stress in the structure increase the damage inside the material, figure 4.53b. After 600 s the mechanical damage is greater than zero and it combines with the thermochemical degradation, the damage is presented at different locations along the thickness of the structure. The maximum damage occurs at the section with the maximum temperature and it reaches 0.5019, on the top of the ceiling the damage is 0.5017, which is really close to the maximum value considering that also the temperatures are almost at the same level. On the side of the structure the damage is smaller and it reaches only 0.1498 showing the effect of a localized heating.

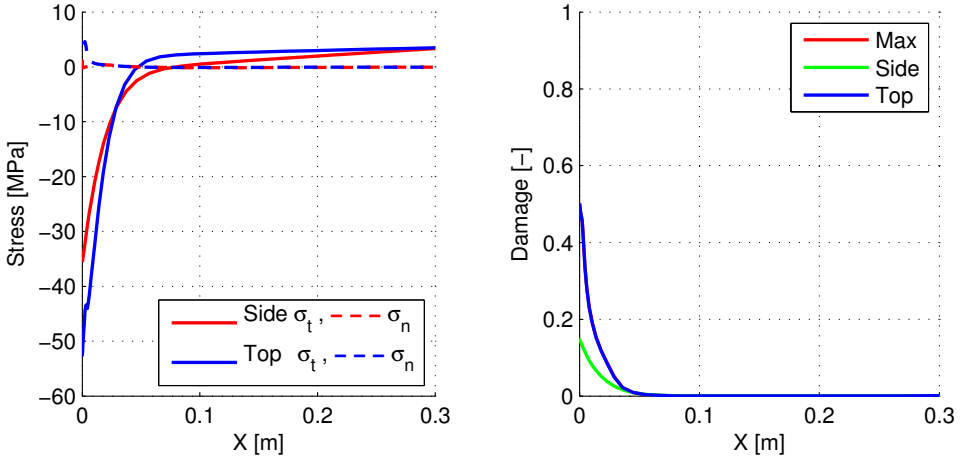

(A) Stresses (B) Total damage

FIGURE 4.53: State of the structure after 600 s

The present comparison shows the capabilities of the coupled analysis for a complex structure, like a tunnel exposed to fire. The boundary conditions imposed on the structure are directly related to the fire scenario with a stronger heating on the top part of the tunnel and a lower part which is colder. In the tunnel vault the stress distribution, the pressure peak and the material damage combine together in the upper part of the tunnel and increase the risk of spalling.

The analysis still presents some instabilities in the structural calculation which prevent to complete the whole simulation. Further development are now under test in the model in order to deal with those instabilities.

4.5 Two ways coupling verification

The previous calculations have been carried out simulating the fire scenario in FDS and later simulating the response of the structure in Comes-HTC. The results are transferred from FDS to Comes-HTC, but they are not transferred back, assuming a negligible influence of the structure's modelling on the flow field. It is necessary to verify how the new temperatures obtained in the structure affect the temperature field in the fluid simulation. From the structural analysis the new surface temperatures and the structure's displacements can be imported in the fluid model. In the two way coupling verification it is necessary to link properly the nodes of Comes-HTC with the elements of FDS. This cannot be done for rounded geometries because the interpolation approach proposed in section 4.1.1 is not designed to work in both directions and could induce large errors. It is thus required to use two geometries that are corresponding in FDS and in Comes-HTC, in order to prevent numerical errors in the coupling of the codes.

The slab exposed to fire previously studied in section 4.3 is perfectly suited for the two way coupling process, since the geometry is rectangular and there is direct link between nodes and elements. The two way coupling is tested considering the fast growing fire scenario burning for 900 s, with a constant HRR of 600 kW/m. The one way coupling from FDS to

Comes-HTC has been already investigated in the previous sections now the coupling of Comes-HTC with FDS needs to be investigated. First, the simulation in FDS runs using the wall model embedded in FDS with a pure conductive calculation. The wall properties are defined in table 4.4 according to Eurocode [130]. From the FDS simulation the results are used as boundary conditions for the structural simulation in Comes-HTC. With the two way coupling approach, the wall temperatures obtained in Comes-HTC are used as new wall temperatures in FDS. The FDS simulations is reran with the new boundary conditions obtained from the structural analysis calculating the new boundary conditions for Comes-HTC. The flow field and the structure continue to be updated until the results are corresponding between to successive iterations.

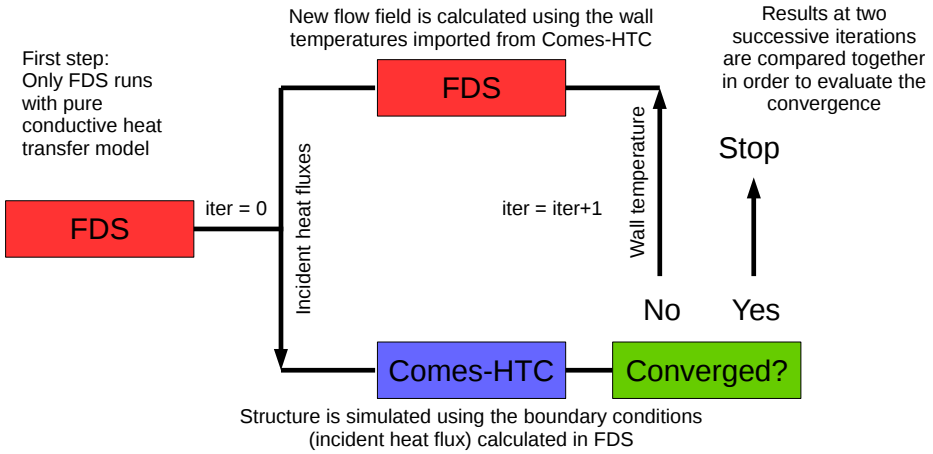

FIGURE 4.54: Two way coupling approach the thermo-structural interaction

The basing scheme of the two ways coupled approach is presented in figure 4.54, but it is necessary to explain also in practice how the coupling has been implemented. The simulations both in FDS and in Comes-HTC run for the whole duration of the fire, 900 s, later the boundary conditions are exchanged from one program to the other and the new coupling iteration is performed. The coupling doesn't link step by step FDS and Comes-HTC because this would required a much larger numerical effort. The boundary conditions for the structural problem are imposed as Robin boundary conditions, these have been widely discussed in 4.1. For the fluid dynamic calculation the wall temperatures are set as boundary conditions, instead of the conductive wall model. The temperature history obtained with Comes-HTC is imposed as a temperature ramp on every element of FDS. The temperature ramp is calculated basing on temperature time history of the corresponding node in Comes-HTC.

In order to assess the convergence of the method it is necessary to compare the simulations at two consecutive iterations, if these are within a certain tolerance then the loop can be exited. In order to compare the simulations the temperatures in the gas and in the material are used. The gas temperatures along the centreline of the fire are compared for three different iterations, the first one with the pure conductive model in FDS and the others with the wall temperature calculated with Comes-HTC.

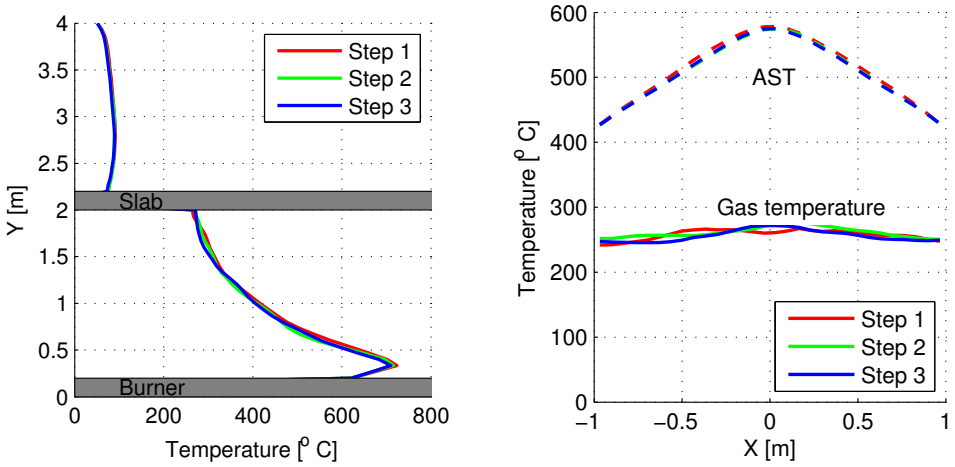

(A) Above the fire (B) Beneath the slab

FIGURE 4.55: Temperature comparison for different loop iterations

The comparison shows that the gas temperatures along the centreline of the flame for the different loops are overlapping, figure 4.55a. Taking a closer look beneath the ceiling, where the influence of the slab modelling should be maximum, the gas temperature profiles show minor differences in the temperature distributions, figure 4.55b. The maximum values for the three iterations are 267.39 °C iter. 1, 276.00 °C iter. 2 and 271.80 °C iter. 3. The difference for the three iterations are within 10 °C which is the 3% of the maximum temperature beneath the ceiling. The AST show a good agreement between the different iterations, figure 4.55b, the maximum is really close for the three iterations: 578.28 °C, iter. 1, 575.02 °C iter. 2 and 574.89 °C. iter. 3. In this case the difference is within 4 °C corresponding to the 0.56% of the maximum temperature.

In the two way coupling the integral heat flux has to be the same for the different iterations once the loop is converged. The comparison of the integral heat flux at different iterations ensures that the loop don't create energy sinks or sources. The integral heat fluxes at different iterations are really close despite the time fluctuations, figure 4.56a. The average value of the integral heat fluxes are 69.25 kW/m for iter. 1, 69.32 kW/m for iter. 2 and 69.42 kW/m for iter. 3.

The wall temperatures are compared for the different iterations in figure 4.56b, the wall temperature is evaluated in FDS on the lower face of the slab above the fire centreline. The temperatures for step 2 and 3 are the results of the Comes-HTC simulations at the steps 1 and 2, while the temperature at step 1 is the result of the FDS conductive model. It is clear that FDS simulations at steps 2 and 3 work with the same wall temperatures. But more important the temperatures of steps 2 and 3 are already obtained with the structural calculation after step 1. The temperature beneath the slab on the most heated point are overlapping for the last two steps, therefore the first simulation of the concrete slab is already capable to calculate the converged wall temperature. The temperature field inside the slab evaluated along the

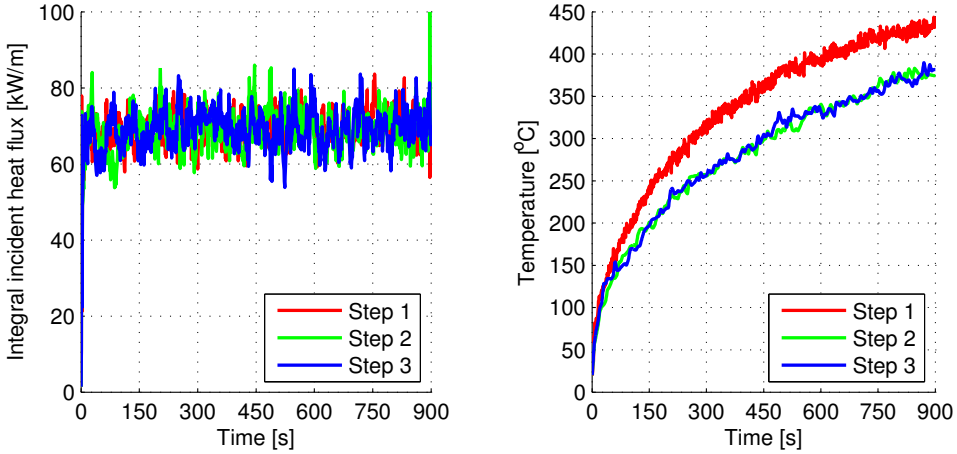

(A) Integral incident flux

(B) Wall temperature

FIGURE 4.56: Integral heat flux and Wall temperature for different loop iteration

thickness is presented for the different steps in figure 4.57a. The temperatures are evaluated at the end of the simulation after 900 s and they show a good agreement. The maximum temperatures are the different steps are 376.75 °C for iter. 1, 385.32 °C iter. 2 and 390.57 °C iter. 3. The results in Comes-HTC are already converged after the first iteration. This is important because the one way coupling, previously investigated, is sufficient for the calculation of the structural response and no further iterations are needed to consider the effect of the different wall modelling.

A two way coupled analysis is usually required for problems with large displacement, Silva proposed for steel structures a coupled analysis FDS FEM with two ways coupling approach[1]. The large displacements of steel structures exposed to fire can modify significantly the geometry of fluid domain so affect the flow field. The maximum displacements are monitored for the concrete structure in order to assess if the displacement is large enough to affect the geometry of the fluid domain. The maximum displacement occurs in the middle of the slab at the lower face because of the bending of the slab symmetrically loaded, figure 4.57b. The displacements for the different cases are overlapping but the most interesting data about the graph is the magnitude of the displacement. The maximum displacement on the slab is -0.0043 m, which is the 0,215 % of the slab length, the new geometry of the slab after 900 s is really similar to the initial one. Moreover the displacement cannot be modelled with the actual mesh because the elements have a edge size equal to 0.067 m.

The two ways coupling analysis shows that for concrete structures the results obtained after one coupling iterations are already already close to the final values. Further iterations in the coupling imposing the results obtained with the structural calculation don't improve the quality of the result. It is thus reasonable to use the simpler approach proposed in section

[1]There are no articles about the topic yet, but it is under development in FDS repository, https://github.com/firemodels/fds/tree/master/Utilities/Structural_Interaction/twowaycode.

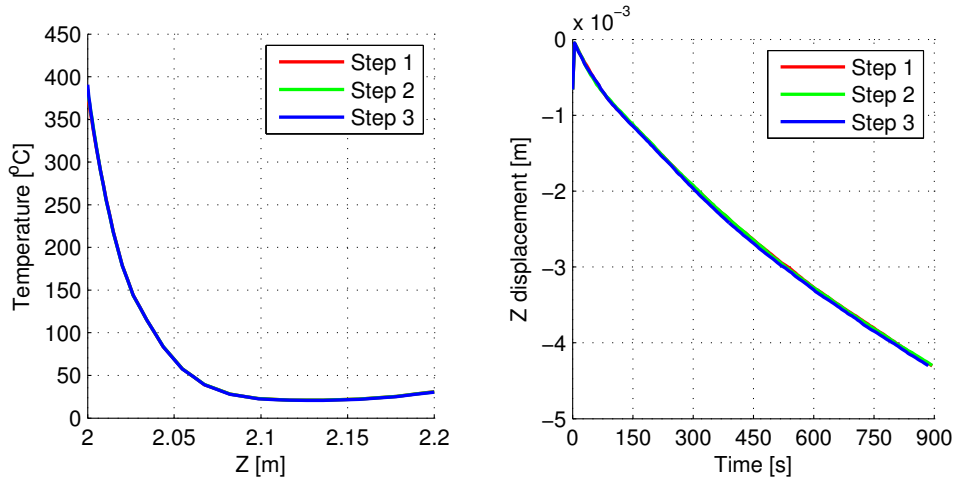

(A) Temperature along the slab (B) Displacement

FIGURE 4.57: Temperature along the slab and displacement for different loop iterations

4.1 which is also more flexible since it doesn't require a direct correspondence between the elements of FDS and the nodes of Comes-HTC.

4.6 Coupled analysis with embedded approach

The one way coupling as well as the two ways coupling are linking FDS and Comes-HTC as two external procedures. This provides several informations about the response of the structure which are not available with a simple thermo-mechanical analysis. However the coupled approach requires many information about the structure such as geometry, mechanical loads, a different grid which has to be interfaced. This requires to the user an advanced knowledge of both FDS and Comes-HTC. A different approach to the problem is to simplify the structural analysis and to embed it in FDS.

FDS has already a conductive heat transfer model which is implemented with a one dimensional approach[2], so a modified version of the Comes-HTC model can be implemented instead of the conductive model. The conductive model is one dimensional therefore also the version of Comes-HTC need to be simplified from two dimensional to one dimensional. This requires to reduce the number of equations inside the model because with a one dimensional approach there is no information about the geometry of the structure. The linear momentum equations are neglected and the model pass from four equations to three: mass conservation of water, mass conservation of dry air, enthalpy balance. The loss of the geometry information requires also another simplification in the model, the mechanical damage needs to be neglected as well. This has a direct influence on the intrinsic permeability which is function of the mechanical and thermochemical

[2] A three dimensional heat transfer model is under development in FDS 6.5.3, https://github.com/firemodels/fds/wiki/FDS-Release-Notes.

damage [139]. Neglecting the mechanical damage the intrinsic permeability remains lower and the gas pressure rises inside the structure [39]. The thermochemical damage on the other hand is kept in the model in order to consider the effect of the degradation of the material [42, 45].

This simplified model considers the concrete as a rigid body which has a slightly different response from the complete model. A similar approach has already been proposed for the study of structures by Zeiml in [140, 141] where the concrete is modelled with a one dimensional approach regarding the thermo-hygral behaviour, while the structure is modelled with a more general three dimensional model. The model therefore can be later coupled with a generic structural solver importing the temperature and gas pressure distribution obtained with this simplified approach. The main advantage of the model is the possibility to simulate a generic fire scenario and to obtain at the same time an estimation of the temperature and pressure distribution inside the material which is modelled basing on Comes-HTC.

This embedded approach is a two way coupling between FDS and Comes-HTC, where instead of evaluating the solid response with a simple conductive model the solid is modelled as a porous media, with heat and mass transfer. The heat transfer solver works directly in FDS and this is called when the wall temperature are updated. FDS is designed with an explicit solver with a predictor corrector solution approach. The heat transfer through the wall is calculated only during the corrector phase and for every element exposed to the flow field. The Comes-HTC model can be coupled with FDS since the structural solver is implicit and the time step used in FDS can be imposed for the calculation in Comes-HTC. The boundary conditions also need to be rearranged for the new problem, as seen in section 4.1 a greater number of boundary conditions is requires for the simulation of concrete as porous media. The gas pressure on the wall is imposed based on the pressure in the flow field and imposing this pressure as Dirichlet (or first-type) boundary condition. The boundary condition for the water flow is imposed as Robin (or third-type) boundary condition as already proposed in the section 4.1. The incident heat flux is imposed as Robin (or third-type) boundary condition, but inside FDS there is no need to calculate the AST because the code is working directly with heat fluxes. The output of the calculation is the state of the concrete layer exposed to fire. The wall temperature on the surface is calculated with the Comes-HTC model, however at this stage the mass fluxes are not coupled therefore the is not water or air release into the domain.

In order to verify the differences between the results obtained with the original model of Comes-HTC and the new simplified version two simulations of the concrete are compared together. The simulation is a simple concrete line of elements which represent the one dimensional approximation. The model of Comes-HTC is simulated without mechanical damage in order to evaluate the differences only induced by the deformability of the material. The concrete is heated from one side with a net heat flux of 30 kW/m^2, the pressure is fixed at the ambient value of 101325 Pa and for the water mass balance the partial pressure of the water is fixes at 1300 Pa with a mass transfer coefficient of 0.0025. The comparison is done for a C60 concrete which has a relative humidity of 80 %. The results are compared in the figure 4.58 in order to show the three variables of the model gas pressure, capillary pressure and temperature.

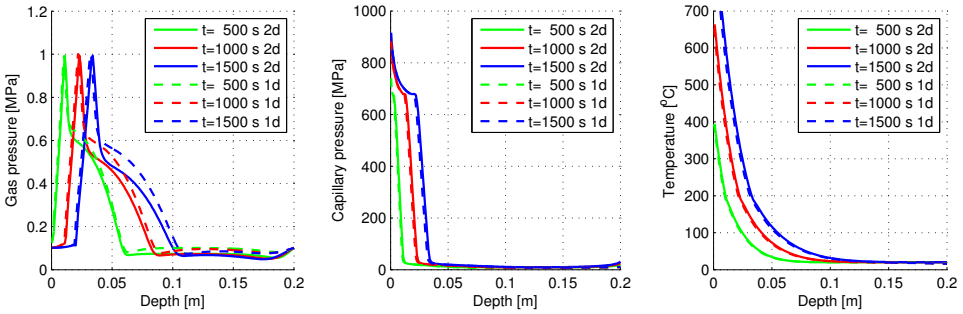

(A) Gas pressure (B) Capillary pressure (C) Temperature

FIGURE 4.58: Comparison of one dimensional and two dimensional model, without mechanical damage

The comparison done as function of time shows that the results are in good agreement for all the state variables of the problem. Some differences occurs due to the effect of the deformability of the concrete skeleton, but these are limited to the gas pressure after the pressure peak. From the figure 4.58a the pressure peak for one dimensional and two dimensional models is the same. It is also important to assess the effect of the mechanical damage on the permeability and consequently on the pressure peak. The comparison of the two models with and without mechanical damage is presented in figure 4.59. As expected the effect of the mechanical damage is mainly evident on the gas pressure, while the capillary pressure and the temperature are not strongly affected by the different modelling. The comparison of the one dimensional and two dimensional models shows that regarding wall temperature and capillary pressure there is no evident difference between the two approaches. The main difference is on the gas pressure, which is overestimated by the one dimensional model due to absence of mechanical damage.

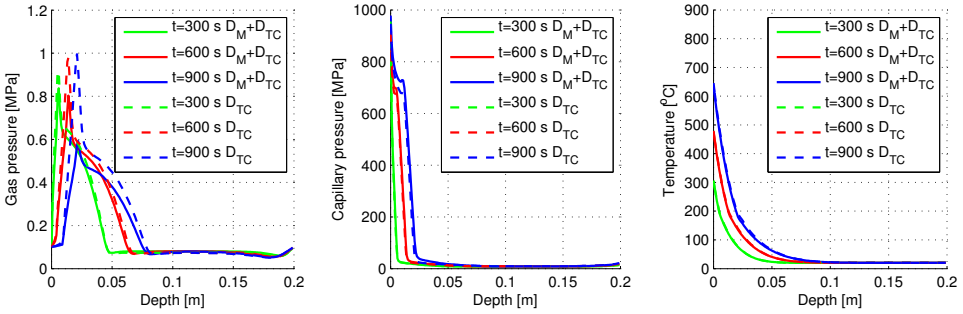

(A) Gas pressure (B) Capillary pressure (C) Temperature

FIGURE 4.59: Comparison of two dimensional models, with and without mechanical damage

The model proposed here is well suited for a first approximation of the state of concrete exposed to fire. With an higher pressure peak we obtain a more conservative estimation of risk for the structure, in particular as seen in section 1.3.2, one of the spalling indicators is directly related to the maximum gas pressure inside the material.

After the first verifications cases the embedded model is tested for a real case where it is possible to evaluate the capabilities of this approach. The slab studied in the sections 4.3 and 4.5 has been simulated using the embedded approach with Comes-HTC inside FDS. The aim of the comparison is to evaluate the differences between the approaches and in particular to evaluate the overestimation of the gas pressure peak. The fire scenario investigated is the the fast growing fire with a constant HRR of 600 kW/m and a burner 1.2 m wide. The concrete material is the same used in the previous analysis with content of water equal to 21.64 kg, relative humidity of 46 %, a saturation of 25 %, pressure of 101325 Pa and temperature of 20 °C. The flow field is first presented in figure 4.60a in order to show the temperature and velocity field near the fire and the slab.

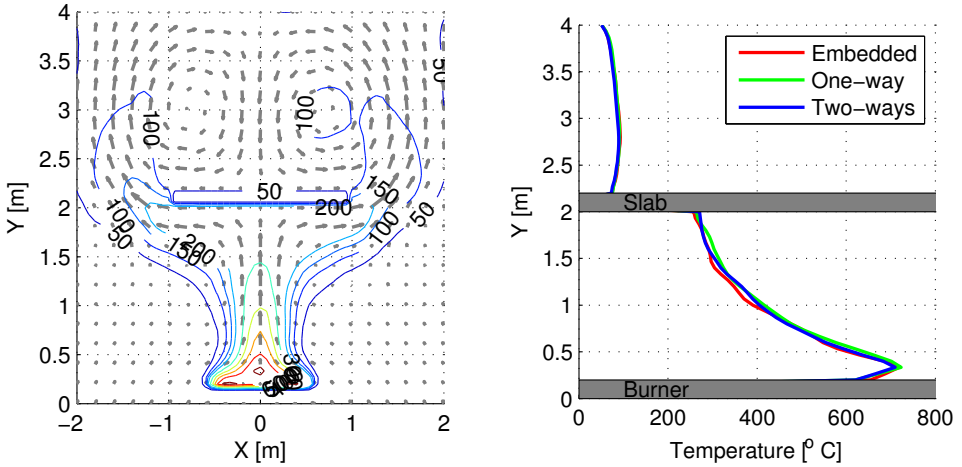

(A) Temperature field near the fire

(B) Comparison along the burner's centreline

FIGURE 4.60: Temperature in case of fire beneath the slab

Comparing the gas temperature along the middle line of burner with other other simulation approaches such the two way coupling, evaluated at step 3, or the one way coupling it is possible to see that the temperature field is not affected by the different wall modelling. Regarding the wall conditions, the one way coupling calculates the temperature using a pure conductive mode and the two ways coupling uses the temperature obtained in Comes-HTC at the previous iteration. With the embedded approach the Comes-HTC modelling is directly used to evaluate the wall temperature on the surface. The wall temperatures are compared together at the centre of the heated face of the slab in figure 4.61a. The temperature of the surface obtained with the embedded model is in good agreement with the concrete temperature obtained with the two ways coupled analysis. This comparison provides two important information about the coupling, first, the one dimensional model is suitable for structures exposed to fire even if these are not one dimensional. As seen in section 4.3.2 the temperature has an high gradient across the thickness of the slab, while the temperatures are more uniform along the width of the slab. This is depicted by the iso temperature lines which are almost parallel to the long face of the slab. The other important result of the comparison is about the accuracy of the coupling, the

embedded model as explained earlier has a direct linking with FDS. Therefore every time step the incident heat flux is calculated in the flow field and imposed as boundary condition for the structural calculation. This is not possible with the external coupling since the amount of data exchanged between the codes would be extremely large. For the one way coupling a sampling time of 1.0 s is usually employed to transfer the results from FDS to Comes-HTC. The comparison of the results shows that this approximation in the data sampling doesn't affect the calculation, but it allows to smooth the strong fluctuations of the incident heat fluxes. The smoothing of the boundary conditions' fluctuations is a fundamental aspect in order to guarantee the numerical stability of the structural calculation.

The embedded code is numerically more stable due to the absence of mechanical damage and displacements. It better handles the strong fluctuations of incoming heat fluxes that are generated by the fire. However the code is not capable to maintain its stability also above the critical point of water at 374 °C, above such temperatures the heat flux fluctuations induce strong fluctuations in the variables which destroy the numerical solution. The simulation with embedded approach could run just for 800 s until the maximum temperature crossed the critical temperature of water.

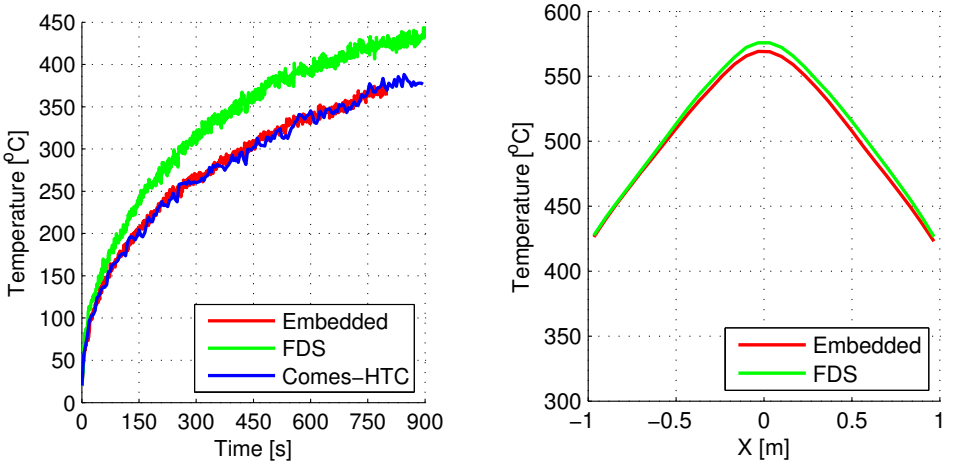

(A) Temperature field near the fire

(B) Comparison along the burner's centreline

FIGURE 4.61: Temperature in case of fire beneath the slab

As done in the two ways coupling the AST are compared for the different wall modelling, figure 4.61b. The pure conductive model and the Comes-HTC embedded model show a good agreement among them and an error within 15 °C. As already propose by Andreozzi [142] the wall's conductivity has a small effect on the AST. The different material properties change the net heat fluxes through the wall and the surface temperatures. If the difference in the surface temperature are small the difference in the AST can be negligible. For concrete structures the wall temperatures obtained with a pure conductive model are not so far from the temperature obtained with a more sophisticated model, so the AST shows minor difference between the two cases.

If the conductive model can provide some the temperature distribution on the surface of the structure, no information are available about the gas

pressure inside. The more advanced model embedded in FDS allows to estimate the pressure distribution along every element and to show its maximum value. Using the results obtained from the embedded analysis and from the one way coupling it is possible to evaluate the differences between the two approaches, figure 4.62. The pressure distributions are evaluated after 800 s of simulation. As expected the pressure is higher with the embedded model due to the absence of damage.

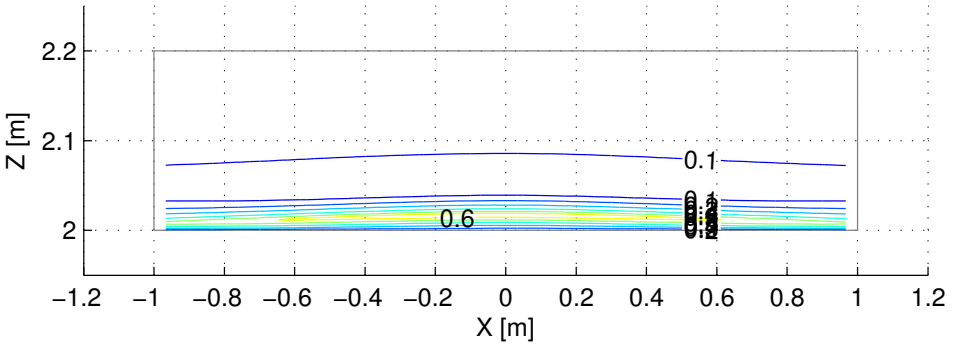

(A) Embedded model

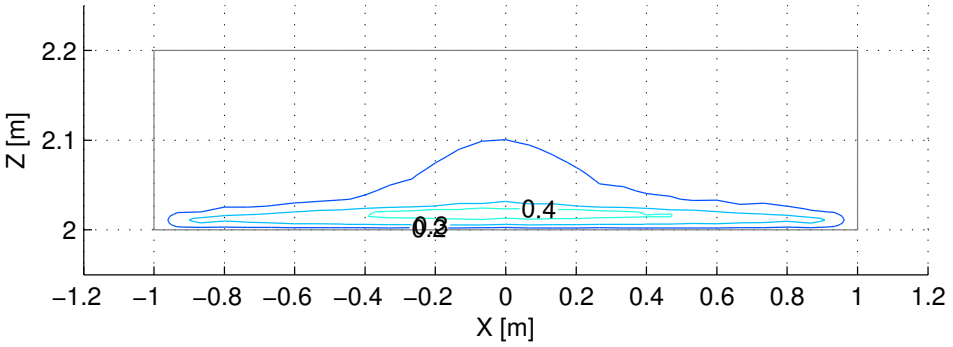

(B) Comes-HTC 2d model

FIGURE 4.62: Gas pressure distribution after 800 s

The pressure in the model without damage is higher, with a maximum of 0.6659 MPa, but also the distribution is also slightly different. The one dimensional model doesn't simulate correctly the pressure rise in the centre of the slab because the pressure distribution is almost uniform along the width of the slab. The two dimensional analysis provides a lower pressure peak in the central region of the slab equal to 0.4635 MPa. On the sides the pressure has lower values compared to the one dimensional calculation.

The last comparison between the two models is done for the temperature field inside the slab after 800 seconds, figure 4.63. The comparison of the temperature field shows a good agreement between the two approaches which are predicting close temperature peaks on the surface, 373.36 for the embedded model 380.58 for the one way coupled model, but also the distribution inside the material. The differences between the two cases are mainly located on the upper face of the slab where the embedded model has an adiabatic surface and the Comes-HTC model is exposed to the hot gasses on the upper face of the slab. The discrepancies near the sides of the slab are consequence of the simple one dimensional modelling, but figure

4.63 shows that the one dimensional model is suitable to the calculation of temperature distributions also in more complex geometries.

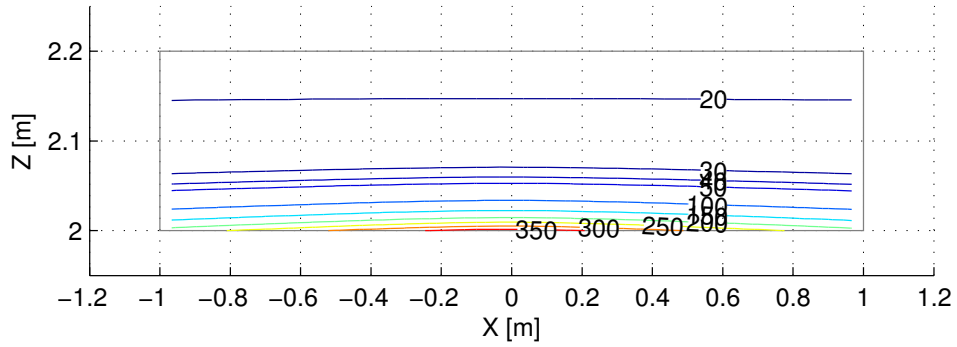

(A) Embedded model

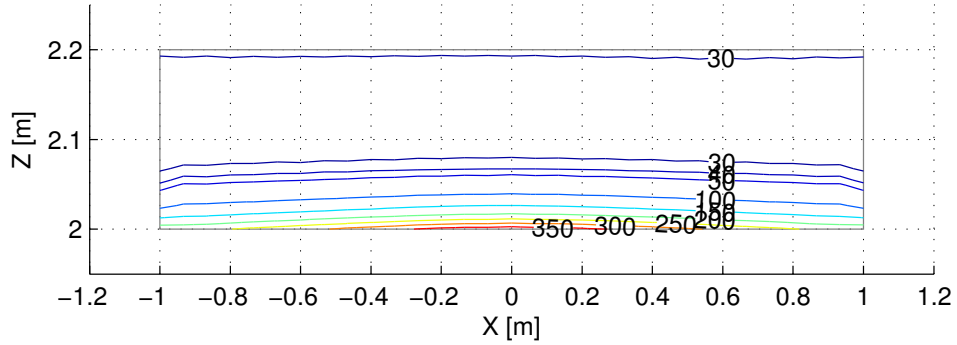

(B) Comes-HTC 2d model

FIGURE 4.63: Temperature distribution after 800 s

The present approach despite its simple implementation, without damage and deformations, is capable to correctly estimate the temperature distribution in a more complex geometry exposed to fire. The embedded calculation provides a result which is strongly coupled with FDS because the heat fluxes and the wall temperature are exchanged with at every time step. However it is clear that the model shows some limits in the estimation of the gas pressure distribution and in the calculation of the maximum pressure in the material due to the lack of mechanical damage. The current model provides directly in FDS an estimation of the maximum pressure inside the structure and the wall temperature which is in good agreement with the full model. This can be useful for an initial estimation of the spalling risk which is directly related with the fire scenario under investigation. The model however needs further developments in terms of stability above the critical point of water and in term of structural results.

For a more complete analysis the results obtained with the thermo-hygral model should be exported to a structural code which is capable to calculate the whole response of the structure and to provide a comprehensive assessment of the failure risk [140, 141].

Chapter 5

Conclusions and future works

The present work investigated different numerical models for the simulations of ventilation, fire scenarios and concrete structures exposed to fire. Longitudinal ventilation and fire scenarios have been simulated with Computational Fluid Dynamic using the code FDS, while the response of the concrete structure has been evaluated with the code developed at University of Padua Comes-HTC.

Numerical simulation of fire are becoming more popular and widespread not only in the research but also in the industry. FDS is commonly used for this purpose because of its specific development, but often the code is used without previous validation. The first part of this work, chapter 2, deals with the validation of FDS in different scenarios.

First, the code has been used to simulate the natural convection and the buoyancy driven flows without involving the combustion process. The small cavity studied by Ampofo in [62] has been reproduced with FDS simulations providing interesting results about the velocity field and the temperature distribution. A poorer agreement was found for the evaluation of the heat transfer coefficient which is modelled in FDS with a simplified approach, however the case of study is out of the usual field where FDS is employed, therefore the results have been considered acceptable.

After the first validation, the fire is included in the simulation considering a fire scenario with natural ventilation. The experiment chosen for the validation has been carried out by Rinne [68], who burned a liquid pool of n-heptane in a large room. The FDS simulation predicted temperatures, CO, CO_2, O_2, soot concentrations and smoke layer height inside the room in good agreement with the experimental measurements.

To complete the early validations a fire scenario in tunnel is simulated in order to study the smoke movement under different longitudinal ventilation conditions, both subcritical and supercritical. The midscale tunnel investigated by Blanchard in [86] has been chosen since it provides several measurements about temperature, velocities and radiative fluxes in different parts of the tunnel. The comparison of the FDS simulations with the measurements assesses the capability of the code to predict temperatures and velocities inside the tunnel. However poorer agreement has been found for the radiative heat fluxes near the fire.

The last validation refers to a midscale tunnel which is different from a tunnel in real scale. After validation of the fire scenario, FDS is used to evaluate the reliability of the Froude scaling for fire in tunnels. The tunnel previously validated is rescaled to the real size, using the Froude scaling theory and simulated with FDS, later the results obtained in the large scale are compared with the rescaled results obtained from the small scale test.

The agreement between the results in different scales shows that the Froude scaling is suitable for the prediction of temperature field, smoke movement and velocities for tunnel geometries.

The Froude scaling theory provides all the equations to rescale a fire scenario and the results from small to large size and vice-versa, but often the results obtained in small scale tunnels are applied to large scale tunnels without these fulfilling all the equations of the scaling theory. Further analysis on the scaling have been carried out changing the thermal properties of the walls' materials and comparing the results with the reference case that has been designed basing on the Froude scaling theory. Two new tunnels are designed, one with highly conductive walls, made of rock, and the other with highly insulating walls, covered with insulating boards. The thermal properties of the walls have an important effect on the gas temperatures, in particular higher insulation leads to higher temperatures and larger smoke backlayering. The comparison of the different simulations shows that the results should be carefully exported from the small scale considering the effect of the heat losses through the vault in order to don't overestimate the thermal losses and underestimate the temperatures and the backlayering inside the tunnel.

After the initial analysis and validations, the first main topic of this work is the assessment of the capability of FDS to simulate longitudinal ventilation devices, jet fans. The validation of FDS has been done on various steps, starting from the validation of a nozzle in a small scale tunnel. Mutama measured pressure and velocity distribution inside a tunnel, [111], this small scale tunnel has been simulated with FDS reproducing the velocities and the pressure profiles. The simulation of this ventilation case gives important informations about the modelling of the ventilation device in particular about the turbulence modelling, the nozzle's geometry, the grid resolution, but it didn't allow to assess the capability of FDS to evaluate the intaken air into the tunnel.

In practical problems the tunnel should be modelled considering the pressure at the portals and evaluating the velocity along the tunnel induced by the jet fans. With the previous experiment this couldn't be assessed due to the lack of information about the tunnel's boundary conditions. Therefore a second validation has been carried out in a tunnel in real scale where the entrainment ratio of the jet fans could be validated. Colella measured the average velocity in a tunnel equipped with jet fans [31], these have been turned on and off with different strategies providing results for different ventilation conditions. With FDS it was possible to simulate the flow field in the tunnel and to calculate the average velocity for the different ventilation scenarios. The comparison of the numerical simulations with the measurements shows a good agreement between FDS and the experiment. Moreover with FDS it was possible to investigate the pressure distribution along the tunnel and depict eventual inefficiencies in the ventilation design.

The previous validations refer to cold flow cases where the fire is not involved, while particular attention should be paid also to the performance of jet fans in case of fire in tunnels. Numerical and experimental studies [8, 18, 30] showed that the fire generates an additional pressure loss in the tunnel and reduces the longitudinal flow induced by the jet fan. This velocity reduction is known as throttling effect and it has been depicted during the

large scale fire test inside the Memorial tunnel [8]. During the Memorial tunnel fire test the tunnel has been equipped with jet fans in order to study the capability of the ventilation to confine the smoke. Different tests have been carried out with different jet fans activated and different power of the fire. Numerical simulations of the memorial tunnel have been carried out in order to reproduce the temperature and the velocity profiles inside the tunnel as well as the air flow intaken by the jet fans. The simulation shows a good agreement with the experimental measurements but some discrepancies occur due to a poor modelling of the atmospheric conditions at the portals. The wind at the south portal of the tunnel affects the smoke movement inside the tunnel when the jet fan are not active and later it reduces the average velocity inside the tunnel which is slightly overpredicted by FDS. However the validation of different ventilation scenarios assess the capability of FDS to simulate correctly the jet fans in both cases with cold flow and hot flow, taking into account the throttling effect, already investigated in[30] .

The current validation highlighted the key parameters that need to be correctly investigated when modelling a jet fan. The grid size need to be enough refined to predict correctly the velocity decay and to approximate correctly the geometry of the jet fan. The wall roughness is another important parameter for the simulation, this often doesn't take into account only the roughness of the wall, but also the effect of the obstacles that are in the tunnel and that cannot be explicitly included in the model. As seen in the validation of the Memorial tunnel case the wind at the portal can increase or reduce the ventilation depending on its direction. This was not considered in the simulation, but further efforts are required in this direction with the validation of experiment where wind blows at the portals. Once the effect of the wind is correctly modelled and validated, its effect should be considered also in the design of ventilation system. As seen in the previous validation, neglecting the wind effect FDS overestimates the volume flow across the tunnel.

The model proposed for the simulation of jet fans has been validated against different experiments but it can be further developed. The validation carried out in this work always required several assumptions about the jet fan performance, such constant discharged volume flow, missing informations about the real geometry and about the secondary flows at the outlet. A more detailed validation of the machine itself is required in order to reveal which simplifications can be done when jet fans are modelled. In this work the effect of the swirl was investigated comparing the performance of two jet fans, one with axial exhaust and the other with swirl at the outlet. The results of the simulations show that the effect can be neglected for tunnel problems, but more accurate investigations are required in this direction.

The jet fan model after this comprehensive validation can be used to verify the ventilation strategy that is usually designed with a one dimensional approach. The advantage of the one dimensional model is the speed of the calculation, however the model doesn't simulate explicitly the ventilation devices, but they are included as a local force. For short tunnel FDS can be used to simulate the whole geometry including the jet fans, this provides a better estimation of the jet fan's performance which consider both the geometry and the location inside the tunnel. However the computational

cost of a tunnel simulation is still huge and not only short tunnels need to be simulated, to tackle this problem a coupled approach with one dimensional and three dimensional model could be used. The approach has been already proposed by Colella coupling an in house built one dimensional code with fluent, [31, 101], the coupled approach has been validated for cold flow in tunnel. FDS has already the possibility to include HVAC system in the simulation using a one dimensional model coupled with the three dimensional model. The HVAC model has not been developed for a multiscale analysis however there are some examples of multiscale modelling applied to FDS by Vermessi [143] and Ang [102]. The multiscale approach in FDS is still affected by numerical instabilities, but this approach is the natural development where the jet fan model can be employed.

The last main topic of this work it the analysis of structures with a fully performance based approach. The behaviour of concrete structures at high temperature has already been modelled by Gawin Pesavento and Schrefler in [35, 37, 42, 45, 125] and implemented in a structural code developed at the University of Padua. The model includes both heat and mass transfer in a deformable solid, this model is highly non linear and the properties of the material are strongly depending on the state of the material and of the structure itself. The structural model has been usually employed for the investigation of concrete structures exposed to fire where the thermal input is imposed based on the temperature curves commonly used in the engineering practice. However the model has been already coupled with CFD codes in [125, 126] but due to the large development in the fire modelling a new coupling has been widely investigated.

The coupling between FDS and Comes-HTC requires the interfacing of a Cartesian mesh with a structured mesh, the discrepancies between the geometries can induce huge errors in the coupling and create sinks or sources of energy if the coupling is not correct. The problem has been partially solved by Silva in [124] combining the adiabatic surface temperature, but in the current approach the incident heat fluxes are combined together. To verify the proposed coupling approach several numerical examples have been carried out showing that the proposed coupling approach is reliable also for the coupling of non corresponding mesh.

The coupled analysis has been first implemented with a one way coupling approach. A simple slab exposed to fire has been studied under different fire scenarios. In order to highlight the capabilities of the coupled analysis, different fire scenarios with the same nominal maximum HRR are compared together showing that both the fluid and the structure are affected by the specific fire. With a coupled approach it is possible to impose a set of boundary conditions which are directly related to the flow field around the structure. In particular from the analysis it was clear that the HRR itself is not a unique parameter which quantifies the risk for the structure, rather the response of the structure need to be studied as function of the incident heat fluxes. The first coupled analysis has been done for geometries which are corresponding in FDS and in Comes-HTC, however this is not always possible, for instance in tunnels, where the ceiling is usually rounded.

A fire scenario in tunnel has been later investigated in order to evaluate the structural response of the vault for a more realistic thermal loads'

distribution. The tunnel has a rounder vault so the geometries are not corresponding and the coupled tool has to interpolate the boundary conditions from FDS to Comes-HTC. Before studying the response of the structure preliminary analysis have been carried out in order to set up a realistic fire scenario representing a burning coach in a tunnel. For long tunnels it is not possible to simulate the whole structure with CFD simulations therefore it is necessary to consider just a smaller portion. One of the preliminary analysis evaluates the effect of the length of the modelled tunnel on the thermal loads on the structure. The second sensitivity analysis evaluates the effect of the fire load height on the thermal input in order to relate the temperature found in the simulations with the results coming from the literature. The FDS simulation provides a complete set of boundary conditions which are imposed to the vault of the tunnel. The structural analysis allowed to evaluate the maximum gas pressure in the tunnel, the stresses and the temperatures. The comparison of these quantities at different sections highlights the effect of a non uniform distribution of thermal loads. However numerical issues prevents from completing the whole structural calculations which reaches only 638 s, further development are required to stabilize the calculation and simulate the whole fire scenario.

The approach proposed here is capable to evaluate the response of a concrete structure starting from the specific fire scenario, the analysis carried out on the slab and on the tunnel show that the thermal input is not uniform on the structure as usually assumed using engineering curves. As well the development of the fire in time can be also different depending on the fire scenario. The analysis previously presented used a one way coupling approach where the boundary conditions from the fire scenario are imported into the structural calculation whose are not used for the simulation of the flow field. A further verification of the proposed coupling is necessary in order to see if a more complex two ways coupling is required.

With a two ways coupling approach, the results from the structural calculation are used as boundary conditions of the fluid dynamic simulation. The process is looped updating the boundary conditions in the two programs until the simulations in two successive iterations are within a certain tolerance. The approach is obviously more expensive in terms of computational time, but the main issue of the coupling can be the correct interfacing from Comes-HTC to FDS. The interpolation process proposed in this work is usually interpolating the results from FDS and transferring them to Comes-HTC and it is not designed to transfer the results back. Therefore in order to verify the two ways coupling the slab exposed to fire has been used since the geometries in the two codes are corresponding. The two ways coupling has been performed and it shows that the results of the FDS simulation are weakly influenced by the results of the structural simulation. There are some differences in the wall temperatures but these don't affect the surrounding fluid. The numerical effort required to couple the Comes-HTC doesn't provide any substantial improvement to the final result. The displacements have been monitored in order to assess if the deformation of the structure modify the flow field, however the maximum displacement in Comes-HTC was much smaller the the element's size used in FDS

The last coupling approach proposed between FDS and Comes-HTC is done embedding the model for concrete in FDS. In order to call Comes-HTC

directly inside FDS some simplifications are required because the structural solver of FDS is implemented with a one dimensional approach. The Comes-HTC model is reduced from two dimensional to one dimensional and the linear momentum equations are neglected. With this approximation the also the mechanical damage is not considered with a consequent reduction of the intrinsic permeability and a rise in the gas pressure peak. The embedded model of Comes-HTC inside FDS has been compared with the two other coupling approaches proposed here. The results show that the embedded model is capable already in FDS to calculate the wall temperature obtained with the two dimensional structural model. The gas pressure is overestimated with the embedded approach due to the lack of damage, but this can be used as an initial estimation for the spalling risk on the structure. The embedded model is strongly coupled with FDS and due to the strong fluctuations in the boundary conditions it is not capable to simulate the concrete above the critical temperature of the water. The current approach requires further development regarding the stability of the code at very high temperature.

The coupled analysis of concrete structure has been proposed here for two dimensional structures. This hypothesis is well suited for tunnel's geometry, but it cannot be extended to generic structures, therefore one of the future steps for the coupled analysis is the extension of the structural code Comes-HTC from two dimensional to three dimensional. This allows to include inside the model not only concrete but also the reinforcement bars which are usually present in the structure.

The other future development that is required in order to improve the coupled analysis is the implementation of an immersed boundary method in FDS which allows to draw not only squared surfaces but also rounded geometries.

Parts of the work of this thesis have been already published by the author in [144–150]

Appendix A

Velocity distribution for a jet fan with swirl

The swirl component has been calculated basing on the assumptions about the blade design and on the efficiency of the machine. The present calculations show how the velocity triangles are obtained staring from the design variable of the jet fan.

Given the thrust of the jet fan the rotation speed and the volume flow rate it is possible to calculate the velocity distribution upstream and downstream the rotor. The thrust of the jet fan is equal to the integral of the pressure on the two sides of the fan, equation A.1.

$$T = \int_A (p_{out,f} - p_{in,f}) dA_{fan} = \int_A (p_{out,r} - p_{in,r}) dA_{rotor} \tag{A.1}$$

For sake of simplicity it is assumed that the force produced by the rotor is equal to the force produced by the fan. The pressure rise on the rotor is related to the equations of Bernoulli, so the pressure difference is related to the specific work exchanged between fluid and machine and to the swirl component of the fluid.

$$\frac{p_{in}}{\rho} + \frac{u_{in}^2}{2} + \Delta H_{fan} - \Delta H_{loss} = \frac{p_{out}}{\rho} + \frac{u_{out}^2}{2} \tag{A.2}$$

Integrating both sides of the equations over the area of the rotor the pressure difference can be written as function of the velocity components and of the losses.

$$T = \int_A \frac{u_{in}^2}{2} + \eta \Delta H_{fan} - \frac{u_{out}^2}{2} dA \tag{A.3}$$

where η is the efficiency of the machine which must be estimated since the energy losses are not known at the design phase of the machine. Equation A.3 doesn't make any assumption on the velocity inside the machine. In order to relate the velocity components at the inlet and at the outlet of the rotor it is necessary to impose a relation between the velocities at the inlet and at the outlet. One of the possible distributions of velocities is the free vortex distribution, which imposes an uniform specific work ΔH_{fan} along the span of the blade and a constant velocity across the rotor. With these assumptions, and assuming an axial inflow, equation A.3 can be written as

$$T = \int_A \eta \Delta H_{fan} - \frac{u_{t,out}^2}{2} dA \tag{A.4}$$

The efficiency of the machine is assumed, while the other two terms of the integral need to be calculated. The integral on the area can be written as function of the radius considering the machine axis symmetric and knowing the radius of the hub and of the tip of the blade.

$$T = \rho \int_{r_hub}^{r_{tip}} \eta \Delta H_{fan} - \frac{u_{t,out}^2}{2} 2\pi r dr \tag{A.5}$$

The tangential component of the velocity can be written as function of the specific work made by the machine.

$$u_{t,out} = \frac{\Delta H_{fan}}{\omega r} \tag{A.6}$$

Equations A.5 and A.6 can be combined together as unique function of the radius.

$$T = \rho \int_{r_{hub}}^{r_{tip}} \eta \Delta H_{fan} - \frac{1}{2} \left(\frac{\Delta H_{fan}}{\omega r} \right)^2 2\pi r dr \tag{A.7}$$

Solving the integral as function of the radius it is possible to write:

$$T = 2\pi \left[\eta \Delta H_{fan} \frac{r_{tip}^2 - r_{hub}^2}{2} - \frac{1}{2} \left(\frac{\Delta H_{fan}}{\omega} \right)^2 (ln(r_{tip}) - ln(r_{hub})) \right] \tag{A.8}$$

The specific work done by the machine can be now calculated knowing the thrust of the fan, the efficiency, the dimensions and the rotation speed.

$$\Delta H_{fan}^2 \left(\pi \rho \frac{ln(r_{tip}) - ln(r_{hub})}{\omega^2} \right) - \Delta H_{fan} \left[\pi \rho \eta \left(r_{tip}^2 - r_{hub}^2 \right) \right] + T = 0 \tag{A.9}$$

Solving the equation of the second order it is possible to calculate the ΔH_{fan} and the tangential component of the velocity along the span of the blade. The axial component of the velocity is calculated basing on the volume flow crossing the jet fan and on the area of the rotor.

Bibliography

[1] M. El-Fadel and Z. Hashisho, "Vehicular emissions in roadway tunnels: A critical review", *Critical reviews in environmental science and technology*, vol. 31, no. 2, pp. 125–174, 2001.

[2] T. Y. Chang and S. J. Rudy, "Roadway tunnel air quality models", *Environmental science & technology*, vol. 24, no. 5, pp. 672–676, 1990.

[3] "NFPA 502, standard for road tunnels, bridges, and other limited access highways", NFPA Codes and Standards, NFPA, 2010.

[4] "Fire and smoke control in road tunnels", PIARC Committee on Road Tunnels, 1999.

[5] "Directive 2004/54/ec of the european parliament and of the council of 29 april 2004 on minimum safety requirements for tunnels in the trans-european road network", Official Journal of the European Union, Directive, EU, 2004.

[6] "Recommendations of the group of experts on safety in road tunnels", Economic Commission for Europe, Inland Transport Committee, UN Economic Council, 2001.

[7] A. Haack, "Fire protection in traffic tunnels: General aspects and results of the eureka project", *Tunnelling and underground space technology*, vol. 13, no. 4, pp. 377–381, 1998.

[8] "Memorial tunnel fire ventilation test program", Massachusetts Highway Department and Federal Highway Administration, Test Report, 1995.

[9] T. Lemaire and Y. Kenyon, "Large scale fire tests in the second benelux tunnel", *Fire technology*, vol. 42, no. 4, pp. 329–350, 2006.

[10] I. J. W. Huijben and Rijkswaterstaat, Bouwdienst, "Tests on fire detection systems and sprinkler in a tunnel", in *Tunnel fires and escape from tunnels, fourth int. conference*, 2002.

[11] Y. Oka and G. T. Atkinson, "Control of smoke flow in tunnel fires", *Fire safety journal*, vol. 25, no. 4, pp. 305–322, 1995.

[12] H. Ingason, Y. Z. Li, and A. Lönnermark, *Tunnel fire dynamics*. Springer, 2014.

[13] R. Carvel and A. N. Beard, *The handbook of tunnel fire safety*. Thomas Telford, 2005.

[14] L. Y. Z. Ingason H. Lönnermark A., "Runehamar tunnel fire tests", SP Technical Research Institute of Sweden, SP Report 55, 2011.

[15] H. Ingason, M. Kumm, D. Nilsson, A. Lönnermark, A. Claesson, Y. Z. Li, K. Fridolf, R. Åkerstedt, H. Nyman, T. Dittmer, *et al.*, "The metro project", Mälardalen University, Final report, 2012.

[16] P. H. Thomas, "The movement of buoyant fluid against a stream and the venting of underground fires", *Fire safety science*, vol. 351, pp. 1–1, 1958.

[17] W. D. Kennedy and B Parsons, "Critical velocity: Past, present and future", in *Seminar smoke and critical velocity in tunnels, london, uk*, vol. 2, 1996.

[18] C. K. Lee, R. F. Chaiken, and J. M. Singer, "Interaction between duct fires and ventilation flow: An experimental study", *Combustion science and technology*, vol. 20, no. 1-2, pp. 59–72, 1979.

[19] J. G. Quintiere, "Scaling applications in fire research", *Fire safety journal*, vol. 15, no. 1, pp. 3–29, 1989.

[20] J. De Ris, "Duct fires", *Combustion science and technology*, vol. 2, no. 4, pp. 239–258, 1970.

[21] Y. Wu and M. Bakar, "Control of smoke flow in tunnel fires using longitudinal ventilation systems – a study of the critical velocity", *Fire safety journal*, vol. 35, no. 4, pp. 363 –390, 2000.

[22] L. Hu, R. Huo, and W. Chow, "Studies on buoyancy-driven back-layering flow in tunnel fires", *Experimental thermal and fluid science*, vol. 32, no. 8, pp. 1468–1483, 2008.

[23] Y. Z. Li, B. Lei, and H. Ingason, "Study of critical velocity and back-layering length in longitudinally ventilated tunnel fires", *Fire safety journal*, vol. 45, no. 6, pp. 361–370, 2010.

[24] N. Tilley, P. Rauwoens, D. Fauconnier, and B. Merci, "On the extrapolation of cfd results for smoke and heat control in reduced-scale set-ups to full scale: Atrium configuration", *Fire safety journal*, vol. 59, pp. 160–165, 2013.

[25] J. Kempf, "Einfluss der wandeffekte auf die treibstrahlwirkung eines strahlgebläses", *Schweizerische bauzeitung*, vol. 83, no. 4, pp. 47–52, 1965.

[26] K. R. Mutama and A. E. Hall, "The experimental investigation of jet fan aerodynamics using wind tunnel modeling", *Journal of fluids engineering*, vol. 118, no. 2, pp. 322–328, 1996.

[27] A. D. Martegani, G. Pavesi, and C. Barbetta, "An experimental study on the longitudinal ventilation system", in *Proc. 8 th int. symp. on aerodynamics and ventilation of vehicle tunnels, liverpool*, 1994, pp. 3–15.

[28] A. D. Martegani, G. Pavesi, and C. Barbetta, "Experimental investigation of interaction of plain jet fans mounted in series", in *Proc. 10 th int. symp. on aerodynamics and ventilation of vehicle tunnels, boston*, 2000, pp. 1055–1078.

[29] A. D. Martegani, G. Pavesi, and C. Barbetta, "The influence of separation, inclination, and swirl on single and coupled jet fans installation efficiency", in *Proc. 9 th int. symp. on aerodynamics and ventilation of vehicle tunnels, aosta*, 1997, pp. 43–54.

[30] A. Vaitkevicius, F. Colella, and R. Carvel, "Investigating the throttling effect in tunnel fires", *Fire technology*, vol. 52, no. 5, pp. 1619–1628, 2016.

[31] F. Colella, "Multiscale modelling of tunnel ventilation flows and fires", PhD thesis, Politecnico di Torino, 2010.

[32] H. Kurioka, Y. Oka, H. Satoh, and O. Sugawa, "Fire properties in near field of square fire source with longitudinal ventilation in tunnels", *Fire safety journal*, vol. 38, no. 4, pp. 319–340, 2003.

[33] Y. Z. Li and H. Ingason, "The maximum ceiling gas temperature in a large tunnel fire", *Fire safety journal*, vol. 48, pp. 38–48, 2012.

[34] J. Mazars and G. Pijaudier-Cabot, "Continuum damage theory-application to concrete", *Journal of engineering mechanics*, vol. 115, no. 2, pp. 345–365, 1989.

[35] D. Gawin, F. Pesavento, and B. A. Schrefler, "Modelling of hygro-thermal behaviour of concrete at high temperature with thermo-chemical and mechanical material degradation", *Computer methods in applied mechanics and engineering*, vol. 192, no. 13, pp. 1731–1771, 2003.

[36] Z. P. Bazant, "Analysis of pore pressure, thermal stress and fracture in rapidly heated concrete", in *International workshop on fire performance of high-strength concrete. proceedings*, 1997.

[37] D. Gawin, F. Pesavento, and B. A. Schrefler, "Towards prediction of the thermal spalling risk through a multi-phase porous media model of concrete", *Computer methods in applied mechanics and engineering*, vol. 195, no. 41, pp. 5707–5729, 2006.

[38] P. Kalifa, F.-D. Menneteau, and D. Quenard, "Spalling and pore pressure in hpc at high temperatures", *Cement and concrete research*, vol. 30, no. 12, pp. 1915 –1927, 2000.

[39] J.-C. Mindeguia, P. Pimienta, A. Noumowé, and M. Kanema, "Temperature, pore pressure and mass variation of concrete subjected to high temperature — experimental and numerical discussion on spalling risk", *Cement and concrete research*, vol. 40, no. 3, pp. 477 – 487, 2010.

[40] R. W. Lewis and B. A. Schrefler, *The finite element method in the static and dynamic deformation and consolidation of porous media*. John Wiley, 1998.

[41] D. Gawin, P. Baggio, and B. A. Schrefler, "Coupled heat, water and gas flow in deformable porous media", *International journal for numerical methods in fluids*, vol. 20, no. 8-9, pp. 969–987, 1995.

[42] D. Gawin, C. E. Majorana, and B. A. Schrefler, "Numerical analysis of hygro-thermal behaviour and damage of concrete at high temperature", *Mechanics of cohesive-frictional materials*, vol. 4, no. 1, pp. 37–74, 1999.

[43] F. Couture, W. Jomaa, and J.-R. Puiggali, "Relative permeability relations: A key factor for a drying model", *Transport in porous media*, vol. 23, no. 3, pp. 303–335, 1996.

[44] T. Harmathy and L. Allen, "Thermal properties of selected masonry unit concretes", *Am concrete inst journal & proceedings*, vol. 70, no. 2, 1973.

[45] D. Gawin, F. Pesavento, and B. A. Schrefler, "Modelling of hygrothermal behaviour and damage of concrete at temperature above the critical point of water", *International journal for numerical and analytical methods in geomechanics*, vol. 26, no. 6, pp. 537–562, 2002.

[46] A. Witek, D. Gawin, F. Pesavento, and B. A. Schrefler, "Finite element analysis of various methods for protection of concrete structures against spalling during fire", *Computational mechanics*, vol. 39, no. 3, pp. 271–292, 2007.

[47] F. Pesavento, "Non linear modelling of concrete as multiphase porous material in high temperature conditions", PhD thesis, University of Padova, 2000.

[48] D. Gawin, F. Pesavento, and B. A. Schrefler, "What physical phenomena can be neglected when modelling concrete at high temperature? a comparative study. part 1: Physical phenomena and mathematical model", *International journal of solids and structures*, vol. 48, no. 13, pp. 1927–1944, 2011.

[49] D. Gawin, F. Pesavento, and B. A. Schrefler, "What physical phenomena can be neglected when modelling concrete at high temperature? a comparative study. part 2: Comparison between models", *International journal of solids and structures*, vol. 48, no. 13, pp. 1945–1961, 2011.

[50] K. McGrattan, S. Hostikka, R. McDermott, J. Floyd, C. Weinschenk, and K. Overholt, "Fire Dynamics Simulator, User's Guide", NIST Special Publication 1019, 2016.

[51] S. B. Pope, *Turbulent flows*. Cambridge University Press, 2001.

[52] R. Rehm and H. Baum, "The Equations of Motion for Thermally Driven, Buoyant Flows", *Journal of research of the nbs*, vol. 83, pp. 297–308, 1978.

[53] J. W. Deardorff, "Numerical investigation of neutral and unstable planetary boundary layers", *Journal of the atmospheric sciences*, vol. 29, no. 1, pp. 91–115, 1972.

[54] B. F. Magnussen and B. H. Hjertager, "On mathematical modeling of turbulent combustion with special emphasis on soot formation and combustion", in *Symposium (international) on combustion*, Elsevier, vol. 16, 1977, pp. 719–729.

[55] R. McDermott, K. Mcgrattan, and J. Floyd, "A simple reaction time scale for under-resolved fire dynamics", *Fire safety science*, vol. 10, pp. 809–820, 2011.

[56] K. McGrattan, S. Hostikka, R. McDermott, J. Floyd, C. Weinschenk, and K. Overholt, "Fire Dynamics Simulator, Technical Reference Guide", NIST Special Publication 1018, 2016.

[57] D. Drysdale, *An introduction to fire dynamics*. John Wiley & Sons, 2011.

[58] T. L. Bergman, F. P. Incropera, D. P. DeWitt, and A. S. Lavine, *Fundamentals of heat and mass transfer*. John Wiley & Sons, 2011.

[59] P. F. Linden, "The fluid mechanics of natural ventilation", *Annual review of fluid mechanics*, vol. 31, no. 1, pp. 201–238, 1999.

[60] C. Rundle, M. Lightstone, P Oosthuizen, P Karava, and E Mouriki, "Validation of computational fluid dynamics simulations for atria geometries", *Building and environment*, vol. 46, no. 7, pp. 1343–1353, 2011.

[61] S.-H. Peng and L. Davidson, "Numerical investigation of turbulent buoyant cavity flow using large eddy simulation", in *Third international symposium on turbulence heat and mass transfer*, vol. 3, 2000, pp. 737–744.

[62] F Ampofo and T. Karayiannis, "Experimental benchmark data for turbulent natural convection in an air filled square cavity", *International journal of heat and mass transfer*, vol. 46, no. 19, pp. 3551–3572, 2003.

[63] F. Penot and A. N'Dame, "Successive bifurcations of natural convection in a vertical enclosure heated from the side", in *Third uk national conference incorporating first european conference on thermal sciences*, vol. 1, 1992, pp. 507–513.

[64] H. Werner and H. Wengle, "Large-eddy simulation of turbulent flow over and around a cube in a plate channel", in *Turbulent shear flows 8*, Springer, 1993, pp. 155–168.

[65] J. Holman, *Heat transfer*. McGraw-Hill Inc, 2001, Eighth, SI Metric Edition.

[66] A. Ganguli, A. Pandit, and J. Joshi, "Cfd simulation of heat transfer in a two-dimensional vertical enclosure", *Chemical engineering research and design*, vol. 87, no. 5, pp. 711–727, 2009.

[67] R. Hasib, R. Kumar, Shashi, and S. Kumar, "Simulation of an experimental compartment fire by cfd", *Building and environment*, vol. 42, no. 9, pp. 3149 –3160, 2007.

[68] T. Rinne, J. Hietaniemi, and S. Hostikka, "Experimental validation of the fds simulations of smoke and toxic gas concentrations", VTT, Finland, Working Paper 66, 2007.

[69] B. Storm and M. Pantesjö, "The use of simulation in fire investigation", Bachelors thesis, Stord/Haugesund University College, 2009.

[70] W. Jahn, G. Rein, and J. Torero, "The Effect of Model Parameters on the Simulation of Fire Dynamics", in *Proceedings of the ninth symposium on fire safety science*, 2008.

[71] G. Rein, J. Torero, W. Jahn, J. Stern-Gottfried, N. Ryder, S. Desanghere, M. Läzaro, F. Mowrer, A. Coles, D. Joyeux, D. Alvear, J. Capote, A. Jowsey, C. Abecassis-Empis, and P. Reszka, "Round-Robin Study of a priori Modelling Predictions of The Dalmarnock Fire Test One", *Fire safety journal*, vol. 44, no. 4, pp. 590–602, 2009.

[72] G. Rein, C. Abecassis Empis, and R. Carvel, "The Dalmarnock Fire Tests: Experiments and Modelling", University of Edinburgh, 2007.

[73] K. McGrattan, C. Bouldin, and G. Forney, "Federal Building and Fire Safety Investigation of the World Trade Center Disaster: Computer Simulation of the Fires in the WTC Towers", National Institute of Standards and Technology, Gaithersburg, Maryland, NIST NCSTAR 1-5F, 2005.

[74] A. Hamins, A. Maranghides, K. McGrattan, Ohlemiller, and R. Anletiner, "Federal Building and Fire Safety Investigation of the World Trade Center Disaster: Experiments and Modeling of Multiple Workstations Burning in a Compartment", National Institute of Standards and Technology, Gaithersburg, Maryland, NIST NCSTAR 1-5E, 2005.

[75] A. Hamins, A. Maranghides, K. McGrattan, E. Johnsson, T. Ohlemiller, M. Donnelly, J. Yang, G. Mulholland, K. Prasad, S. Kukuck, R. Anleitner, and T. McAllister, "Federal Building and Fire Safety Investigation of the World Trade Center Disaster: Experiments and Modeling of Structural Steel Elements Exposed to Fire", National Institute of Standards and Technology, Gaithersburg, Maryland, NIST NCSTAR 1-5B, 2005.

[76] X. Zhang, M. Yang, J. Wang, and Y. He, "Effects of computational domain on numerical simulation of building fires", *Journal of fire protection engineering*, vol. 20, no. 4, pp. 225–251, 2010.

[77] Y. He, C. Jamieson, A. Jeary, and J. Wang, "Effect of computation domain on simulation of small compartment fires", *Fire safety science*, vol. 9, pp. 1365–1376, 2008.

[78] M. J. Hurley, D. T. Gottuk, J. R. Hall Jr, K. Harada, E. D. Kuligowski, M. Puchovsky, J. M. Watts Jr, C. J. Wieczorek, *et al.*, *Sfpe handbook of fire protection engineering*. Springer, 2015.

[79] D. Stroup and A. Lindeman, "Verification and Validation of Selected Fire Models for Nuclear Power Plant Applications", United States Nuclear Regulatory Commission, Washington, DC, NUREG-1824, Supplement 1, 2013.

[80] N. Pope and C. Bailey, "Quantitative comparison of fds and parametric fire curves with post-flashover compartment fire test data", *Fire safety journal*, vol. 41, no. 2, pp. 99 –110, 2006.

[81] H. Yaping, F. Anthony, and L. Mingchun, "Determination of interface height from measured parameter profile in enclosure fire experiment", *Fire safety journal*, vol. 31, no. 1, pp. 19 –38, 1998.

[82] H. Ingason and Y. Z. Li, "Model scale tunnel fire tests with longitudinal ventilation", *Fire safety journal*, vol. 45, no. 6–8, pp. 371 –384, 2010.

[83] J. Ji, C. Fan, W. Zhong, X. Shen, and J. Sun, "Experimental investigation on influence of different transverse fire locations on maximum smoke temperature under the tunnel ceiling", *International journal of heat and mass transfer*, vol. 55, no. 17–18, pp. 4817 –4826, 2012.

[84] S. R. Lee and H. S. Ryou, "An experimental study of the effect of the aspect ratio on the critical velocity in longitudinal ventilation tunnel fires", *Journal of fire sciences*, vol. 23, no. 2, pp. 119–138, 2005.

[85] E. Blanchard, "Computational study of water mist for a tunnel fire application", PhD thesis, Université Henri Poincaré – Nancy Université, 2013.

[86] E. Blanchard, P. Boulet, S. Desanghere, E. Cesmat, R. Meyrand, J. Garo, and J. Vantelon, "Experimental and numerical study of fire in a midscale test tunnel", *Fire safety journal*, vol. 47, pp. 18 –31, 2012.

[87] R. Carvel, A. Beard, and P. Jowitt, "The influence of longitudinal ventilation systems on fires in tunnels", *Tunnelling and underground space technology*, vol. 16, no. 1, pp. 3 –21, 2001.

[88] V. Babrauskas, "Estimating large pool fire burning rates", *Fire technology*, vol. 19, no. 4, pp. 251–261, 1983.

[89] N. Danziger and W. Kennedy, "Longitudinal ventilation analysis for the glenwood canyon tunnels", in *Proceedings of the fourth international symposium aerodynamics and ventilation of vehicle tunnels*, 1982, pp. 169–186.

[90] J. Kunsch, "Simple model for control of fire gases in a ventilated tunnel", *Fire safety journal*, vol. 37, no. 1, pp. 67–81, 2002.

[91] J. S. Roh, H. S. Ryou, D. H. Kim, W. S. Jung, and Y. J. Jang, "Critical velocity and burning rate in pool fire during longitudinal ventilation", *Tunnelling and underground space technology*, vol. 22, no. 3, pp. 262–271, 2007.

[92] W Tang, L. Hu, and L. Chen, "Effect of blockage-fire distance on buoyancy driven back-layering length and critical velocity in a tunnel: An experimental investigation and global correlations", *Applied thermal engineering*, vol. 60, no. 1, pp. 7–14, 2013.

[93] J Quintiere, B. J. McCaffrey, and T Kashiwagi, "A scaling study of a corridor subject to a room fire", *Combustion science and technology*, vol. 18, no. 1-2, pp. 1–19, 1978.

[94] H. Ingason, "State of the art of tunnel fire research", *Fire safety science*, vol. 9, pp. 33–48, 2008.

[95] P. J. DiNenno, *Sfpe handbook of fire protection engineering*. SFPE, 2008.

[96] C. Clauser and E. Huenges, "Thermal conductivity of rocks and minerals", *Rock physics & phase relations: A handbook of physical constants*, pp. 105–126, 1995.

[97] M. G. Vega, K. M. A. Díaz, J. M. F. Oro, R. B. Tajadura, and C. S. Morros, "Numerical 3d simulation of a longitudinal ventilation system: Memorial tunnel case", *Tunnelling and underground space technology*, vol. 23, no. 5, pp. 539–551, 2008.

[98] K. C. Karki, S. V. Patankar, E Rosenbluth, and S Levy, "Cfd model for jet fan ventilation systems", in *Bhr group conference series publication*, Bury St. Edmunds; Professional Engineering Publishing; 1998, vol. 43, 2000, pp. 355–380.

[99] C. M. Se, E. W. Lee, and A. C. Lai, "Impact of location of jet fan on airflow structure in tunnel fire", *Tunnelling and underground space technology*, vol. 27, no. 1, pp. 30 –40, 2012.

[100] D. Borello, G. Giuli, and F. Rispoli, "A cfd methodology for fire spread and radiative effects simulation in longitudinal ventilation tunnels: Application to the memorial tunnel", in *International phoenics user conference*, Moscow, 2002.

[101] F. Colella, G. Rein, R. Carvel, P. Reszka, and J. Torero, "Analysis of the ventilation systems in the dartford tunnels using a multi-scale modelling approach", *Tunnelling and underground space technology*, vol. 25, no. 4, pp. 423 –432, 2010.

[102] C. D. E. Ang, G. Rein, J. Peiro, and R. Harrison, "Simulating longitudinal ventilation flows in long tunnels: Comparison of full cfd and multi-scale modelling approaches in fds6", *Tunnelling and underground space technology*, vol. 52, pp. 119 –126, 2016.

[103] V. Betta, F. Cascetta, M. Musto, and G. Rotondo, "Numerical study of the optimization of the pitch angle of an alternative jet fan in a longitudinal tunnel ventilation system", *Tunnelling and underground space technology*, vol. 24, no. 2, pp. 164 –172, 2009.

[104] V. Betta, F. Cascetta, M. Musto, and G. Rotondo, "Fluid dynamic performances of traditional and alternative jet fans in tunnel longitudinal ventilation systems", *Tunnelling and underground space technology*, vol. 25, no. 4, pp. 415 –422, 2010.

[105] S. Bari and J. Naser, "Simulation of smoke from a burning vehicle and pollution levels caused by traffic jam in a road tunnel", *Tunnelling and underground space technology*, vol. 20, no. 3, pp. 281 –290, 2005.

[106] G. Hua, W. Wang, Y. Zhao, and L. Li, "A study of an optimal smoke control strategy for an urban traffic link tunnel fire", *Tunnelling and underground space technology*, vol. 26, no. 2, pp. 336 –344, 2011.

[107] F. Wang, M. Wang, S. He, J. Zhang, and Y. Deng, "Computational study of effects of jet fans on the ventilation of a highway curved tunnel", *Tunnelling and underground space technology*, vol. 25, no. 4, pp. 382 –390, 2010.

[108] R. Lewis, *Turbomachinery performance analysis*. Butterworth-Heinemann, 1996.

[109] K. McGrattan, S. Hostikka, R. McDermott, J. Floyd, C. Weinschenk, and K. Overholt, "Fire dynamics simulator, technical reference guide, volume 2: Verification", NIST Special Publication 1019, 2016.

[110] E. Jacques and P. Wauters, "Improving the ventilation efficiency of jet fans in longitudinally ventilated rectangular ducts", in *Proceedings of the us mine ventilation symposium*, 1999, pp. 503–507.

[111] K. R. Mutama, "Wind tunnel investigation of jet fan aerodynamics", PhD thesis, University of British Columbia, 1995.

[112] W. Kümmel, "Technische strömungsmechanik", *Theorie und praxis*, vol. 3, 2004.

[113] X. Deckers, S. Haga, N. Tilley, and B. Merci, "Smoke control in case of fire in a large car park: Cfd simulations of full-scale configurations", *Fire safety journal*, vol. 57, pp. 22 –34, 2013.

[114] H.-M. Jang and F. Chen, "On the determination of the aerodynamic coefficients of highway tunnels", *Journal of wind engineering and industrial aerodynamics*, vol. 90, no. 8, pp. 869–896, 2002.

[115] D. Fletcher, J. Kent, V. Apte, and A. Green, "Numerical simulations of smoke movement from a pool fire in a ventilated tunnel", *Fire safety journal*, vol. 23, no. 3, pp. 305 –325, 1994.

[116] K. Van Maele and B. Merci, "Application of rans and les field simulations to predict the critical ventilation velocity in longitudinally ventilated horizontal tunnels", *Fire safety journal*, vol. 43, no. 8, pp. 598–609, 2008.

[117] K. McGrattan and A. Hamins, "Numerical simulation of the howard street tunnel fire", *Fire technology*, vol. 42, no. 4, pp. 273–281, 2006.

[118] J. S. Li and W. Chow, "Numerical studies on performance evaluation of tunnel ventilation safety systems", *Tunnelling and underground space technology*, vol. 18, no. 5, pp. 435 –452, 2003.

[119] L. Hu, W. Peng, and R. Huo, "Critical wind velocity for arresting upwind gas and smoke dispersion induced by near-wall fire in a road tunnel", *Journal of hazardous materials*, vol. 150, no. 1, pp. 68 –75, 2008.

[120] E. Kim, J. P. Woycheese, and N. A. Dembsey, "Fire dynamics simulator (version 4.0) simulation for tunnel fire scenarios with forced, transient, longitudinal ventilation flows", *Fire technology*, vol. 44, no. 2, pp. 137–166, 2008.

[121] C. Zhang, J. G. Silva, C. Weinschenk, D. Kamikawa, and Y. Hasemi, "Simulation methodology for coupled fire-structure analysis: Modeling localized fire tests on a steel column", *Fire technology*, vol. 52, no. 1, pp. 239–262, 2016.

[122] J. C. G. Silva, A. Landesmann, and F. L. B. Ribeiro, "Performance-based analysis of cylindrical steel containment vessels exposed to fire", *Fire safety journal*, vol. 69, pp. 126–135, 2014.

[123] J. Silva, A. Landesmann, and F Ribeiro, "Interface model to fire-thermomechanical performance-based analysis of structures under fire conditions", in *Proceedings of the fire and evacuation modeling technical conference*, 2014.

[124] J. Silva, "Tridimensional interface model to fire-thermomechanical analysis of structures under fire conditions", in Portugese, PhD thesis, Federal University of Rio de Janeiro, 2014.

[125] B. Schrefler, P Brunello, D Gawin, C. Majorana, and F Pesavento, "Concrete at high temperature with application to tunnel fire", *Computational mechanics*, vol. 29, no. 1, pp. 43–51, 2002.

[126] B. Schrefler, R Codina, F Pesavento, and J Principe, "Thermal coupling of fluid flow and structural response of a tunnel induced by fire", *International journal for numerical methods in engineering*, vol. 87, no. 1-5, pp. 361–385, 2011.

[127] U. Wickström, D. Duthinh, and K. B. McGrattan, "Adiabatic surface temperature for calculating heat transfer to fire exposed structures", in *Proceedings of the eleventh international interflam conference. interscience communications, london*, vol. 167, 2007.

[128] M. Zeiml, R. Lackner, F. Pesavento, and B. A. Schrefler, "Thermo-hydro-chemical couplings considered in safety assessment of shallow tunnels subjected to fire load", *Fire safety journal*, vol. 43, no. 2, pp. 83–95, 2008.

[129] A. Paajanen, T. Korhonen, S. Merja, S. Hostikka, M. Malendowski, and R. Gutkin, "Fds2fem–a tool for coupling fire and structural analyses", in *Iabse symposium report*, International Association for Bridge and Structural Engineering, vol. 100, 2013, pp. 218–224.

[130] E. Committee *et al.*, "Eurocode2: Design of concrete structures-part 1-2: General rules-structural fire design", ENV 1992-1-2, Tech. Rep., 2004.

[131] C. Steinert, "Smoke and heat production in tunnel fires", in *The international conference on fires in tunnels*, vol. 123, 1994, p. 137.

[132] G Hadjisophocleous, D. Lee, and W. Park, "Full-scale experiments for heat release rate measurements of railcar fires", in *International symposium on tunnel safety and security (istss), new york*, 2012, pp. 457–466.

[133] H. Ingason, S. Gustavsson, and M. Dahlberg, "Heat release rate measurements in tunnel fires", in *The international conference on fires in tunnels*, 1994.

[134] C. Barber, A. Gardiner, and M. Law, "Structural fire design of the øresund tunnel", in *Proceedings of the international conference on fires in tunnels*, 1994, pp. 313–332.

[135] A. Lönnermark, J. Lindström, Y. Li, A. Claesson, M. Kumm, and H. Ingason, "Full-scale fire tests with a commuter train in a tunnel", SP Report 05, 2012.

[136] M. Cheong, M. Spearpoint, and C. Fleischmann, "Calibrating an fds simulation of goods-vehicle fire growth in a tunnel using the runehamar experiment", *Journal of fire protection engineering*, vol. 19, no. 3, pp. 177–196, 2009.

[137] J. Trelles and J. R. Mawhinney, "Cfd investigation of large scale pallet stack fires in tunnels protected by water mist systems", *Journal of fire protection engineering*, vol. 20, no. 3, pp. 149–198, 2010.

[138] A. Witek, "The impact of the admixture of polypropylene fibers on the fire resistance of concrete", in Polish, PhD thesis, Lodz University of technology, 2015.

[139] D Gawin, F Pesavento, and B. Schrefler, "Simulation of damage–permeability coupling in hygro-thermo-mechanical analysis of concrete at high temperature", *Communications in numerical methods in engineering*, vol. 18, no. 2, pp. 113–119, 2002.

[140] Y. Zhang, M. Zeiml, C. Pichler, and R. Lackner, "Model-based risk assessment of concrete spalling in tunnel linings under fire loading", *Engineering structures*, vol. 77, pp. 207 –215, 2014.

[141] M. Zeiml, R. Lackner, F. Pesavento, and B. A. Schrefler, "Thermo-hydro-chemical couplings considered in safety assessment of shallow tunnels subjected to fire load", *Fire safety journal*, vol. 43, no. 2, pp. 83 –95, 2008.

[142] A. Andreozzi, N. Bianco, M. Musto, and G. Rotondo, "Adiabatic surface temperature as thermal/structural parameter in fire modeling: Thermal analysis for different wall conductivities", *Applied thermal engineering*, vol. 65, no. 1, pp. 422–432, 2014.

[143] I. Vermesi, F. Colella, G. Rein, and G. Jomaas, "The feasibility of multiscale modeling of tunnel fires using fds 6", in *6th international symposium on tunnel safety and security*, 2014.

[144] F. Pesavento, M. Pachera, P. Brunello, and B. Schrefler, "Concrete exposed to fire: From fire scenario to structural response", *Key engineering materials*, pp. 556–563, 2016.

[145] M. Pachera, P. Brunello, and M. Raciti Castelli, "Comparison between rans and les approaches to the simulation of natural convection in a differentially heated square cavity", *Wseas transactions on heat and mass transfer*, vol. 9, pp. 261–269, 2014.

[146] M. Pachera, P. Brunello, F. Pesavento, B. Schrefler, and K. Bergmeister, "Numerical methods for the analysis of ventilation and structural response of tunnel in case of fire", in *Vgr conference valutazione e gestione del rischio negli insediamenti civili ed industriali*, in Italian, vol. 1, 2016.

[147] M. Pachera, A. Witek, F. Pesavento, D. Gawin, and P. Brunello, "Combined approach for high temperature concrete simulations", in *11th conference on performance-based codes and fire safety design methods*, vol. 1, 2016.

[148] M. Pachera, P. Brunello, and M. Raciti Castelli, "Validation of fire dynamic simulator (fds) for pool fire in large enclosures", in *7th european combustion meeting*, 2015.

[149] M. Pachera and P. Brunello, "Numerical investigation on jet fans for fire control in short tunnels", in *7th international symposium on safety and security in tunnels*, 2016.

[150] M. Pachera, F. Pesavento, and P. Brunello, "Advanced numerical methods in fire safety engineering", in *32th international cae conference*, 2016.